PRIMARY COSMIC RADIATION IN 1958

AND VARIATIONS

Thesis by

Hugh R. Anderson

Submitted in Partial Fulfillment of the

Requirements for the Degree

of Doctor of Philosophy

California Institute of Technology

1961

ACKNOWLEDGEMENT

The author wishes to thank Professor H. V. Neher, who planned this set of measurements and made some of them. I am grateful for his advice and help in analyzing the data and preparing this thesis. The Office of Naval Research supported this work, and their assistance is hereby acknowledged.

Many persons have indirectly helped to make the balloon flights. In particular the author wishes to thank the U. S. Weather Bureau at Bismarck, North Dakota, Commander Price Lewis Jr., and the officers and men of the U. S. S. Staten Island, the officers and men of the U. S. S. Eastwind, and the personnel of Awarua Radio Station at Invercargill, New Zealand. The United States Air Force made the work at Thule Air Base possible.

Mr. Don Barelli accompanied the author to Bismarck and to the Antarctic, and Mr. Ralph Miles has been to the Arctic three times and has discussed the data with me at length. Their help has been essential.

Finally, I wish to thank the Jet Propulsion Laboratory of NASA, which has been very understanding during the last eight months of work on this thesis, and has given three tuition grants during this time.

ABSTRACT

During the summer and fall of 1958, 38 pairs of simultaneous measurements of cosmic ray ionization in the atmosphere were made with integrating ionization chambers carried to high altitudes by balloons, and accompanied by barometric sensors. One of each pair of measurements was made at a base station and the other at a roving station which released balloons at a set of different geomagnetic latitudes ranging from 87°N to 79°S.

The base station data exhibit variations with time corresponding to changes in the primary flux. The effects of the time variations upon the roving station measurements are partially removed with the aid of the base station data leaving the ionization as a function of latitude only. The symmetry of the geomagnetic field in the northern and southern hemispheres is studied by means of the latter data. By assuming a charge spectrum, the differential rigidity spectrum of primary cosmic rays in 1958 is calculated from the ionization as a function of latitude by means of geomagnetic theory. The corresponding integral spectrum shows that $N_{\text{all nuclei}}(>0.6\ \text{Bv}) = 0.107$ particles/cm^2 sec sterad, $N_{\text{all nuclei}}(>16\ \text{Bv}) = 0.012$ particles/cm^2 sec sterad.

A primary rigidity spectrum is calculated from similar data taken by Neher, et al. in 1954. The ionization at Thule, Greenland, from 1951-1960 is presented. These data show the inverse correlation between cosmic ray intensity and sunspot number, and suggest that the intensity modulation lags the sunspot number by about 6 months.

TABLE OF CONTENTS

TABLE OF TABLES

PREFACE

This thesis first describes how the effects of cosmic radiation vary with position on the earth at any particular time and how this spatial distribution itself varies with time. Some of the ways in which these effects are observed are discussed, including the work at the CIT Cosmic Ray Laboratory during recent years which has generated the set of measurements which form the principal subject of this paper. This much will explain the purpose of performing the experiment and will allow one to follow the rest of the paper with the author's goals in mind.

The present set of measurements is then described in some detail, and the data obtained are reduced to absolute units and presented complete.

The next chapter then explains a way to deduce from these data a primary cosmic ray spectrum as well as a description of its day to day variations during the period measurements were made. The conclusions of this work are stated.

Finally, these results and the experimental data are compared with observations made at other times and by other laboratories.

I. INTRODUCTION

If we choose a time when no special solar activity and no geomagnetic disturbances are observed at the earth, then the cosmic radiation in the region of the earth's orbit but beyond the significant influence of the geomagnetic field consists of a uniform, isotropic flux of charged particles constant in time over periods of several hours. (It is not yet known if the flux of particles having energy greater than 10^{16} ev is isotropic and constant.) About 86% of these are protons, 12.7% alpha particles, and 1.3% are heavier nuclei. Quite recently a flux of electrons has been observed which is about 3% of the proton flux. By flux of particles we mean the unidirectional flux, which may be measured in units of particles $cm^{-2} sec^{-1} sterad^{-1}$. If the flux is denoted by F, then $F\, d\Omega\, dS\, dt$ equals the number of particles moving in a solid angle $d\Omega$ steradians which cross an area dS cm^2 normal to the direction of $d\Omega$ in time dt. The flux of a particular type and energy particle may depend upon the location of dS, the direction of $d\Omega$ and upon time. The cosmic ray particles are distributed in energy, and this distribution may be described by a differential energy spectrum, $J_i(E)$, where

$$J_i(E)\,dE = \frac{\text{nucleons contained in nuclei of type i}}{\text{cm}^2\ \text{sec sterad}} \qquad (1)$$

when the nuclei have kinetic energy between E and E + dE. Alternatively one may describe the numbers of particles by their distribution in magnetic rigidity, $J_i(R)$, where

$$J_i(R)\,dR = \frac{\text{nucleons contained in nuclei of type i}}{\text{cm}^2\ \text{sec sterad}} \qquad (2)$$

if the nuclei have a rigidity between R and R + dR. Magnetic rigidity is defined as the momentum of a particle divided by its charge, and is ordinarily described in volts. In this case

$$R_i = \frac{pc(\text{in electron volts})}{Z_i}\ , \qquad (3)$$

numerically, and so the kinetic energy E_i is given by

$$E_i = \sqrt{(M_i c^2)^2 + (Z_i R_i)^2} - M_i c^2\ , \qquad (4)$$

with R in volts, and E_i and $M_i c^2$ in electron volts. Z_i is the net number of electronic charges of the type i nuclei. It is worth remembering that in these units the radius of curvature, in cm, of a particle moving in a uniform field of B gauss is

$$\rho = \frac{1}{B}\ \frac{R}{300}\ . \qquad (5)$$

The total flux of nucleons in space is then

$$\sum_i \int_0^\infty dR\ J_i(R) = \sum_i N_i(>0)\ \frac{\text{nucleons}}{\text{cm}^2\ \text{sec sterad}} \qquad (6)$$

where $N_i(>R)$ equals the flux of nucleons in type nuclei which have a rigidity greater than R. The total flux of nuclei is

$$\sum_i \int_0^\infty dR\ \frac{J_i(R)}{A_i} = \sum_i \frac{N_i(>0)}{A_i}\ \frac{\text{nuclei}}{\text{cm}^2\ \text{sec sterad}} \cdot \qquad (7)$$

Customarily the term cosmic radiation applies only to nuclei with energies above some value of the order of 100 mev per nucleon or a rigidity of 0.4 Bv. In this paper the term cosmic rays will mean particles with greater than this rigidity and coming from interstellar space into the solar system. It is not known at present whether or not lower energy particles occur beyond the solar system but they have not yet been observed at the earth.

It is now known that the sun ejects protons with energies from nearly zero to greater than 1 Bev on occasion, and must eject equal numbers of electrons as well. The lower energy flux is termed solar plasma, while the higher energy protons are called solar protons or solar cosmic rays.

If equation 7 is integrated from 0.4 Bv to ∞ the total cosmic

ray flux $\sum_i \frac{N_i(>.4\ \mathrm{Bv})}{A_i}$ is obtained which varies from about 0.1 to 0.25 particles/cm^2 sec sterad in the vicinity of earth's orbit.

Particles occur with energies at least as high as 10^{19} ev. The relative numbers of different kinds of nuclei may be independent of energy. The particles with rigidity greater than 5 Bv are distributed so that approximately 86% are protons, 12.7% are alphas, and the rest heavier nuclei. Recent measurements show that in 1960 the flux of primary electrons with R > 0.5 Bv was about 3% of the proton flux. If there are any primary photons their flux is half of this or less.

At the top of the earth's atmosphere equation 7 no longer gives the particle flux even from directions above the horizon. The geomagnetic field deflects the particles so that at a particular location on the earth a particle must have a rigidity greater than some value R_{min} to reach that point from infinity and be moving in a given direction at the point it reaches the earth. The value of R_{min} depends upon both this direction and upon the location on the earth. Since the earth's field is nearly symmetrical about the magnetic axis, R_{min} in a given direction depends primarily upon magnetic latitude and only slightly upon longitude, as is discussed at length in Chapter VI. For this reason the variation of R_{min} with location on the earth is normally called a latitude variation, the smaller variation with longitude being understood under this name.

Thus, to reach the earth moving vertically downward at the magnetic equator a particle requires $R > 16$ Bv, and this minimum rigidity decreases at higher latitudes until it reaches zero at the magnetic pole. Also at any location on the earth, except at the poles, particles from the western part of the sky can arrive with lower rigidity than particles from the east if the particles have positive charges, and vice versa if they bear negative charges; the exact value of R_{min} depending upon both azimuth and zenith angle (1).

It is remarkable that because of Liouville's theorem on the constant density of points in phase space the flux $J_i(R)$ reaching the earth at any location from any direction must have one of two values. Either it is zero or else it has the same value as it has in free space for the same beam of particles, provided that only static magnetic fields or completely absorbing bodies act upon the particle beam in its passage from free space to the earth. Of course, this theorem holds for any location, and is not confined to points on the earth's surface. That is, if $J_i(R)$ beyond the geomagnetic field is homogeneous and isotropic, as is thought to be normally the case, then on the earth $J_i(R)$ has either this free space value or zero. On the contrary, if $J_i(R)$ depends upon position and direction in free space, then its value at the earth will be zero or will have the value which characterized the particular beam of particles in question outside the earth's

field. The initial position and direction of the beam may be found by tracing back along the orbits of a pencil of particles from the earth through the geomagnetic field.

In deciding whether or not $J_i(R)$ is homogeneous and isotropic in free space we need only consider a spherical shell of space surrounding the earth beyond the limit of the geomagnetic field. The field limit may be defined as the surface where the geomagnetic field strength has dropped to the intensity of the general interplanetary field in the region of earth's orbit or has deviated from the predicted radial dependence, or else where it has dropped to a strength such that the radius of curvature of the least rigid particle to be considered is some large multiple of the distance to earth's center. In the light of recent measurements, the field may be regarded as ending at 13 earth radii, at least at the subsolar point. Magneto hydrodynamic waves exist as close as 7 earth radii and possibly closer (2).

At any particular time, then, the distribution of primary cosmic rays over the earth depends upon the functions $J_i(R)$ in space beyond the earth's field, and upon the existing geomagnetic field. We shall assume that the undisturbed field prevails unless the contrary is stated. When the intensity of radiation within or above the earth's atmosphere at any particular time and place is measured with an instrument, the number obtained really depends upon these factors:

1) The instrument's response to the primary and secondary radiation which appears at the point of measurement.

2) The relationship between the fluxes of secondary and primary radiations present at the point of measurement, and the primary flux above the atmosphere at the particular location of the measurement. In general, this relationship depends upon the nature and direction of flux at the point of measurement, the distribution of mass overhead, and the direction of the primaries' motion. Insofar as the amount and direction of returning albedo flux depends upon the geomagnetic field, the coupling between primary radiation and total radiation depends upon the geomagnetic coordinate of the location of measurement. This coupling will also depend upon location if one considers the influences of the geomagnetic field upon the trajectories of particles within the atmosphere.

3) The primary flux overhead and its distribution in azimuth and zenith angle, which in turn depends upon

a) The primary flux beyond the earth's field.

b) The geomagnetic field's effect at the location of the measurement.

The way in which these factors determine the result of a measurement may be expressed by an integral equation. Such equations are discussed in Chapter VI. Dorman (3) considers such expressions at length.

The results of a measurement may be used to study any of the factors named above, but in this paper we shall be chiefly interested in 3a), the primary flux. Complete knowledge of the primary flux near the earth would consist of knowing the differential rigidity or energy spectra of each type of particle and the dependence of this flux upon direction and time. Furthermore, one would like to know how the flux depends upon solar activity and upon the condition of interplanetary space, and to know over what volume of space the sun affects the cosmic ray flux. To complete our knowledge of the radiation we would like to know how the flux is distributed throughout interstellar space and to know where it comes from.

Most of this information is not yet in hand. Measurements have so far been made only at the earth's surface or within some portion of its atmosphere with the exception of a few experiments in satellites and space probes. From those results we may draw the following description of the primary radiation and measurements of it.

1) As stated above, we may consider particles with rigidity greater than 0.4 Bv. The flux of such particles beyond the earth's field varies from 0.1 or somewhat less to at least 0.25 particles/cm^2 sec sterad. The relative numbers of different sorts of nuclei, i.e., the charge spectrum, may be independent of energy. For all particles above 5 Bv rigidity the distribution is approximately 86% protons, 12.7%

alphas, 1.3% heavier nuclei, and an electron flux a few percent of the proton flux.

2) At most times the variation of measured intensity with latitude can be explained entirely by the action of the geomagnetic field, and need not be ascribed to anisotropic primary flux (4, 5). Hence the latitude variation reflects the primary rigidity spectrum. (The term primary flux is used to mean the flux near the earth's orbit.)

3) The primary integral spectrum at any time may be expressed by $N_i(>R) = \text{constant}_i / R^n$ for $R > 2.5$ Bv. The constant is different for different kinds of nuclei, but probably n is not. The exponent lies between 1 and 1.5 for $R < 15$ Bv, and increases slowly with increasing R. At 100 Bv it is reported that $n = 1.3 \pm .2$, and from 4×10^{15} to 10^{18} volts $n \simeq 2.13$. See Neher (4). Particles having $R < 2.5$ Bv do not always have a spectrum with the above form.

4) The primary flux is observed to vary with time, and usually the flux of lower energy particles ($R < 5$ to 10 Bv) changes much more than the flux of higher energy ones. Between 0.4 and 2.5 Bv the fluctuations are greatest, the differential spectrum sometimes showing a maximum in this interval and sometimes apparently not. Evidence of this sort of fluctuation is presented later in the present paper. At intermediate rigidities, 2.5 to 16 Bv, both the constant and exponent

of the spectrum change, but the form is preserved. At greater rigidities the percentage variation apparently decreases with increasing R.

Consequently, the amplitude of variation measured by an instrument depends strongly upon the energy of primary to which it responds. The variations are usually classified by their period and cause instead of by amplitude. We will discuss the variations in some detail because this paper is concerned with some of them. Exhaustive discussions of the variations may be found in Dorman (3) and in review articles by Singer (6), Neher (5), Sarabhai (7), Elliott (8), and others.

There are, first of all, variations produced by changes in the atmosphere which affect all measurements within the atmosphere. These may be separated into a variation with the mass of air overhead (the barometric effect) and variations with the distribution of that mass with altitude (the temperature effect). The latter variation is caused by the production of unstable particles by the primary particles, and so does not affect those secondary particles, such as neutrons, which do not have unstable ancestors. In considering the effects upon μ meson detectors at low altitudes, the temperature effect has been regarded as consisting of a positive coefficient for the temperature at depths less than 300 g/cm^2 approximately, plus a negative effect for the temperature throughout the atmosphere. The positive effect occurs because when the air becomes less dense π mesons are more likely to decay into μ mesons than to suffer collisions. The negative effect

appears because more μ mesons decay before reaching the detector when the atmosphere is rarefied by having a higher temperature. See Duperior (9) for analyses in terms of two coefficients. More precise calculations use a temperature coefficient which varies continuously with altitude above the measuring station. See Dorman (3).

The barometric coefficient is taken to be -0.30%/mm of Hg at Huancayo, and -0.18%/mm of Hg for a shielded ion chamber at Cheltenham, Maryland (10), and -1.28%/mm of Hg for neutron monitors (11). (Note: 760 mm of Hg $\simeq$ 1013 millibars.) According to Dorman (3), the coefficient for a shielded ion chamber at sea level for a 1°C increase of temperature in the whole atmosphere is about -0.29%.

The atmosphere changes in a regular way with latitude, and also varies periodically both daily and seasonally. In addition, it experiences both lunar and solar tides. The temperature of the very high atmosphere may increase when a solar flare emits additional radiation. Thus the atmosphere varies with some of the same periods which one may expect to find in primary cosmic ray variations.

Despite this it has been possible to measure some true primary variations. Table I lists the amplitudes of some of these measured in various ways. The table contains data given by Dorman, but the figures marked with an asterisk have been added by the author. The variations listed there are:

TABLE I. Time Variations of Cosmic Ray Intensity (amplitude in % except as noted)

Type	Hard Component 60 mwc Underground	Sea Level Hard Component $\lambda=50°$	Sea Level Hard Component $\lambda=0°$	Ground Level Nucleonic Component $\lambda=50°$	Ground Level Nucleonic Component $\lambda=0°$	Ionization at 20 g/cm^2	Presumed Cause
Seasonal		2-4	$\lesssim 0.5$				Atmospheric Temperature effect
Diurnal		~ 0.15	~ 0.15				
11 year		~ 2	~ 2				Modulation
Annual		0.5-1	0.5-1			Factor of 2*	of galactic cosmic rays by plasma and magnetic fields ejected from the sun
27 day		~ 0.3	~ 0.35	1		~ 10*	
Diurnal	.05	~ 0.3	~ 0.35	0.6	0.43	1-2	
Semi-diurnal	.02	~ 0.3	~ 0.3				
Day to day non periodic						5-10*	
Forbush decreases	$\lesssim .5$	$\lesssim 10$	$\lesssim 10$			20	
Large increases following solar flares	$\lesssim 0.5$	~ 400	~ 20	~ 5500	~ 50	Factor of 8 at least ▼	Solar cosmic rays
Small increases following solar flares		~ 0.3†		~ 0.6		$\lesssim 10$	
Sidereal	$\lesssim .02$	$\lesssim .02$	$\lesssim .02$				Anisotropic flux of galactic cosmic rays

Data without reference are taken from Dorman (3).

*Present paper

† Apparently due to variation in temperature of the upper atmosphere resulting from changing ultraviolet radiation from the sun.

▽ J. Winckler, J. Geophys. Res., 65, 1331-1359 (1960).

a) Solar diurnal and semi-diurnal. The existence of these has not been firmly established. It is thought that they might be produced by corpuscular streams from the sun shielding the earth from galactic rays arriving from certain directions. The sun might also produce a steady flow of protons (or heavier nuclei) with cosmic ray energies which arrive anisotropically. See Singer (6).

b) Steller diurnal or sidereal. There is no positive evidence for this variation, but it would be expected if one part of the galaxy produces more cosmic rays than another, and if these reach us along relatively straight or at least orderly orbits. In particular, one might expect to see sidereal variations in the very high energy particles which should not be scattered as much as the lower energy ones on the way from any source to us. See Elliot and Dolbear (12), Sarabhai (7), Sekido (13), and Galbraith (14).

c) 27 day variations. These are only semi-periodic, persisting for a few periods and then dying out or changing phase. These variations must be produced by solar corpuscular streams and perhaps solar protons of cosmic ray energy which flow out from some region of the sun which persists for more than a solar rotation. The streams modulate the intensity of galactic cosmic rays, while the solar protons increase the total intensity. The streams are presumed to affect the flux at the earth only when their source lies in a particular region of the solar disc visible from earth. The sun's 27 day period of rotation

then induces a similar periodic change in the particle flux. See Lange and Forbush (10,15,16) and Simpson (17).

d) Annual variation. Existence of this variation is doubtful. See Forbush (15).

e) 11 year variation. This is the largest periodic variation known. The cosmic ray intensity varies inversely with the sunspot number which indicates the general activity of the sun, and which varies with an eleven year period. The sun, when it is active, apparently prevents some of the cosmic rays from interstellar space from reaching the region of the earth's orbit. No anisotropy is observed and particles with rigidity above 10 Bv are affected so that it is thought that the inhibitions must occur many AU from the sun. Results from the space probes Pioneer I and V show that the depressed flux is constant out to at least 2×10^6 km from the earth (20). See Forbush (16) and Neher (18,19). In this variation the flux of particles with rigidities from 0.5 Bv (possibly less) to more than 10 Bv changes, but down to at least 0.9 Bv some particles remain even when the sun is active.

f) Non-periodic reductions during the times of magnetic storms. These are called Forbush decreases. Characteristically, the cosmic ray intensity measured by shielded ion chambers at sea level drops $\lesssim 10\%$ in $\lesssim 1$ hour and remains at the lower level for several days, gradually returning to its former value. The drop often

coincides with a magnetic storm's onset, but not always, and conversely, not all magnetic storms produce Forbush decreases. Recent results from the space probe Pioneer V show that such a decrease occurred 8 million kilometers from the earth following a solar event which also produced a decrease at the earth (20). Hence the decreases are not all caused by solar plasma or corpuscular beams interacting with the geomagnetic field, but can be an interplanetary phenomenon. Apparently the clouds of solar plasma ejected from an active region on the sun sweep out some cosmic rays so that the flux is depressed within the clouds and only slowly leaks back in or else leaks in as the cloud dissipates in some way. The same kind of cloud sometimes causes a magnetic storm when it collides with the earth's field. Often these clouds arrive at the earth 24 to 36 hours after a large solar flare.

g) On some occasions geomagnetic storms cause variation in the intensity at particular locations by changing the geomagnetic cutoff at those locations. These variations complicate observations of Forbush decreases and solar cosmic ray fluxes since they may appear concurrently. See Winckler (21).

The variations listed above as a to f are caused, so far as is known, by modulations of the interstellar, i.e., galactic, cosmic ray flux within the solar system. The flux in the vicinity of the earth

remains isotropic throughout the variations c, e, and f. Observations with Pioneer V (20) show that the Forbush decreases and the 11 year cycle of depression of intensity occur outside the geomagnetic field.

h) Another sort of variation observed by cosmic ray detectors is caused by energetic particles ejected by the sun. The sun throws out large numbers of particles with energies in the kilovolt range. Some of these are ejected continuously, it is believed, and constitute the so-called solar wind. Their number changes and this variation apparently affects the modulation of galactic cosmic rays. In addition, particles, presumed mostly protons and electrons, with energies up to 30 Mev are ejected from time to time, but these have not yet been directly measured. Occasionally, particles having energies as high as 10 Bev are thrown off, apparently at the same time that flares erupt on the sun. On a few occasions the energies have been so great that increases were detected at sea level. See Dorman (3) for a discussion of the first four observations of such increases.

The increases did not occur simultaneously at all observation points and were distributed so that it is inferred that outside the earth's field the flux was not isotropic during the initial increase. The high flux persisted and became isotropic. On 23 February 1956 it is estimated that the flux of particles with cosmic ray energy outside the geomagnetic field reached 250 times cosmic ray background.

In the past two years similar increases have been observed at high altitudes which were not seen at sea level. K. Anderson (22) and Winckler (21) have reported observations with balloon-borne instruments and Rothwell and McIlwain (23) with an earth satellite. An enhanced flux has also been seen by Pioneer V (22). The particles appeared with a differential energy spectrum proportional to i/E^5 down to 30 Mev, the instrumental cutoff. The histories of various events differ, but a typical sequence appears to be as follows.

About an hour after a solar flare the solar cosmic rays arrive at the earth anisotropically. Subsequently the flux at the earth becomes isotropic. A day to one and one-half days after the flare a cloud of solar plasma arrives at the earth and produces a geomagnetic storm and Forbush decrease of the galactic cosmic rays that is detected at sea level. The solar cosmic rays continue to arrive during these events and persist for several days, slowly dying away (23, 21).

Thus these solar particles are intimately related to the phenomena which modulate galactic cosmic rays. They will not be discussed further in this paper, since our measurements did not detect them except perhaps on one flight on 16 October 1958 which has already been reported (24). However, their appearance forms one object of the study of cosmic ray variations.

Before describing the present work, we shall discuss a few techniques used for the study of cosmic ray variations. No attempt

is made to list all the experiments concerned with this problem. Nor are experiments designed to study high energy interactions using cosmic rays as a source of particles discussed. The results of this work will be assumed here. See Rossi(25). for a general discussion.

Most information about cosmic ray variations has been obtained by fixed ground monitor stations using neutron monitors, shielded ion chambers, and geiger counter telescopes with absorber. The latter two devices measure the hard component, i.e., those particles which can penetrate 10 to 15 cm of lead. At sea level the hard component consists of μ mesons almost entirely. The neutron monitor responds to the flux of particles which react with nuclei, namely nucleons and at ground level a few π mesons. The device is described by Simpson (26), who developed it. Shielded ion chambers suitable for monitors have been described by Compton (27) and also more recently by Dorman (3). Meson telescopes have been used in many forms but a standard monitoring instrument was recommended for IGY work (28).

The ion chambers operated by the Carnegie Institute have run continuously longer than any other instruments. Data have been published for the period 1936 to 1957 (15,16,10). Results from the University of Chicago neutron monitors have been published at intervals by Simpson and others (26, 29). During the IGY many observing stations have used the three types of monitors listed above and data from these

are being issued by IGY data centers. Neutron monitor data appear in (11), ion chamber data in (30), and counter telescope data in (31).

Other special ground monitor instruments have been used, notably narrow angle telescopes (8,12,13) and extensive air shower detectors (14).

Data from the former are used to study the cyclic variations, meteorological variations, and anisotropies in the primary radiation and the latter are used to investigate the spectrum and directional dependence of very high energy primaries ($E > 10^{15}$ ev).

Ground monitors have the advantage that they can operate continuously and can be made large enough to have high counting rates and hence high time resolution with good counting statistics. In order to study the latitude variation one must use a number of stations recording simultaneously. Ground monitors suffer from meteorologically caused variations. As was mentioned earlier the barometric effect is typically -0.18%/mm of Hg (10) for shielded ion chambers and -1.28%/mm of Hg (11, 26) for neutron monitors, both at sea level, with some dependence upon latitude. The effect of an increase in temperature throughout the atmosphere is -0.29%/C for shielded ion chambers (3) and -0.02%/C or less for neutron monitors (26). Counter-telescopes have the same response as ion chambers. It can be seen from the data in Table I that meteorological variations may easily exceed the

amplitude of other variations. However, the barometric effect may be easily corrected for. To correct for the temperature effect large numbers of radiosonde ascents are required.

Ground level monitors have the further disadvantage that they respond to fairly high energy primary particles, and hence show variations with small amplitude. They will not respond at all to variations of sufficiently low energy primaries. The neutron monitor responds to lower average energy primaries than does the shielded ion chamber. As an example of this, note that the increase in going from o° to 50° geomagnetic latitude is about 10% for a shielded ion chamber, and 90% for a neutron monitor at sea level (26), and a factor of three or more for an unshielded ion chamber at 50 g/cm^2 pressure (see below). See also Table I and reference (32).

Instruments similar to those used in fixed ground stations have been carried aboard ship to measure the latitude variation (33, 34, 35, 36, 37). These instruments have most of the advantages and disadvantages of fixed ground monitors. During the course of weeks required for a shipboard survey they record both the latitude variation and any variations with time which occur during the voyage. If the latitude variation is to be studied with great accuracy it is necessary to correct for the time variations by using the results from fixed monitors located at appropriate latitudes. This has been done with some of the more recent measurements listed.

The confusion of time and latitude variations has been partially overcome by using aircraft which can complete a latitude survey in a time short compared with many of the time variations. Forbush decreases and the arrival of solar cosmic rays can distort even these surveys, however, unless the results are compared with fixed station data. Some of these surveys are reported in the following references: (38), (5), (39), (40). Various instruments were used in this work. At the time these measurements were made aircraft could reach about 310 g/cm^2 atmospheric depth. Both latitude and time variations are greater at this altitude than at sea level but the variations become even greater at shallower atmospheric depths. (See (26) and also below.)

Measurements made at high altitudes with balloon-borne instruments possess to advantage most of the characteristics which are disadvantages of ground monitors and vice versa. They respond to low energy primaries as well as high and are more free of meteorological variations. However, they do not operate continuously and cannot always be made to operate as reliably or to give high counting rates. If measurements are made during ascent or descent the quantity measured may be obtained as a function of atmospheric depth. This dependence can be of great use as the discussion below will show.

High altitude measurements may be thought of as belonging to one of two categories. The first comprises measurements intended

to detect more or less transitory phenomena, such as auroral X-rays, solar cosmic rays, and other solar related phenomena. Examples of such work are discussed in (21), (23), (41), (42), and references therein.

The second category consists of measurements of regular time variations and/or latitude variations with the aim of investigating changes in the primary spectrum. Clearly the two categories sometimes overlap. Experiments in the second category may again be conveniently separated into those which measure the charge and/or energy spectrum of the incident particles directly and those which depend upon the earth's field to determine the energy of the incident flux. The experiments of McDonald (43, 44, 45, 46, 47, 48), of Webber (49), and of Meyer (50) belong to the first group, as does the work using nuclear emulsions.

Experiments in the latter group have been reported by Pomerantz (51), by Winckler (21), and by Neher (18, 19, 52-54). Details of further work by Neher and others are discussed below.) If a single station makes a latitude survey of cosmic ray intensity which requires several days to complete, the latitude and time variations are again mixed, and cannot in general be separated without additional data from other sources. In the work to be reported here this was done by using data taken by a fixed station which sent up balloons simultaneously with the roving station. Ideally high altitude measurements should be made simultaneously by a number of stations distributed in latitude, but no laboratory has carried out such a program to date.

High altitude rockets have been used to extend the balloon measurements to zero atmospheric depths. Results of work by the Iowa group are reported by Meredith et al. (55).

The utility of satellites and space probes in studying cosmic ray variations appears in the results of Pioneer V already cited (2, 22), and will be discussed further at the end of the paper. Their value in investigating auroral radiation, trapped radiation, and any other geomagnetically associated fluxes, is obvious.

We now return to the work of Neher and his group during the past decade, which the work reported herein continues.

Starting in 1951 a large number of measurements has been made using essentially identical instruments. The radiation detector is an integrating ionization chamber with a steel wall 0.5 gm/cm^2 thick surrounding approximately 8 liters of argon at 8 atmospheres pressure. The instrument has been described by Neher et al. (56, 57, 58) and will be considered in detail in the next chapter. These instruments are calibrated against standards and are comparable with each other and with the earlier electroscope models used by Millikan, Neher, et al. (5, 33). Data are reduced to ion pairs per cm^3 sec per atmosphere of air.

During a balloon flight, the ionization chamber is attached to a radio transmitter which telemeters the rate of ionization to a ground receiver at the balloon launching station. An aneroid pressure unit is

also attached to the transmitter and the air pressure is telemetered along with the rate of ionization. Thus the result of each balloon ascent is a record of the rate of ionization versus air pressure overhead beginning at the launch station and terminating at 10 to 20 g/cm^2.

In July-August 1951, such balloon flights were made simultaneously from Bismarck, North Dakota, and from a ship that cruised from Boston, 55°N, to Thule, Greenland, 88°N geomagnetic latitude (52). Four flights were then made at Thule and Bismarck simultaneously.

In summer of 1954 a similar set of measurements was made, again using Bismarck as a base station (18).

During the summers of 1955, 1956 and again in 1957, balloon flights were made at Thule only (53, 54). In 1958 a survey of the latitude effect was made in both the northern and southern hemispheres using Bismarck, North Dakota, and Invercargill, New Zealand, respectively, as base stations. In 1959 and 1960 measurements were again made only at Thule. The 1958 work constitutes the basis of the present paper.

This work has led to a number of conclusions, of which a partial list follows:

1) Ionization chambers of the type used maintain their calibration well enough so that measurements with different instruments may be compared to within $\pm$ .5% (52, 56, 57, 58).

2) The rate of ionization at atmospheric depths less than 50 g/cm^2 sometimes fluctuates 10% from day to day at latitudes north of 56°N geomagnetic latitude (52).

3) Usually these fluctuations are the same at a station located at 56°N (Bismarck) and at points north of this. This similarity is observed in a sequence of simultaneous flights at Bismarck, North Dakota, 56°N, and Thule, Greenland, 88°N. It is also suggested by the fact that if the data obtained by a roving station that cruises from the latitude of Bismarck to that of Thule are corrected by subtracting the deviations of the base station data from the ionization obtained at the base station on a reference day, then the roving station data vary more smoothly with latitude than if they are not so corrected (52, 18). Therefore the latitude and time variation may be partially disentangled by using a base station.

4) It is also observed that day to day fluctuations observed at high altitudes above Bismarck correlate well with variations observed by ion chamber and neutron monitors on the ground, but that the high altitude fluctuations are of the order of 10 times larger (32).

5) On a few occasions, though, radiation appeared at the location of one balloon flight which did not appear simultaneously at the location of another (52, 24).

6) The inverse relationship between solar activity and cosmic ray intensity discovered by Forbush (16) is very much more pronounced

at high altitudes than at ground level (18). When the sun exhibits a minimum activity in its eleven-year cycle, as was the case in 1954, the ionization at high altitudes (say 30 g/cm^2 and above) increases monotonically from 52°N to near the geomagnetic pole. It is also found that the rate of ionization increases steadily with decreasing depth in the atmosphere up to 15 g/cm^2, at least, for locations north of 53°N.

However, when the sun is nearer a maximum of activity (as it was in 1958) the ionization at high altitudes does not increase much with latitude north of about 56°N, and it is found that the increase of radiation with decreasing atmospheric depth tends to level off at depths less than 50 g/cm^2. The point at which the intensity versus latitude curve for a given atmospheric depth levels off is called the "knee."

In 1957, when the sun was approaching a maximum of activity, the ionization vs. depth curve observed at Thule 88°N actually passed through a maximum at about 60 g/cm^2 and declined for more shallow atmospheric depths (54). Although a survey in latitude was not made, it was supposed that a knee in the intensity vs. latitude curve occurred near 55°N that year also, and that the intensity north of it was lower than it had been in 1951. Certainly the intensity north of the knee was higher in 1951 than in 1957, the same year that Carmichel and Dymond measured the rate of ionization vs. atmospheric depth near Thule and

found that it passed through a maximum (59, 53).

It appears , then, that when the sun is active few particles with rigidity less than the geomagnetic cutoff rigidity corresponding to the knee can reach the earth (1.5 Bv in 1951) while in a year of solar minimum like 1954, particles appear which have energies down to at least 150 Mev if they are protons. Less energetic particles could not have penetrated the air above the instrument, and so it is not known if they were present. The numbers of particles with rigidities greater than 1.5 Bv was greater in 1954 than in 1951 as well.

7) The flux of primary cosmic rays to be expected above the geomagnetic pole was calculated from the ionization data. The estimated flux, in particles/cm^2 sterad, was 0.24 in 1954 and 0.056 in 1957 (58). These have been recalculated by Neher (19), using data to be given in this paper. He finds 0.27 in 1954 and .047 in 1958. These data seem in agreement with fluxes measured above the atmosphere by rockets when the effect of neutrinos on the ionization measurements and albedo upon the rocket measurements is taken into account (4). However, data obtained by McDonald (48) indicate a somewhat higher flux than the above during solar maximum.

In view of the great changes in cosmic ray flux which took place from 1954 to 1957, it seemed important to continue the measurements of intensity in 1958 when the sun was expected to be more active

than in 1957. The latitude dependence had not been measured at solar maximum using measurements at a base station to separate time and latitude fluctuations. It was hoped that if the latitude effect were so measured it could be compared with the effect observed at solar minimum in 1954, and that from these data primary rigidity spectra could be deduced for the two parts of the solar cycle.

Furthermore, a series of measurements at a base station would reveal what sort of day to day fluctuations take place at high altitudes during solar maximum. Hopefully, the relation between these fluctuations, the fluctuations at solar minimum, and the change of intensity from solar minimum to maximum would reveal something about the mechanism which generates the changes.

Finally, by measuring the latitude variation in both hemispheres it would be possible to see if the variation were symmetric with respect to the geomagnetic field deduced from surface measurements of the field. Such comparisons had been made previously using ground level cosmic ray surveys (33) and also measurements at airplane altitudes, 310 g/cm^2 depth (5), but had not been done with high altitude data corrected for time variations.

The work to be described in the following pages was undertaken with these motivations.

II. DESCRIPTION OF EXPERIMENTAL APPARATUS

Ionization Chamber

Each of the measurements in 1958 and 1959 was made with an instrument as nearly like all the others as was possible. A complete flight instrument consisted of three parts: an integrating ionization chamber, an aneroid pressure measuring unit, and a telemetry circuit comprising batteries, a simple encoding system, and a pulsed CW transmitter.

The ionization chamber has been described before (52, 57, 58). For discussion of an earlier model chamber see Neher (56). The volume from which ions are collected is a sphere with 12.8 cm radius filled with argon gas at approximately 8 atmospheres, i.e., 117 psi pressure at room temperature. This pressure varies less than 5 psi from one chamber to another. The walls are made of a spinning grade steel .025" thick with .0005" to .001" copper plated on the inside and a coating of copper, copper oxide, and krylon paint on the outside. Total wall thickness is close to 0.5 gm/cm^2. A small quantity of silver-copper eutectic solder joins the sphere together at an equator. The density of pure argon at (8 x 76) cm of Hg and 20°C is .0153 gm/cm^3 and so the gas thickness across a diameter is about .383 gm/cm^2. A quartz rod about 1 mm in diameter, coated with aquadag

and lying along a diameter of the sphere serves as the collecting electrode. This rod is fused to the quartz integrating system so that the whole thing is one piece. This integrating system is surrounded by a double shield with a hole in one end through which the collector passes. The whole quartz system and the shield cans are mounted on a header that is clamped hermetically tight to a short neck which projects from the sphere. A copper gasket and pair of clamping rings make this seal. The metallic parts of the header and shield system are either copper or silver plated. The quartz parts are either bare or covered with aquadag. The quartz system is fastened to a pure silver holder with silver chloride which is melted into the joint between quartz and silver (m.p. of $AgCl_2$ is 455°C). After the header has been sealed onto the neck the latter is evacuated through a filling tube and baked at 350° to 400°C for several hours until the pressure drops to the order of 2×10^{-5} mm Hg. The sphere is then cooled and filled with argon to 8 atmospheres and finally sealed off. Commercial grade argon was used here, but the best results were obtained when this argon was passed over hot copper turnings just before it entered the ionization chamber. It is thought that this removes organic impurities which might otherwise settle on the integrating system and cause the fiber to stick to the collector. At least it was found that a smaller fraction of ion chambers had sticking fibers when the argon was so treated.

The hot copper also removes oxygen which, if allowed into the chamber, would reduce the latter's collection efficiency by forming negative ions.

The fiber itself is made of quartz, is about 7 microns in diameter and 0.2 inches long, and is coated with evaporated gold or platinum covered with aquadag. It is mounted so that when there are no electrical forces it lies a millimeter or so from the end of the collector. When battery voltage, V = 270 v., is applied, the inner shield rises immediately to the potential V, and the fiber and its mounting charge through a load resistor R = $10^6 \Omega$ to V in a time determined by R and the capacitance of the fiber, and leads. The collector, however, does not reach V, since it has a larger capacitance to the sphere than to the inner shield can. The fiber is attracted over to it and charges it up to V, after which no electric fields exist inside the inner shield and the fiber can move away from the collector. The latter then remains at V unless an ion current in the gas produced by radiation lowers the collector's potential. If this occurs, the fiber will again be attracted to the collector when the latter reaches V - ΔV; ΔV is the order of 60 v in the instruments used here. The fiber then recharges the collector to V and the cycle begins again.

When the fiber recharges the collector it drops in voltage to V - δV as the collector rises from V - ΔV to V - δV, where

$\frac{\delta V}{\Delta V} = \frac{C_C}{C_C+C_F+C_{Ex}}$, in which C_C is the capacitance of the collector to its surroundings and C_F that of the fiber and internal support, and C_{Ex} that of the external wiring including the signal lead to the amplifier. This drop occupies about 1 μsec, after which the fiber voltage returns to V in a time interval of about 10 μsec. The pulse is about $-7\ v = -\delta V$ high with the external circuit used. These observations are made when the ion chamber is connected to the circuitry to be described later, and has a Tektronix probe of 10 megohms and 8 μμf attached to the signal lead as well. It is estimated that $C_{collector} =$ 1 to 2 μμf and $C_{fiber} =$ 1 to 2 μμf.

One may inquire if the fiber remains in contact with the collector until both have recharged through R to V. It seems almost certain that it does because the calibration of the ionization chambers remains unchanged when R, and consequently the time to recharge from $V - \delta V$ to V are altered by a factor of ten. Furthermore, one can see no breaks in the pulse shape which would correspond to the fiber breaking its contact with the collector. Probably the mechanical momentum of the fiber is sufficient to hold some point of it against the collector after electrical forces have vanished.

Thus a pulse appears on the fiber lead after a definite amount of charge has been accumulated by the collector; this charge is of the

order of 10^{-10} coulombs. Hence the total current to the collector equals a constant divided by the time between pulses. Leakage current across the quartz appears to be less than 10^{-16} amperes. This was measured by timing the pulses in an evacuated chamber (60).

If an ionization chamber is illuminated by a constant flux of γ rays, for instance from Co^{60}, then the dependence of pulse rate upon V, the applied voltage, is about +.055% per volt if V > 100 volts (58). This was measured when the rate of ionization was 3600 ion pairs, i.e., about 6 times the maximum observed on any balloon $\frac{\text{pairs}}{\text{cm}^3 \text{ sec atm}}$ flight even during solar minimum. This small coefficient indicates that the fiber "sees" almost no potential but that of the inner shield and collector, and further, that volume and columnar recombination are very small at this level of ionization. As Johnston points out (61), there may be a little recombination in the argon, but this affects a constant fraction of all ion pairs for the electric fields tested.

The dependence of the pulse rate upon temperature is about .02% per °C in the range 0 to 80°C. The calibration depends upon the acceleration forces about 5% per g in a direction parallel to the fiber's motion. The fiber is oriented so that this parallel component goes as cos θ where θ is the angle of the chamber's inclination from its normal position with the collector vertical.

The ion chamber wall is made of steel .5 g/cm^2 thick. This thickness corresponds to the range of 17 Mev protons, 68 Mev alphas,

7.5 Mev $\pi^{\pm}$ and 6.7 Mev $\mu^{\pm}$ mesons (62). It is the extrapolated range of 1.1 Mev electrons (63), but of course different approximate relationships for range vs. energy of electrons give slightly different values. These energies are nearly the same for an equal thickness of argon.

The radiation length in iron is 14.1 g/cm^2 and in argon 19.8 g/cm^2; corresponding critical energies are 24.3 and 35.2 Mev (64). These are the parameters which describe an electron-photon cascade's development. The values in air are 37.7 g/cm^2 and 84.2 Mev (64). The geometrical mean free path for nuclear collisions is 107 g/cm^2 in iron, 95.5 g/cm^2 in argon, and about 68 g/cm^2 in air. The value for air is taken from Rossi and it is assumed that the mean free path varies as $A^{1/3}$ in computing the other two.

The proper procedure for calibrating these ion chambers to give the true ionization produced by cosmic radiation in the atmosphere has been studied by Johnston (61). The effective volume of gas, the gas density, and the charge per pulse of a standard instrument may be measured in the laboratory. In order to deduce the rate of ionization in the atmosphere from the number of ion pairs/cm^3 sec atmosphere of argon, in an 8 atmosphere argon chamber, one must allow for the following effects:

1) The chamber wall may modify the cosmic ray flux (primary and secondary) before it reaches the gas. The wall does not affect the

flux in exactly the same way that an equal thickness of air would because it has a different Z.

2) The ionization in the argon may not depend upon the charge and velocity of the ionizing particles the same way in air and argon. Thus a calibration which is correct at one altitude and latitude may not be correct at another. The ionization measured in the argon depends upon two things:

a) The total specific ionization in argon produced by various charged particles.

b) The fraction of ion pairs collected.

3) The ion chambers are calibrated in the laboratory using gamma rays from ThC'' or Co^{60}, but the cosmic ray flux comprises charged particles and neutrons as well as photons. In the case of the gamma rays the ionization is produced by Compton electrons generated in the walls and filling gas. The electron flux in equilibrium in any medium with a gamma ray flux depends upon both the materials of the wall and the gas, and upon the gas density.

Only item 2) can affect the relative calibrations of the flight instruments because they are all similar. Johnston (61) has estimated that the ratio of ionization in air to ionization in argon may vary 1% or less with altitude and latitude. This is much less than the uncertainties due to neutrino loss and the temperature effect which will be discussed later. The instruments' calibration constants have been adjusted to a best single value of I_{air}/I_{argon} for cosmic rays.

Johnston calibrated an air filled ion chamber absolutely using a gamma source. It is found that his calibration agrees within 0.3% with a calibration made years before by Millikan (53, 65), which was still carried by ionization chambers maintained in the laboratory.

The instruments used in 1958 and 1959 were all calibrated by comparing them with seven older chambers of similar design (same wall and filling) which carried the calibration of Millikan and Johnston. Several Co^{60} sources were fixed so as to illuminate a region somewhat larger than an ionization chamber with a constant photon flux. The ionization produced at this position in each of the seven standards was measured by hanging them up successively in that region. This determination has been repeated at intervals over a two year period to ensure that the Co^{60} decay was being allowed for properly. Each determination gives an average rate of ionization whose standard deviation is $\pm$ 0.25%.

The chambers to be used in the field were hung in this position and their constants determined several times spread over several months. The constants, k, are defined by the relationship

$$\frac{k}{\Delta t \text{ in sec between pulses}} = I \quad \frac{\text{ion pairs}}{\text{cm}^3 \text{ sec atm of air}} .$$

Those instruments which did not exhibit a fixed value of k were discarded. These tests were run with a laboratory power supply and

pulse amplifier attached. Eight chambers having the most constant k were chosen to be field standards and four of these were taken to each of the field stations. The remaining good instruments were fitted with barometric pressure sensors and telemetering units, and their constants were again measured.

In the field, before any cosmic ray measurements were made, all available instruments were again compared with each other using a fixed flux of Co^{60} γ rays. Instruments whose readings differed from the average ionization by more than 0.3% were not used. The average of all instruments' readings differed from the average of the four field standards by no more than 0.11% in any case. During the course of a protracted series of cosmic ray measurements the instruments were so compared more than once. For instance, this was done on the trip to Antarctica before the ship left Seattle and again while it was anchored in New Zealand. At the end of each field trip the field standards were brought back to Pasadena and compared with the seven standards and each other. The averages of each set of four and of the seven differed by less than 0.3% on all occasions.

Thus we may say that the results of every balloon flight are comparable to within $\pm$0.5% in ionization, neglecting a possible 1% variation in the ratio I_{air}/I_{argon}, and that these data may also be so compared with earlier ionization chamber measurements made by Millikan, Neher, et al. Ionization is referred to air at 24°C and 74 cm

of Hg pressure, which is called one atmosphere in this work (66). To transform the data herein to ionization in STP air (0°C, 76 cm Hg), which is the atmosphere used to define the Roentgen, multiply by the ratio of densities which is $\frac{76}{74} \cdot \frac{297}{273} = 1.117$. To convert our I, $\frac{\text{ion pairs}}{\text{cm}^3 \text{ sec atm}}$, to r/hr, multiply by $1.117 \cdot 3600 \cdot 4.8 \cdot 10^{-10}$. That is, $\text{r/hr} = I \cdot 1.932 \cdot 10^{-6}$. Strictly speaking, the Roentgen is defined for γ rays only.

Barometric Element

Neher has described an aneroid unit similar to the one used in the present work (67). The pressure sensor is a bellows from a sensitive altimeter manufactured by Kollsman Instrument Company. It is temperature compensated and expands more per unit pressure change under small pressures than under high. At one end this bellows is fixed to an aluminum base. The free end carries a phosphor bronze arm which holds a platinum contact against a coil also fixed to the base. The coil consists of three platinum wires wound together in a triple helix and insulated from one another. As the bellows expands it carries the contact along the coil so that it touches the wires successively 1, 2, 3, 1, 2, 3, etc., making about 25 complete cycles or 75 contact changes between sea level pressure, 1030 g/cm^2, and 5 g/cm^2. The next section explains how changing contacts are telemetered to the ground.

The barometric units were calibrated by placing them in a bell jar and connecting the wires and contact arm electrically to neon bulbs which lighted up when the corresponding wire was being touched by the contact. A vacuum pump evacuated the bell jar slowly and a special aneroid gauge measured the pressure in it. The latter was checked against a mercury manometer during each calibration run. Each barometric unit was calibrated several times and those exhibiting erratic behavior were discarded. The remaining units repeated themselves within $\pm$ 2 g/cm^2 at 1000 g/cm^2 pressure and $\pm$0.5 g/cm^2 at 10 g/cm^2 pressure, so that this is the accuracy claimed for the pressure measurements during balloon flights. Barometric units were checked in the field prior to use, in a portable "bell jar" using a water manometer with the free end open to the atmosphere. Atmospheric pressure during these checks was obtained from a sensitive aneroid barometer and/or a mercurial barometer when the balloon flights were made from weather stations.

Telemetering System

Figure 1 shows the circuit of the complete flight instrument. Power is supplied to this circuit by two batteries. A 1-1/2 v wet battery, soaked in water just before use supplies the filaments, although a flashlight battery will do. A simple 300 v dry cell tapped to give

+270, +30, -15, -30 supplied the rest. The filament battery limits the lifetime of the system to ≃ 12 hrs , since drain on the +300 v battery is small.

While the unit is operating the CK 526 AX normally conducts, and the RK 61 thyratron and 958A acorn transmitter tube are cut off. The neon relaxation oscillator flashes at a rate fixed by the capacitor (4) and the resistance from point "B" to ground, which is determined by the barometer element resistance so long as the capacitor (3) is charged up. When the bulbs flash, a 20 to 30 v positive pulse appears at the input to the 958A grid which is sufficient to turn the transmitter tube on. The latter the oscillates at about 160 mc/sec for 100 μsec radiating about one watt. Thus as long as the ion chamber doesn't pulse the transmitter radiates 100 μsec bursts at one of three rates, depending upon which winding the barometer contact is on. As the instrument ascends, these rates cycle through slow, medium, fast; slow, medium, fast; etc., and each change of rate marks attainment of a known air pressure.

When the ionization chamber pulses, a 30 v positive pulse from the amplifier tube makes the thyratron conduct, and 3 discharges through it until its voltage drops low enough to turn off the thyratron. The neon relaxation oscillator then pulses very rapidly as 3 recharges through R_1. About six or eight pulses are produced, starting four

times as fast as the normal "fast" barometer rate and gradually returning to the rate fixed by the barometer. This coding distinguishes ionization chamber pulses from the regular barometric pulses and from most noise which may appear in the ground receiver. All the circuitry, the barometric sensor and the 300 v battery are contained in an aluminum box fitted beneath the ionization chamber. The transmitter is shielded from the rest as the dashed lines in Figure 1 show. A 1/4 wave dipole antenna projects downward from this box; the box and ionization chamber acts as the other arm of the dipole. The ionization chamber weighs 2 lb 14 ox, and the circuitry and battery 2 lb 6 oz. In flight the circuit box and ion chamber are surrounded by red cellophane held one to two inches away by cardboard spacers. So long as the sun is up this wrapping holds the temperature inside between 18° and 35°C. (Temperature was measured on a couple of trial flights made near Pasadena.)

The ground receiving station comprises two units. A vertical dipole antenna and receiver tunable to 160 mc/sec detects the signal. The output circuits of the receiver are arranged so that a one-shot multivibrator closes a relay every time an rf pulse of greater than a certain amplitude reaches the receiver. This relay activates the pen on a recorder. The latter pulls 16 mm paper tape past the pen at about 33 cm/min. A spring-wound clock puts a special mark on this

tape once per minute so that the station does not rely upon local power for its time standard. This system has received the telemetered signal from as far away as 300 miles with a directional antenna. The simple dipole receiving antenna gave more than adequate signal strength in every case. The receiving system suffers from being very sensitive to "popping" or "crackling" noises with 160 mc/sec frequency components. Apparently thunderstorms can be heard, and unshielded engine ignitions are troublesome if they approach closer than 300 feet. The ionization chamber and barometric element could be adapted to modulate an fm transmitter, and this would probably simplify operation in populated areas if routine measurements were undertaken.

III. THE FLIGHTS

Table II lists the time and date and location of every flight made in 1958 and 1959. Figure 2 is a map of the locations. Both time and date are expressed in GMT and refer to the time a balloon was released. The approximate time when the instrument reached 50 g/cm^2 is given as well. Geographic position means the coordinates of the roving station at the time of balloon launching. The flights at sea were made from the icebreakers USS Atka in the Atlantic Ocean and USS Staten Island in the Pacific. Within the United States flights were made from a portable station and from the U.S. Weather Bureau

TABLE II. Balloon Flights Made in 1958 and 1959.

Date GMT	Base Launch Time GMT	Station Time at 50 g/cm^2 GMT	Roving Launch Time GMT	Station Time at 50 g/cm^2 GMT	Geographic Position of Roving Station Lat.	Long.	Comments
1958							
22 June	1152	1320	1127	1250	28°48'N	97°00'W	Base station at Bismarck, N.D.
24 June	1151	1304	1339	1454	32°5' N	96°28'W	46°47'N 100°46'W
26 June	1253	1426	1141	1252	34°10'N	97°8' W	
27 June	1136	1307	1130	1240	37°49'N	96°52'W	
29 June	1441	-	1130	1253	41°17'N	96°00'W	
30 June	1237	1400	1137	1249	43°33'N	96°44'W	
2 July	1704	1822	1700	1835	46°37'N	100°46'W	
12 July	1357	1525	1340	No data	43°14'N	65°30'W	
14 July	1400	1528	1346	1541	47°32'N	52°28'W	
15 July	1359	1527	1351	1504	52°42'N	52°14'W	
17 July	1401	1536	1350	1458	63°13'N	52°42'W	
19 July	1402	1528	1329	1438	73°30'N	57°45'W	
20 July	1412	1550	1356	1520	75°50'N	61°20'W	
	Bismarck		Invercargill		Position of Inver. NZ		
15 Oct	2029	2144	2037	2158	46°27'S	191°36'W	Simultaneous flights at Bismarck, N.D. and Invercargill, New Zealand
16 Oct	2029	2145	2031	2206	46°27'S	191°36'W	

TABLE II (continued)

Date GMT	Base Launch Time GMT	Station Time at 50 g/cm^2 GMT	Roving Launch Time GMT	Station Time at 50 g/cm^2 GMT	Geographic Position of Roving Station Lat.	Long.	Comments
							Invercargill is Base Station
23 Oct	2203	2326	2228	2436	48°12'N	122°59'W	46°27'S 191°36'W
24 Oct	2200	2336	2155	2413	44°32'N	125°02'W	
26 Oct	2156	2328	2208	-	about 34°N	121°30'W	
29 Oct	2152	2324	2208	-	25°29'N	124°40'W	
31 Oct	2201	2327	2232	-	17°42'N	131°56'N	
2 Nov	2201	2333	2158	2305	8°53'N	138°52'W	
4 Nov	2200	2320	2204	2308	0°37'N	145°25'W	
7 Nov	2203	2344	2202	-	11°27'S	154°25'W	
9 Nov	2211	2336	2201	2348	19°40'S	161°32'W	
11 Nov	2200	2324	2223	2404	26°41'S	167°26'W	
12 Nov	2200	2359	2203	2312	30°29'S	170°25'W	
13 Nov	2202	2345	2200	2434	33°43'S	173°40'W	
14 Nov	2201	-	2201	2347	37°37'S	178°12'W	
15 Nov	2158	2335	2210	2325	41°17'S	183°26'W	
23 Nov	1806	2011	1910	2104	43°34'S	187°10'W	
26 Nov	0520	0656	0409	0620	47°37'S	185°24'W	
26 Nov	2203	2319	No flight		-	-	
27 Nov	2157	2327	No flight		-	-	

TABLE II (continued)

Date GMT	Base Launch Time GMT	Station Time at 50 g/cm^2 GMT	Roving Launch Time GMT	Station Time at 50 g/cm^2 GMT	Geographic Position of Roving Station Lat.	Long.	Comments
28 Nov	2209	2328	2223	2328	54°40'S	182°24'W	
2 Dec	0150	0309	0129	0405	65°26'S	180°20'W	
3 Dec	2353	2515	2221	2321	71°20'S	183°50'W	
11 Dec	No flight		2054	2158	72°50'S	188°43'W	
22 Dec	2134	2304	2157	2406	77°45'S	193°36'W	
	Flights at Thule, Greenland in 1959						
	Geographic Position of Thule is 76°33'N 68°50'W						
29 July	1437	1626					
31 July	1340	1555					
2 Aug	1423	1603					
4 Aug	No data		Floater				
5 Aug	1303	1432					
6 Aug	1203	1359					
9 Aug	1301	1430					
11 Aug	1044	Floater	Reached minimum pressure of about 52 g /cm^2 at 1300				
12 Aug	1224	1341					
15 Aug	1356	1458					

facilities at Bismarck, N.D. At Invercargill the facilities of Awarua Radio Station were used.

About three-quarters of the instruments launched from the U. S. were recovered, and it was found that most of them drifted less than 100 miles, predominantly in an E-W direction. On the basis of this meager evidence, it is estimated that the instrument remains within $\pm 1°$ of latitude from the launch station.

Single neoprene balloons weighing 1750 gms and filled to give about 1 kg net free lift were used for all flights so that the instruments ascended similarly in most cases. The air pressure at the instrument can be expressed by

$$\ln p = \ln p_o - \alpha(t - t_o) \qquad (8)$$

where p_o = pressure at launching time, t_o. Since an average balloon requires two hours to rise from 1030 g/cm^2 to 10 g/cm^2 a typical value of α is .038 min^{-1} or .00064 sec^{-1}. Actually in the tropics α becomes greater after the balloon gets above 200-300 g/cm^2 depth, changing from .034 min^{-1} to .073 min^{-1}; the change is not as pronounced at latitudes above 45°. This is undoubtedly due to the different distributions of atmospheric temperature found in the tropics and in the polar regions.

Insofar as the atmospheric pressure is a simple exponential function of height, the above indicates that the balloons ascended at a

constant linear speed or possibly two different speeds in the lower and upper atmosphere. The ascent continues until the balloon ruptures and the instrument falls rapidly. No radiation data were taken during the fall but usually several pressure points were obtained. Since a plot of p vs t on semi-log paper appears as a straight line during both ascent and descent, it is possible to fix the time the balloon broke and the minimum pressure attained by finding where the ascending and descending p vs t plots intersect.

IV. REDUCING DATA

The preceding paragraphs describe how data from a balloon flight is recorded. One begins to interpret this record by tabulating the times when the barometer pulse rate changed and thence plotting on semi-log paper air pressure versus time. As equation 8 indicates, this plot is nearly a straight line or two straight lines in the case of equatorial balloon flights. In the second step one determines the time between ionization chamber pulses by measuring distance between them on the tape and also the distance between minute marks. It may be remarked that distance can easily be measured to 0.1% and that the minute marking clock is at least this good as well so that no significant error is introduced in measuring time between ion chamber pulses during a flight.

Actually as ionization chamber pulses become more frequent at smaller depths in the atmosphere enough ion chamber pulses are included in a single measurement so that the time interval remains 2 to 3 minutes. This interval may be called Δt for n pulses. Hence one obtains an average time per pulse, $\Delta t/n$, and the average ionization during Δt is then determined by $I_{\Delta t} = \frac{k}{\Delta t/n}$, where k is the constant for the instrument. This value of I is assigned to the time at the midpoint of Δt. The pressure at this time is then obtained from the pressure vs time plot, and a table and a rectangular plot can then be made of ionization vs pressure. Figure 3 shows such plots, typical for 1958. The root mean square deviation of these points from the smooth curves represented in Table III is typically 1.27 ion pair/cm^3 sec atm at depths from 0 to 150 g/cm^2.

It may be asked what sort of systematic error is incurred by assigning the average ionization during an interval to the air pressure at the midpoint of that interval. Assume that the cosmic ray flux is constant in time throughout a flight's duration. Then I, the rate of ionization, is a definite function of air pressure and thence of time since the air pressure at the instrument is a definite function of time. Let Q represent total ion pairs/cm^3 atm of air; Q is proportional to the total charge which reaches the collector. Then $I = dQ/dt$. If we denote by t_a the time at one recharging of the collector and by t_b the next, then the chamber actually measures

TABLE III. Ionization vs Depth in the Atmosphere - 1958, 1959.

Data from flights of summer, 1958

A = Roving Station
B = Base station, Bismarck, N. Dakota

Ionization, ion pairs/cm^3 sec atm of air
Parenthesis indicates extrapolated value.

Air Overhead	June 22		June 24		June 26		June 27		June 29	
	A	B	A	B	A	B	A	B	A	B
	time		time		time		time		time	
$g\ cm^{-2}$	1127	1152	1339	1151	1141	1253	1130	1136	1130	1441
0	(114.0)	(222.0)	(149.2)	(216.6)	(133.8)	(224.2)	(158.8)	(228.0)	(201.8)	
5	(119.4)	(225.6)	(153.0)	(223.6)	(145.6)	230.0	(170.8)	(233.6)	(209.2)	
10	(125.4)	(229.4)	(157.0)	(230.6)	156.7	235.0	182.8	(233.8)	216.7	-
15	(131.4)	233.2	(161.0)	(237.6)	167.8	240.3	193.8	(243.2)	223.7	-
20	(137.2)	237.0	(164.8)	244.6	177.0	245.8	202.1	(247.4)	230.1	-
30	(149.0)	244.6	(172.8)	251.8	191.0	255.0	213.8	254.6	239.0	-
40	160.8	249.3	(181.2)	253.8	201.5	258.6	221.2	257.2	243.3	-
50	169.1	250.2	188.7	254.8	207.2	259.1	226.3	257.0	244.8	-
60	173.9	248.4	194.5	253.4	209.8	257.0	229.1	254.3	243.3	-
70	176.0	244.6	197.4	250.2	210.8	253.0	229.2	249.4	240.0	244.2
80	175.5	239.8	197.8	244.8	209.8	247.8	226.3	243.1	235.5	238.9
90	173.8	234.0	198.0	238.0	207.0	241.4	222.2	235.8	229.2	232.8
100	171.2	226.6	192.0	230.3	202.9	234.4	217.1	228.1	222.0	226.1

TABLE III (continued)

Ionization, ion pairs / cm^3 sec atm of air

Air Overhead	June 22		June 24		June 26		June 27		June 29	
	A	B	A	B	A	B	A	B	A	B
	time		time		time		time		time	
$g\ cm^{-2}$	1127	1152	1339	1151	1141	1253	1130	1136	1130	1441
120	163.8	208.9	182.1	215.3	191.5	218.4	204.8	212.4	206.2	210.2
140	154.0	191.2	170.6	199.6	177.8	199.8	190.3	195.6	190.1	192.2
160	143.5	174.6	158.6	182.7	164.2	180.9	175.1	178.4	174.5	173.7
180	133.0	158.5	146.0	164.1	149.8	163.5	159.4	161.9	158.6	157.1
200	122.3	142.6	133.4	147.0	135.4	147.3	144.1	146.3	142.8	141.3
220	111.7	127.8	120.0	131.1	121.0	132.1	128.3	132.0	127.5	127.2
240	101.0	114.0	106.9	116.7	107.9	117.4	113.5	118.3	113.0	114.5
260	90.6	102.2	94.5	104.2	96.2	103.7	101.0	105.4	100.2	102.3
280	80.6	90.9	83.4	93.4	85.2	91.4	89.8	93.1	89.1	90.2
300	71.4	80.4	74.7	83.5	75.0	80.3	79.4	81.2	79.0	79.1
320	63.2	70.6	65.2	74.0	66.0	70.4	68.0	71.0	69.5	70.0
340	56.0	61.7	59.0	64.7	58.7	61.7	61.1	62.8	61.7	62.1
380	43.4	46.8	45.5	47.9	44.5	47.0	46.4	48.3	47.0	47.2
420	33.0	(36)	34.9	36.7	34.4	35.9	36.2	36.7	35.8	35.0
460	25.9	(27)	27.1	(27)	27.6	(27)	28.5	28.3	27.9	27.6
500	20.8	(21)	21.9	(21)	22.6	(21)	22.7	(21.8)	22.4	(21)

TABLE III (continued)

Air Overhead	June 30		July 2		July 12		July 14	
	A	B	A	B	A	B	A	B
	time		time		time		time	
g cm^{-2}	1137	1237	1700	1704	1340	1357	1346	1400
0	(201.0)	(211.0)	(206.2)	(212.2)	-	(205.8)	(197.4)	(202.6)
5	(208.8)	(220.0)	(215.0)	(218.6)	-	(210.6)	(205.4)	(211.8)
10	216.4	229.6	223.2	224.8	No barom. record	(215.6)	213.0	220.6
15	224.2	236.0	230.0	230.8		(220.6)	220.6	227.4
20	231.5	241.0	235.1	235.5		(225.6)	226.2	232.2
30	241.5	247.4	242.2	243.0		234.4	234.1	238.4
40	245.6	250.9	245.8	246.3		238.2	238.8	241.3
50	246.0	251.2	246.8	246.7		239.2	241.2	241.5
60	244.8	248.2	245.3	244.5		238.4	239.8	240.1
70	242.0	243.0	242.0	241.0		235.2	235.4	236.8
80	238.2	237.2	237.4	236.6		230.1	230.0	231.9
90	233.2	231.4	231.6	230.8		224.4	224.0	225.8
100	227.5	225.4	224.2	223.8		218.1	218.0	219.3
120	213.0	211.3	208.7	207.4		204.2	203.9	204.1
140	196.0	194.1	192.5	191.3		188.9	187.2	187.6
160	179.0	178.2	175.7	174.6		173.4	170.0	171.2
180	162.4	163.1	158.5	157.2		157.6	153.5	154.8
200	147.1	144.3	141.9	140.0		142.0	138.9	138.5

TABLE III (continued)

Air Overhead	June 30		July 2		July 12		July 14	
	A	B	A	B	A	B	A	B
	time		time		time		time	
$g\ cm^{-2}$	1137	1237	1700	1704	1340	1357	1346	1400
220	132.7	127.0	126.2	124.1		126.5	124.3	123.8
240	118.1	111.8	111.7	110.3		112.5	110.6	111.5
260	104.0	98.8	99.1	97.3		100.5	97.6	100.1
280	91.0	87.2	87.4	85.1		89.7	85.5	89.1
300	79.7	76.8	76.5	74.2		79.7	74.6	79.4
320	69.8	68.0	66.5	65.2		70.4	65.0	70.8
340	60.9	60.6	58.9	57.4		61.2	57.2	62.8
380	47.2	47.7	46.0	44.9		46.2	45.1	48.3
420	37.3	36.1	36.5	35.9		35.5	35.8	36.5
460	29.0	27.8	28.7	(28)		26.9	28.0	27.7
500	22.0	22.1	22.2	(22)		(22)	21.6	21.1

	July 15		July 17		July 19		July 20	
	A	B	A	B	A	B	A	B
	time		time		time		time	
	1351	1359	1350	1401	1329	1402	1356	1412
0	(212.6)	(208.6)	(218.2)	(211.0)	(202.0)	(211.0)	(216.0)	(210.6)
5	(218.2)	(212.0)	(222.4)	(217.6)	(215.0)	(218.4)	(224.6)	(217.9)
10	224.2	(219.8)	229.0	224.1	228.2	225.8	233.0	(225.4)

TABLE III (continued)

Air Overhead	July 15		July 17		July 19		July 20	
	A	B	A	B	A	B	A	B
	time		time		time		time	
$g\ cm^{-2}$	1351	1359	1350	1401	1329	1402	1356	1412
15	229.6	225.2	234.6	229.8	236.6	231.9	241.4	232.5
20	234.1	230.3	239.2	234.2	241.7	236.6	247.1	238.7
30	240.2	237.7	245.2	240.9	247.4	243.8	253.0	245.8
40	243.7	241.7	248.3	245.1	249.8	248.4	254.6	249.2
50	244.8	242.4	248.1	246.8	250.0	249.2	254.6	249.8
60	244.1	240.9	245.9	245.9	248.3	248.0	252.9	248.1
70	241.4	237.6	242.4	243.2	245.2	243.4	248.6	244.4
80	237.3	232.9	237.8	239.1	240.8	238.2	242.3	238.9
90	231.4	226.6	232.0	233.6	235.2	232.4	235.6	232.2
100	224.2	219.4	225.3	226.6	228.5	225.8	228.7	225.0
120	208.3	203.7	209.1	210.1	213.0	211.7	213.0	209.3
140	192.1	186.2	192.1	193.4	196.7	195.5	195.8	192.6
160	176.1	168.8	174.9	177.0	179.7	178.0	179.4	175.2
180	160.1	152.5	158.6	159.4	162.8	160.5	162.7	157.2
200	144.6	137.0	142.4	142.9	144.7	144.1	146.6	141.0
220	128.6	122.7	126.5	127.8	128.7	129.2	130.4	125.8
240	113.4	110.3	111.4	113.5	114.1	115.0	115.3	112.4
260	100.0	98.1	98.6	100.1	100.8	102.2	101.2	100.0

TABLE III (continued)

Air Overhead	July 15		July 17		July 19		July 20	
	A	B	A	B	A	B	A	B
	time		time		time		time	
g cm^{-2}	1351	1359	1350	1401	1329	1402	1356	1412
280	87.9	85.8	87.4	87.7	88.5	91.0	88.6	89.2
300	77.1	76.6	77.4	77.7	77.9	80.7	78.7	79.1
320	66.0	68.2	68.0	69.0	69.0	71.0	70.0	69.6
340	59.6	60.0	60.5	61.0	60.3	61.9	61.3	60.8
380	47.2	45.7	46.9	46.0	46.2	46.9	47.1	47.4
420	36.5	35.6	36.0	(36)	35.8	36.1	36.4	36.4
460	28.1	27.8	27.9	(28)	28.3	28.0	28.7	26.4
500	22.4	(21)	22.3	(21)	22.4	(21)	22.8	(21)

TABLE III (continued)

Summary of Flights, Fall, 1958

A = Roving Station
B = Base Station, Invercargill, New Zealand

Air Overhead	15 Oct		16 Oct		23 Oct		24 Oct		26 Oct	
	A GMT	B	A GMT	B	A GMT	B	A GMT	B	A GMT	B
g/cm^2	2029	2037	2029	2031	2228	2203	2155	2200	2208	2156
0	(229.4)	(218.8)	(224.4)	(207.6)		(193.6)	(197.6)	(227.0)		(211.0)
5	(235.8)	(222.4)	(230.8)	(214.6)	no data	(208.0)	(203.4)	(232.6)	-	(217.2)
10	242.0	(226.4)	(237.4)	(222.0)		(206.4)	(209.1)	238.0	-	(223.4)
15	247.6	(230.2)	244.0	229.6		(212.8)	214.8	242.8	-	229.2
20	252.0	233.8	250.0	235.8		218.8	220.6	246.8	-	234.6
30	259.2	241.4	259.6	244.4		228.4	231.4	252.0	-	241.2
40	263.0	248.2	261.2	249.6		234.4	239.6	255.2	-	244.4
50	261.8	251.6	266.6	252.4		236.8	244.6	256.4	-	246.0
60	258.6	250.0	268.4	252.8		237.2	245.2	256.0	-	245.8
70	253.8	246.2	278.4	249.2		235.6	241.6	251.4	-	243.2
80	247.4	241.4	314.0*	243.6		232.0	236.4	245.4	-	238.4
90	238.8	235.6	291.8	237.0		226.4	230.4	238.8	-	231.4
100	230.2	228.8	242.0	229.6		-	223.2	231.2	-	223.2
120	214.6	213.2	220.0	213.0		-	207.6	213.8	-	205.8

*Note: Maximum of spike on 16 Oct, A station, is at 84 g/cm^2, ioniz = 321.

TABLE III (continued)

Air Overhead	15 Oct		16 Oct		23 Oct		24 Oct		26 Oct	
	A GMT	B	A GMT	B	A GMT	B	A GMT	B	A GMT	B
g/cm^2	2029	2037	2029	2031	2228	2203	2155	2200	2208	2156
140	199.4	196.0	198.4	195.0		-	192.0	197.0	-	188.8
160	182.2	178.8	180.6	177.0		-	176.4	180.6	-	172.4
180	164.8	162.4	163.2	160.2		-	161.0	161.8	-	156.4
200	148.4	146.2	145.0	144.2		-	145.6	143.0	123.0	140.8
220	133.0	130.8	127.8	129.0		-	128.0	128.0	111.2	125.6
240	119.2	115.8	113.4	115.4		-	113.8	114.2	100.0	111.0
260	106.8	101.8	100.6	102.6		-	101.8	101.0	90.2	98.0
280	94.8	89.0	89.0	90.2		-	90.4	88.4	81.4	86.2
300	83.2	78.2	79.0	78.6		-	80.0	77.4	73.2	75.8
320	73.0	69.3		68.8		-	70.8	68.2	65.1	66.9
340	63.8	61.8	-	60.2		-	62.2	61.2	57.2	59.0
380	47.6	48.6	-	46.0		47.2	46.6	48.2	43.6	44.8
420	36.-	36.6	-	36.8		36.4	35.8	36.0	35.2	35.0
460	30.-	27.6	-	29.6		27.8	27.8	27.6	28.0	27.6
500	26.-	21.8	-	23.6		22.0	(22)	22.2	21.9	(22)

TABLE III (continued)

Air Overhead g/cm^2	29 Oct A GMT 2208	29 Oct B GMT 2152	31 Oct A GMT 2232	31 Oct B GMT 2201	2 Nov A GMT 2158	2 Nov B GMT 2201	4 Nov A GMT 2204	4 Nov B GMT 2200	7 Nov A GMT 2202	7 Nov B GMT 2203
0		(212.4)		(217.8)	(35.8)	(210.6)	(36.0)	(210.8)	(47.0)	(216.2)
5	no data	(219.8)	no data	(224.0)	42.8	(219.8)	41.6	(216.6)	(53.2)	(221.6)
10		227.2		230.4	49.2	228.0	46.8	222.0	(58.1)	227.0
15		234.0		235.8*	55.2	234.8	51.0	228.0	(62.2)	232.2
20		239.6		240.0*	60.4	240.0	54.4	233.4	(65.6)	237.4
30		247.2		246.6*	69.8	247.4	60.4	243.0	(71.2)	247.0
40		252.2		250.6*	76.8	253.6	65.2	248.2	(75.8)	250.0
50		253.6		252.8*	82.6	255.0	69.2	249.2	(79.2)	251.0
60		252.4		252.6*	85.4	253.2	72.2	248.8	(82.1)	251.0
70		250.2		249.4	86.4	249.4	74.4	246.6	84.0	248.2
80		244.6		244.6	87.0	244.6	76.0	241.4	85.6	242.6
90		237.2		239.0	87.6	239.0	77.0	234.6	86.6	236.6
100		230.2		232.4	87.8	232.0	77.6	226.8	87.2	229.8
120		215.0		215.4	87.0	214.8	77.7	210.6	87.0	214.0
140		198.0		194.4	85.4	195.0	76.2	194.0	84.2	196.0
160		179.6		179.0	82.4	176.0	73.8	177.0	80.4	177.4
180		161.8		163.2	78.4	159.8	70.6	160.4	75.8	160.0

*Interpolation. Data is missing.

TABLE III (continued)

Air Overhead g/cm^2	29 Oct A GMT	29 Oct B GMT	31 Oct A GMT	31 Oct B GMT	2 Nov A GMT	2 Nov B GMT	4 Nov A GMT	4 Nov B GMT	7 Nov A GMT	7 Nov B GMT
	2208	2152	2232	2201	2158	2201	2204	2200	2202	2203
200		144.8		143.4	73.4	144.4	66.6	144.4	70.6	144.2
220		128.8		126.8	67.6	130.2	62.0	129.2	64.8	129.0
240		114.6		113.8	62.0	116.2	57.2	114.2	59.2	114.6
260		101.6		102.0	56.6	102.8	52.0	100.0	53.6	101.0
280		89.4		90.6	51.2	90.2	47.0	88.0	49.0	89.4
300		78.4		79.8	46.2	79.2	42.6	78.4	44.6	79.4
320		69.0		69.4	41.4	69.0	38.4	69.8	40.7	70.2
340		60.8		60.2	36.8	60.0	34.8	62.0	37.2	61.6
380		47.0		46.6	29.4	45.6	28.8	48.6	30.2	47.4
420		36.2		36.8	23.8	36.4	23.2	38.0	24.2	35.0
460		28.8		28.2	19.4	28.6	(19.4)	28.6	19.8	(28)
500		22.8		(22)	15.4	21.6	(15.4)	-	16.4	(22)

	9 Nov A GMT	9 Nov B GMT	11 Nov A GMT	11 Nov B GMT	12 Nov A GMT	12 Nov B GMT	13 Nov A GMT	13 Nov B GMT	14 Nov A GMT	14 Nov B GMT
	2201	2211	2223	2200	2203	2200	2200	2202	2201	2201
0	(38.8)	(204.8)	(49.0)	(201.2)	(70.0)	(200.2)	(87.0)	(184.4)	(110.4)	
5	(44.4)	(212.6)	(56.0)	(210.2)	77.4	(207.4)	(94.0)	(194.0)	(120.6)	-
10	(50.2)	220.6	(63.2)	(219.4)	85.0	214.8	(101.2)	(203.6)	(131.2)	-
15	56.0	228.0	(70.4)	228.0	92.0	221.4	(108.4)	(213.2)	141.4	-

TABLE III (continued)

Air Overhead	9 Nov		11 Nov		12 Nov		13 Nov		14 Nov	
	A GMT	B	A GMT	B	A GMT	B	A GMT	B	A GMT	B
g/cm^2	2201	2211	2223	2200	2203	2200	2200	2202	2201	2201
20	61.4	234.8	77.2	234.8	98.4	227.2	115.2	222.0	151.0	-
30	72.0	245.0	89.2	242.8	109.2	235.8	128.8	236.4	164.0	-
40	79.6	250.4	97.4	247.0	117.8	241.6	139.2	245.4	172.8	-
50	85.2	251.8	103.4	248.8	124.8	243.0	145.4	249.2	179.4	-
60	89.4	251.8	108.0	247.6	129.4	241.8	149.4	248.6	183.2	-
70	92.2	249.6	111.0	244.4	132.6	239.2	151.8	245.6	184.6	249.6
80	94.2	243.4	113.0	239.6	134.4	235.2	153.0	241.0	184.6	243.6
90	95.2	236.4	114.0	233.8	135.4	230.0	153.0	234.4	182.6	237.0
100	95.2	229.0	114.2	226.8	135.2	223.2	152.0	225.6	179.0	229.6
120	93.4	213.0	112.8	210.6	131.0	206.6	146.0	209.0	170.4	214.0
140	90.2	195.8	108.6	192.0	123.4	189.0	137.4	193.6	160.0	196.2
160	86.2	178.2	102.8	175.6	115.2	172.2	128.4	178.2	148.8	176.8
180	81.4	162.2	96.0	160.8	107.0	155.8	119.4	162.8	136.4	159.8
200	76.2	144.8	88.4	145.4	98.6	140.2	110.2	147.2	123.8	144.0
220	70.6	128.8	80.6	130.2	90.0	125.8	100.2	131.6	111.2	129.0
240	64.4	115.2	73.4	115.6	81.4	111.8	90.4	116.0	99.8	115.4
260	58.2	102.4	66.6	102.2	73.2	99.2	81.4	100.6	89.0	102.6
280	52.0	90.4	60.0	90.0	65.4	87.8	72.8	88.0	79.6	90.4
300	46.4	79.8	53.6	79.4	58.6	77.8	64.6	77.8	70.6	79.2

TABLE III (continued)

Air Overhead g/cm^2	9 Nov A GMT 2201	9 Nov B GMT 2211	11 Nov A GMT 2223	11 Nov B GMT 2200	12 Nov A GMT 2203	12 Nov B GMT 2200	13 Nov A GMT 2200	13 Nov B GMT 2202	14 Nov A GMT 2201	14 Nov B GMT 2201
320	41.5	70.8	47.7	69.8	52.8	68.3	57.2	68.9	62.4	68.8
340	37.2	62.6	42.2	60.8	47.4	59.6	50.6	60.8	54.8	60.2
380	29.6	48.4	33.2	46.6	37.8	46.2	39.6	47.8	42.8	47.2
420	24.0	37.4	26.6	36.8	(29)	36.0	31.4	39.6	34.4	36.6
460	19.4	(29)	22.2	29.0	(23)	27.6	24.8	32.6	27.8	28.0
500	15.6	(22)	18.6	22.2	(19)	21.6	19.4	25.8	22.2	22.0

	15 Nov A GMT 2210	15 Nov B GMT 2158	23 Nov A GMT 1910	23 Nov B GMT 1806	26 Nov A GMT 0409	26 Nov B GMT 0520	26 Nov A GMT B 2203	27 Nov A GMT B 2157
0	(147.6)	(201.4)	(171.6)	(209.8)	(211.0)	(217.6)	(191.0)	(203.0)
5	(160.0)	(213.6)	(180.0)	(216.8)	(224.8)	226.0	(201.8)	213.0
10	172.6	225.0	188.6	223.8	(233.0)	233.4	(212.8)	221.6
15	182.4	233.6	197.0	230.0	(238.8)	239.6	222.8	230.0
20	189.8	239.2	204.2	236.0	243.4	244.8	232.8	236.2
30	200.8	246.8	216.2	246.2	250.2	252.4	243.0	245.2
40	208.2	251.0	225.2	252.6	254.6	255.8	248.2	251.6
50	214.0	252.8	232.0	254.6	256.6	256.0	250.4	253.2
60	216.4	252.4	234.2	254.4	256.2	253.8	250.2	251.4
70	215.6	250.0	234.2	250.8	253.8	249.2	246.8	248.4
80	212.6	244.4	231.8	245.2	249.8	243.2	242.2	244.2

TABLE III (continued)

Air Overhead	15 Nov		23 Nov		26 Nov		26 Nov	27 Nov
	A GMT	B	A GMT	B	A GMT	B	A GMT B	A GMT B
g/cm^2	2210	2158	1910	1806	0409	0520	2203	2157
90	208.0	237.2	227.2	238.8	243.8	235.6	236.6	238.8
100	202.8	229.6	221.4	232.0	235.8	226.8	230.0	232.2
120	191.2	212.4	206.8	217.0	218.2	209.2	212.6	216.0
140	178.2	192.2	191.2	201.2	200.2	194.0	195.2	198.2
160	164.0	175.0	175.2	184.2	182.2	174.0	178.6	180.4
180	149.8	159.6	158.8	166.2	165.2	157.4	162.0	163.4
200	135.8	144.8	143.2	147.8	148.6	143.8	145.2	146.8
220	122.4	130.2	128.0	130.6	131.8	130.4	128.0	131.0
240	109.6	116.0	113.6	115.4	116.0	116.0	113.0	115.6
260	97.6	102.4	100.4	102.4	102.0	102.2	99.2	101.8
280	86.2	89.8	89.0	90.4	89.6	90.6	87.2	90.4
300	75.6	78.8	78.6	79.4	79.0	79.8	77.0	79.8
320	66.2	69.8	69.0	69.4	70.4	69.8	68.7	70.5
340	58.2	61.8	60.8	61.0	63.0	61.4	61.4	62.2
380	46.0	47.4	47.0	46.8	50.2	48.0	48.4	47.0
420	37.6	35.6	35.2	36.2	(36)	36.0	36.8	36.0
460	30.6	27.8	27.0	28.0	(27)	27.8	27.6	27.8
500	(22)	22.0	21.2	21.2	(22)	22.0	(22)	21.8

TABLE III (continued)

Air Overhead	28 Nov		2 Dec		3 Dec		11 Dec	22 Dec	
	A GMT	B	A GMT	B	A GMT	B	A GMT B	A GMT	B
g/cm^2	2223	2209	0129	0150	2221	2353	2054 No Flight	2157	2134
0	(212.0)	(192.6)	(224.0)	(206.8)	(239.0)	(209.0)	(246.8)	(235.2)	(204.2)
5	(223.4)	(201.6)	(232.4)	(216.0)	(246.8)	(215.6)	(250.0)	(241.0)	(212.8)
10	234.2	(210.4)	(240.6)	225.0	254.0	222.6	253.2	246.6	(221.4)
15	242.8	(219.0)	(249.0)	233.0	260.0	229.0	256.2	252.4	229.4
20	248.0	227.0	256.2	239.2	263.2	234.4	258.8	256.6	236.0
30	255.0	238.0	262.8	247.4	266.8	243.8	262.8	263.0	245.2
40	257.8	243.8	265.0	252.4	268.8	251.2	265.6	266.4	250.8
50	257.4	246.6	264.2	255.0	269.0	254.2	265.8	266.0	253.8
60	254.8	246.8	260.2	255.6	266.6	253.8	263.0	262.8	252.2
70	250.0	244.4	254.4	254.0	260.8	251.2	256.8	258.2	249.0
80	244.0	240.2	247.2	248.2	253.4	247.0	248.8	251.4	244.6
90	237.2	234.2	239.2	241.2	244.2	240.6	240.6	243.6	238.8
100	229.6	226.6	230.4	233.6	234.4	232.6	232.6	235.2	231.8
120	211.2	209.2	212.0	217.2	219.2	216.0	215.8	217.4	214.0
140	(192)	191.4	192.8	199.2	200.2	198.8	196.2	198.2	196.2
160	(172)	176.2	172.6	180.8	177.2	181.0	174.6	179.0	178.8
180	(153)	161.0	153.8	163.0	159.0	164.0	157.8	160.8	161.8
200	(137)	144.0	137.6	146.6	143.8	147.2	142.4	143.8	145.6

TABLE III (continued)

Air Overhead g/cm^2	28 Nov A GMT 2223	28 Nov B GMT 2209	2 Dec A GMT 0129	2 Dec B GMT 0150	3 Dec A GMT 2221	3 Dec B GMT 2353	1 Dec A GMT 2054	1 Dec B GMT No Flight	22 Dec A GMT 2157	22 Dec B GMT 2134
220	(122)	127.8	122.4	132.2	129.8	131.6	128.0		128.6	130.8
240	(108)	113.4	108.0	118.2	116.8	117.2	114.8		115.2	117.4
260	(94)	101.4	94.8	104.8	103.8	104.6	102.2		102.8	104.4
280	(82)	90.0	82.8	92.4	91.4	92.6	90.0		91.2	92.2
300	(73)	79.4	72.8	81.0	80.0	81.4	78.8		80.0	81.2
320	(64)	69.4	64.0	70.9	69.8	71.4	68.7		70.0	71.8
340	(56)	60.0	56.2	61.8	(62)	62.2	60.0		61.2	63.4
380	(43)	46.8	42.6	47.8	(47)	47.4	48.0		47.6	48.6
420	(32)	37.2	(32)	37.8	(37)	37.2	(37)		37.2	36.4
460	(24)	28.6	(24)	29.4	(29)	28.8	(29)		29.2	29.0
500	(20)*	-	(20)	-	(23)	-	(23)		22.8	23.6

*Extrapolated from 2 Dec.

TABLE III. (continued)

Thule Ionization, 1959

I, ion pairs/cm^3 sec atm

P	29 July	31 July	2 Aug	5 Aug	6 Aug	9 Aug	12 Aug	15 Aug
0	-							
5	-			No data				
10	-							
15	236.0							
20	241.5							
30	247.5							
40	249.5							
50	250.0							
60	248.0							
70	243.0							
80	237.0							
90	230.5							
100	223.0							
120	207.0							
140	189.0							
160	170.0							
180	153.0							
200	139.5							
220	126.5							
240	114.0							
260	101.5							
280	90.0							
300	78.5							
320	67.5							
340	57.5							
380	44.5							
420	35.0							
460	25.5							
500	20.5							

The ionization on the other days listed above fell within 1% of that on 29 July except on 15 Aug the ionization at depths from 80 to 300 g/cm fell 7 ion pairs/cm^3 sec atm below that on 29 July. At depths less than 40 g/cm^2 it lay about 4 ion pairs higher.

$$\frac{\int_{t_a}^{t_b} (dQ/dt)\, dt}{\int_{t_a}^{t_b} dt} = \overline{\frac{dQ}{dt}} = \frac{Q(t_b) - Q(t_a)}{t_b - t_a} \quad . \qquad (9)$$

$Q(t_b) - Q(t_a)$ is proportional to the total charge collected during one recharging cycle. Now define the midpoint of $t_b - t_a$ by $\bar{t} = \frac{t_b + t_a}{2}$ and let $\delta = t_b - \bar{t} = \bar{t} - t_a$. Expand the quantity $Q(t_b) - Q(t_a)$ in a Taylor series about the time $\bar{t}$. The dot denotes time differentiation.

$$Q(t_b)-Q(t_a) = \dot{Q}(\bar{t})(t_b-t_a) + \frac{\dddot{Q}(\bar{t})}{\lfloor 3} \left[(t_b-\bar{t})^3 - (t_a-\bar{t})^3\right] + \cdots \qquad (10)$$

where all even terms equal zero identically. Thence

$$\frac{Q(t_b)-Q(t_a)}{t_b - t_a} = \overline{\frac{dQ}{dt}} = \dot{Q}(\bar{t}) + \frac{\dddot{Q}(\bar{t})}{\lfloor 3} \delta^2 + \cdots$$

$$= \dot{Q}(\bar{t}) + \frac{1}{\lfloor 3} \frac{dp}{dt} \frac{d}{dp} \left(\frac{dp}{dt} \frac{d}{dp} \dot{Q} \right) \Bigg|_{\substack{t=\bar{t} \\ p=p(\bar{t})}} \delta^2 + \cdots \qquad (10a)$$

Now from equation 8, $\frac{dp}{dt} = -ap$, and $\frac{d}{dp}\frac{dp}{dt} = -a$. Therefore

$$\overline{\frac{dQ}{dt}} = \dot{Q}(\bar{t}) + \left\{ \frac{a^2 p}{\lfloor 3} \left[\frac{d}{dp} \dot{Q} + p \frac{d^2}{dp^2} \dot{Q} \right] \right\} \Bigg|_{\substack{t=\bar{t} \\ p=p(\bar{t})}} \delta^2 + \cdots$$

In practice $\delta = 3$ or 4 minutes at most and, as stated above, $\alpha = .038\ \text{min}^{-1}$. Actually the larger values of δ were used when it happened that α was small. Thence $(\alpha\,\delta)^2 \quad (3 \times 0.038)^2 = 0.013$. In the usual units $\left|\frac{dQ}{dp}\right| \lesssim 1$ in the region $\dot{Q} = 200$, $p = 125$, and the maximum of $\frac{d^2}{dp^2}\dot{Q}$ occurs where $\frac{d}{dp}\dot{Q} = 0$, $\dot{Q} = 260$, and $p = 50$. At this point $\frac{d^2}{dp^2}\dot{Q} = -0.1$. Thence in one case the second term equals -0.25 when $\dot{Q}(\bar{t})$ equals 200, and in the second case the second term is -0.5 when $\dot{Q}(\bar{t})$ is 250. Thus $\frac{\overline{dQ}}{dt} = \dot{Q}(\bar{t})$, or $\dot{Q}(p(\bar{t}))$, is a good approximation.

As figure 3 shows, a smooth curve is drawn through the data points and is extended to zero pressure by a tangent straight line. This extrapolation must be made in order to integrate the area under the I vs p curves. However, except in performing this integration extrapolated points will not be regarded as data. From the smooth curve the ionization at fixed pressures is read off and tabulated. Table III contains all of these points. Ionization is in units of ion pairs/cm^3 sec atmosphere of air; one atmosphere of air is defined to be air at 74 cm Hg and 24°C.

Parentheses have been placed around extrapolated numbers.

V. COSMIC RAY ENERGY

Flux Brought into the Atmosphere

The energy carried into the top of the atmosphere by cosmic

radiation dissipates itself in several ways. The primary nucleons' rest energy is conserved since the nucleon number is conserved. (Anti-nucleons have not been identified in the primary flux.) The primary kinetic energy, then, is distributed among the secondaries, and these eventually dissipate it in one of the following ways.

1) Charged secondaries (and primaries) lose energy by ionizing the atmosphere.

2) Some energy is carried into the earth by charged particles and dissipated by ionization there.

3) When oxygen and nitrogen nuclei are broken up by fast primaries and secondary particles some energy is lost in overcoming the binding energy of these nuclei.

4) Energy is lost to neutrinos in the decays of π and μ mesons and other unstable particles. The neutrinos carry this off into outer space.

5) The splash albedo particles carry some energy upward out of the atmosphere. A fraction of this is returned to the earth by the returning albedo particles. This fraction is probably near one at the geomagnetic equator and declines to zero at the poles.

The amount of energy going into these modes has been discussed by a number of authors (68, 69, 70, 71, 72). They have taken the experimental data on secondary cosmic ray energy spectra, and have estimated the total energy in each secondary component at all altitudes.

The pertinent data have improved greatly during the past decade, and so the later calculations should probably be given the most consideration. Table IV contains a summary of the results given by Puppi (71) and Komori (72). These writers have drawn on the work of Rossi (68), as well as later work. Komori based his calculations of the energy dissipation upon experimental data which were published in the references noted in Table IV. Counter telescopes with absorbers were used in all cases, and the energy fluxes are for unit solid angle in the vertical direction. The data at $\lambda_m = 56°$ were measured in 1947 to 1950, those at $\lambda_m = 28°$ in 1949, and those at $\lambda_m = 3°$ in 1952 to 1953. Thus the data from higher latitudes where the cosmic ray intensity varies most with the sunspot cycle were obtained near solar maximum. Hence we expect that Komori's calculations apply to the flux in 1958, but may slightly underestimate the energy lost to neutrinos then because solar activity was greater in 1958 than in 1947-1950, and the average primary particle energy was probably somewhat higher.

The total energy which is brought into the atmosphere may be estimated from measurements of the particle flux by vertical telescopes near the top of the atmopshere. Both Puppi and Komori have given such estimates, and they are shown in Table IV.

Puppi attributes the difference between the calculated rate of energy dissipation and the measured incident energy flux to the unknown energy dissipated by very slow nucleons. Komori, however, suggests

TABLE IV. Energy Balance of Cosmic Ray Flux

a) According to Puppi (1956). Calculations are for geomagnetic latitude 50°.

Component Energy dissipated by	Vertical Energy Flux mev/cm^2 sec sterad
Production of charged pions	409
Production of neutral pions	256
Nucleonic component	300
Total	965

Another way to divide this energy up is:

Energy lost in ionization	615
Energy lost to neutrinos	232
Energy set against the binding energy of nuclei	80
Residual at sea level	38
Total	965

The energy lost in ionization is obtained by subtracting the sum of the others from the total.

Puppi claims that the measured vertical energy flux is 1200.

TABLE IV (continued

b) According to Komori (1955). Calculations are for three geomagnetic latitudes, 56°, 28°, 3°.

Energy dissipated by	Vertical energy flux mev/cm^{2}sec sterad λ=56°, λ=28°, λ=3°		
	c	d	e
Collision loss of protons with 5 g/cm^2 brass $\leq$ range $\leq$ 100 g/cm^2 air	54±6	42±6	30±6
Collision loss of protons with range $\geq$ 100 g/cm^2 air	30±4	26±2	22±2
Collision loss of μ mesons in air	80±7	69±5	61±5
Collision loss of μ mesons underground	37±4	37±4	37±4
Collision loss of electrons	340±20	250±20	190±20
Sum of above collision losses	540±20	420±20	340±20
Correction due to angular spread	86±3	8	3
Energy loss by nuclear disintegration	200±40	81±16	57±12
Neutrino loss in decay of π mesons	97±5	86±5	76±5
Neutrino loss in decay of μ mesons	240±10	210±10	180±10
Total	1200±100	810±50	660±40
Total incident energy[a,b]	1910±60	1150±40	880±40

Total incident energy is calculated from data published by:

a. Winckler, J., et al., Phys. Rev. 79, 656 (1950);

b. Peters, Prog. in Cosmic Ray Physics I, (North Holland Publishing Co., Amsterdam, 1952).

The dissipation of the vertical energy flux is calculated from data published by:

c. Puller and Dymond, Prog. in Cosmic Ray Physics II, (North Holland Publishing Co., Amsterdam, 1953);

d. Vidale and Schein, M., Nuovo Cimento 8, 774 (1952);

e. Pomerantz, M., Phys. Rev., 95, 531 (1954).

that the difference is due mostly to the albedo particles being counted by vertical telescopes at high altitudes. He has also estimated the energy lost to neutrinos which may result from heavy mesons' decay, and states that this amount does not make up the difference although it may contribute to it.

Other differences between the two calculations should be considered. Puppi has considered only neutrinos produced by μ meson decay while Komori includes the result of π decay as well. Under the heading "energy loss by nuclear disintegration" Komori places both binding energy and the energy of slow fragments (evaporation particles) which are not seen by a counter telescope, while Puppi lists binding energy separately. Both have made a correction for angular spread; Komori lists it separately. This correction must be added because the vertical fluxes at high altitudes have been deduced from those at lower altitudes under the assumption that all secondary particle generation and propagation proceeds co-linearly with the direction of the primaries' motion. However, lower energy secondaries do not move parallel to their ancestors and they also suffer Coulomb scattering. Puppi has corrected for this angular spread in the nucleon to charged π to μ chain but not in the π^0 to γ to e cascade because the latter correction is so uncertain. Komori simply uses the average velocity of primaries to transform the motions of particles generated in a nucleon collision from the CM system to the lab system. (See

the work of Rossi (68).) The correction becomes small at low latitudes where the average primary energy is high. The fraction of energy given to neutrinos, however, increases in going to lower latitudes because a relatively greater energy goes into producing mesons when the average primary energy becomes higher. According to Komori these fractions are

λ_m =	56°	28°	3°
$\frac{\text{energy to neutrinos}}{\text{total calculated energy dissipation}}$ =	.28	.366	.388

If we suppose that at 56° 80 mev/cm^2 sec sterad goes into overcoming nuclear binding energy, as Puppi calculates for 50°, and that this quantity decreases toward lower latitudes in the same proportion as the total energy loss by nuclear disintegration then we find the following fractions:

λ_m =	56°	28°	3°
$\frac{\text{energy set against binding energy}}{\text{total calculated energy dissipation}}$ =	.067	.040	.034

The sums of these numbers and the fractions of energy going to neutrinos should equal the fraction of the total energy lost in processes other than ionization. These totals are:

λ_m =	56°	28°	3°
$\frac{\text{energy to neutrinos + binding energy}}{\text{total calculated energy dissipation}}$ =	.35	0.41	0.42

Probably a somewhat greater fraction of energy is lost to neutrinos by obliquely moving secondaries than by vertical ones, and somewhat less to binding energy. These fractions do not include energy carried by albedo particles. This fraction will be discussed later in connection with the ion chamber data.

The rate at which energy dissipates in the atmosphere as ionization produced by particles moving in all directions is measured by the rate of ionization throughout the atmosphere. More precisely, the number of ion pairs/sec in a column with one cm^2 cross-section extending between two levels in the atmosphere is proportional to the area under the ionization vs pressure curve between those two levels. This can be seen from the equation

$$\frac{\text{ion pairs}}{cm^3\,sec} \text{ in the atmosphere at height } h = I(h)\ \rho(h)/\rho_o \text{ (Std. atm)}$$

where ρ stands for density and $I(h)$ is the ionization at h in $\frac{\text{ion pairs}}{cm^3\,sec\,atm}$. Thence $\frac{\text{ion pairs}}{cm^2\,sec}$ between h_1 and h_2 =

$$\int_{h_1}^{h_2} dh\, I(h)\, \rho(h)/\rho_o = \frac{1}{\rho_o} \int_{p(h_2)}^{p(h_1)} dp\, I(h(p)) \qquad (12)$$

since $dh\, \rho = - dp$. The energy dissipated in the column then equals the integral times w, the average energy/ion pair. The value of w in air has been measured with various ionizing particles and it is relatively independent of charge and velocity. Johnston (61) has surveyed the literature of this subject and concludes that the best average value of w for cosmic rays in the atmosphere is 34.3 ev/ion pair. This value will be used throughout.

The energy dissipated by ionization between the top of the atmosphere and 500 g/cm^2 is found by integrating the data given in Table III. Simpson's rule was applied to the points contained in that table. The results are shown in column 3 of Table V in units of $Bev/cm^2 sec$.

To obtain the ionization vs pressure between 500 g/cm^2 and sea level (1033 g/cm^2) it was assumed that the ionization decays exponentially from the value at 500 g/cm^2 given in Table III to a value at sea level obtained in 1934-35 by Millikan and Neher (33) using unshielded ion chambers calibrated to the same standard as the present ones. The exponential dependence was found by Bowen et al. (73) using similar ion chambers carried to 29,000 ft. in 1935 on the equator.

TABLE V. Calculation of Total Energy Flux into the Atmosphere.

Date	Station A=Roving B=Base	Bev/cm^{2}sec 0 to 500 g/cm^2	Bev/cm^{2}sec 500 to 1033 g/cm^2	Bev/cm^{2}sec 0 to 1033 g/cm^2	Bev/cm^{2}sec into Earth	Bev/cm^{2}sec Total Measurable	Neutrino + binding energy correction factor	Total energy flux into atmosphere Bev/cm^{2}sec
22 June	A	1.435	.148	1.58	.061	1.64	1.64	2.69
	B	1.842	.151	1.99	.062	2.05	1.54	3.16
24 June	A	1.581	"	1.73	.062	1.79	1.64	2.94
	B	1.890	"	2.04	.062	2.10	1.54	3.24
26 June	A	1.639	"	1.79	"	1.85	1.63	3.02
	B	1.894	"	2.04	"	2.10	1.54	3.24
27 June	A	1.760	"	1.91	"	1.97	1.60	3.15
	B	1.888	"	2.03	"	2.09	1.54	3.22
29 June	A	1.816	"	1.96	"	2.02	1.58	3.20
	B	similar to 22 June	"	-	"	2.05*	1.54	3.16
30 June	A	1.851	"	2.00	"	2.06	1.58	3.26
	B	1.842	"	1.99	"	2.05	1.54	3.16
2 July	A	1.821	"	1.97	"	2.03	1.54	3.12
	B	1.806	"	1.95	"	2.01	1.54	3.10
12 July	A	-	"	-	"	-	-	-
	B	1.796	"	1.94	"	2.00	1.54	3.08
14 July	A	1.773	"	1.92	"	1.98	1.54	3.05
	B	1.802	"	1.95	"	2.01	1.54	3.10
15 July	A	1.826	"	1.97	"	2.03	1.54	3.12
	B	1.784	"	1.93	"	1.99	1.54	3.06

*Extrapolated value

TABLE V. Calculation of Total Energy Flux into the Atmosphere. (continued)

Date	Station A=Roving B=Base	Bev/cm^{2}sec 0 to 500 g/cm^2	Bev/cm^{2}sec 500 to 1033 g/cm^2	Bev/cm^{2}sec 0 to 1033 g/cm^2	Bev/cm^{2}sec into Earth	Bev/cm^{2}sec Total Measurable	Neutrino + binding energy correction factor	Total energy flux into atmosphere Bev/cm^{2}sec
17 July	A	1.830	.151	1.98	.062	2.04	1.54	3.14
	B	1.831	"	1.98	"	2.04	1.54	3.14
19 July	A	1.852	"	2.00	"	2.06	1.54	3.17
	B	1.817	"	1.96	"	2.02	1.54	3.11
20 July	A	1.871	"	2.02	"	2.08	1.54	3.20
	B	1.832	"	1.98	"	2.04	1.54	3.14
15 Oct	Bis	1.918	"	2.06	"	2.12	1.54	3.26
	Inv	1.858	"	2.00	"	2.06	1.54	3.17
16 Oct	Bis	-	"	-	"	-	-	-
	Inv	1.854	"	2.00	"	2.06	1.54	3.17
23 Oct	A	-	-	-	-	-	-	-
	B	-	-	-	.062	-	1.54	-
24 Oct	A	1.819	"	1.97	"	2.03	1.58	3.21
	B	1.873	"	2.02	"	2.08	1.54	3.20
26 Oct	A	-	.114	-	-	-	-	-
	B	1.805	.151	1.95	.062	2.01	1.54	3.10
29 Oct	A	-	-	-	-	-	-	-
	B	1.865	.151	2.01	.062	2.07	1.54	3.19
31 Oct	A	-	-	-	-	-	-	-
	B	1.864	.151	2.01	.062	2.07	1.54	3.19
2 Nov	A	0.809	.114	.92	.055	.97	1.71	1.66
	B	1.862	.151	2.01	.062	2.07	1.54	3.19

TABLE V. Calculation of Total Energy Flux into the Atmosphere. (continued)

Date	Station A=Roving B=Base	Bev/cm^{2}sec 0 to 500 g/cm^2	Bev/cm^{2}sec 500 to 1033 g/cm^2	Bev/cm^{2}sec 0 to 1033 g/cm^2	Bev/cm^{2}sec into Earth	Bev/cm^{2}sec Total Measurable	Neutrino + binding energy correction factor	Total energy flux into atmosphere Bev/cm^{2}sec
4 Nov	A	0.754	.113	.85	.055	.90	1.72	1.55
	B	1.847	.151	1.99	.062	2.05	1.54	3.16
7 Nov	A	0.802	–	.91	.055	.96	1.72	1.65
	B	1.857	.151	2.00	.062	2.06	1.54	3.17
9 Nov	A	0.841	.114	.95	.055	1.00	1.70	1.70
	B	1.862	.151	1.91	.062	1.97	1.54	3.04
11 Nov	A	0.992	.131	1.12	.058	1.18	1.68	1.98
	B	1.843	.151	1.99	.062	2.05	1.54	3.16
12 Nov	A	1.138	.140	1.28	.059	1.34	1.67	2.24
	B	1.799	.151	1.95	.062	2.01	1.54	3.10
13 Nov	A	1.274	.149	1.42	.061	1.48	1.65	2.44
	B	1.843	.151	1.99	.062	2.05	1.54	3.16
14 Nov	A	1.479	.151	1.63	.062	1.69	1.63	2.76
	B	Similar to 9 Nov	"	-	.062	1.97*	1.54	3.03*
15 Nov	A	1.673	"	1.82	"	1.88	1.59	2.99
	B	1.855	"	2.00	"	2.06	1.54	3.17
23 Nov	A	1.772	"	1.92	"	1.98	1.58	3.13
	B	1.876	"	2.02	"	2.08	1.54	3.20
26 Nov	A	1.895	"	2.04	"	2.10	1.56	3.28
	B	1.861	"	2.01	"	2.07	1.54	3.18

*Extrapolated value.

TABLE V. Calculation of Total Energy Flux into the Atmosphere. (continued)

Date	Station A=Roving B=Base	Bev/cm^{2}sec 0 to 500 g/cm^2	Bev/cm^{2}sec 500 to 1033 g/cm^2	Bev/cm^{2}sec 0 to 1033 g/cm^2	Bev/cm^{2}sec into Earth	Bev/cm^{2}sec Total Measurable	Neutrino + binding energy correction factor	Total energy flux into atmosphere Bev/cm^{2}sec
26 Nov	A	-	.151	—	.062	-	-	-
	B	1.842	"	1.99	"	2.05	1.54	3.16
27 Nov	A	-	"	—	"	-	-	-
	B	1.867	"	2.01	"	2.07	1.54	3.18
28 Nov	A	1.810	"	1.96	"	2.02	1.54	3.11
	B	1.828	"	1.97	"	2.03	1.54	3.12
2 Dec	A	1.830	"	1.98	"	2.04	1.54	3.14
	B	1.889	"	2.04	"	2.12	1.54	3.26
3 Dec	A	1.921	"	2.07	"	2.13	1.54	3.28
	B	1.881	"	2.03	"	2.09	1.54	3.22
11 Dec	A	1.899	"	2.05	"	2.11	1.54	3.25
	B	-	"	-	"	-	-	-
22 Dec	A	1.913	"	2.06	"	2.12	1.54	3.26
	B	1.874	"	2.02	"	2.08	1.54	3.20

Actually, the absorption length must become greater as depth in the atmosphere increases and the average energy of μ mesons becomes greater. The data of Bowen et al. (73) show an absorption length of approximately 187 g/cm^2 from 400 to 600 g/cm^2 depth and 240 g/cm^2 from 500 to 1000 g/cm^2. See Table VI. However, it will be assumed that the absorption length is constant from 500 g/cm^2 to sea level for the purpose of computing the area under the curve.

Table VI shows the data used for this computation and the results. The ionization at 500 g/cm^2 is taken from Table III. The sea level data are then obtained by Millikan et al. (33). Although these data were obtained in 1934-35, they are close enough to the 1958 value for the present purpose. We deduce this from the 4% peak to peak amplitude of the solar cycle variation observed by Forbush (10,15,16) with shielded ion chambers.

The calculated energies between 500 and 1033 g/cm^2 presented in Table VI are entered in column 4 of Table V. These are added to the corresponding energies contained in column 3; the sum equals the energy/cm^{2}sec dissipated by ionization in a column of air extending from sea level to the top of the atmosphere. These energies are presented in column 5 of Table V. The relation

$$\frac{\text{ion pairs}}{\text{cm}^3\,\text{sec atm of air}} \cdot \frac{\text{g}}{\text{cm}^2} \cdot \frac{\text{energy/ion pair}}{\text{density of an atm of air}} = \frac{\text{energy}}{\text{cm}^2\,\text{sec}} \qquad (13)$$

TABLE VI. Ionization between 500 g/cm^2 and 1033 g/cm^2 Atmospheric Depths.

Geom. Lat. λ_m	I* (Sea level)	I (500)	Abs. length g/cm^2	$\frac{\text{ion pairs}}{\text{cm}^3 \text{sec atm}} \cdot \frac{\text{gm}}{\text{cm}^2}$	Energy Dissipated Bev/cm^{2}sec
> 40°	2.9	22.4	260	5070	.1505
30°	2.8	18.6	280	4430	.1315
20°	2.7	15.6	300	3870	.115
10°	2.65	15.4	300	3840	.114
0°	2.64	14.8	310	3800	.113

*Millikan, R. A., et al., Phys. Rev. 50, 15 (1936).

has been used to convert the area under the ionization vs pressure curves to energy/cm^2sec, with w = 34.3 ev/ion pair and ρ_o(atm of air = 74 cm Hg, 24°C) = .001157 g/cm^3.

The energy carried into the earth and dissipated by ionization there must be accounted for. This energy flux has been estimated in two ways. First, the vertical flux at sea level given by Puppi and Komori, 37 mev/cm^2sec sterad, has been integrated over all zenith angles under the assumption that the energy flux depends upon zenith angle in the same way as the μ meson flux. (Actually the energy spectrum of μ mesons depends slightly upon zenith angle, but this is neglected here. See Heisenberg (74). Under this assumption the energy flux goes as $\mathcal{E}(\zeta) = \mathcal{E}(\text{vertical}) \cos^{1.8}\zeta$ when ζ = zenith angle. Then the total energy flux into the earth is

$$\mathcal{E}_{\text{total}} = 37 \cdot 2\pi \int_0^1 d(\cos\zeta) \cos\zeta \cos^{1.8}\zeta \qquad (14)$$

$$= 61 \text{ mev/cm}^2\text{sec}$$

The other estimate of energy carried into the earth is made from a measurement of the ionization under water down to a depth below which the ionization is negligible. If the values of ionization so obtained are converted to $\frac{\text{ion pairs}}{\text{cm}^3\text{ sec in water}}$ then the area under the ionization depth curve is again proportional to the energy dissipated.

Such an underwater measurement has been published by Millikan (65). The work was carried out in Lake Arrowhead and Gem Lake in Southern California. The ionization is given from 9 to 70 meters water equivalent but is not referred to an exact air pressure in the chamber. However, if one normalizes his data at 10 mwe (i.e., 1000 g/cm^2 depth) to later data obtained by Millikan and Neher at sea level and the same latitude, given in Table VI, then the results may be compared with the present work. The area under Millikan's curve is then $24.0 \frac{\text{ion pairs}}{\text{cm}^3 \text{ sec atm of air}} \cdot \text{mwe}$ from 10 to 70 mwe.

For relativistic particles $\frac{dE}{dx}$, $\frac{\text{energy lost}}{\text{g/cm}^2}$, is about the same in air and water since the average ionization potentials of the two are similar. Hence the total energy dissipated under water is

$$24.0 \cdot \frac{(dE/dx)_{water}}{(dE/dx)_{air}} \cdot \frac{\rho_{water}}{\rho_{air}} \cdot \frac{w_{air}}{w_{water}} \cdot w_{water} = 71 \frac{\text{mev}}{\text{cm}^2 \text{ sec}} \qquad (15)$$

This agrees pretty well with the first estimate which will be used here. (Neher has calculated the flux of energy into the earth from data more complete than are used here. He finds 90 mev/cm^{2}sec (60).) It is assumed, then, that at latitudes greater than 40° the energy flux into the earth is 61 mev/cm^{2}sec and that this amount declines toward the equator in the same fraction as the ionization at sea level, see Table VI.

These fluxes are given in column 6, Table V, and the sums of columns 5 and 6 are listed in column 7. These sums represent the total energy dissipated in the atmosphere and underground by ionization, or more precisely, the total energy loss which an ion chamber detects.

The uncertainties in the measurable energy dissipation arise from the following causes:

1) Extrapolating I(p) to O g/cm^2.

2) The unknown amount of non-reentrant albedo.

3) Interpolating I(p) between 500 and 1033 g/cm^2 depth.

4) Instrumental uncertainty.

We will attempt to estimate the size of each of these.

Most of the balloon flights attained a depth of as little as 20 g/cm^2. The particles present in the depth range, 20 to 0 g/cm^2, may be classified into splash and return albedo, primary and secondary particles which penetrate deeper into the atmosphere than that range, and primary particles which stop in that depth range. Table VII shows the energies of particles whose range in air equals 5, 10, and 15 g/cm^2, which spans the minimum depths attained by the balloons. The table also shows the geomagnetic latitude at which the Störmer cutoff in the vertical direction just equals the rigidity defined by range. Neher has published similar data in graphical form (18).

No flights made at latitudes greater than 60° gave data above 10 g/cm^2. Hence the data reported in Table III cannot show whether

TABLE VII. Relation between Range, Energy, and Vertical Störmer Cutoff.

Particle	Range in air, g/cm^2	Kinetic energy, mev	Rigidity Mv	Vertical cutoff lat.
Proton	5	73.4	370	66°
	10	108.0	460	65°
	15	136	512	64.5°
Alpha	5	295	750	62°
	10	432	920	60°
	15	542	1130	58.5°
	5	4910	1250	57.5°
Z=12.35	10	7670	1620	55°
A=23.6	15	9680	1850	53.5°
μ meson	5	28.8	83	74°
	10	43.9	106	73°
	15	57.5	124	72.5°
Electron assuming only ionization loss "Feather relation"	5	9.5	9.5	81°
	10	18.7	18.7	79°
	15	27.9	27.9	78°

or not any particles with shorter range reach the earth at high latitudes. If such short range particles were present they would produce very few secondaries with greater range provided the primaries were nuclei because the mean free path for nuclear collision is the order of 70 to 110 g/cm^2 of air. However, if soft electrons were present they would produce bremsstrahlung X-rays which could be detected below 10 g/cm^2. Such X-rays have been detected at balloon altitudes in the auroral zone, but usually appear in fairly short bursts with rapidly changing intensity (41, 42, 75).

We shall suppose that no steady flux of X-rays or electrons existed during our measurements although our data do not disprove the existence of such fluxes. As stated above, our data can prove nothing about the flux of primary nuclei having ranges less than 10 g/cm^2 of air.

Consider now the case of particles able to penetrate deeper than 10 g/cm^2. If nothing more is known about the primary energy spectrum than that no particles with less than that range occur, one can still make some statements about the ionization at lesser depths. No primary particle's specific ionization can increase significantly with decreasing depth, and therefore the ionization due to primaries from the vertical cannot increase with smaller depth but must remain constant or decrease. Also no increase in the number of secondaries moving vertically downward will occur at depths less than 10 g/cm^2

because the interaction lengths are too long. The geometrical mfp for nuclear collision is the order of 80 g/cm^2 and the radiation length in air is 38 g/cm^2. Hence only obliquely moving particles can increase the ionization above 10 g/cm^2. Some information about this contribution can be obtained from the ionization at greater depths by means of the Gross transformation.

The Gross transformation applies only when all secondary products move co-linearly with their generating primaries and when no particles decay in flight. However, at depths less than 500 g/cm^2 electrons and primaries comprise the majority of particle flux and so at depths less than 150 g/cm^2 or so the principal part of the ionization must be due to electrons and primaries, not μ mesons. If the effects of scattering and π meson decay are neglected then the Gross transformation will have some validity above 150 g/cm^2. Under these assumptions, the flux of particles with specific ionization, s, at depth, p, from a direction with zenith angle ζ depends only upon the ratio $x = p/\cos\zeta$, so that i, the ionization due to particles from unit solid angle with zenith angle ζ equals i(x). Then if I is the total ionization due to flux through a unit sphere from the upper hemisphere, so that $I(p) = \int_{2\pi} d\Omega\, i(p/\cos\zeta)$, then the Gross transformation states that

$$2\pi i_{vert}(p) = I(p) - p\,\frac{dI}{dp} \quad . \tag{16}$$

Thence, $2\pi \frac{di_{vert}}{dp} = -p \frac{d^2I}{dp^2}$.

Thence, we see from figure 3 curve A (Bismarck 26 Jan) and B(Roving Sta. 4 Nov.) that i(x) increases up to about 140 g/cm^2 = x and 240 g/cm^2 = x at Bismarck's latitude (56°) and at the equator, respectively. At a vertical depth of 10 g/cm^2 these air masses are seen at zenith angles 82° and 89°, while the earth's horizon occurs at about 95° (76). Thus at 56° and points north, i can increase with decreasing depth above 10 g/cm^2 only at zenith angles between 82° and 95°. The i for $\zeta < 82°$ must decrease while i_{vert} must decrease or remain constant. A similar statement applies to i at the equator with 89° substituted for zenith angle 82°. The solid angle subtended by the region $82° \leq \zeta \leq 95°$ is $0.23 \times 2\pi$ steradians while the region with $\zeta < 82°$ subtends $0.84 \times 2\pi$ steradians. Thence for I to increase above 10 g/cm^2 at latitudes above 56° we find that in the region of the sky where $\zeta > 82°$, i must increase more than three times as fast as i decreases where $\zeta < 82°$. The condition is even more stringent at more shallow depths or in lower latitudes. But from figure 3 and equation 16 we see that the above conditions cannot be satisfied. Hence it is concluded that I cannot increase at depths less than 10 g/cm^2 on any flight reported in Table III, due to the action of primaries with range > 10 g/cm^2. Furthermore, on those occasions such as 26 June when data were obtained at lesser depths, I

decreased between 10 and 5 g/cm^2, so that unless the primary flux was unique those days our extrapolation really begins at 5 g/cm^2.

Assuming that the Gross transformation applies precludes consideration of albedo particles, for the latter arise from the angular divergence of secondaries from the primary direction. This divergence is generated at the time of secondary production, by subsequent elastic scattering, and in the high atmosphere by the action of the geomagnetic field. If a splash albedo particle has less than the cutoff rigidity, for its position and direction, then it will return to the earth, and, as Treiman (77) has pointed out, it will return at nearly the same latitude in either the same or the opposite hemisphere as that from which it departed provided that it does not scatter off an atom high in the ionosphere into an escape orbit or decay in flight. At the equator a particle will tend to move in a helix, possibly dipping into the atmosphere many times before it loses all its energy (78). Thus albedo particles may be counted many times by instruments high in the atmosphere and may considerably increase the apparent unidirectional flux. (See the review by Singer (6).)

However, when the total energy dissipated in the atmosphere as ionization is measured by the area under an ionization vs pressure curve, the albedo can distort the result in two ways only. The splash albedo which escapes to infinity does not lose its energy to ionization

and consequently dissipates a fraction of the incident energy which cannot in principle be measured by an ion chamber. The splash albedo which does not escape loses some energy by ionizing the atmosphere above the maximum height attained by the ion chambers in this work and if this ionization differs from the extrapolated value, an error is introduced.

Complete albedo data are not available, but some fluxes have been measured in the vertical direction. McDonald (47) has published the following results.

TABLE VIII

Geomagnetic Latitude	Fast splash albedo at 0 g/cm^2, particles/ cm^2 sec sterad	Splash + reentrant albedo, at 0 g/cm^2, plus protons with 100 mev $\leq E \leq$ 350 part/cm^2 sec sterad
4°	.0022 $\pm$ .0002	.0006 $\pm$ .0003
53°	.0084 $\pm$ .0008	.003 $\pm$ .0015
55°	.0084 $\pm$ .0008	.004 $\pm$ .0015

Fast splash albedo means upward moving particles with $\beta = 1$. He concludes that most of the fast particles are electrons with range > 10 g/cm^2, and that their flux is nearly constant above 50 g/cm^2 depth. The results are extrapolated from measurements at $\sim$ 5 g/cm^2. His results agree with those of K. Anderson (79, 80) at the higher latitudes but are somewhat smaller at the equator. The primary flux

in the same units is about .01 and .1 at 4° and 56° respectively. (See results of this paper and also (48).)

One expects that most of the fast vertical splash albedo is produced by obliquely moving primaries because more secondaries are projected forward than backward. For the same reason the albedo flux should be greater at large zenith angles than in the vertical direction. However, since the vertical flux is constant above 50 g/cm^2 the oblique flux should be too. Consequently, the ionization produced by fast albedo, both splash and reentrant, should be nearly constant above 10 g/cm^2.

The slow albedo may diverge more from the primary direction than the fast, and so more of it may be generated by vertically moving primaries. Hence its flux and ionization are not expected to increase above 10 g/cm^2 either.

In the light of this discussion it is concluded that at depths less than 10 g/cm^2 the ionization must lie between the two extremes of declining linearly with pressure to zero at 0 g/cm^2, and remaining constant for depths < 10 g/cm^2. The areas bounded by these extremes correspond to 34.8 $\frac{mev}{cm^2 sec}$ and 6.9 $\frac{mev}{cm^2 sec}$, respectively on 26 June at $\lambda_m = 56°$ and 4 Nov. at $\lambda_m = 3°$. These are 1.7% and .7% of the total measured energy flux at these latitudes. However, the

ionization cannot fall to zero at the top of the atmosphere but rather to some value resulting from primary particles only. Thence, the uncertainty due to the extrapolation is certainly not more than $\pm$ .4% at the equator and $\pm$ .8% at the base station latitudes.

The uncertainty in the energy flux due to uncertain calibration of the ionization chambers is $\pm$ 0.5% relatively (intercomparison of different flights) and $\pm$ 1.0% absolutely, the latter being a systematic not a statistical uncertainty. The barometric elements' calibration is believed to be correct within $\pm$ 2 g/cm^2 at sea level and $\pm$ 0.5 g/cm^2 at 10 g/cm^2 depth. Even if the calibration were off 2 g/cm^2 at all depths, this would introduce a .1% error at the equator and .3% at the base stations and higher latitudes so that the uncertainties are $\pm$ half of these values --- quite negligible.

The energy dissipated between 500 g/cm^2 and 1033 g/cm^2 is somewhat uncertain because the ionization has been approximated by a simple exponential absorption curve. As stated previously, an exponential with increasing absorption length may be more accurate. It is found that if the ionization vs pressure curve given by Bowen (73) is integrated from 500 g/cm^2 to sea level in two segments with different absorption lengths, a value of $\int I\,dp$ is obtained which is about 12% lower than the one calculated from a simple exponential. This is about 1% of the total energy dissipation. Hence it is inferred that the

total measurable energy fluxes stated in Table V may be not more than 1% too large because the energy dissipated between 500 g/cm^2 and sea level has been overestimated.

The flux of energy into the ground may have been assigned a value as much as 1% too low judging from the two calculations made of it. Taking all of these uncertainties together, it is estimated that the absolute measurable energy fluxes given in Table V are correct to $\pm$ 2%, and that the uncertainty in the relative values must be less than this. Certainly, the error in the measured latitude dependence is small compared with the uncertainty of the energy lost to neutrinos and to non-reentrant albedo.

The energy carried upward in the splash albedo may be the order of 10% of the total energy flux into the atmosphere. Rossi (68) estimates 5 to 15%, depending upon the average angle of secondary emission if the primaries have $p/mc = 10$, and more for lower momentum primary particles. The vertical splash albedo fluxes reported in Table VIII amount to 20% and 10% of the primary particle flux at 0° and 50° respectively, so that a 10% energy flux implies a very high albedo flux at large zenith angles and/or a high average energy of albedo particle. These data of McDonald suggest that less than 10% of the energy flux is projected upwards. Since electrons are fourth

generation particles, their average energy must be less than 1/4 of the primaries' energy assuming more than one π meson is made in the primary collision. Thence less than 5% and 3% of the energy flux is projected upward at 0° and 55°. Enhanced flux at large zenith angles may increase this number.

The exact dependence of the returning fraction upon latitude is not known but may depend upon the local field or upon quadrupole and higher order terms (81). Meredith et al. (55) find that the particle flux above the atmosphere measured by rocket-borne instruments is consistent with all the splash albedo returning at latitudes less than 55° and with none returning at the poles. Their data were obtained in 1952-53 when a knee occurred in the latitude curve and a number of simplifying assumptions were made in arriving at this conclusion. However, this result agrees with what one expects from considering the rigidity needed to escape the earth's field.

No corrections for the varying amount of return albedo have been made to the energy fluxes given in Table V. If we accept Meredith's results, the correction to the measurable flux would be zero at the equator and probably up to latitudes of 55°. The energy flux at the pole should be increased 10% or less, with smaller increases at latitudes down to 55°. Since our measurements suggest that E° is constant for $\lambda_m \geq 55^{\circ}$, the albedo correction would make

the true E° increase above 55°. Yet from Table VII it is seen that no additional primary particles are allowed by the geomagnetic field above 65° which can reach 10 g/cm^2 depth. Thus if the true E° increases above 65°, the increase must be due to opening shadow cones or some other increase of the allowed region of the sky. Results presented in the next section indicate that the shadow cones are not large enough to produce a 10% increase. Hence our results indicate that either the albedo energy flux is small or else that the fraction escaping is constant above 65° geomagnetic latitude.

The measurable flux, column 7, Table V, has been corrected for the energy lost to neutrinos and nuclear binding energy by multiplying column 7 by the factor in column 8 to obtain the total flux listed in column 9. The factor has been obtained from the neutrino loss calculated by Komori and the nuclear binding energy calculated by Puppi adjusted for the latitude variation. If the fraction of the total calculated energy going to neutrinos + binding energy is α, then the factor in column 8 is $1/(1-\alpha)$. Alpha is assumed constant for latitudes above 56°. In years of solar minimum when additional particles arrive at higher latitudes α may decline between 56° and 90°.

From Table IV it is seen that the uncertainty in neutrino energy is $\pm$ 5% and in the total calculated energy $\pm$ 6% to $\pm$ 8%. This is superposed on the $\pm$ 2% uncertainty in the measurable energy flux. Thence

the uncertainty in the total flux values is the order of $\pm$ 8% and there may be a systematic error in the latitude dependence due to uncertainty in the function $1/(1-a)$. The uncertainties due to neutrino and albedo loss are much greater than those arising from the instruments and extrapolation of $I(p)$.

VI+ ANALYSIS OF DATA

One may hope to extract information about three phenomena from the data obtained in these experiments. The variation of ionization versus pressure with latitude would yield an integral rigidity spectrum of primary cosmic rays if the latter did not change during the course of measurements, and if the influence of the earth's magnetic field were exactly known. The variations in the I vs p curves observed from day to day at the base stations would give information about the primary spectrum's day to day changes if we knew how the primaries interacted with the atmosphere. Finally, some data on the symmetry of the earth's field is contained in the measurements of latitude dependence, but it is obscured by the changing primary flux.

The data contain this information mixed together since the primary spectrum did change during the period of measurement and since neither the effect of the earth's field nor the primaries' interactions with the atmosphere are known exactly. The following analysis is intended to determine a primary spectrum on a particular day or days in 1958, to describe the spectrum of the day to day changes in this spectrum during the period of measurement, and to place some limits on the asymmetry of the geomagnetic field.

The Geomagnetic Field

It is well known that the earth's magnetic field at the surface may be approximated by the field of a magnetic dipole source located at the center of the earth. The field is determined by measuring its vector at a large number of locations on the earth's surface. The measurements are all corrected to a single time. If no currents pass through the earth's surface (which may be regarded as a sphere in this discussion) the field at the surface may be represented by the gradient of a scalar potential, and this same representation will apply throughout a connected region which contains no currents. The scalar potential may be expressed, in spherical coordinates, as the sums of two series of spherical harmonics corresponding to currents inside and outside the earth. Equation 17 is one of these series. If the magnetic field were known exactly over the whole earth, it would be possible to find all coefficients in each of these series, thus determining how much of the field resulted from internal currents and how much from external. However, the location and amount of current would not be uniquely specified. Furthermore, the amount of current actually passing across the surface could be determined by calculating the vertical component of curl B (82).

Procedures have been devised for calculating a finite number of terms in these series from the finite number of measurements (83, 84). This analysis shows that less than 1%, and probably none, of the permanent field is due to external currents and that currents through the earth's surface are only a few amperes per square kilometer. Hence the field may be well represented by a potential arising from internal sources only. Vestine gives values of the first six coefficients in the expansion for epoch 1945. Coefficients for epoch 1955, derived from new magnetic surveys of the earth, are given by Finch and Leaton (85) and for the first six spherical harmonics; i.e., the first forty-eight coefficients are given. See Table IX for the first eight of them. These numbers are called Gauss coefficients, are denoted by g and h, and appear in the expression for the potential as

$$V = a \sum_{n=1}^{\infty} (A/r)^{n+1} \sum_{m=0}^{n} [g_n^m \cos m\phi + h_n^m \sin m\phi] P_n^m(\theta), \quad (17)$$

where P_n^m is an associated Legendre polynomial normalized so that

$$\frac{1}{4\pi} \int_{4\pi} d\Omega \, [P_n^m(\theta) \begin{matrix}\cos \\ \sin\end{matrix} m\phi]^2 = \frac{1}{2n+1} , \quad (18)$$

and a = radius of earth, mean value 6367.6 km.

θ = colatitude measured from north pole,

ϕ = east longitude.

TABLE IX. The First Eight Gauss Coefficients for the Earth's Field

Epoch 1955*

	Gauss		Gauss
g_1^0	+.3054	g_1^1	+.0226
		h_1^1	-.0592
g_2^0	+.0228	g_2^1	-.0524
		h_2^1	+.0330
		g_2^2	-.0137
		h_2^2	-.0022

*From Finch, H. F., and Leaton, B. R., Royal Astr. Soc. Monthly Not 7, 314 (1957).

If the coordinate system is rotated, different (primed) coefficients are obtained, and in particular if it is rotated so that $g_1^{1'} = h_1^{1'} = 0$, the coordinate axis coincides with the dipole axis, and the new coordinates are called centered dipole coordinates. The dipole strength is then $g_1^{0'} a^3 = M$ in gauss cm^3. $M = 8.054 \times 10^{25}$ gauss cm^3 in 1955. Geomagnetic latitude is measured from the geomagnetic equator, defined by the plane perpendicular to the dipole axis passing through the dipole center, and geomagnetic longitude is measured eastward from the meridian half plane bounded by the dipole axis and containing the south geographic pole.

If the coordinate axes are now translated without rotation another set (double primed) of gauss coefficients results. The dipole coefficients, $g_1^{0'}$, $g_1^{1'}$, $h_1^{1'}$ do not change value, so that $g_1^{1''} = h_1^{1''} = 0$, and $g_1^{0''} a^3 = M$, but in general the other coefficients change. The translation may be chosen so that three of the five quadrupole coefficients vanish, i.e., $g_2^{0''} = g_2^{1''} = h_2^{1''} = 0$, leaving $g_2^{2''}$ and $h_2^{2''}$ which have the same values, $g_2^{2'}$, $h_2^{2'}$ that they had in the center dipole system (82). The origin of these coordinates is called the magnetic center. This translation is also that one which makes the root mean square of the quadrupole potential integrated over the earth a minimum. The root mean square potential of nth order is defined by

$$|V_n| = \left[\sum_{m=0}^{n} (g_n^m \; g_n^m + h_n^m \; h_n^m) \; \frac{1}{2n+1} \right]^{1/2}$$

The values of V_1 and V_2 in center dipole coordinates computed from Table IX have the values

$$|V_1'| = .1802$$

$$|V_2'| = .030$$

These may be compared with values quoted by Bartels (86) for epoch 1885.

$|V_1'| = .1865$ $|V_2'| = .0151$ $|V_3'| = .0085$ $|V_4'| = .0040$ in the center dipole system,

and $|V_1''| = .1865$ $|V_2''| = .0091$ in the eccentric dipole system.

The coordinate system defined above is called the eccentric dipole system. A magnetic field generated by a dipole of strength located at the magnetic center is often used to approximate the earth's field, and is called an eccentric dipole field. It best approximates the real field only in the sense that $|V_2|^2$ has been minimized. It possesses also the same convenient feature that the center dipole coordinates have: $g_1' = h_1' = 0$.

The points at which the dipole's axis intersects the earth's surface are called geomagnetic poles and may be computed from the

location of the magnetic center and the inclination of the dipole. Table X gives this and other information. The geomagnetic poles have also been computed by Parkinson and Clearly (87).

Transforming Coordinates

It is sometimes convenient to transform the location of a point on the earth's surface from geographic coordinates to geomagnetic, either centered or eccentric. Define a geographic Cartesian coordinate system by

$$x = a \sin\theta \cos\phi$$

$$y = a \sin\theta \cos\phi$$

$$z = a \cos\theta$$

where θ = colatitude measured from north pole

ϕ = east longitude

These may be transformed to Cartesian geomagnetic coordinates by rotation and translation matrices. Center dipole geomagnetic coordinates, denoted by single prime, are given by

$$\begin{pmatrix} x' \\ y' \\ z' \end{pmatrix} = x' = Ax \tag{19}$$

Eccentric dipole Cartesian coordinates, denoted by double prime, are given by

TABLE X. The Magnetic Center and the Geomagnetic Poles.

Year	Position of mag. center			Geographic position of geomagnetic poles				Magnetic dipole moment
	Geographic coord.		Distance from earth	Center dipole		Eccentric dipole		
	Lat.	Long.	center	Lat.	Long.	Lat.	Long.	gauss cm^3
1922[1)]	6.5°N	161.8°E	342 km	78.5°N 78.5°S	291.2°E	80.1°N 76.3°S	277.3°E 121.2°E	8.13×10^{25}[3)]
1945[2)]	14°N	154°E	400 km	78.6°N	289.8°E	80.1°N	277.3°E	8.06×10^{25}[4)]
1955[2)]	15.3°N	151.1°E	433 km	78.2°N	291.0°E	80.9°N 75.0°S[3)]	276.7°E 120.4°E[3)]	8.05×10^{25}[3)]

Note: The US Navy Hydrographic Office has published maps of the magnetic field and its secular change for epoch 1955. Charts are numbers 1700, 1701, 1702, 1703, and 1706 with each number having an equatorial and two polar projections.

1) J. Bartels, Terr. Mag. and Atm. Elec. 41, 225 (1936) (Ref. 86).

2) W. Webber, Nuovo Cimento, Suppl. to 8, Ser. X, 2nd trimester (1958), p. 532 (Ref. 88). The 1945 values are calculated from data given by Vestine et al. (83, 84). The 1955 values are calculated from data given by Finch and Leaton (85), based on a 1955 magnetic survey.

3) Calculated by author. Location of south geomagnetic pole was calculated from Webber's values of tilt and location of eccentric dipole. The dipole moment was calculated from $M = |g_1^0| a^3$ with g_1^0 taken from Bartels, and Finch, and using a = 6367 km as a mean radius of the earth.

4) Vestine et al. This reference also contains magnetic field maps, information on secular changes in the field, etc., for epoch 1945 (83, 84).

$$\begin{pmatrix} x'' \\ y'' \\ z'' \end{pmatrix} = x'' = A(x - \underline{\underline{\Xi}}) \, . \tag{20}$$

The Cartesian geographic position of the magnetic center is

$$\underline{\underline{\Xi}} = \begin{pmatrix} \xi \\ \eta \\ \zeta \end{pmatrix} \, , \tag{21}$$

and

$$A = \begin{pmatrix} \cos\Theta \cos\Phi & \cos\Theta \sin\Phi & -\sin\Theta \\ -\sin\Phi & \cos\Phi & 0 \\ \sin\Theta \cos\Phi & \sin\Theta \sin\Phi & \cos\Theta \end{pmatrix}. \tag{22}$$

Here Θ and Φ are the geographic colatitude and east longitude of the center dipole north geomagnetic pole. Geomagnetic angular coordinates are related to x' and x'' in the same way θ and ϕ relate to x.

When the 1955 data from Table X are substituted into these formulae one obtains

$$\underline{\underline{\Xi}} = \begin{pmatrix} -.057422 \\ +.031698 \\ +.017943 \end{pmatrix} \quad a, \text{ with } a = 6367.6 \text{ km}, \tag{21a}$$

and

$$A = \begin{pmatrix} .35080 & -.91385 & -.20450 \\ .93358 & .35837 & 0 \\ .07329 & -.19092 & .97887 \end{pmatrix}. \tag{22a}$$

It is assumed above that the earth is spherical, which seems justified, since the polar and equatorial radii are 6356.9 and 6378.4 km, respectively, the difference being small compared with the distance between the magnetic center and the earth's center. The distance between any location on earth and the magnetic center is given by

$$r'' = (x''^2 + y''^2 + z''^2)^{1/2} \quad \text{obviously.} \tag{23}$$

The radius of the earth may be conveniently used as the unit of length in such calculations.

Motion of Charged Particles in the Geomagnetic Field

The orbits of charged particles moving in the geomagnetic field have usually been approximated by motion in a dipole magnetic field and various perturbations of this motion have been used to more closely describe motion in the real field.

C. Störmer first investigated motion under the influence of a pure dipole magnetic field about 1904 in an attempt to explain the polar aurora, and he continued to study this problem up until his death. His recent book (89) summarizes this work as well as that of other workers, notably Lemaitre and Vallarta (90-92). As a result principally of these men's work, the following conclusions may be stated:

1) The equations of motion cannot be integrated analytically in terms of any known functions except in the case of motion confined to the equatorial (geomagnetic) plane in which case the motion is described by elliptic functions.

2) Consider a location on the earth and a differential element of solid angle in a particular direction centered on this location, and suppose that particles can pass through the earth without being absorbed. Particles with a given magnetic rigidity, R, may or may not be able to reach the given location in the element of solid angle if they start an infinite distance from the dipole. Magnetic rigidity is defined by

$$R = \frac{pc}{Ze} ,$$

and its dimensions are usually chosen so that numerically R equals pc in electron volts divided by Z, the number of electronic charges. In these units $B\rho = \frac{R}{300}$ with B in gauss and ρ the instantaneous radius of curvature, in centimeters. In cosmic ray work R is usually written as so many Bv to distinguish it from energy in Bev.

A consequence of Liouville's theorem is that the intensity of particles of given rigidity (particles/cm^2sec sterad) along a pencil of orbits in a static magnetic field remains constant. Therefore, if particles with rigidity R starting infinitely far from the dipole can reach a given location from an element of solid angle in a given direction, then they will arrive with the same intensity which they had at

infinity. So, if particles of rigidity R occur with homogeneous and isotropic intensity at infinity, then they will arrive at any location on earth from all allowed directions with that same intensity; from other directions they will not arrive at all. The latter directions are called forbidden.

3) Consider a particular location, and suppose that all the particles have positive charge. Maintain the assumption that the particles can pass through the earth unaffected by its presence.

The whole sky (4π steradians) is allowed to particles with sufficiently high rigidity, and it is all forbidden to low rigidity particles. For particles with an intermediate rigidity, the sky may be divided into three regions. The eastern part of the sky is entirely forbidden. This forbidden region is bounded by the Störmer Cone, which can be determined analytically from the equations of motion. To the west of the Störmer Cone lies the Main Cone, and all directions west of it are allowed. The solid angle bounded on the west by the Main Cone and the east by the Störmer Cone is called the penumbral region. It is filled with alternating allowed and forbidden directions. These bands and also the Main Cone must be determined by integrating numerically the equations of motion (90-93). With increasing rigidity these regions and bounding cones move to the east until the whole sky is allowed. The pattern of regions is reversed from east to west for negatively charged particles, i.e., it is reflected in the meridian plane.

The penumbral region is supposed to be filled with a non-dense set of forbidden zones in the absence of an absorbing earth and it is conjectured that the forbidden zones form a set of measure zero (94). However, when the impenetrable earth is taken into account it is found that most of the penumbra is forbidden at the equator, and up to latitude 30°, while most of it is allowed in higher latitudes (90-94). At intermediate latitudes it is occupied by alternating allowed and forbidden zones.

Singer (6) gives the following table of penumbral transparency. He gives Schwartz (95) as the origin of the data, although the abstract of Schwartz' talk does not contain this table.

λ_m	Percentage Transparency
0-20°	0
30°	31
35°	1
41°	50
45°	53
50°	71

Schwartz has since published a report of his work in Nuovo Cimento (95) which contains these results and other data.

4) When absorption of particles by the earth is taken into account some further allowed regions become forbidden in addition to the zones of the penumbra discussed above. Clearly all directions

in the lower hemisphere are forbidden. In addition, at any particular location certain connected regions in the upper hemisphere are forbidden to particles of appropriate rigidity because orbits from these directions would pass through the earth at other locations on their way inward from infinity. The boundaries of these connected regions are termed the earth's simple shadow cones, and were first calculated by Schremp (94). Recent calculations show that Schremp's calculations are in error and that the shadow cones are much smaller than the earlier calculations showed (96), as had been long suspected from experimental results. Previous calculations by Schwartz (95) and by Vallart et al. (97) confirm the newer result, although the latter authors attribute the smaller calculated shadow cones to the effect of the quadrupole field which they have included in their calculations.

These cones and regions are defined by their intersections with an upper hemisphere of unit radius centered on the location in question and may be represented by the orthogonal projections of this hemisphere upon a horizontal plane together with the loci of the intersections with the cones. The allowed solid angle then appears as a projected area denoted by $A(R, \lambda)$ where λ = geomagnetic latitude. (In the general case of a non-dipole field, λ can represent location.)

$$A(R,\lambda) = \int_{\Omega_a(R,\lambda)} d\Omega(\psi,\zeta) \cos\zeta \tag{24}$$

where $\Omega_a(R, \lambda)$ = allowed solid angle

ψ = azimuth

ζ = zenith angle

$d\Omega$ = $\sin \zeta \, d\psi \, d\zeta$.

Figures 4 and 5 show the value of $A(R, \lambda)$ for various λ. The curves marked Störmer Cone are drawn assuming that the penumbra is entirely allowed and those marked Main Cone under the assumption that it is all forbidden.

The Main Cone has not been given for $\lambda > 30°$, but the penumbra is supposed to change from mostly forbidden at 30° to mostly allowed at 50°. Nor have the earth's simple shadow cones been included for $\lambda < 30°$ since they contribute a negligible forbidden solid angle at lower latitudes (96). The values of A bounded by the Störmer Cones were calculated analytically from the Störmer theory. Values bounded by Main Cones and simple shadow cones were obtained by graphically integrating cone diagrams published by Lemaitre and Vallarta (91) and Kasper (96), respectively.

Figure 6 shows the minimum value of R which a particle may have and be able to arrive vertically and the R for which $A = \pi/2$, as a function of latitude. These data were taken from the preceding figures and from Stormer theory. Note that the vertical Störmer cutoff is also that rigidity for which the Störmer Cone fills half the sky.

A function $a(\zeta, R, \lambda)$ will be used later which is defined as follows: a = amount of azimuthal angle at zenith angle ζ which falls within the allowed cone for the given R and λ. That is

$$\Omega(R,\lambda) = \int_0^{\pi/2} d\zeta \sin\zeta \int_{\psi_1(R,\lambda,\zeta)}^{\psi_2(R,\lambda,\zeta)} d\psi$$

$$= \int_0^{\pi/2} d\zeta \sin\zeta \; a(\zeta, R, \lambda) , \tag{25}$$

and of course

$$A(R,\lambda) = \int_0^{\pi/2} d\zeta \sin\zeta \cos\zeta \; a(\zeta, R, \lambda) . \tag{26}$$

Values of Ω, A, and a have been published in various places; see for example (98, 99). But some of the data used in these papers have been superceded. The 1955 dipole moment and the radius, a, given in Table X, have been used in preparing Figures 4 to 6 from the published cone diagrams. The form of these curves remains the same independently of the dipole strength and the distance from the dipole to the observation point. The absolute value of R which appears in them depends, however, upon M, and a, through the Störmer relation.

$$s^2 = \frac{M}{R/300} \tag{27}$$

where s = Störmer unit of length, and a is measured in units of s. The equations of motion become dimensionless when all lengths are measured in units of s. At a given latitude the cones are the same at all distances, r, from the dipole provided that r/s, the radius in Störmer units remains the same. Thus the rigidity R scales from one radius r and dipole M to another according to

$$R = \frac{300M}{r^2} \quad (\frac{r^2}{s^2}), \text{ with } r^2/s^2 = \text{constant.} \tag{27a}$$

All of the above results apply to the motion of individual particles only; if the particles' flux becomes great enough that their current appreciably alters the dipole field, then these results are not valid. A simple criterion for the particles not being able to affect the dipole field is that

$$\frac{B^2_{\text{dipole}}}{8\pi} > \text{kinetic energy density of particles.}$$

In the case of galactic cosmic rays, the kinetic energy density 1 ev/cm^3, while the magnetic field energy density at the earth's surface is $\frac{0.3^2}{8\pi} = .00358$ erg/cm^3 $= 2.24 \times 10^9$ ev/cm^3. Hence the inequality would hold out to $\sim$1000 earth radii if the only field in space were the earth's dipole field and the only particles were galactic cosmic rays.

It is now known that at distances greater than 10 to 15 earth radii the dipole field may be disrupted by the solar wind at some times, if not continuously, near the sub-solar point, so that the effect of galactic cosmic rays upon the field may be neglected in comparison with disturbances generated by other phenomena (2).

General discussions of cosmic rays' motion in a dipole field are found in reviews by Neher (5), and Singer (6).

Motion in the Real Field

Two problems arise in trying to actually determine what portion of the sky is allowed at any particular location to particles starting at infinity. One of these occurs because we do not know what currents may flow outside the earth's surface. Although it is observed that less than 1% of the surface field arises from external currents during geomagnetically quiet times, this is not enough to specify just what currents may flow. In particular, it has been suggested by several workers (89,100,101), that a ring current may flow around the earth in or near the geomagnetic equatorial plane. Such a current may move the impact zone for particles shot out by the sun many degrees, but may still produce a small surface field. For instance, according to Stormer (89), a current which produced only .0002 to .0005 gauss at the surface is sufficient to move the calculated auroral zone from

within a few degrees of the geomagnetic pole to 23° away from it, where the aurorae are most often observed. The influence of such a ring upon other impact zones has been calculated as well. See, for example, references (102) and (103). The existence of such a current has not yet been either proved or disproved by comparing calculated orbits with experimental results. As stated above, deviations from a dipole field and varying fields have been directly observed at 10 to 15 earth radii by the space probe Pioneer V (2).

The second problem arises from the fact that the geomagnetic field known to have its origin within the earth is not a pure dipole field. In order to find the allowed cones at a particular location the effect of higher order multipoles must be treated as a perturbation on the influence of a dipole alone, or else the orbits in the exact field must be integrated directly. Although the latter is possible, the numerical work required is very great and results are not available for many locations or directions.

Partly because of these difficulties the cosmic rays themselves have been used to determine the allowed cones at various locations on the earth. If the incident direction and rigidity of incoming primaries could be measured at the top of the atmosphere, then the allowed cones could be directly so determined. Since such measurements have not been feasible until quite recently, indirect methods have been used to

learn as much as these methods allow. For the most part, it is assumed in these studies that the cosmic ray flux is homogeneous and isotropic at great distances from the earth and remains constant during the period of measurement. The geomagnetic field and any external currents must also be supposed to remain constant during the measurements, and efforts are usually made to exclude periods of geomagnetic or solar disturbance from the data. It is usually supposed in interpreting cosmic ray data that the amount of allowed solid angle at any location increases monotonically with R or else remains constant. Furthermore, it is often supposed that if a particular direction is allowed at some locations for particles with rigidity R, then it is allowed for all greater R. In the dipole case this is not true within the penumbra but is correct if the direction lies within the main cone.

It is of interest to consider the results of some cosmic ray surveys and to compare them with the geomagnetic field's intensity.

Millikan and Neher (33) present the results of their measurement of the rate of ionization at sea level in a map showing lines of equal sea level cosmic ray intensity. It may be noted that the minimum occurs near 12° N lat. 90° E long. in geographic coordinates. Relative minima are, of course, found in going from north to south along every meridian, and the locus of these minima may be thought of as a cosmic ray equator which would correspond with the geomagnetic equator if the earth's field were pure dipole. The cosmic ray equator so defined crosses the

geographic equator at about 150° E long. and 25° W long. (geographic) reaching farthest south at 90° W long, and farthest north at 115° E long. Simpson (34) shows a plot of just this minimum for comparison with his own data. When this map of equal intensity is compared with a map showing lines of equal vertical cutoff rigidity in an eccentric dipole field (see, for example, Kodama et al. (104) for the 1945 dipole, and Webber (88)), it can be seen that the cosmic ray equator intersects the geographic equator at longitudes 40° to 50° west of where one would expect from considering the cutoffs in a dipole field. Also the minimum of cosmic ray intensity lies 40° to 50° west of the position of the maximum cutoff which corresponds to the dipole's eccentricity. The change in the dipole between 1930-35 and 1945 is not significant for this comparison.

Simpson (34) has published just such a comparison. He gives the position of a cosmic ray equator, determined from data taken with neutron monitors and vertical meson telescopes carried aboard ships. The effects of world-wide fluctuation of intensity have been removed and corrections have been made for changing barometric pressure. The cosmic ray equator is determined by a least squares fit to the data, assuming that the c.r. equator has the form of a sine wave on a mercator projection. This curve agrees pretty well with the c.r. equator deduced by Simpson from the data of Millikan and Neher (33).

However, it lies 40 to 45° west of the magnetic equator of either a center or eccentric dipole but has about the same tilt as the magnetic equator with respect to geographic coordinates. Simpson suggests that this discrepancy cannot be due to deviations of the internally generated field from a dipole, but must be caused by the field's being altered at some distance from the earth by external currents. The latter may arise from the interaction between the earth's rotating dipole field and the interplanetary plasma. It may be remarked that Simpson's cosmic ray equator more nearly coincides with the magnetic equator defined by the line of zero dip than with the dipole equators. See also Rose et al. (105).

Kodama (35) has published a map of lines of equal sea level cosmic ray neutron and meson intensity which he has deduced from several workers' data normalized to one another. This is compared with a map of equal vertical cutoff rigidity in an eccentric dipole field published by Kodama et al. (104). Kodama concludes that the cosmic ray pattern is indeed shifted some 45° west of the dipole cutoff pattern at the equator but less so at higher latitudes so that the amount of shift may be approximated by 45° cos λ, with λ = geomag. lat. In an erratum (106) he notes that the distribution of cosmic ray intensity agrees better with cutoffs calculated by Quenby and Webber (107) using multipole terms up to 6th order.

The idea that the local field determines the allowed rigidities at each location has been put forward by Rothwell (37) and Rothwell and Quenby (36). She assumes that locations where the sea level neutron intensity is equal have equal vertical cutoff rigidities and that the latter are determined in part by the local field. The effect of the local field is approximated by a dipole located at earth's center and with its strength and inclination defined by the local field from the equations

$$\tan \lambda_s = \frac{\tan \delta}{2}$$
$$H_{hor} = \frac{M_s}{a^3} \cos \lambda_s \qquad (28)$$

with δ = dip angle, H_{hor} = horizontal field intensity and λ_s = geomagnetic latitude with respect to the hypothetical dipole, and M_s = strength of this dipole. A vertical cutoff R_s corresponding to the locally determined dipole is then calculated from Störmer theory. If R_D represents the vertical cutoff due to the centered dipole, then it is stated that an effective cosmic ray cutoff, R_C, is related to R_S and R_D by

$$R_C = 0.9 R_S + (1 - 0.9) R_D \left(\frac{R_D}{R_S} \right) . \qquad (29)$$

The fraction 0.9 has been determined from the sea level neutron data,

and it is found that after fixing this one parameter, all points having equal R_C have nearly equal neutron intensities and that plotting intensity in various parts of the world against the appropriate R_C produces a smooth curve with little scatter. The plot includes data from the region of magnetic anomaly off the South African coast.

The values R_C and R_S are also compared with alpha particle cutoffs measured directly in experiments able to determine both charge and energy of vertically incident particles. It is found that the minimum rigidities observed at various places agree much better with R_C and R_S than with the center dipole cutoff. Rothwell concludes that the divergence between cosmic ray intensity distribution and dipole vertical cutoff proceeds from the effect of local field deviations from the dipole field and not from unknown distortions of the field by external currents.

Quenby and Webber (107) approach the problem of allowing for local anomalies' effects rather differently than Rothwell. They argue on theoretical grounds that a particle arriving vertically with just a little more than the minimum possible rigidity moves on a path just before reaching the earth which depends upon the local field, and hence that the vertical cutoff rigidity at a particular location depends strongly upon the local field. They then assign the difference between the local field and the center dipole field to multipoles of order 2 through 6 and determine a local effective dipole from the center dipole and the local

difference weighted to allow for the decline of multipole strength with altitude above the earth. Different procedures are applied to high latitude and equatorial regions. Effective vertical cutoffs are then computed from this effective dipole which are similar to Rothwell's. The writers show that their effective cutoff fits the minimum observed alpha particle rigidities and the distribution of flux from the Feb. 23, 1956, flare better than eccentric dipole cutoffs. The effective cutoff also fits the cosmic ray equator determined by Simpson on airplane flights carrying neutron monitors, and the northern auroral zone better than the dipole cutoffs do. The effective cutoff rigidity differs from the eccentric dipole cutoff by as much as 4 Bv off the coast of South Africa.

Neher (5) has used data taken with meson telescopes carried aboard a B-29 to investigate the shape the allowed cones have at geomagnetic latitude 64° N to 0° along geographic longitude 80° W. For experimental details, see references (38) and (108). He assumes that the allowed cones published by Vallarta (91) are correct at the geomagnetic equator, and by comparing the fluxes measured in various directions there with those observed at more northerly latitudes he calculates the minimum allowed rigidities at the vertical up to latitude 22.5° N and at 45° east and west of the vertical up to latitudes approximately 50° N and 45° . These cutoff rigidities mostly fall between the

Störmer and main cone cutoffs given by Vallarta (91). Thus it appears that the data are consistent with the cones at medium latitudes being related to those at the equator as if they resulted from a pure dipole field. Neher has corrected for the tilt and eccentricity of the dipole so that actually eccentric dipole coordinates have been used. This study does not measure any cutoff rigidity directly so that the calculated cutoffs are known only to within a constant factor.

This brief discussion by no means exhausts the list of surveys of cosmic ray intensity and the attempts to fit the observed intensities to the geomagnetic field. In particular, it should be remarked that workers have calculated orbits and vertical cutoff rigidities in the dipole plus quadrupole field (97, 109) and have calculated the effect a ring current would have upon orbits (103). Results of the quadrupole calculations do not appear complete enough to compare with experiment. Apparently the accuracy of present cosmic ray data can neither prove nor disprove the existence of some ring current. During magnetic storms, the cutoff rigidities appear to change at some latitudes, presumably because of the same external currents which generate the storm (21), but such periods of geomagnetic activity will not be considered here.

In conclusion, it may be said that the world-wide intensity distribution of cosmic rays measured at sea level resembles the

pattern that an eccentric dipole would produce but that it is shifted with respect to the dipole. Furthermore, when the rigidity of particles is measured directly, the minimum observed seems not to agree with that calculated from the geomagnetic dipole. However, it appears that local deviations of the earth's field from that of the eccentric dipole agree pretty well with deviation of cosmic ray intensity and cutoff rigidity from values calculated from a dipole field. It does not seem necessary to invoke external currents to explain anomalous effects although the present experimental results cannot disprove the existence of some such current.

In the rest of this paper it will be assumed that at any location on the earth the shape of the allowed cones is that which a dipole would produce. The agreement between the cosmic ray data reported herein and various effective dipoles will be considered in the next chapter.

Analysis

The analysis which follows resembles the schemes used by several cosmic ray physicists to relate observations made in the atmosphere to the primary radiation above. Dorman (3) has given an especially complete method for relating the secondary and primary radiations. However, the system used here has been worked out to analyze the data obtained by us, and is presented without further reference to the work of others.

Let $J_i(R)$ equal the flux of nucleons in type i nuclei with rigidity between R and R + dR, the differential flux being measured in units of nucleons/cm^2 sterad sec Bv. Then the ionization measured at a depth p and geomagnetic latitude (locations in general) λ can be written

$$I(p,\lambda) = \int_{2\pi} d\Omega \cos\zeta \int_{R_{min}(\lambda,\zeta,\psi)}^{\infty} dR \sum_i J_i(R)\, m_i(R,p,\zeta) \qquad (30)$$

where $d\Omega = d(\cos\zeta)\, d\psi$ the element of solid angle from which primary radiation comes

ζ = zenith angle

ψ = azimuth angle

$R_{min}(\lambda,\zeta,\psi)$ = minimum allowed rigidity from direction ζ, ψ at location λ,

m_i = response function

if the following assumptions are made:

1) Each primary particle acts independently. This allows I to be linear in J, i.e., m does not depend upon J.

2) $J_i(R)$ does not depend upon direction except as a particular R is either allowed or forbidden. This follows from geomagnetic theory when J_i is homogeneous and isotropic at infinity, so that it is the latter condition which is assumed. This would certainly not be the case when particles arrive directly from the sun but such times are excluded from the discussion.

3) The production and propagation of secondary particles does not depend upon the magnetic field, so that m is independent of λ and ψ. This is expected to be essentially true for secondaries moving in the atmosphere because scattering and nuclear interactions mask the deflection produced by the field. Albedo particles' motion obviously depends upon the local field where the particles originate. So long as all albedo returns, however, an omni-directional detector should respond nearly the same at all locations. There is evidence that when $\lambda < 60°$ nearly all albedo returns (55). At higher latitudes, of course, an increasing proportion escapes. The significance of this fact will be discussed later.

4) The geomagnetic effects are the same over the entire region in which primaries can reach the atmosphere and affect a fixed detector.

5) A particular direction is allowed for all rigidities above the direction's cutoff, and forbidden for all lower rigidities. The function m_i will depend upon the distribution of mass overhead, that is upon temperature distribution, but this will not be written explicitly.

The energy per cm^2 per second brought into the atmosphere by cosmic rays may be written

$$E^{o}(\lambda) = \int_{2\pi} d\Omega \cos\zeta \int_{R_{min}}^{\infty} dR \sum_i E_i(R)\, J_i(R) \qquad (31)$$

where $E_i(R)$ is the kinetic energy per nucleon in a type i nucleus with rigidity R.

The orders of integration may be reversed in these expressions so that for given rigidity the flux is integrated over the allowed solid angle and then integration is carried out over all rigidities.

$$I(p,\lambda) = \sum_i \int_o^{\infty} dR\, J_i(R) \int_o^{1} d(\cos\zeta)\cos\zeta\, a(\zeta, R, \lambda) m_i(R, p, \zeta) \qquad (30a)$$

and

$$E^{o}(\lambda) = \sum_i \int_o^{\infty} dR\, E_i(R)\, J_i(R)\, A(R,\lambda) \qquad (31a)$$

where the functions a and A which describe the allowed cones have the meanings stated in the previous chapter.

The functions m_i may be calculated, in principle, from the appropriate scattering and interaction cross-sections. However, not all of these are known and if they were, the problem would remain extremely complicated. It appears more practical to determine m_i from the data and the above expression for I. (See Neher (5) for calculations of quantities similar to the m_i from other data.) This means that the differential rigidity spectra J_i must be calculated from the energy fluxes obtained in Chapter V by means of the equation for E^o. This equation can only determine the sum $\sum_i E_i(R)\, J_i(R)$ as a function of R, and some additional assumptions must be made in order to define the J_i individually.

The question of how the primary composition, i.e., the charge spectrum depends upon energy and of how it may vary with time has not been fully answered. In a recent review article, Waddington (110) concludes that the rigidity spectra of protons, alphas and heavier nuclei of the light medium and heavy groups (abbreviated p, α, L, M H, see Table XI for definitions) probably have the same rigidity dependence over the latitude sensitive range from 1.5 to 16 Bv. He has taken account of the eleven year variation in comparing measurements. It is possible, according to Waddington, that the L nuclei numbers decline more rapidly with increasing rigidity than the other groups, but the data are not precise enough to decide whether this is

the case or not. Webber (88) has reached much the same conclusion in an earlier paper.

Furthermore, Waddington states that the evidence on fluxes of p and α with greater rigidity indicates that the rigidity dependence of the spectra are the same. There is no data above 10^5 Bev/nucleon. A single measurement of the flux of M and H nuclei with $E \geq 10^5$ Bev/nucleon is consistent with the M and H rigidity spectra having the same dependence as the p and α spectra in this region.

These conclusions contradict Singer's (6) deductions that heavier nuclei have a steeper rigidity dependence than light. However, Waddington bases his statements upon recent data at higher rigidities which show a higher flux than did the data available to Singer. Very little is known about the primary electron energy spectrum, but recent data show that the flux of electrons with $R > 0.50$ v is 3% of the proton flux in 1960, or possibly more (121,122). The electron flux is neglected in this analysis.

The problem of whether the different primary components vary in the same way is more confused. McDonald's (48) measurements show that the proton spectrum had the same rigidity dependence as the alpha spectrum in 1955-56 and again in 1957-58 when the fluxes were lowered by the increased solar activity. During both periods the p/α ratio was about 6.5 : 1. Measurements extend from 0.75 to 16 Bv

approximately. No data are given for heavier nuclei.

Meyer (50) finds that between 1957 and 1958 the proton flux decreased $\sim 15\%$ while the flux of alphas with KE > 530 mev/nucleon did not. However, during a Forbush decrease in 1957 the two components changed in the same way. Meyer also observed a possible diurnal variation in the alpha flux which he suggests may be caused by solar alpha particles.

In 1954 Fowler et al. (111) found that the alpha flux did not increase in going north from Minneapolis to Saskatoon. The total intensity of ionizing particles did. Hence it is concluded that the alpha spectrum at low rigidities differed from the proton spectrum.

In spite of these uncertainties we shall suppose that modulation of galactic cosmic rays affects all components similarly. We shall also assume that the rigidity spectra of all nuclei depend upon rigidity in the same way. These are the simplest possibilities which can be chosen, and they appear reasonable in the light of present data.

The abundances to be used are taken from Waddington, whose results are reproduced in Table XI. The data are for nuclei with rigidity $\geq$ 5 Bv, but we are assuming that the ratios remain the same for all rigidities. Hence we can write

$$J_p = 0.53\, J_o(R)$$

$$J_a = 0.314\, J_o(R) \qquad (32)$$

$$J_h = 0.156\, J_o(R)$$

for the fluxes of nucleons in the corresponding sorts of nuclei. The average value of A in the nuclei with $Z > 2$ (this group will be denoted by h) may be defined as the ratio of nucleons to nuclei in this group and works out to 17.25. The average value of Z/A in the h group is computed to be 0.522 by using the given distribution of Z within the group.

The kinetic energy per nucleon, $E_i(R)$, was computed from the usual formula taking account of the fact that $M_a = 3.97$ and $Z/A_{heavy} = .522$. An average energy $E_{av}(R)$ may then be defined by

$$E_{av}(R) = 0.53\, E_p(R) + 0.314\, E_a(R) + 0.156\, E_h(R) \qquad (33)$$

and then

$$\sum_i E_i J_i = J_o(R)\, E_{av}(R) .$$

The problem of finding the J_i has been reduced to finding $J_o(R)$ from

$$E^o(\lambda) = \int_o^\infty dR\, J_o(R)\, E_{av}(R)\, A(R,\lambda) \qquad (31b)$$

where $J_o(R)$ = flux of nucleons with rigidity between R and R + dR.

TABLE XI. Composition of the Primary Radiation.

Nuclear Group[a]	Flux at Texas[a] part/m^2 sterad sec	Number above a constant rigidity: Number of nucleons	% nuclei[b]	% nucleons[b]	Average A[b]	Average Z[b]	Definition of group[a]
H	600 ± 30	600	85.9	53.0	1	1	$Z=1$
He	89 ± 3	356	12.7	31.4	4	2	$Z=2$
L	$2.0 \pm .2$	19	.29	1.67	9.5	4	$3 \leq Z \leq 5$
M	$5.60 \pm .20$	78	.80	6.9	14	7.5	$6 \leq Z \leq 9$
	$1.88 \pm .30$	45	.27	3.95	24	14.5	$10 \leq Z \leq 19$
	$0.69 \pm .16$	34	.09	3.0	49	24	$20 \leq Z \leq 28$

a) Waddington, C. J., Prog. in Nucl. Phys. (Pergamon, 1960), Vol. 8, pp. 1-45 (110).

b) Derived by author.

$$A = \frac{\text{flux of nucleons}}{\text{flux of nuclei}}$$

Z = mean of nuclear group

The flux of nuclei is then

$$j_{\text{nuclei}} = \left(0.53 + \frac{0.314}{4} + \frac{0.156}{17.25}\right) J_o = 0.62\, J_o \quad . \qquad (34)$$

The equation for I may be rewritten

$$I(p, \lambda) = \int_o^{\infty} dR\, J_o(R) \int_o^{1} d(\cos\zeta)\, \cos\zeta \quad a(\zeta, R, \lambda)\, m(R, p, \zeta) \qquad (30b)$$

where $J_o(R)m(R,p,\zeta) = \sum_i J_i\, m_i$ defines m. Now if the geomagnetic effects incorporated in $A(R,\lambda)$ were precisely known, and if $E^o(\lambda)$ were known for one instant of time over a range of λ, then we would solve for $J_o(R)$ in equation 31b for a corresponding range of R. This function could then be substituted into equation 30b and by using simultaneously measured values of $I(p,\lambda)$ some information about $m(R,p,\zeta)$ could be obtained. However, $A(R,\lambda)$ is not exactly known, and neither E^o nor I are known as functions of λ free of variations in time. We set aside the uncertainty in A for the moment and consider how to separate fluctuations in time from latitude variations.

Variations in $I(p,\lambda)$ are observed at the λ of the base stations over a period of time. It is assumed that these variations oorrespond to changes in $J_o(R)$ beyond the earth's field and that J_o remains homogeneous and isotropic there throughout these changes. It is also supposed that the geomagnetic field does not vary. Under these assumptions the base station data are to be used to correct the observations

made by the roving station to what they would have been had all been made at the same time. Thus, if at a base station one observes a variation $\Delta J_o(R)$ of J_o from its form at a particular time chosen as a reference, then ΔE^o and ΔI at the roving station are given by

$$\Delta E^o(\lambda) = \int_o^\infty dR \ \Delta J_o \ E_{av} \ A \tag{35}$$

λ = latitude (location) of roving station

and

$$\Delta I(p,\lambda) = \int_o^\infty dR \ \Delta J_o \int_o^1 dx \ x \ a \ m \ , \tag{36}$$

with $x = \cos \zeta$,

provided that no particles are allowed at the roving station that do not reach the base station. Nothing is known about J_o for R which are not allowed at the base station. If particles with rigidities below the base station cutoff reach the roving station when it is at higher latitude than the base station, it is impossible to correct for variations in these using base station data. It is also not possible to allow for the different atmospheric temperature distributions at the base and roving stations without using meteorological data, nor can one known a priori if the primary intensity variations at the base station are world-wide;

i.e., know if the flux remains homogeneous and isotropic beyond the earth's field.

However, Neher (52) has observed in the past that similar variations usually occur at Bismarck and at points north. We will proceed by assuming that all primary variations are world-wide and that meteorological variations are small. Then, if the base station corrections to roving station data do not always "improve" the latter, we shall see if the failure can be attributed to meteorological effects or to non-isotropy of the primary radiation.

Now if the function m is unknown, then equation 36 is of no use, and it is impossible to deduce ΔJ_o from ΔI at the base station. Thence it is impossible to find ΔE^o and ΔI at the roving station. Of course, if it were possible to calculate ΔJ_o from ΔI at the base station then one could also calculate J_o from I at a high latitude station and the latitude survey would be unnecessary. Hence, one must use some information about m or J_o obtained from other studies of cosmic rays in order to obtain from the data reported here J_o at a reference time and the variations ΔJ_o.

An iterative method will be used. The best order of operations appears to be:

a) Study $I(p, \lambda)$ measured at the two base stations and using any known properties of m derive ΔJ_o or at least some conditions on ΔJ_o.

b) Apply this information to correct I and E^o at the roving station to what would have been obtained on the reference day. If the corrections smooth the functions $E^o(\lambda)$ and $I(p,\lambda)$ vs λ, then they may be assumed to be more or less correct.

c) From the corrected values of E^o calculate J_o from equation 31b.

d) Then, using J_o, calculate as much as possible about m from equation 30b.

e) Using m, calculate better values of ΔJ_o from the base station data on ΔI.

f) And so on, until satisfactory J_o, ΔJ_o and m are obtained. The size of the corrections and the rate of improvement will decide how may times to iterate.

Figure 7 shows the variations in I observed at the base stations at selected atmospheric depths. Several features should be noted.

1) Fluctuations are greater at shallow depths than at great ones.

2) Although a cyclic variation occurred during the summer, no secular trend appears. No secular trend appears during the autumn either.

3) The ionization at Bismarck did increase between 20 July and 15 October.

4) The simultaneous flights on 15 October at Bismarck and Invercargill show that the ionization was greater at Bismarck. This

may be because the primary flux beyond the geomagnetic field was not homogeneous and isotropic that day or because the geomagnetic cutoff rigidity at Invercargill is higher than at Bismarck. Data favoring the latter reason will be presented later.

5) Unless the ionization at Bismarck was anomalously high on 15 October, the data are consistent with a world-wide increase of intensity between 20 July and 15 October.

July 20th was chosen to be the reference date for the summer flights, and October 15th for the fall, the latter being selected because of the simultaneous flights at the two base stations, and the former because the ionization was about average for the summer that day. Figures 8 and 9 show the amount $I(p, \lambda)$ at the base stations varied from its values on the respective reference days. The uncertainty of the points shown there is at least $\pm$ 0.7% because they represent the differences between curves with uncertainties of $\pm$0.5%.

The Δ I at Bismarck have these characteristics:

1) The curves either lie within $\pm$ 2 ion pairs of zero or else they have a shape similar to the $I(p, \lambda)$ curves with the exception noted under 2).

2) On the 27th of June and 12th of July $|\Delta I|$ increased with decreasing pressure rather than levelling off or turning over as the other curves do. This form appears much more pronounced in the Δ I for 15 October - 20 July at Bismarck and also in the difference between

the Invercargill and Bismarck 15 October ionizations.

3) There is some evidence for a relative extremum at about $p = 280$ g/cm^2.

Effect 3) and also deviations of $\pm$ 2 from a smooth curve are interpreted as the result of temperature changes in the overlying atmosphere and experimental error. Note that 2.5 = 1% of 250, the maximum in $I(p, \lambda)$. Similarity between ΔI and I indicates that ΔJ and J have roughly the same dependence upon R for some range of J. The curves noted in 2) must arise from the presence or absence of low energy particles which are absorbed without producing a maximum in $I(p, \lambda)$. Some idea of the energies such particles must have may be gained by comparing the $I(p, \lambda)$ observed by the roving station at different latitudes. Even without correcting these for time variations it can be seen that particles allowed above a latitude corresponding to a vertical cutoff rigidity = 3 to 5 Bv produce no maximum in the I vs p curve, while higher rigidity particles do produce such a maximum.

The variation in I observed at Invercargill has the same characteristics. Most of the ΔI are near zero or approximate the shape of the I curve. The curves which clearly show the presence or absence of low energy particles are 23, 24 October, 13 November, the first flight on 26 November, and possibly 28 November.

It may be asked if particles allowed only at higher latitudes than the base stations fluctuated without being observed at the base stations. On the average, very few more particles reach the earth north of Bismarck than appear at that station, as can be seen from figures 11 and 12, which show that Bismarck lies to the north of the knee. Furthermore, if the I at Bismarck is subtracted from the I obtained simultaneously by the roving station on those days when the latter was north of Bismarck, the difference is nowhere greater than 9 ion pairs/cm^2 sec atm. See figure 10a. On all but two days the differences appear to be due to experimental error and temperature effect. On 14 July, a few rapidly absorbed particles reached Bismarck that did not arrive at the roving stations. The two were at nearly the same geomagnetic latitude so that this may be due to a higher cutoff rigidity at the roving station. On 20 July more low energy particles apparently arrived at the roving station, then near the geomagnetic pole, than at Bismarck. Both of these differences may be error and temperature effect, since they are small. It is concluded that no systematically increasing flux is seen in going north from Bismarck, and that no large fluctuations occurred in the flux of particles with rigidities below the Bismarck cutoff. However, the data do not exclude 1-2% fluctuation.

When we turn to the corresponding curves in the southern hemisphere, it is obvious that low energy particles were reaching points south of Invercargill which could not reach the latter base station. See figure 10b. The difference for the first flight on 26 November, which does not show the extra ionization due to low energy primaries, corresponds to a day when the roving station was near the latitude of the base station. The large differences at higher pressure on 26 November and 2 December may be caused by a real anisotropy in the primary radiation far from the earth, as indeed may the much smaller differences observed deeper in the atmosphere on all the days.

We may expect, then, that corrections for fluctuations in high latitude data will succeed in the northern hemisphere better than in the southern. We may expect less success also on days when figure 10 shows an excess of radiation present at the roving station over that at the base station. In making these corrections, it is assumed that the fluctuations in the primary spectrum have the form

$$\begin{aligned} \Delta J_o(R) &= b\, J_o(R) \quad \text{for } R < R_{max} \\ &= 0 \qquad\quad \text{for } R > R_{max} \end{aligned} \tag{37}$$

where b = constant on any particular day but varies from one day to another. It is assumed that $R_{max} < \infty$ because nearly all observations of spectral variations show that $\Delta J_o / J_o$ becomes smaller as R

increases. See, for example, Neher and Forbush (32). Equation 37 is a simple approximation to the true circumstance that b $\simeq$ const. for small R (2 to 10 Bv) and b $\rightarrow$ 0 as R $\rightarrow \infty$.

For the first iteration it is supposed that R_{max} = 17 Bv, or more exactly, that the radiation which can reach the equator does not fluctuate. Under this simple approximation the corrections have the following forms:

$$I_o(\lambda) - I(\lambda_m) = \frac{I_o(\lambda_{base}) - I_o(\lambda_m)}{I_T(\lambda_{base}) - I_o(\lambda_m)} \quad [\, I_T(\lambda) - I(\lambda_m) \,] \qquad (38a)$$

with λ_m = latitude corresponding to vertical cutoff = R_m in equation 37

λ = latitude of roving station

I_T = ionization on any day

I_o = ionization on the reference day

All I in equation 38a correspond to the same p, and 38a holds for all p. The corresponding equation for the energy flux into the atmosphere is

$$E_o^o(\lambda) - E^o(\lambda_m) = \frac{E_o^o(\lambda_{base}) - E^o(\lambda_m)}{E_T^o(\lambda_{base}) - E^o(\lambda_m)} \quad [E_T^o(\lambda) - E^o(\lambda_m)] \,. \qquad (38b)$$

If we put $R_m = \infty$ then $E^o(\lambda_m)$ and $I(\lambda_m)$ would be zero

although λ_m is not defined in this case. When both roving and base station lie above the knee so that the fluctuations at the roving station may be assumed to be the same as at the base station, the corrections take the form

$$I_o(\lambda) = I_T(\lambda) - [I_T(\lambda_{base}) - I_o(\lambda_{base})] , \tag{39a}$$

$$E_o^o(\lambda) = E_T^o(\lambda) - [E_T^o(\lambda_{base}) - E_o^o(\lambda_{base})] . \tag{39b}$$

These join smoothly with equations 38a,b at $\lambda = \lambda_{base}$ as an expansion of the denominator in equation 38a,b will show. Note that equations 39 apply without the assumption that b = const. in equation 37, although equations 38 do not. Figures 8 and 9 show that this assumption was poor on only two days when the roving station made observations below the knee. These were 24 October and 13 November.

In correcting the present data we use equation 38a,b with $\lambda_m = 0$ for data taken at latitudes lower than the base station. Data taken at higher latitudes are corrected using equation 39a,b, even though Invercargill is not quite above the knee. Figure 11 shows the improvement which this correction brings about. The corrected E^o also appear in Table XII. The corrected E^o calculated assuming that $R_m = \infty$ are listed also. The summer data are corrected to 20 July and the fall to 15 October. No attempt is made to adjust the summer to the fall data because the spectrum of additional particles in the fall differs from the total spectrum in the summer and fall.

TABLE XII. Energy Flux, E^o, Before and After Correction for Time Fluctuations.

Date	E^o, Bev/cm^2 sec Uncorr.	Corr.	Corr. with $R_m = \infty$
22 June	2.69	2.68	-
24	2.94	2.86	2.85
26	3.02	2.93	2.92
27	3.15	3.07	
29	3.20	3.18	
30	3.26	3.24	
2 July	3.12	3.16	
12	-	-	
14	3.05	3.09	
15	3.12	3.20	
17	3.14	3.14	
19	3.17	3.20	
20	3.20	3.20	
15 Oct Bis	3.26	3.26	
15 Oct Inv	3.17	3.17	
24 Oct	3.21	3.18	
2 Nov	1.66	1.66	1.65
4 Nov	1.55	1.55	
7	1.65	1.65	
9	1.70	1.71	1.77
11	1.98	1.98	1.99
12	2.24	2.27	2.29
13	2.44	2.45	
14	2.76	-	
15	2.99	2.99	
23	3.13	3.11	3.10
26	3.26	3.25	
28	3.11	3.16	
2 Dec	3.14	3.05	
3	3.28	3.23	
11	3.25	-	
22	3.26	3.23	

In the northern hemisphere the correction makes the curve of I vs p smooth at 50 g/cm^2 and 20 g/cm^2 depth but does not markedly improve the curves at greater depths. The corrected curves are, if anything, worse than the uncorrected in the southern hemisphere. The poorer results in the southern hemisphere are expected from the observation that the lowest rigidity primary radiation present in the fall could not reach the base station at Invercargill. The poorer results at great depths in the atmosphere probably arise from the variations in I at these depths induced by changing temperatures overhead. Not only does this distribution vary from day to day at the base station but it also changes systematically with latitude.

Discussion of Temperature Effect

Figure 12 shows the temperature at constant air pressure observed at Bismarck during the period of measurement (112). Figure 13 shows temperature vs pressure at Bismarck and Thule in summer and winter (112). The fractional variation in the hard meson flux at depth p_o due to deviations of the overlying atmosphere's temperature from some reference temperature distribution is given by

$$\frac{\delta N_\mu(p_o)}{N_\mu(p_o)} = \int_o^{p_o} dp\, W_T(p, p_o)\ \delta T(p) \qquad (40)$$

with p_o = pressure at observation point

$\delta T(p)$ = temperature deviation at depth p

The weighting function W depends upon the minimum energy meson considered, the directional characteristics of the detector, and the "standard" atmosphere from which the temperature deviations are measured. Dorman (3) has given formulae for W_T as well as a few numerical results. It is possible to estimate from these the variation in the total ionizing component which a given δT will produce. At 300 g/cm^2

$$\frac{\delta N(p_o)}{N(p_o)} = .057\% \ \delta T(p_o) + 0.53 \ \frac{\delta N_\mu(p_o)}{N_\mu(p_o)} \qquad (41)$$

is obtained from Dorman's estimate of the various secondary components. The coefficients do not change very rapidly with depth. The size of $\delta N_\mu / N_\mu$ at 250 g/cm^2 may be computed from data given by Dorman if N_μ is the vertical meson flux. It is found that if δT is uniform in the overlying atmosphere, $\delta N_\mu / N_\mu = 0.36\%/°C$ for vertical flux at 250 g/cm^2, .49%/°C for the same at 100 g/cm^2, and is larger at greater zenith angles. The contribution of μ mesons is not expected to increase with decreasing depth above 300 g/cm^2. Thus the 10°C fluctuations which appear in figure 12 can easily produce a change of 2% in the total ionizing component, which is sufficient to account for fluctuations of 2 to 3 ion pairs in the ionization at the base station

between 200 and 300 g/cm^2. The difference in the temperatures at Bismarck and Thule shown by figure 13 are sufficient to produce 2% differences in ionization at the two locations.

These numbers are only an estimate of the temperature effect. However, a more exact calculation would not improve the accuracy of the primary energy spectrum to be calculated, and so does not seem worth carrying out. A more serious problem connected with the temperature effect is that the systematic change in temperature with latitude for latitudes lower than the knee induces a corresponding change in the fraction of energy lost to neutrinos. This effect is given by Dorman (3) for the vertical muon intensity at sea level and 250 mb pressure. The variation of temperature with latitude induces a 4% increase over the equatorial value at sea level in going from $\lambda = 0°$ to $\lambda = 55°$, while a decrease equal to 3% of the equatorial value is produced for 250 mb depth. The former number amounts to a temperature effect upon the energy flux into the earth and was included in our calculation of $E^o(\lambda)$ by the use of measured values of sea level muon intensity and energy flux. The effect of temperature effect at higher levels has not been so allowed for. Komori does not include this effect in his calculation of energy balance. Judging from the result at 250 mb, a 2 to 3% uncertainty in $E^o(\lambda)$ presented in Table XII may be ascribed to this temperature effect. This is probably

no larger than other uncertainties in the fraction of energy lost to neutrinos. Accordingly, the values of I and E^o are not corrected for variations in the atmosphere's temperature.

Effective Geomagnetic Latitude

The next step in the iterative procedure would be to use the value of E^o corrected for time fluctuations to obtain $J_o(R)$ by means of equation 31b. However, the effective geomagnetic latitude from which to calculate $A(R, \lambda)$ along the roving station's route is not known. In order to estimate what system of calculating effective geomagnetic latitude best fits the present data, E^o and I at selected pressures have been plotted against cutoff rigidities calculated in three ways.

First, the geomagnetic latitude at each location from which a successful flight was launched was calculated in centered dipole and eccentric dipole coordinates and also in the local field determined dipole system, defined by equation 28. The distance from the eccentric dipole and the dipole moment determined by the local field were computed as well for each location. These data appear in Table XIII in units of mean earth radius a, and dipole moment M. The cutoff rigidity corresponding to each latitude is taken from figure 6. This cutoff is defined to be that rigidity for which $A = \pi/2$, i.e., for which

TABLE XIII. Geomagnetic Coordinates and Cutoff Rigidities.

Date	Local Field Coordinates $^{o}\lambda$	M/M_{center}	R_c, Bv	Eccentric Dipole Coordinates $^{o}\lambda$	a^2/r^2_{ecc}	R_c, Bv	Center Dipole Coordinates $^{o}\lambda$	R_c, Bv
22 June	39.2N	1.087	6.28	37.7N	.974	6.25	38.9N	5.9
24	43.5	1.077	4.52	41.1	.974	4.89	42.3	4.6
26	46.0	1.083	3.76	43.1	.976	4.20	44.3	3.9
27	50.8	1.074	2.55	46.7	.980	3.32	48.0	2.98
29	55.3	1.036	1.50	50.1	.984	2.46	51.4	2.24
30	58.2	1.026	1.16	52.4	.984	2.00	53.7	1.82
2 July Bismarck	61.1	1.057	.845	55.3	.994	1.54	56.3	1.38
12	58.2	1.010	1.14	52.2	.950	1.99	55.0	1.58
14	56.8	.972	1.28	55.4	.944	1.44	58.7	1.08
15	60.8	.959	.800	60.3	.952	.845	63.8	.55
17	69.5	.942	.197	70.5	.974	.172	74.2	.066
19	76.6	.860	.030	80.7	.997	< .01	84.6	< .01
20	78.9	.898	.015	83.2	1.004	< .01	87.1	< .01
- Thule	80.9	.931	.009	84.7	1.007	< .01	88.3	< .01
15 Oct Invercargill	56.1S	1.138	1.61	54.7S	1.062	1.75	51.7S	2.20
23 Oct	55.0N	1.044	1.65	54.3N	1.03	1.75	54.1N	1.74
24	50.6	1.047	2.52	50.6	1.03	2.50	50.2	2.48
26	39.4	1.065	6.05	-	-	-	-	-

TABLE XIII. Geomagnetic Coordinates and Cutoff Rigidities. (continued)

Date	Local Field Coordinates			Eccentric Dipole Coordinates			Center Dipole Coordinates	
	$^{o}\lambda$	M/M_{center}	R_c, Bv	$^{o}\lambda$	a^2/r^2_{ecc}	R_c, Bv	$^{o}\lambda$	R_c, Bv
29 Oct	30.1N	1.093	11.05	31.6N	1.025	9.58	31.7N	9.3
31	20.6	1.048	14.3	22.7	1.04	13.71	22.7	13.1
2 Nov	10.2	1.041	16.1	14.0	1.03	15.35	14.2	14.9
4	2.1	1.058	17.3	3.0	1.058	17.18	3.3	16.2
7	10.5S	1.090	16.8	11.0S	1.067	16.41	10.3S	15.5
9	21.3	1.107	14.9	20.9	1.072	14.6	19.7	13.8
11	29.7	1.121	11.5	29.4	1.072	11.18	27.8	11.3
12	34.4	1.128	8.96	33.9	1.072	8.85	32.1	9.1
13	38.2	1.133	6.98	37.9	1.07	6.80	35.9	7.28
14	43.1	1.128	4.85	42.8	1.068	4.70	40.6	5.24
15	48.0	1.121	3.36	47.7	1.063	3.26	45.2	3.68
23	51.6	1.133	2.49	50.8	1.06	2.51	48.1	2.94
26 1st flight	55.6	1.143	1.71	54.3	1.055	1.79	51.7	2.18
28	62.4	1.115	.747	60.3	1.04	.915	57.8	1.19
2 Dec	73.3	1.099	.093	68.8	1.01	.244	67.1	.320
3	77.1	1.081	.031	74.5	1.00	.063	71.2	.155
11	79.7	1.112	.0145	76.2	1.00	.029	74.8	.057
22	76.8	1.100	.036	79.8	.99	.012	78.9	.017

half the sky is open. This rigidity, R_c, is larger than the vertical cutoff in those low latitudes where the penumbra is mostly dark. This choice will be discussed in the next section. In view of Neher's work (5), it may be more appropriate to consider the penumbra more than half transparent $\lambda = 30°$, so that $R_c(30°)$ would lie between the vertical Störmer cutoff and the main cone cutoff chosen. This has not been done. However, so long as $R_c(\lambda)$ is chosen in a consistent way, the fit of the data to an effective geomagnetic latitude will remain the same. The values of R_c from figure 6 have been altered in the case of eccentric dipole and local field coordinates to allow for the changing radius from the dipole and dipole moment, respectively. The values of R_c have been scaled according to the Stormer relation

$$s^2 = \frac{M\ 300}{R} \tag{27}$$

with s = Störmer unit of length. The cutoffs so calculated are given by Table XIII.

Figures 14 through 16 show corrected ionization at selected pressures plotted against R_c calculated for each of the three coordinate systems. It has been necessary to show I at 20 and 50 g/cm^2 depth separately from I at greater depths in order to avoid confusion.

The summer and fall data do not coincide because of the increased number of lower energy primaries observed in the fall. However, if the only change in the primary spectrum between summer and fall is this increase, then we expect the fall data to coincide with the summer for sufficiently large R_c and to rise above it where smaller rigidities can reach the earth. The ionization in the fall should never lie below that in the summer at the same R_c unless the primary spectrum was depleted over some range of R in the fall. If we assume that the latter did not occur, then the appearance of figures 14 through 16 may be used to decide which definition of R_c (and effective latitude) best fits the present data.

Consider the figures showing I at 20 and 50 g/cm^2. The eccentric dipole cutoff does not fit at all because in that system the summer and fall curves cross at $R_c \simeq 2$ Bv. Both center dipole and local field determined R_c appear acceptable, although the curves for local field determined R_c join more smoothly. When one turns to the plots of I at greater depths, the eccentric dipole coordinates are at once ruled out because Bismarck and Invercargill appear at nearly the same R_c and because I in the fall lies below I in the summer when $R > 2$ Bv. The latter discrepancy seems to rule out the local field determined R_c as well. However, the summer data appear high at $R_c > 4$ Bv mostly because the data from the 22 June flight are high. Thus the inconsistency in the local field determined R_c depends upon

one flight and appears only at depths greater than 50 g/cm^2 where temperature effects may become important.

It should be noted that the eccentric dipole model puts Bismarck and Invercargill at nearly the same cutoff, which is not consistent with the different ionizations observed on the simultaneous flights of 15 October.

In short, comparison of data taken in the two hemisphers shows that along the route of this survey the data may

a. Best be fitted to center dipole cutoffs.

b. Would fit local field determined cutoff as well as center dipole ones if the data from 22 June at depths greater than 50 g/cm^2 were ignored.

c. Do not fit eccentric dipole determined cutoffs.

These observations are contrary to what other workers have found. Two partial explanations for this suggest themselves. For one thing, the ion chamber has omni-directional sensitivity, while the instruments used in the other surveys were either vertical telescopes or were operated at so great an atmospheric depth that they were sensitive only to fairly vertically incident primaries. Particles arriving at large zenith angles have travelled some distance near the earth while vertically incident particles have not. Thus the motion of the former probably depends less upon the local field at this point of arrival than does the motion of vertically arriving particles. This argument

suggests that the local field does not strongly affect the effective cut-off for particles arriving from the entire upper hemisphere, and that a model field fitted to the real field over a larger portion of the earth should be more appropriate. However, the best dipole fit to the entire field is the eccentric field. Thus one might expect that it would fit the data better than the center dipole.

The other possible explanation stems from the fact that this survey did not cover regions of the earth where the dipole fields and the real field differ greatly. For instance, the trip crossed the equator at a longitude where the dip and dipole equators closely coincide. Also we did not pass near India, where the sea level cosmic ray intensity has a minimum. Thus a small systematic experimental error may have generated the apparent best fit to the center dipole coordinates.

The present experiment, of course, does not measure cutoff rigidity directly. The experiments of Webber, McDonald, and others which do have shown that the observed minimum vertical cutoffs agree better with a local field cutoff than with any dipole model.

Consequently, we shall calculate the primary rigidity spectrum $J_o(R)$ using both the center dipole geomagnetic field, which fits our data, and the local field model, which fits the work of others.

Calculation of $J_o(R)$, the Rigidity Spectrum

The differential rigidity spectrum, $J_o(R)$, may now be calculated from $E^o(R)$ and equation 31b. It should be understood that in this context λ stands for location, not just latitude, and that the form of A as a function of R depends upon this location. We have assumed in discussing effective geomagnetic coordinate systems that A always has a form corresponding to some location in a dipole field. Under this assumption, A may be written as $A(R; \lambda_e, M)$ where λ_e is the effective latitude and M the effective dipole moment. M may be regarded as taking on various values either because the moment defined by the local field varies according to equation 28 or because the distance to the magnetic center changes. In either case, a change in M scales the values of R according to equation 27 but does not change the form of A as a function of R, the form depending only upon λ_e.

Now in the foregoing section a single cutoff, R_c, was assigned to each location, and it was supposed that at locations with equal values of R_c equal values of I(p) should be observed in the absence of time variations and atmospheric differences. This procedure conceals the further assumption that I(p) changes in the same way when either M or λ_e vary by corresponding amounts. In general, this can be true only if the form of A as a function of R depends upon some single

function of M and λ_e. Such is not the case. The assumption may be justified by noting in Table XIII that M does not deviate more than about 13% from earth's dipole value, which generates a change of the same size in R_c. This change corresponds to a shift of only 2 or 3 degrees of latitude. The form of $A(R; \lambda_e, M)$ changes so little over this interval that the change may be neglected. That is, we may write $A = A(R, \lambda_o)$ where now $\lambda_o = \lambda_o(\lambda_e, M)$ and A has the form it would have at latitude λ_o at a radial distance, a, from a moment M_{earth}; i.e., at latitude λ_o in the earth's center dipole field.

To each value of λ_o is related a value R_c defined by $A(R_c, \lambda_o) = \pi/2$. Hence, one may write $A = A(R, R_c)$. The observed energy fluxes, E^o, are assigned to the values of R_c corresponding to the locations, i.e., the λ_e and M or equivalently λ_o, where they were measured. Equation 31b then appears as

$$E^o(R_c(\lambda_e, M)) = \int_o^\infty dR\ J_o\ E_{av}(R)\ A(R, R_c)\ . \qquad (31c)$$

Figure 17 shows E^o uncorrected for time variations plotted against R_c calculated for center dipole coordinates. Figures 18 and 19 show E^o corrected for time variations plotted against R_c in the center dipole and local field coordinates. A differential spectrum J_o will be calculated from each of the latter two figures.

A convenient way to solve equation 31c makes use of the special form of A as a function of R. As figures 4 and 5 show, A may be represented by the sum of a step function from 0 to π at some point $R = R_o$ plus a function which is non-zero over a limited range of R. This latter function may be denoted by B, and if R_o is chosen appropriately B has the form 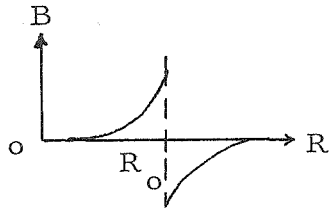

. Clearly, the exact shape of B depends upon R_o but the general form of B remains the same for a range of R_o. By using this representation of A, equation 31c may be rewritten

$$E^o(R_c) = \pi \int_{R_o}^{\infty} dR\, J_o(R)\, E_{av}(R) + \int_{o}^{\infty} dR\, J_o(R)\, E_{av}(R) B(R, R_c; R_o) \quad (31d)$$

Both J_o and E_{av} are smooth, positive functions of R. Hence it is possible to choose R_o so that the second term in equation 31d equals zero. Denote this value of R_o by $R_o^{(\infty)}$. The value of $R_o^{(\infty)}$ depends upon the form of $J_o(R)$ as well as upon R_c. However, if $R_o^{(\infty)}$ were known, then J_o could be easily found from equation 31d, which takes the form

$$E^{o}(R_c) = \pi \int_{R_o^{\infty}(R_c)}^{\infty} dR\, J_o\, E_{av} \,, \qquad (31e)$$

whence $\frac{dE^o}{dR_c} = -\frac{dR_o^{(\infty)}}{dR_c}\, \pi\, J_o(R_o^{\infty})\, E_{av}(R_o^{(\infty)})$, with R_o^{∞} evaluated at R_c.

This equation can be solved for J_o.

The easiest way to find J_o is to iterate.

1) Choose a value $R_o^{(1)}$ of R_o, and from it calculate $J_o^{(1)}$ from equation 31e.
2) Determine a better value $R_o^{(2)}$ of R_o from $J_o^{(1)}$ and $A(R, R_c)$
3) Calculate $J_o^{(2)}$ from $R_o^{(2)}$ and equation 31e.
4) Etc.

This may be regarded as a sub-routine or iteration on the whole iteration procedure outlined earlier in this chapter.

It is convenient to choose $R_o^{(1)} = R_c$ since this simplifies equation 31e, and because R_c was defined so that it should be a reasonable approximation to $R_o^{(\infty)}$. The function $J_o^{(1)}$ generated by this choice of $R_o^{(1)}$ is shown in figure 20 for the center dipole case. The function dE^o/dR_c was obtained by differentiating graphically the curve in figure 18. In the log log coordinates of the former figure a straight line with slope $-\gamma$ corresponds to a power function $J_o = \text{const}/R^{\gamma}$.

Since γ changes only slowly with R, $R_o^{(2)}$ can be estimated by finding an exact R_o for different values of γ at various values of R_c.

This was done by integrating graphically the function $A(R,R_c)/R^{\gamma}$. The values R_o which resulted appear in Table XIV.

TABLE XIV. Effective Cutoff $R_o^{(\infty)}$ for Various Latitudes.

λ_m	R_c, Bv	Slopes = γ				
		2.75	2.5	1.9	1.4	1.1
		Effective cutoffs $R_o^{(\infty)}$, Bv				
0	16.4	16.7	17.0	17.6		
30°	10.1	10.7		11.0	11.5	11.8
50°	2.55			2.8	3.1	3.1

The values of R_o appropriate for the slope γ were obtained by graphically interpolating from the data in Table XIV. The slope γ is taken from figure 20.

Table XV shows the resulting values of $R_o^{(2)}$.

TABLE XV. Applicable Effective Cutoffs for Center Dipole.

λ_m	R_c, Bv	$R_o^{(2)}$, Bv	$R_o^{(2)}/R_c$
0°	16.4	16.7	1.018
30°	10.1	11.0	1.09
50°	2.55	3.1	1.22

Values of $R_o^{(2)}$ (R_c) and $dR_o^{(2)}/dR_c$ were obtained by graphing these data, and thence a spectrum $J_o^{(2)}$ was calculated from equation 31e. dE^o/dR_c is again taken from figure 18. The function $J_o^{(2)}$ is drawn in figure 21. Comparison with figure 20 shows that $J_o^{(2)}$ differs little from $J_o^{(1)}$, and in particular, that γ has not changed significantly. Hence, further iteration would not improve the accuracy of J_o much, and will not be carried out.

Exactly the same procedure has been followed with E^o plotted against local field determined R. Figure 22 shows $J_o^{(1)}$ calculated in this case. Table XVI contains the applicable values of $R_o^{(2)}$ and figure 23 shows $J_o^{(2)}$.

TABLE XVI. Applicable Effective Cutoffs for Local Field Dipole.

λ_m	R_c, Bv	$R_o^{(2)}$, Bv	$R_o^{(2)}/R_e$
0°	16.4	17.15	1.045
30°	10.1	11.25	1.112
50°	2.55	3.00	1.175

It should not be supposed that $J_o^{(2)}$ for the summer (northern hemisphere) can be joined smoothly at $R \simeq 9$ Bv to $J_o^{(2)}$ calculated from data obtained in the fall (southern hemisphere). The summer $J_o^{(2)}$ must rise above that for the fall before it joins it at sufficiently large R.

The dotted line in figure 23 suggests a possible curve. Since this sort of variation of J_o with time is not expected, it is concluded that the local field determined R_e does not fit the present data.

Hence, figure 21, calculated from the center dipole R_c, contains the best J_o obtained from the present data. In the remainder of this paper we will use only this J_o unless the contrary is stated specifically.

The particle spectra are obtained from J_o by using equation 34, which states that $j_{\text{all nuclei}} = 0.62\, J_o$. (Lower case j denotes flux of nuclei.) The differential spectrum of protons, $j_p(R)$, is shown in figure 24. This curve also represents $j_a \times 6.75$ and $j_h \times 58.6$. The total flux of nuclei $j = j_p \times 1.16$.

Denote the integral flux by $N_i(>R)$, which equals the flux of type i nuclei having rigidity greater than R. Values of $N_o(>R) - N_o(>16)$, for $R < 16$, have been obtained by graphically integrating

$$\int_R^{16} dR\, 'J_o(R') = N_o(>R) - N_o(>16) .$$

The flux $N_o(>16)$ may be estimated from $J_o(16)$ and $E^o(16)$ by assuming that $J_o = \text{const}/R^{\gamma}$ with γ a constant for all $R > 16$ Bv. It is known that γ changes only very slowly as $R \longrightarrow \infty$. The following values appear in the literature:

1) When R is approximately 100 Bv, $\gamma = 2.3 \pm .2$ (Ref. 113)

2) When $4 \times 10^{15} \leq R \leq 10^{18}$ Bv, $\gamma = 3.13$ (Ref. 114)

3) For alpha particles with kinetic energy per nucleon between 0.3 and 800 Bev, the integral energy spectrum is proportional to $1/(m_p c^2 + E/\text{nucleon})^{1.5\pm.2}$ which is equivalent to $1/R^{1.5\pm.2}$ for relativistic particles. Thus $\gamma = 2.4 \pm .2$ (Ref. 115).

Particles with R > 100 Bv contribute little to $N_i(> 16 \text{ Bv})$ and $E^o(16)$ so that the slow increase of γ with R may be disregarded. Hence we have

$$E^o(16) = \pi \int_{16}^{\infty} dR\, J_o\, E_{av}$$

$$N_o(>16) = \int_{16}^{\infty} dR\, J_o \qquad (42)$$

with $J_o(R) = J_o(16)\ 16^{\gamma}/R^{\gamma}$ where $R \geq 16$ Bv, and $E_{av}(R) = .768\ R - 1$ from equation 4 for $R \geq 16$ Bv. The values $J_o(16) = .00215$ and $E^o(16) = 1.58$ are obtained from figures 21 and 18 respectively. With these numbers equation 42 may be solved for γ and $N_o(>16)$, and it is found that

$$\gamma = 2.80$$

$N_o(>16) = .0191$ and thence $N_p(>16) = .0101$ particles/cm^2 sec sterad.

This value of γ agrees reasonably well with the slope of J_o at R = 16 and with the other measurements quoted above, and so .0191 is accepted as the best value of $N_o(>16)$ which can be derived from the present data.

Adding this number to $N_o(>R) - N_o(>16)$ gives $N_o(>R)$ and thence the integral proton spectrum $N_p(>R)$, which is shown in figure 25. N_p bears the same relation to integral fluxes of other particles as does j_p to other differential fluxes.

Further Improvements upon the Corrections for Time Variations

The next step in the iteration procedure described at the beginning of this section is to calculate m from equation 30b and the spectrum J_o. This coupling function may then be employed to calculate the time variations ΔJ_o in the primary spectrum which correspond to the variations ΔI observed at the base stations. Finally, the functions ΔJ_o could be used to correct the roving station's data for time variations.

The function m is of interest itself because it may be used to interpret other ionization chamber data. However, it appears that even if this function were exactly known it would not be possible to improve significantly the time corrections to the present data. Two sorts of improvement are desired. One would decrease the scatter of points about the smooth curve which almost surely describes I(p), $E_o(R)$ and other functions. This scatter is most evident at cutoffs above the knee and in $E^o(R)$ at R from 13 to 16 Bv. The other would change the shape of corrected functions when ΔI has exhibited a progressive change

over a period of time during which the roving station took several observations. Such a change occurred during the summer. See figure 7.

The differences between roving and base station data which remain unaccounted for limit the first kind of improvement. Figure 8 shows that these differences amount to 2 to 3% of I when the roving station is at higher latitude than the base station. This is of the same order as the scatter of points about the I(R) curves for the northern hemisphere so that no further improvement can be expected. In the southern hemisphere the base station did not see the lowest energy particles present. Variations in these particles appear to have caused some of the scatter in the roving station data, but further analysis cannot correct for it. Allowing for the temperature effect might reduce the observed scatter, but since doing this would not improve the accuracy of J_o at rigidities greater than the cutoff at the knee, this calculation will not be made.

Scatter in the data at low latitudes affects the derived J_o as inspection of figure 18 shows. Here two alternative interpolations are given, and the derived $J_o^{(1)}$ are plotted in figure 20. The two values of γ are 2.95 and 1.69. The scatter in this region is again 2 to 3% of E^o and unless the spectrum for $R > 16$ Bv varies with time, this scatter must be caused by experimental error and temperature effect.

It is possible that $|\Delta J_o| > 0$ for $R > 16$. The crosses in figure 18 show the corrected values of E^o which result assuming that $\Delta J_o/J_o$ is constant for all R instead of becoming zero for $R > 16$ Bv, as has been assumed in making the other corrections. There is an appreciable difference between the two corrected values at $R_c = 13.8$ Bv, so that an improved knowledge of ΔJ_o for large R would better define E^o in the region $13 \leq R_c \leq 16$ Bv. However, ΔJ_o certainly decreases as R increases and hence the true corrected value of E^o must lie between the extremes plotted in figure 18 , i.e., near the "best" curve drawn in that figure.

There were virtually no corrections applied to the northern hemisphere data at 5.9 Bv and 1.8 Bv cutoff rigidity because the base station measured very small ΔI on 22 June and 30 June. Consequently, the corrections affect the shape of $E^o(R)$ between 1.8 and 5.9, but not the overall slope. In view of the uncertainties outlined in the next section, further corrections do not appear to be useful.

VII. THE ACCURACY OF J_o AND DISCUSSION

The uncertainty in relative calibration of the ion chambers is estimated to be less than $\pm 0.5\%$. The uncertainty in I(p) contributed by uncertainty in p is less than this for the I(p) observed in 1958. Because several observations define functions such as $E^o(R)$, systematic error in these functions arising from instrumental uncertainty

must be less than 0.5%. The absolute instrumental uncertainty is estimated to equal ±1%, and so the absolute values of I and E^o are uncertain by this amount due to the instruments used.

Four other major sources of uncertainty in calculating E^o exist. These are the fraction of energy lost to neutrinos and binding energy, the energy lost to albedo, the effect of variation of atmospheric temperature with latitude, and the possibility that the relative nuclear abundances change with energy.

According to Table IV, Komori gives the relative uncertainties of the energy lost to neutrinos and the total calculated energy as ±5% and ±8% respectively. Assuming that the uncertainty in the energy set against binding energy is not much greater than 5%, the uncertainty in the fraction of total energy lost to neutrinos and binding energy is of the order of ±9%. Thence the uncertainty in the number by which the measured energy is multiplied to obtain the total energy has an uncertainty of ±6%. All values of E^o and hence of J_o have this uncertainty. The J_o derived may be incorrect by this percentage at all R. Moreover, since the fraction of energy lost to neutrinos depends upon latitude, the derived dependence of R upon latitude may be wrong. For example, the derived J_o may be correct at R = 16 but 6% high at R = 2 Bv.

Energy is lost to albedo only when the latter is non-reentrant. It is generally supposed that all albedo returns when $\lambda < 60°$ and that the fraction returning declines to zero in going from 60° to 90°. The

discussion in Chapter V suggests that the energy projected upward is less than 10% of the incoming energy flux.

It is possible, then, that E^o calculated at R = 1.5 Bv is as much as 10% low with respect to that at 16 Bv because of the albedo effect. If this is not the case, then E^o at R = 0 is low by the same amount with respect to E^o at R = 1.5 Bv, since the return albedo must decrease to zero at the pole. The latter case is more likely.

The temperature effect has been discussed already. The variation of atmospheric temperature with latitude produces a decrease in the vertical muon flux at 250 g/cm^2 equal to 3% of the equatorial value. The total change in measurable energy dissipation must correspond to about a 3% change in the fraction of energy lost to neutrinos. This is considerably less than the other uncertainties in this fraction.

If the charge spectrum changed systematically with R between 2 and 16 Bv, the real particle flux would be different than that calculated. We can set an upper limit to this possible effect by supposing that only protons occur with rigidities from 2-3 Bv. The differential proton flux calculated from $E^o(R)$ (fig. 18) is then 1.32 times greater at 2 Bv than the value plotted in figure 21. A similar calculation may be made at 16 Bv. The results appear in Table XVII.

TABLE XVII. Integral Fluxes in 1958 Assuming Two Different Compositions.

Cutoff, Bv	Differential Flux with Normal Primary Composition		Differential Flux Assuming Primary Protons Only
	j_{proton}	$j_{all\ nuclei}$	j_p
2	.0136	.0159	.018
16	.0011	.00129	.00154

The differences are quite large, but this is an extreme assumption. For small changes in the fraction of nuclei heavier than protons the derived proton flux changes linearly. For instance, a 10% decrease in the fraction of heavier increases the calculated proton flux about 5%.

Some limitations to the accuracy of E^o and J_o have been discussed above. In particular, it should be stressed that $E^o(R)$ is not well defined where $11 < R < 16$ Bv and consequently, J_o is not precise in this range of R. Although the exponent γ in $J_o = K/R^{\gamma}$ surely increases as R increases from 10 to 16 Bv, the slope at 15 Bv may really be anywhere from 2 to 3.3 judging from the alternate possibilities drawn in figures 18 and 20.

The other region of R for which J_o is uncertain corresponds to the knee, i.e., the point where $E^o(R)$ appears to flatten out, and to smaller values of R. The data points are quite scattered here and so it is not possible to determine $E^o(R)$ precisely, but it appears that the

knee occurs between 1.8 and 2.5 Bv and that E^o remains constant or may decline 1 to 2% as R goes to zero. This suggests that J_o drops sharply for R < (1.8 to 2.5 Bv).

Supose that J_o drops discontinuously to zero at R = 2.5 Bv (λ_m = 50°) and that for R > 2.5 Bv, J_o is smooth with slowly changing γ. The break in the slope of $E^o(R)$ will not be perfectly sharp but will occur over a range of 0.7 Bv in R_c (4° of latitude) corresponding to the fact that $A(R, R_c)$ goes from 0 to π in this range of R at R_c = 2 Bv.

At smaller values of R the energy flux into the atmosphere must be constant except for the opening shadow cones. At λ_m = 50°, the shadow cones for 5.4 Bv particles amount to .12 or 3.8 % of A = π. At 60° the same shadow cone amounts to 1.3 % of π. Since particles with R > 5.4 Bv contribute a little more than half of $E^o(2.5)$ the increase in E^o due to opening shadow cones cannot be much greater than 2% = .06 Bev/cm^2 sec.

The measurable energy flux decreases as R_c goes to zero because of escaping albedo. Provided that no albedo escapes at 50° = λ_m the measurable flux may decrease as much as 10%. In addition the temperature effect increases the measurable flux 2 to 3% if one uses the temperature difference shown in figure 13 and the weighting function for muons from Dorman (3). See discussion of temperature effects.

According to these estimates, the shadow cone plus the temperature effect cancel one-half or more of the albedo effect. However, the estimates are rough and without further calculation one can only say that E^o may either increase or decrease a few percent above the knee in the event that $J_o = 0$ for $R < R_{knee}$. The present values of E^o are not inconsistent with this possibility.

In order to determine how large J_o can be when $R < R_{knee}$ and still be consistent with the present data, it is necessary to consider I as a function of R_c at shallow depths. Particles with these small rigidities do not penetrate far into the atmosphere and consequently their presence does not affect E^o so much as it does I at shallow depths. Figure 16 shows I vs R_c at various depths, together with the R_c corresponding to particles which can just reach those depths.

The curves of I vs R_c at 20 g/cm^2 and 50 g/cm^2 depth show that some new particles appear with decreasing R_c down to about 1.4 Bv. Since these particles do not influence I at $p \geq 100$ g/cm^2, it is possible to estimate their numbers by using the energy dissipated at depths less than 100 g/cm^2. Doing this eliminates the observed fluctuations in I at depths 100 to 300 g/cm^2 (see fig. 9 and 10), part of which are attributed to temperature changes. Thus, if we consider the flights of 30 June and 2 July, the latter at Bismarck, we find the following:

	Energy, Bev/cm^{2}sec		
	Total E^o	E^o above 100 g/cm^2	R_c, Bv
30 June	3.24	1.072	1.82
2 July	3.16	1.091	1.38

These data are corrected for fluctuations at Bismarck, and the measured energies are multiplied by 1.54 to take account of neutrino losses. Although the total energy appears to be less at the lower R_c, one is inclined to ascribe this to atmospheric temperature fluctuations (not latitude temperature variations, the two stations being quite close together) and to say that at least 1.091-1.072 = .019 Bev/cm^{2}sec additional energy reaches the earth at the lower cutoff. The mean rigidity in this interval is 1.60 Bv. The heavy primaries can reach the instrument below 10 g/cm^2 over only half this range, so that $E_{average}(1.6) = .599$ Bev. Thence the mean flux J_o in this range is

$$J_o(1.6) = \frac{.018}{.599} = .0096 \text{ particles/cm}^2\text{sec sterad}$$

and the proton flux equals

$$j_p(1.6) = .0051 \text{ protons/cm}^2\text{sec sterad.}$$

The mean rigidity between these two stations according to the local field approximation is 1.0 Bv and in this case one finds

$$J_o = .012 \text{ and } j_p(1.0) = .0065 .$$

The values of J_o and j_p calculated from the center dipole R_c are plotted in figures 21 and 24. They lie far below the maxima of J_o and j_p. Hence the evidence of high altitude I(p) only is that J_o falls rapidly as R decreases below 2.5 Bv.

VIII. COMPARISON OF RESULTS WITH OTHER DATA

The results obtained here and presented in figures 24 and 25 may be compared with measurements made by other workers during the same period of time. McDonald (47, 48) has reported differential and integral proton and alpha fluxes. He concludes from the results of several measurements that the alpha differential rigidity, spectrum multiplied by 6.5 is essentially the same as the proton differential spectrum from 1 to 15 Bv. Accordingly, proton fluxes and alpha fluxes times 6.5 plotted together define his rigidity spectra for different parts of the solar cycle. A differential spectrum from .9 to 2.6 Bv was obtained in 1958 from two balloon flights made from Minneapolis, Minnesota ($\lambda_m = 55°$) on 2 February and 2 July 1958. There appears to be no significant difference between the fluxes measured on these two dates. This spectrum is plotted in figure 24, expressed in the appropriate units.

McDonald gives an integral rigidity spectrum calculated from the data of the above two flights plus a flight on 4 February 1959 at

$\lambda = 41°$ and one on 30 January 1957 at $\lambda = 4°$. The latter is expected to be comparable with the other flights because there is only a small variation in the equatorial flux.

The two integral spectra agree very well over the entire range of our measurements, although he measures a slightly higher flux at the equator than was calculated in this paper. His differential spectrum agrees with ours at 2.5 Bv and then drops off rapidly at lower rigidities in accord with our values of E^{o} at rigidities less than the knee. The value of J_p at 1.6 Bv calculated from high altitude results only is much lower than McDonald's spectrum at this rigidity. It should be noted that McDonald does not find a cutoff rigidity in the .8 to 2.6 Bv interval, below which there are no particles. However, his results and ours taken together show a sharp break in the slope of the rigidity spectrum at 2.5 Bv. It is possible that if the two sets of data spanned overlapping rigidity ranges, the derived differential spectra would merely cross at 2.5 Bv. Thus the agreement between the differential spectra may be only apparent.

The agreement between integral spectra is real, and suggests that the two differential spectra really agree as well. However, McDonald finds by directly measuring the momentum of alpha particles, that the geomagnetic cutoffs are closer to the local field determined cutoffs than to center dipole cutoffs, and the data reported here indicate the opposite.

Meyer (50) reports a series of balloon flights using apparatus similar to McDonald's. The flights in 1958 were made on 12 and 22 July from a geographic location 50°N 99°W, which is north of the knee. He reports the flux of all singly charged particles able to penetrate the instrument to be equal to 0.16 particles/cm^2 sec sterad at an atmospheric depth of 13.5 g/cm^2. This is more than the .092 = $N_p(R>1.0)$ obtained by McDonald (fig. 25).

The flux of alphas with R > 2.35 Bv, extrapolated to the top of the atmosphere, is found to be .0139 according to Meyer. This contrasts with .0107 derived from figure 25.

We should like to consider next the variations with time of the ionization observed at the base stations and to compare this with other high altitude measurements and with solar data. The variations have been discussed already with regard to correcting for their effect. These variations are exhibited in figures 7 through 9, and may be summarized as follows:

1) Between 22 June and 20 July a sinusoid-like variation is observed which has an apparent period of about 30 days and a peak to peak amplitude, at 50 g/cm^2, of 20 ion pairs or 8%. The maximum occurs about 26 June and the minimum between 2 and 12 July.

2) Between 20 July and 15 October, the ionization increased; the increase amounted to 12 ion pairs or 5% at 50 g/cm^2.

3) The rate of ionization remained nearly constant, on the average, from 15 October to 22 December. However, a number of decreases occurred during this period. Those observed occurred on the following days: (L = charge at depths < 100 g/cm^2 only. M = charge at depths between 100 and 200 g/cm^2.)

a) 15 October to 23 October — L ?

b) 24 October to 26 October — L + M

c) 2 to 4 November — L

d) 11 to 12 November to 13 November — L + M

M returns, L decreases on 13 November

e) 26 November, 0520 to 2203 GMT — L

f) 27 November to 2> November — L + M

g) a very small decrease from 2 December to 3 December

This should not be interpreted as a complete list of decreases for the period, since observations were spaced several days apart on many occasions.

4) The variations noted in 1) resulted from primary variations with a spectral form $\Delta J_o(R) \propto J_o(R)$ approximately for R up to at least 5-7 Bv. A possible exception is 12 July, when only low energy particles appeared to be depleted. This could be interpreted by saying that after the decrease from 2-12 July the higher energy particles

reappeared before the lower. There is some evidence for a decrease of medium energy particles from 26-27 June and of lower energy ones from 27 to 30 June.

5) The change noted under 2) was produced by an increased number of particles with lower average energy than the average primary at that time. However, some additional particles able to increase the ionization at 200-300 g/cm^2 appeared also.

6) The variations listed under 3) appear mostly at high altitudes corresponding to changes in the lower energy primaries. Specifically:

a) The variations appear to be due to rapidly absorbed particles but data are missing at depths greater than 90 g/cm^2.

b) Rapidly absorbed particles change and some change occurs in particles able to influence ionization at 150-200 g/cm^2.

c) Low energy particles decrease.

d) Low and medium energy particles decrease from 11 to 12 November; between 12 and 13 November more very low energy disappeared while medium energy returned. This is similar to the behavior on 12 July, noted in 4).

e) Only low energy particles changed.

f) Low and medium energy particles decreased.

In the above remarks low energy particles means those completely absorbed at a depth of 100 g/cm^2, and low plus medium means particles

whose effect reaches to 200 g/cm^2 deep in the atmosphere, but which do not produce a maximum in the I(p) curves. If Invercargill, the base station, had been above the knee, the variations might have appeared more dominated by low energy particles.

In comparing the cosmic ray intensity with solar activity, it is not obvious which features of the sun should be considered. It is known that sunspot number correlates well with cosmic ray intensity over an 11-year cycle (see next chapter) and that following solar flares by 24 to 36 hours, one sometimes observes geomagnetic storms and/or Forbush decreases and/or solar protons at the earth. The correspondence between flares and the latter effect is not unique. It may well be that some phenomena at the sun's surface which cannot be directly observed from the earth would correlate much better with cosmic ray variations occurring in 27 days or less than does any presently known phenomenon.

However, we will consider here the sunspot numbers and the flare index, primarily because they are readily available and because in the former case they have been measured for many years. Figure 26 shows the Daily Flare Activity Index taken from High Altitude Observatory Quarterly Summaries (116). The index is proportional to the total energy released by flares into the visible spectrum in the given day. Figure 27 shows the Final Relative Sunspot Numbers for the Whole Disc as computed by the Zurich Observatory (117, 118) Both daily values and monthly means are shown.

The following observations can be made about the cosmic ray intensity and the Flare Index.

1) The activity of 28 June and 2 July occurred after the ionization was already declining from its observed maximum on 26 June. The flare activity may have influenced the further decline of ionization.

2) The next high activity which coincided with our observations occurred in late October. The activity of either 17 or 21 October may have been followed by a decrease of intensity which our observations can only fix between 15 and 23 October.

3) On 24 October, activity was very high. Cosmic ray intensity was high that day also, but two days later had declined.

4) Activity on 28 October produced no observed change in cosmic ray intensity.

5) The intensity decrease on 11-13 November was not preceded by special flare activity.

6) The high activity on 24 November was followed by a sharp decline of cosmic ray intensity on 26 November.

7) No observations were made following the high activity of 11 December until 22 December.

In short, items 3) and 6) agree with the pattern of a flare producing effects at the earth 1 to 2 days later. Items 4, 5) do not fit this pattern, and the others are indeterminate.

No general correlation of cosmic ray intensity with sunspot number appears from our data. The following may be noted:

1) The cyclic change from 22 June to 20 July correlates negatively with the sunspot number of 10 days earlier.

2) During the two months preceding the June-July series of measurements, the monthly sunspot numbers were lower than in the two months preceding the October-December series of measurements.

3) The daily mean sunspot number varies more from the monthly mean during October-December than it does during June-July.

It is not clear that these facts are more than coincidences.

It is of interest to compare our measurements of the time variations in cosmic ray intensity with others made during the same period. Two other series of observations will be considered.

The first of these is reported by Winckler (21). Most of these measurements were made with an ion chamber, a geiger counter, and a nuclear emulsion stack at balloon altitudes near Minneapolis (λ_m=55°). He draws the following conclusions with regard to galactic cosmic rays:

1) Measurements of ionization over Minneapolis are 16% lower on the average than the values measured at Bismarck during the same period by the CIT group. Since no latitude effect is observed between Minneapolis and points northward on normal days, one expects the measurements by the two groups to agree.

When standard ionization chambers made by the two groups were compared in the laboratory, the calibration of the Minnesota instrument was found to be 16% lower than the CIT calibration. Thus, when the instruments are normalized in the laboratory, the high altitude measurements are found to agree. The reason for the difference in absolute calibrations has not yet been discovered.

2) Forbush decreases appear to change the energy spectrum in much the same way as does the solar cycle change from 1954 to 1957. That is, the low energy particles change the most. One decrease cited occurred on 28 June 1958.

This behavior agrees with our conclusions about some of the variations observed in the October-December measurements and possibly with our observations of the 27 to 30 June decrease. The sinusoid-like variation observed by us in June-July has a different character.

The variations with time of the ionization at 10 g/cm^2 observed by Winckler does not have exactly the same appearance as the I at 20 or 50 g/cm^2 shown in figure 7. In particular, the form of the Forbush decrease at the end of June does not coincide with our observations. However, the two sets of measurements were not made on the same days so that agreement cannot be expected considering how much the radiation is observed to change in one or two days. If more data are published in the future, a more thorough comparison may be possible.

The other series of measurements has been reported by S. N. Vernov et al. (119). In this work single geiger counters and counter telescopes were used to measure the charged particle flux at high altitudes at the geomagnetic latitudes 41°, 51°, and 64° N.

The authors have published the results of a statistical analysis of the counting rate at the Pfotzer maximum, at 60 g/cm^2 depth. The principal ones seem to be as follows:

1) The 27 day variation is removed by the method of sliding averages. The remaining "secular" variation is plotted, and clearly shows a Forbush decrease at the end of June, which continues on through July, amounting to nearly 5%. An increase of similar size occurs from 1 November to 5 December, approximately.

2) It is found that the secular variation correlates positively with the sunspot number of 20 days earlier.

3) The 27 day variations were examined by the Chree and periodogram methods. The amplitude of this variation was found to decline from the latter half of 1957 to the latter half of 1958. Furthermore, a negative correlation between intensity and sunspot number was found from 1 July 1957 to 31 January 1958. A weaker negative correlation was found from 1 February to 30 June 1958, and no correlation was found during the period 1 July to 31 December 1958.

4) Several statements are made about the latitude effect between the three stations.

a) In 25 out of 97 cases analyzed, no latitude effect was observed between 51° and 64°. The effect is seen to change rapidly.

b) When the very high altitude (above 50 g/cm^2) intensity at 64° increases, the intensity at 51° decreases.

c) When the latitude effect between 51° and 64° increases, the intensity at 41° declines.

The conclusion derived from these facts is that when the flux of particles with less than 1.5 Bev increases, the flux of more energetic primaries declines. This effect was expecially strong on 8 July following the flare of 7 July.

With regard to item 1), our data show a recovery of the intensity from 12 to 20 July from the decline of early July. This recovery does not appear until about 25 July in data presented by Vernov. Also, we do not see the increase in intensity during November. No reasons for these discrepancies can be given at present. The two sets of data are not comparable with regard to 2) and 3).

We have observed no variation of the type described in 4). However, we may have seen the opposite effect when higher energy particles had reappeared after a decrease while the low energy ones were still depressed. If this represents a gradual recovery from a sudden event, then the chance of seeing a recovery phase with intermittent observations is greater than of seeing the onset of an event.

More frequent and regular observations than were carried out by us are needed to study the rapid variations with time.

IX. THE 11-YEAR VARIATION

Finally, we would like to compare the data reported here with measurements made by H. V. Neher, et al., in other years. All of these measurements have been made with the same sort of ion chamber and it is thought that all data are comparable to within ± 1%. The results obtained in 1951-1957 have been published previously (18, 52-54). Some 1958 data were reported in the Moscow Conference (120) and other 1958 data have been published by Neher (19). The 1959 and 1960 data have not been published before. The 1960 data were obtained by H. V. Neher and R. F. Miles, but are included here for the sake of completeness.

Figure 28 shows the ionization at Thule in 1951-1960 under selected pressures, together with concurrent sunspot data. Figure 29 shows I(p) [illegible] at Thule. It is evident from inspection that the difference between curves becomes greater with decreasing pressures.

The straight lines in figure 28 connecting ionizations in different years must be considered suggestions only, since the ionization may change several percent from day to day. The extreme values observed at 20 g/cm^2 during each year's series of measurements are shown, but these cannot directly be compared with one another, since the number of measurements and the duration of the sequence varied.

The small variation observed in 1959 is remarkable, however. Six standard flights were made between 23 July and 12 August in 1959. The data obtained on these did not vary more than 1% at any pressure. Yet on 12 July and again on 22 August, large flares occurred which were followed by magnetic storms, polar blackouts, solar protons, and Forbush decreases.

One would expect that the Forbush decreases at least would have been detected by our instruments at Thule, and probably the solar protons as well. It is interesting that the flux remained so constant during two weeks between these events. Evidently the July activity was not sufficient to change by very much the overall suppression of cosmic ray intensity corresponding to solar maximum.

Figure 30 shows the ionization under 15 g/cm^2 of air versus geomagnetic latitude. The data for 1937, 1951, and 1954 have been published by Neher (18). These curves will be discussed later.

Figure 31 shows the Thule ionization at 20 g/cm^2 plotted against quarterly mean sunspot number. (The author is indebted to Marcia Neugebauer for pointing out that such diagrams show the phase lag between cosmic ray intensity and sunspot number.) Curves have been constructed using the mean number for the same quarter in which ionization was measured (third quarter) and for each preceding quarter up to five quarters earlier. These phase diagrams indicate that the high altitude cosmic ray intensity negatively correlates with the sunspot

number of about half a year earlier. Probably the intensity does not respond in this inverse fashion to sunspot changes which occur in much less than six months' time. Forbush reports that the Huancayo ionization lags the sunspot number by about one year (15). Only primaries with R > 15 Bv reach Huancayo.

According to Vernov (119), secular variations positively correlate with the sunspot number of 20 days earlier. Forbush decreases presumably correlate with sunspots only insofar as flares and magnetic storms are more likely to occur when there are many spots on the sun. It is not clear whether or not they are excluded from the secular variations by Vernov's analysis.

We return now to figure 30, which shows the ionization at 15 g/cm^2 depth in various years plotted versus center dipole geomagnetic latitude. In 1951 and 1954, as in 1958, Bismarck was used for a base station and observations at the latter have been used to remove the effect of time variations from the roving station data. The curve for 1937 is actually a composite one. The points at 3° and 38° were obtained in 1936, the one at 17° in 1938. The points at 60° and 85° were measured in 1937, the latter by Carmichael and Dymond (59). The latter data were normalized to the results of Neher et al. (18).

Several points should be observed.

1) There is very little change near the equator between the two years for which there are data.

2) The position of the knee varies slightly over the solar cycle.

3) The ionization below the knee varies a great deal from one year to another, and the ionization above still more.

4) In 1954 there does not appear to have been any knee.

One may draw the following conclusions from this.

1) There was little difference in the flux of particles having $R > 15$ Bv between 1937 and 1958.

2) The flux of particles with rigidities between 15 Bv and 2 Bv, the approximate vertical cutoff at the position of the knee, changed a great deal from one year to another.

3) In addition, the flux of particles with $R < 2$ changed sufficiently to change the position of the knee and in 1954 to make it disappear. The knee in 1958 corresponds to a decrease of the differential rigidity spectrum below a certain rigidity but not to a sharp cutoff, and changes in the way the spectrum falls off will shift the knee. It is not necessary to invoke changes in a sharp cutoff.

In order to investigate these changes in the primary spectrum we shall calculate the spectrum from the 1954 data, following the same procedure that was used for the 1958 results.

Data are available from Bismarck and the roving station in 1954 on the dates shown in Table XVIII. July 17 has been selected as the base date. The Bismarck ionization at 437 g/cm^2 depth on this day was

TABLE XVIIIa. Measurable Energy Fluxes in 1954.

Date 1954	Station	λ_m	R_c	$E_m^{o'}$ Energy Flux Bev/cm^{2}sec	$\Delta E_m^{o'}$ Base Station Bev/cm^{2}sec	$E^{o'}$, corr. Rov. Station Bev/cm^{2}sec
11 July	Bis		1.38	.761	-.010	
	Rov	53°	1.95	.739		.749
17 July	Bis		1.38	.771	0	.771
	Rov	56°	1.45	.778		.778
19 July	Bis		1.38	.771	0	
	Rov	65°	.455	.864		.864
28 July	Bis		1.38	.891	.120	
	Rov	81°	.01	.919		.919
10 Aug	Bis		1.38	.792	.0208	
	Rov	89°	0	.919		.919

λ_m = Center dipole geomagnetic latitude from H. V. Neher, PR 103, 228 (1956).

R_c = Cutoff for which A = $\pi/2$.

$E_m^{o'}$ = Measurable energy flux minus 2.08, the flux of 20 July, 1958, λ_m = 87°.

$E_m^{o'} = E_m^{o'}$ at base station minus $E_m^{o'}$ at base station on 17 July 1954.

TABLE XVIIIb. Total Energy Flux in 1954.

Date	E_o, Bev/cm^{2}sec A	B	R_c, Bv
11 July	3.95	4.35	1.95
17 July	3.98	4.40	1.45
17 July Bis	3.97	4.39	1.38
19 July	4.06	4.54	.455
28 July	4.12	4.62	.01
10 Aug	4.12	4.62	0

only 4 ion pairs higher than the ionization at Bismarck and Thule on 20 July 1958; i.e., it was about 10% higher. Although there are no data from the CIT measurements for greater depths in 1954, monitor data show that at the latitude of Bismarck the sea level ionization was about 5% higher in 1954 than in 1958. The 1954 data also show that the ionization was essentially the same at Bismarck and the roving station from 140 g/cm^2 to 240 g/cm^2, the greatest depth for which roving station data were obtained. Consequently, one may assume that the roving station ionization was the same as that at Bismarck on the same day from 140 g/cm^2 to 500 g/cm^2 (and hence to 1030 g/cm^2), and that both were 10% higher at 500 g/cm^2 and 5% higher at 1030 g/cm^2 than in 1958. Since the measurable energy dissipated at depths greater than 500 g/cm^2 is about 8% of the total in 1958, the excess in 1954 at these depths amounts to about 0.6% of the total in 1958. This may be neglected in comparison with the excess at more shallow depths.

Using these assumptions, one may calculate the measurable energy dissipated in the atmosphere by integrating the area under I(p) curves. Table XVIIIa shows these measurable energy fluxes as the excess over the measurable energy flux observed by the roving station, λ_m = 87°N, on 20 July 1958, which equalled 2.08 Bev/cm^{2}sec.

These 1954 data are not uniformly reliable.

1) More than half of the difference between the roving station I(p) curves for 28 and 19 July appear between 120 and 200 g/cm^2, the

remaining difference occurring at greater altitudes. Data on 19 July were not obtained above 30 g/cm^2 by the roving station. Thus it is not impossible that $E_m^{o'}$ for 19 July should be as great as for 28 July and 10 August. Data for the latter two days appear the same and equal to data taken on 17, 18, 19 August at $\lambda_m = 88°N$.

2) There are no data from the roving station above 40 g/cm^2 on 11 July. Because of the extrapolation required, it is possible that $E_m^{o'}$ for this day should be .005 to .01 Bev/cm^{2}sec lower than given in Table XVIIIa.

3) Data from Bismarck on 19 July run from 94 to 190 g/cm^2 depth only. The point at 94 g/cm^2 falls slightly below the 17 July data. However, for want of data we have assumed that the 19th and 17th were the same.

4) The ionization on 10 August at Bismarck exceeds the 17 July data only between 130 and 240 g/cm^2 depth. Since no difference appears at shallower depths, this difference may be spurious, and will be assumed zero in making corrections to the roving station data.

5) Finally, the ionization at Bismarck on 28 July shows an increase over 17 July down to 300 g/cm^2 and has a different shape above 70 g/cm^2 depth. As has been discussed elsewhere (18, 120), no corresponding change appeared at higher latitudes, the data for 28 July and 10 August being almost identical. It is thought that the geomagnetic cutoff at Bismarck decreased that day to let in lower energy

particles, but that the primary cosmic ray flux beyond the earth's field did not change.

Consequently, the roving station data have been corrected only for the 11 July variation at Bismarck. The total energy fluxes in 1954 are shown by Table XVIIIb under two different assumptions. Column B shows the total flux supposing that the additional particles present in 1954 lost the same fraction of energy to neutrinos, etc., as did the primary particles in 1958. Column A shows the total flux supposing that no energy is lost to neutrinos, etc., by the additional particles present in 1954. The truth probably lies between these extremes. These two columns are plotted against R_c in figure 32, which also shows the 1958 energy flux redrawn from figure 18. The total energy fluxes computed under assumption B will be used to calculate a primary energy spectrum.

It is possible to calculate a differential rigidity spectrum from $E^o(R_c)$ in the region $R < 2$ Bv for which we have data in 1954. This has been done by the same method used to calculate the 1958 spectrum. One iteration was employed, and the same charge spectrum was assumed to apply in 1954 as in 1958. The resulting differential proton spectrum is shown in figure 33. The point at $R = 2.44$ Bv is obtained from dE^o/dR_c at $R_c = 2.00$ because $R_o\ (2.00) = 2.44$ in this case.

It is remarkable that the differential spectrum at R = 2.5 Bv was about the same in 1954 as in 1958 although at some greater rigidities the spectrum in 1954 must rise above that in 1958. This is true because $E^{o}(2.00)$ is greater in 1954 than in 1958. Yet at sufficiently great R, the spectra must be nearly the same in the two years since monitors responding to more energetic primaries show a smaller difference than do our high altitude data. Presumably very high energy particles do not vary at all from year to year.

It is possible that these curves correctly show the changes in $j_p(R)$ between 1954 and 1958. The increased number of particles with R > 2.5 Bv cannot be doubted. However, $j_p(R)$ below 2.5 Bv may be higher in 1954 than shown for any one of several reasons.

1) The data are incorrect or are plotted against inapplicable geomagnetic cutoffs.

2) Geomagnetic cutoffs were different in 1958 and 1954.

3) At low rigidities the charge spectrum does not have the character assumed. For instance, if we suppose that only protons occur with less than 2.5 Bv rigidity, we find that our data predict a differential proton flux 1.3 times as great as that given at 2 Bv. Thus, by adjusting the charge spectrum it is possible to smooth out the resulting differential proton spectrum. This does not appear to be justifiable in view of McDonald's data for 1955-1956 (48), which shows the same proton to alpha ratio as in 1958.

4) We may not have accounted for non-reentrant albedo properly. If 10% of the incident energy flux is projected upward, and if all returns where the cutoff is 2 Bv and none at 0.5 Bv, then dE^o/dR_c in this range would be 4.5 times greater than calculated here, as would the corresponding j_p. Thus it is clear that a small change in dE^o/dR_c to account for albedo could change the calculated $j_p(R)$ for 1954 so that it lies above the 1958 spectrum everywhere. It appears hopeless to correct for albedo in view of the great sensitivity of the resulting $j_p(R)$ to the correction.

Thence we may state that figure 33 shows our calculated $j_p(R)$ for 1958, keeping in mind the sources of uncertainty just listed. No attempt is made to extend the curve below 0.6 Bv because our data do not clearly show an increase in E^o between $R_c = 0.5$ and $R_c = 0$.

Figure 33 shows the proton differential spectrum published by McDonald (48). The 1958 data join nicely with our results as has been discussed. His results for 1955-56 lie far above our 1954 spectrum between 2.5 and 1.7 Bv and then fall rapidly below at lower rigidities. According to figure 28, the primary flux was lower in 1955-56 than in 1954, which may explain the difference between $j_p(R)$ at $R < 1.7$ obtained by McDonald and by us. However, we cannot thus explain the difference in j_p between 1.7 and 2.5 Bv. It is possible that the two results represent the true primary variation between 1954 and 1955-56.

It may also be noted that the j_p for $1.7 \leq R \leq 3.0$ Bv given by McDonald might be extrapolated to join our spectrum at 6 to 10 Bv if that is the region in which the 1954 spectrum exceeds the 1958. However, there is no evidence to justify doing this, and so the two curves must be regarded as either disagreeing or as representing an unexpected primary variation.

In order to calculate an integral rigidity spectrum it is necessary to estimate N(>2.44 Bv). This can be done crudely by looking at the difference between the I(p) at Bismarck for the two years. The difference appears in figure 34. R_c = 1.4 Bv at Bismarck. Such a steeply rising curve is produced by fairly low energy particles. The differences between I(p) at closely spaced latitudes measured in 1958 show that only primaries which arrive where $R_c \leq 5.2$ Bv can produce an I(p) without a maximum. We thus conclude that the average rigidity of the particles which produced the additional ionization shown in figure 34 was less than 5.2 Bv and that the average rigidity of the particles which bring in the excess E^{o}(2 Bv) in 1954 had rigidities between 2.0 and 5.2 Bv. Judging from the shape of the curves a good guess for the average rigidity is 4.0 Bv. The total integral proton flux in 1954 assuming this number and also in case the upper limit of 5.0 Bv is assumed are

Average R, Bv	N_p (> 2.44 Bv), protons/cm^{2}sec sterad
4.0	.157
5.0	.138

The integral flux at lower rigidities may then be calculated by integrating $j_p(R)$ from figure 33.

The integral proton rigidity spectrum calculated from our 1954 result is given in figure 35, together with the integral spectra of 1958. Some integral fluxes are listed in Table XVII as well. Particle fluxes listed in that table mean the fluxes of all nuclei, and are the fluxes a counter telescope would measure in the absence of albedo particles. The 1958 integral fluxes for R < 2.5 Bv are calculated by combining our differential spectra for R > 2.5 Bv, and McDonald's for the region 2.5 > R > 1.0 Bv.

TABLE XIX. Integral Fluxes.

Year	Integral Proton Flux part/cm^{2}sec sterad			Integral Particle Flux part/cm^{2}sec sterad		
	N_p(>16)	N_p(>2.5)	N_p(>0.6)	N (>16)	N (>2.5)	N (>0.6)
1954	-	.157	.253	-	.183	.294
1958	.01	.073	.092	.0116	.085	.107

Estimated uncertainty for these fluxes is ±10%.

X. SUMMARY AND CONCLUSION

This paper discusses data obtained with sounding balloons and ionization chambers during 1958 and 1959, and compares it with data from other sources. A schematic diagram of the sort of instrument used in this work is shown in figure 1.

In a typical sounding, the balloon is released near sea level, 1033 g/cm^2 pressure or depth of air, and lifts the ionization chamber and a barometer to about 15 g/cm^2 depth in two to two and one-half hours. The balloon breaks usually between 20 and 10 g/cm^2 depth and the flight ends. While ascending, the apparatus transmits the air pressure and ionization every few minutes so that one may construct a curve showing ionization as a function of atmospheric depth for each flight. The ionization produced by all particles able to penetrate the 0.5 g/cm^2 steel wall of the ion chamber is measured. Figure 3 shows the actual data obtained on three flights. Atmospheric depth is expressed in g/cm^2 and ionization in ion pairs/cm^3 sec atmosphere of

air. In this work an atmosphere means air at 24°C and 74 cm of Hg. Ionization measured on different flights has a relative uncertainty of $\pm$ 0.5%, while that obtained during a single flight has a smaller uncertainty. The barometric elements maintain their calibration to within $\pm$ 2 g/cm^2 at 1000 g/cm^2 pressure, and $\pm$0.5 g/cm^2 at 5 g/cm^2.

Table II shows the times and locations where flights were made in 1958-59. Results are given in Table III, which shows the ionization at selected pressures taken from smooth curves drawn through the transmitted data. In every case simultaneous flights were made from a roving and a base station. In the summer Bismarck, N. D., was the base station, while in the fall Invercargill, New Zealand, served as a base station. Simultaneous flights at Invercargill and Bismarck were made on 15 and 16 October. Table XIII lists the geomagnetic coordinates and cutoff rigidities at the location of each launching.

The energy dissipated in the atmosphere by ionization is proportional to the integral of $\int_0^\infty I(p)\,dp$, where $I(p)$ is the ionization at depth p. The sum of this energy and the energy lost to neutrinos and nuclear binding energy is identified with the flux of energy brought into the top of the atmosphere by primary cosmic rays. The correction for the neutrinos and binding energy is made with the help of Table IV, and the primary energy flux is calculated in Table V from the results of each flight. The energy flux is plotted against the geomagnetic latitude in figure 11a. Figures 11b and 11c show ionization vs latitude before

and after correction for time variations.

Analysis of this data proceeds in the following steps:

1) By using the variations in ionization observed at the base stations the effect of these variations upon the roving station data are removed.

2) Step one leaves the roving station data showing only the latitude effect, ideally. At the same time, some information is obtained about the energy spectrum of the time variations.

3) The latitude effects in the northern and southern hemispheres are compared to determine which system of geomagnetic coordinates best fits the data.

4) The rigidity spectrum of the primary radiation is calculated from the latitude variation of the total energy flux.

Figures 7-9 show the variations in ionization at the base station. It is concluded from these figures that the energy spectrum of particles which vary from day to day during the summer observations is similar to the spectrum of all primary particles. By 15 October an additional flux of low energy, rapidly absorbed particles had appeared. However, again during the fall the energy spectrum of varying particles resembled that of all particles with exceptions on some days.

Accordingly, the roving station data were corrected by assuming that all primary particles with less than 15 Bv rigidity varied in the

same way from day to day; particles with greater rigidity were assumed to remain constant. Summer data were reduced to 20 July, and fall data to 15 October. The summer and fall data have not been normalized to each other.

Figures 11a,b,c show the improvement effected by this correction. Also compare figures 17, 18.

The three geomagnetic coordinate systems, center dipole, eccentric dipole, and local field determined coordinates (see Eq. 28) were compared with the latitude variation measured by the roving station. The cutoff rigidities in each system, defined to be the rigidities for which half the sky is allowed, have been calculated for each launch position and are listed in Table XIII. Ionization and energy flux are plotted against these rigidities in figures 14-19.

It is concluded that the data fit the center dipole coordinates best of the three systems tried, and the local field coordinates second best. This is contrary to many recent studies which find that the local field coordinates are best.

The primary rigidity spectrum was computed from the dependence of energy flux upon cutoff rigidity in both center dipole and local field determined cutoffs as shown in figures 18, 19. In deriving the rigidity spectrum, it is assumed that the nuclei of all different kinds (different Z) occur with the same rigidity spectra except for a multiplying

constant so that the numbers of nuclei in any particular rigidity interval are in the ratio shown by equation 32, which derives from Table XI.

The rigidity spectra which result appear in figures 21 and 23. The function J_o given there is related to the proton rigidity spectrum by $J_{proton} = 0.53\ J_o$, and the spectra of alpha and heavier particles go as $J_\alpha = 0.314\ J_o$, $J_h = 0.15\ J_o$, according to equation 32. The actual proton spectra for the center dipole case appear in figures 24, 25.

Some solar activity data for the period of our observations appear in figures 26, 27. Comparison with the ionization at the base stations, figure 7, does not show any obvious correlation. Our observations are few and random, so that it does not seem worthwhile to make a statistical analysis of their results.

The data obtained by Neher and others using similar instruments in other years is now considered. The ionization measured at Thule, Greenland, at center dipole geomagnetic latitude 88.3°N is shown in figures 28, 29, while the results of various latitude surveys appear in figure 30.

It is obvious from figure 29 that the ionization at high altitudes at Thule inversely or negatively correlates with sunspot number between 1951 and 1960. The phase diagrams, figure 31a-f, show that this ionization at a given time best correlates with the sunspot number of about six months earlier. The negative correlation has been observed

during this and the previous 11 year solar cycle by Forbush (15, 16). Sunspot number should be regarded as only an index of solar activity, not necessarily a direct cause of cosmic ray variations.

The latitude surveys, figure 30, show that the flux of particles with rigidities up to at least 10-15 Bv varies during an eleven year solar cycle, but that the flux of particles with rigidities of 2 Bv and less changes much more. See figure 29. The primary rigidity spectrum in 1954 was calculated from the ionization vs pressure curves exactly as was done in 1958. The energy flux derived from the ionization data appears in figure 32, and the resulting primary spectra in figures 33 and 35. The shape of the 1954 differential spectrum may be spurious, but the increase over the 1958 flux at both high and low rigidities cannot be doubted. Table XIX summarizes the integral fluxes to be expected at the geomagnetic pole.

In conclusion, we may say that the data of 1951-1960 exhibit two kinds of time variations. One of these occurs during the course of a few days, and the high altitude ionization may change several percent within 24 hours. The changes appear to be world-wide as shown by the similar variations at base stations and roving stations in 1951 (52), and the correlations between high altitude variations at Thule and ground level monitors at lower latitudes (32). The correlation between

roving and base station variation was not as close in 1958 as in 1951. Although this may result from atmospheric variations, the author suggests that the difference arises from the greater solar activity in 1958. This activity may produce anisotropies in the primary flux and may also perturb the earth's field enough to cause the variations of local intensity. It is not just the lowest energy particles present that are modulated from day to day. Particles with at least 5-7 Bv fluctuate at some times also, the fractional change in J(R) being more or less independent of R from 2 to 6 Bv or more. The time scale of the change suggests that these variations occur over a volume 1 to 5 AU in diameter if the clouds of solar material indeed travel about one AU per day. None of these small variations observed in 1958 can be positively identified as a Forbush decrease from our data. No correlation between these day to day variations and solar activity was found. However, Vernov (119) reports that the charged particle flux at 50 g/cm^2 positively correlates with the sunspot number 20 days earlier. His data were obtained more regularly and during a longer period of time than ours.

The other variation occurs during the 11 year period of solar activity. The ionization at 20 g/cm^2 changes by a factor of two during this cycle, and inversely correlates with the sunspot number about 6 months earlier. Particles with low rigidities change more than those with higher rigidity, but ground monitors show that the primaries with

R > 15 Bv change a few percent over a solar cycle. Forbush (16) states that the latter flux inversely correlates with the sunspot number 12 months earlier. This observation is consistent with the idea that modulation of higher energy particles lags solar activity by longer than that of lower energy particles.

It is possible that the solar phenomena which modulate the cosmic ray flux lags 6-12 months behind the sunspot number. If this does not happen, then the time delay suggests that the modulation extends over a large volume. The radius of it may be 180 AU for the lower energy cosmic rays if we suppose that the plasma clouds which produce the modulation travel steadily at 1 AU/day, and that they do not exert their full effect upon the flux at the earth until they reach the boundary of the modulated region. The volume would be smaller if the clouds' radial velocity decreases with time. For instance, if the volume rate of change remains constant, then the clouds reach 5.6 AU after 180 days if they reach 1 AU after one day.

Throughout the 11 year cycle the cosmic ray flux remains isotropic to within 1-2%. Also the data from Pioneer I and V suggest that the flux is constant within 2% out to 2×10^6 kilometers from the earth (20). According to Fan et al. (20), the latter data require that the flux change with increasing radial distance from the sun $+ 15 \pm 20\%$ per AU in the region inside the earth's orbit. This suggests that the flux is constant throughout the modulated volume, and that it rises to

the interstellar value across a boundary shell where newly arriving plasma clouds continually push back the interstellar flux.

If the lag is produced by a transit time, and if the lag is greater for higher energy particles than for low, then the boundary for higher energy particles must lie farther from the sun than that for lower energy ones. Simply on the basis of the relative radii of curvature of the particles' orbits in any existing field the opposite is expected. Hence we conclude that the time lag probably does not represent a simple transit time, but must be a combined transit, relaxation and diffusion time of the clouds, magnetic fields, and cosmic ray particles. In this connection it would be interesting to learn if the flux lags behind sunspot number the same amount during the waxing and waning parts of the solar cycle. It may be that the flux rises gradually with increasing distance from the sun to the interstellar value, and that the rate of rise depends upon particle energy. Whatever the spatial distribution is, the flux gradients must be small enough to have escaped detection so far.

Any mechanism of depressing the galactic cosmic ray flux which depends upon transit, diffusion and relaxation times seems to be consistent with the pattern that variations which occur in a short time should lag solar activity by less time than variations which take place during a longer interval. Both long and short variations should

negatively correlate with solar activity. Vernov's observation of a positive correlation between flux and sunspot number does not fit this pattern. The author suggests that either solar cosmic rays produced this result, or else that a semi-periodic (27 day) variation in solar activity has masked the true inverse correlation which should be found with some lag different than 20 days.

This discussion of models for the cosmic ray modulation has been extremely brief, and has not touched the different mechanisms which have been proposed by various people. Further consideration of various models does not seem necessary in this discussion of experimental results.

Finally it should be remarked that the flux measured in 1954 may not be the full interstellar flux. If the sun was ejecting any plasma at that time, then presumably some particles were still excluded from a region around the sun. There may also have been a large flux of particles near the earth with less than 150 Mev energy, although the ion chamber could not detect them in 1954 because of the absorbing air overhead at the maximum altitude attained. If any such soft particles existed near the earth, then one would expect many more of them in interstellar space.

Future study of the eleven year modulation should solve the following problems among others:

1) Does the low energy primary flux continue to lag the sunspot number by about 6 months? Does the lag time really depend upon the primary energy?

2) At the next solar minimum ($\sim$ 1965) will the flux reach the same level as in 1954?

3) At this same time, what is the flux of particles down to zero energy in the vicinity of the earth's orbit? What is the charge spectrum of these low energy particles?

4) Does the cosmic ray flux depend upon the distance to the sun over the range 0.5 to 2 AU during any part of the solar cycle?

5) Does a sharp barrier really exist between the modulated volume and interstellar space? What is the flux outside the barrier?

Items 1-3 can be approached using high altitude balloons and earth satellites with apogees outside the effective geomagnetic field. Item 4 can be studied using the spacecraft soon to be launched toward the minor planets. Direct investigation of 5 must wait for longer space flights than are scheduled as yet. Indeed, if the barrier lies at 180 AU, it will be a long time before a spacecraft will reach it. Eventually, though, it should be possible to give some answers to three questions which give this subject astrophysical significance. Namely: What particles and fields are present in interplanetary space? How does the sun affect this space? and How is the galactic cosmic ray flux produced?

REFERENCES

1. L. Janossy, Cosmic Rays (Oxford, 1948), pp. 266-289.

2. P. J. Coleman, Jr., et al., Phys. Rev. Lett., 5, 43-46 (1960).
C. P. Sonnet, J. Geophys. Res., 65, 55-68 (1960).
C. P. Sonnet, Phys. Rev. Lett., 5, 46-48 (1960).

3. L. I. Dorman, Cosmic Ray Variations (State Publ. House for Technical and Theoretical Literature, Moscow, 1957; transl. by Tech. Documents Liaison Office, MCLTD, Wright-Patterson AFB, Ohio), pp. 102-229.

4. H. V. Neher, "The Primary Cosmic Radiation," Ann. Rev. Nucl. Sci. (Annual Reviews, Inc., Palo Alto, 1958), Vol. 8, pp. 217-242.

5. H. V. Neher, "Recent Data on Geomagnetic Effects," Prog. in Cosmic Ray Physics (North Holland Publ. Co., Amsterdam, 1952), Vol. 1, pp. 245-314.

6. S. F. Singer, "The Primary Radiation and Its Time Variations," Prog. in Cosmic Ray Physics (North Holland Publ. Co., Amsterdam, 1958), Vol. 4, pp. 205-330.

7. V. Sarabhai and N. W. Nerurkar, "The Variation of Primary Cosmic Rays," Ann. Rev. of Nuclear Sci. (Annual Reviews, Inc., Palo Alto, 1956), Vol. 6, pp. 1-42.

8. H. Elliot, "Time Variations of Cosmic Ray Intensity," Prog. in Cosmic Rays Physics (North Holland Publ. Co., Amsterdam, 1952), Vol. 1, pp. 455-548.

9. A. Duperier, Proc. Phys. Soc. Lond., 57, 464-477 (1945);
Nature, 158, 196-198 (1946)
Proc. Phys. Soc. Lond. 62A, 684-696 (1949).
Nature, 167, 312-313 (1956).

10. I. Lange and S. E. Forbush, Cosmic Ray Results (Carnegie Inst. of Washington Publ. 175, 1948 and 1957), two volumes.

11. Cosmic Ray Intensity during the IGY; Bi-hourly Neutron Intensity (Nat'l. Comm. for the IGY, Sci. Council of Japan, Ueno Park, Tokyo; World Data Center C-2 for Cosmic Rays, 1959, 1960).

12. H. Elliot and D. W. N. Dolbar , Proc. Phys. Soc. Lond. 63A, 137-144 (1950). J. Atm. and Terr. Phys. 1, 205-222 (1951).

13. Y. Sekido, et al., J. Geomag. and Geoelect. 2, 66-70 (1950). J. Geomag. and Geoelect., 6, 22-33 (1954). Nature, 177, 35-36 (1956). Phys. Rev. 113, 1108-1114 (1959).

14. W. Galbraith, Extensive Air Showers (Academic Press, Inc., New York, 1958), pp. 160-180.

15. S. E. Forbush, J. Geophys. Res. 63, 651-669 (1958).

16. S. E. Forbush, J. Geophys. Res. 59, 525-542 (1954).

17. J. A. Simpson, H. W. Babcock, H. D. Babcock, Phys. Rev. 98, 1402-1410 (1955).

18. H. V. Neher, Phys. Rev., 103, 228-236 (1956).

19. H. V. Neher, Nature, 184, 423-425 (1959).

20. C. Y. Fan et al., Phys. Rev. Lett., 5, 269-271 (1960). Phys. Rev. Lett., 5, 272-274 (1960).

21. J. Winckler, J. Geophys. Res., 65, 1331-1359 (1960).

22. K. A. Anderson, et al., J. Geophys. Res., 64, 1133-1147 (1959).

23. P. Rothwell and C. McIlwain, Nature, 184, 138-140 (1959).

24. H. R. Anderson, Phys. Rev., 116, 461-462 (1959).

25. B. Rossi, High Energy Particles (Prentice-Hall, Inc., New York, 1952), 569 pp.

26. J. A. Simpson, et al., Phys. Rev., 90, 934-950 (1953).

27. A. H. Compton, et al., Rev. Sci. Instr., 5, 415-422 (1934).

28. Annals of the IGY (Pergamon Press, New York, 1957), Vol. 4, pp. 345-393.

29. J. A. Simpson, et al., Phys. Rev., 94, 426-440 (1954).

30.)
31.) IGY Cosmic Ray Data are being collected in the three World Data Centers for Cosmic Rays, A, B-2, and C-2. These are directed by The School of Physics, Univ. of Minn., Minneapolis, Minn.; The Academy of Sciences of the USSR, Moscow; and the Nat'l. Comm. for the IGY, Science Council of Japan, Ueno Park, Tokyo. Data will be published as they become available. General information may be obtained in the U.S. by writing to:

Director, World Data Center A
Nat'l. Acad. of Sciences
2101 Constitution Ave., N.W.
Washington 25, D. C.

32. H. V. Neher and S. E. Forbush, Phys. Rev., 87, 889-890 (1952).

33. R. A. Millikan and H. V. Neher, Phys. Rev., 50, 15-24 (1936).

34. J. A. Simpson, et al., Phys. Rev., 102, 1648-1652 (1956).

35. M. Kodama, J. Geomag. and Geoelect., 10, 37-46 (1959).

36. P. Rothwell and J. Quenby, Nuovo Cim. Suppl. 8, 249-256 (1958).

37. P. Rothwell, Phil. Mag., 3, 961-970 (1958).

38. A. Biehl, et al., Phys. Rev., 76, 914-932 (1949).
Phys. Rev., 83, 1169-1174 (1951).

39. J. A. Simpson, Phys. Rev., 73, 1389-1391 (1948).
Phys. Rev., 74, 1214 (1948).
Phys. Rev., 83, 1175-1188 (1951).

40. J. R. Storey, Phys. Rev., 113, 297-304 (1959).
Phys. Rev., 117, 573-577 (1960).

41. K. A. Anderson, J. Geophys. Res., 65, 551-564 (1960).

42. J. Winckler and K. A. Anderson, Phys. Rev., 93, 596-605 (1954).

43. F. B. McDonald, Phys. Rev., 104, 1723-1729 (1956).

44. F. B. McDonald, Phys. Rev., 107, 1386-1395 (1957).

45. F. B. McDonald, Phys. Rev., 109, 1367-1375 (1958).

46. F. B. McDonald, Nuovo Cim. Suppl. 8, 500-507 (1958).

47. F. B. McDonald and W. R. Webber, Phys. Rev., 115, 194-205 (1959).

48. F. B. McDonald, Phys. Rev., 116, 462-463 (1959).

49. W. R. Webber, Nuovo Cim. 4, 1285-1306 (1956).

50. P. Meyer, Phys. Rev., 115, 1734-1741 (1959).

51. M. A. Pomerantz and G. W. McClure, Phys. Rev., 86, 536-545 (1952).

52. H. V. Neher, et al., Phys. Rev., 90, 655-674 (1953).

53. H. V. Neher, Phys. Rev., 107, 588-592 (1957).

54. H. V. Neher and H. R. Anderson, Phys. Rev., 109, 608 (1958).

55. L. Meredith, et al., Phys. Rev., 99, 198-209 (1955).

56. H. V. Neher, Rev. Sci. Instr., 24, 99-102 (1953).

57. H. V. Neher and A. Johnston, Rev. Sci. Instr., 25, 517-518 (1954).

58. H. V. Neher and A. Johnston, Rev. Sci. Instr., 27, 173-174 (1956).

59. H. Carmichel and E. G. Dymond, Proc. Roy. Soc. Lond., A171, 321-344 (1939).

60. H. V. Neher, Private Communication.

61. A. Johnston, Thesis, California Institute of Technology, 1956 (unpublished).

62. E. Segre, Experimental Nuclear Physics, (John Wiley and Sons, Inc., New York, 1953), Vol. 1, p. 222.

63. R. Evans, The Atomic Nucleus (McGraw-Hill Book Co., New York, 1955), p. 625.

64. B. Rossi, High Energy Particles (Prentice-Hall, Inc., New York, 1952), p. 295.

65. R. A. Millikan and G. H. Cameron, Phys. Rev., 31, 921-930 (1928).

66. R. A. Millikan, Phys. Rev., 39, 391-402 (1932).

67. H. V. Neher, Rev. Sci. Instr., 24, 97-98 (1953).

68. B. Rossi, Rev. Mod. Phys., 20, 537-583 (1948).

69. G. Puppi and N. Dallaporti, "The Equilibrium of the Cosmic Ray Beam in the Atmosphere," Prog. in Cosmic Ray Physics (North Holland Publ. Co., Amsterdam, 1952), Vol. 1, pp. 317-391.

70. V. Benzi, Nuovo Cim., 11, 686-687 (1954).

71. G. Puppi, "The Energy Balance of Cosmic Radiation," Prog. in Cosmic Ray Physics (North Holland Publ. Co., Amsterdam, 1956), Vol. 3, 341-388.

72. H. Komori, Prog. in Theor. Phys., 13, 205-216 (1955).

73. I. S. Bowen, Phys. Rev., 50, 579-581 (1936).

74. W. Heisenberg, Vorträge über Kosmische Strahlung (Springer Verlag, Berlin, 1953), pp. 391-410.

75. J. Winckler, et al., J. Geophys. Res., 64, 597-610 (1959).

76. E. C. Pressley, Phys. Rev., 89, 654-655 (1953).

77. S. B. Treiman, Phys. Rev., 91, 957-959 (1953).

78. H. Greim and S. F. Singer, Phys. Rev., 99, 608 (1955).

79. K. A. Anderson, Nuovo Cim. Suppl. 5, 389-416 (1957).

80. J. R. Winckler and K. A. Anderson, Phys. Rev., 93, 596-605 (1953).

81. R. Gall and J. Lifschitz, Phys. Rev., 101, 1821-1824 (1956).

82. S. Chapman and J. Bartels, Geomagnetism (Oxford, Clarendon Press, 1940), Vol. 2, pp. 543-697.

83. E. H. Vestine, et al., The Geomagnetic Field, Its Description and Analysis (Carnegie Inst. of Wash. Publ. 580, 1947).

84. E. H. Vestine, et al., Description of the Earth's Main Magnetic Field and Its Secular Change (Carnegie Inst. of Wash. Publ. 578, 1947).

85. H. F. Finch and B. R. Leaton, Mon. Not. Roy. Astr. Soc. Geophys. Suppl. 7, 314-317 (1957).

86. J. Bartels, Terr. Mag. and Atm. Elect., 41, 225-250 (1936).

87. W. D. Parkinson and J. Clearly, Geophys. J., 1, 346-348 (1958).

88. W. R. Webber, Nuovo Cim. Suppl. 8, 532-545 (1958).

89. C. Störmer, The Polar Aurora (Oxford, Clarendon Press, 1955), pp. 209-392.

90. G. Lemaitre and M. S. Vallarta, Phys. Rev., 43, 87-91 (1933).
Phys. Rev., 49, 719-726 (1936).
Phys. Rev., 50, 493-504 (1936).

91. M. S. Vallarta, Phys. Rev., 47, 647-651 (1935).

92. M. S. Vallarta, Outline of the Theory of the Allowed Cone of Cosmic Radiation (Univ. of Toronto Press, Toronto, 1938).

93. M. S. Vallarta, Phys. Rev., 74, 1837-1840 (1948).

94. E. J. Schremp, Phys. Rev., 54, 153-162 (1938).

95. M. Schwartz, Bull. Am. Phys. Soc., Ser. II, 1, 319 (1956).
M. Schwartz, Nuovo Cim. Suppl. 11,27-59 (1959).

96. J. E. Kasper, Nuovo Cim. Suppl. 11, 1-26 (1959).

97. M. S. Vallarta, R. Gall and J. Lifschitz, Phys. Rev., 109, 1403-1404 (1958).

98. E. J. Schremp, Phys. Rev., 58,662-663 (1940).

99. T. H. Johnson, Rev. Mod. Phys., 10, 193-244 (1938).

100. S. Chapman and V. C. A. Ferraro, Nature, 126, 129-130 (1930). Terr. Mag. and Atm. Elect., 36, 77-97, 171-186 (1931). Terr. Mag. and Atm. Elect., 37, 147-156 (1932).

101. S. Chapman and J. Bartels, Geomagnetism (Oxford, 1940), pp. 799-845.

102. F. Firor, Phys. Rev., 94, 1017-1036 (1954).

103. E. C. Ray, Phys. Rev., 101, 1142-1148 (1956). Phys. Rev., 102, 1689 (1956). Phys. Rev., 104, 1459-1462 (1956).

104. M. Kodama, et al., J. Sci. Res. Inst. 51, 138-157 (1957).

105. D. C. Rowe, et al., Canad. J. of Phys., 34, 968-984 (1956).

106. M. Kodama, J. Geomag. and Geoelect., 11, 37 (1959).

107. J. J. Quenby and W. R. Webber, Phil. Mag., 4, 90-113 (1959).

108. H. V. Neher, Phys. Rev., 78, 674-680 (1950).

109. F. S. Jory, Phys. Rev., 102, 1167-1173 (1956).

110. C. J. Waddington, "The Composition of the Primary Cosmic Radiation," Prog. in Nuclear Physics (Pergamon Press, New York, 1960), Vol. 8, pp. 1-45.

111. P. H. Fowler, et al., Phil. Mag., 2, 157-175 (1957).

112. U. S. Weather Bureau, WBAN 33 Charts for 1200 GMT Release.

113. U. Haber-Schaim, Nuovo Cim. Suppl. 2, 336-338 (1955).

114. G. Clark, et al., Nature, 180, 353-356, 406-409 (1957).

115. P. H. Fowler and C. J. Waddington, Phil. Mag., 1, 637-650 (1956).

116. Solar Activity Summary II, III, and IV for 1958. (High Altitude Observatory, Univ. of Colorado, 1959).

117. M. Waldmeier, J. Geophys. Res., 55, 211-213 (1950).
56, 439-441 (1951).
57, 413-416 (1952).
58, 405-407 (1953).
59, 295-297 (1954).
60, 349-351 (1955).
61, 283-285 (1956).
62, 309-311 (1957).
63, 409-410 (1958).
64, 1347-1349 (1959).
65, 1639-1642 (1960).

118. E. J. Chernosky and M. P. Hagan, J. Geophys. Res., 63, 775-788 (1958).

119. S. N. Vernov, et al., Proc. of the Moscow Cosmic Ray Conference (International Union of Pure and Applied Physics, Moscow, 1960), Vol. 4, pp. 51-64.

120. H. V. Neher and H. R. Anderson, Proc. of the Moscow Cosmic Ray Conference (International Union of Pure and Applied Physics, Moscow, 1960), Vol. 4, pp. 101-107.

121. J. A. Earl, Phys. Rev. Lett., 6, 125-128 (1961).

122. P. Meyer and R. Vogt, Phys. Rev. Lett., 6, 193-196 (1961).

FIGURES

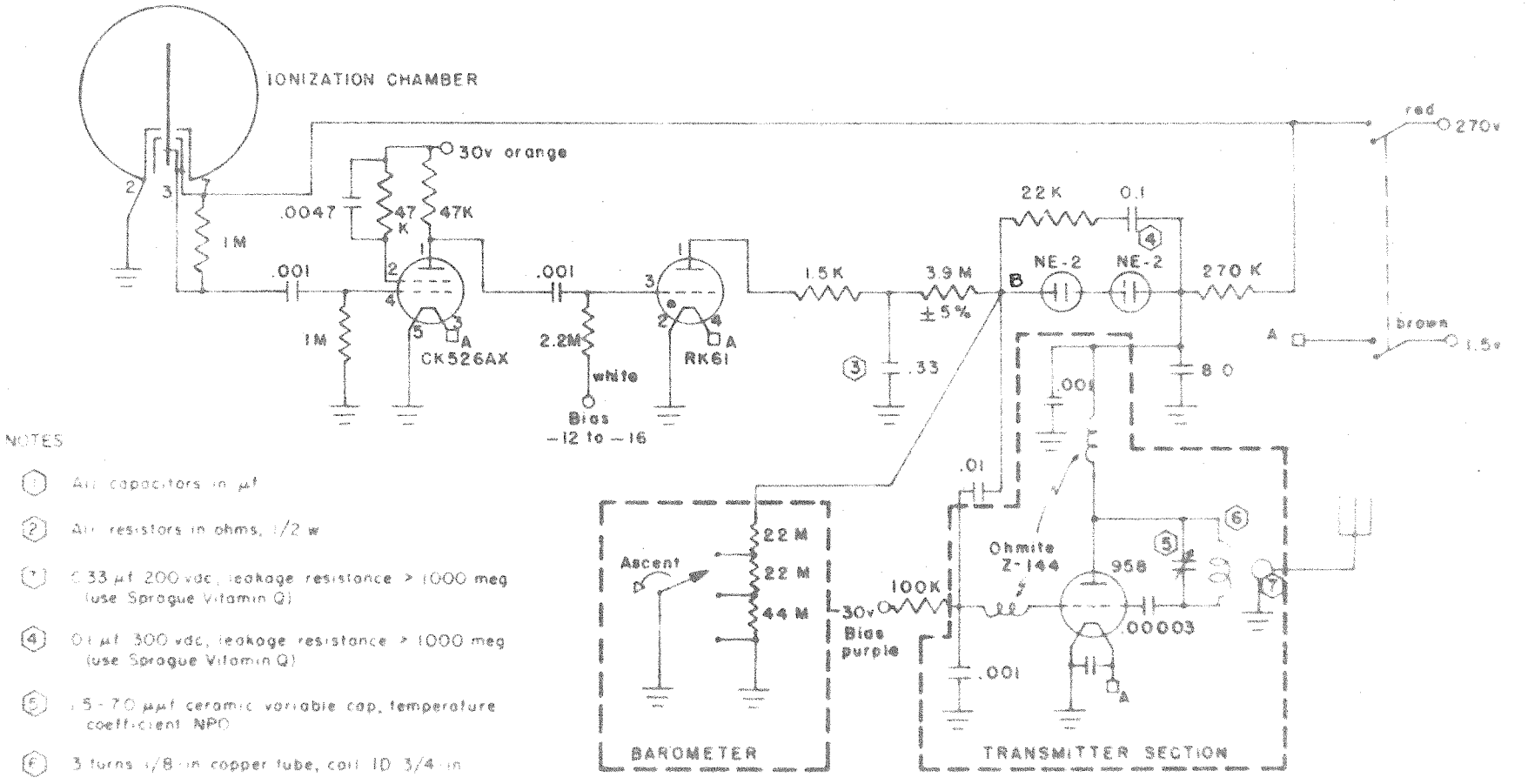

NOTES

1. All capacitors in μf
2. All resistors in ohms, 1/2 w
3. 0.33 μf 200 vdc, leakage resistance > 1000 meg (use Sprague Vitamin Q)
4. 0.1 μf 300 vdc, leakage resistance > 1000 meg (use Sprague Vitamin Q)
5. 5 - 70 μμf ceramic variable cap, temperature coefficient NPO
6. 3 turns 1/8 in copper tube, coil ID 3/4 in
7. 2 3/4 in, No 20 solid conductor insulated wire

FIG 1 IONIZATION CHAMBER TELEMETERING APPARATUS

FIG 2 LOCATIONS of the FLIGHTS

Numbers are days of the months.

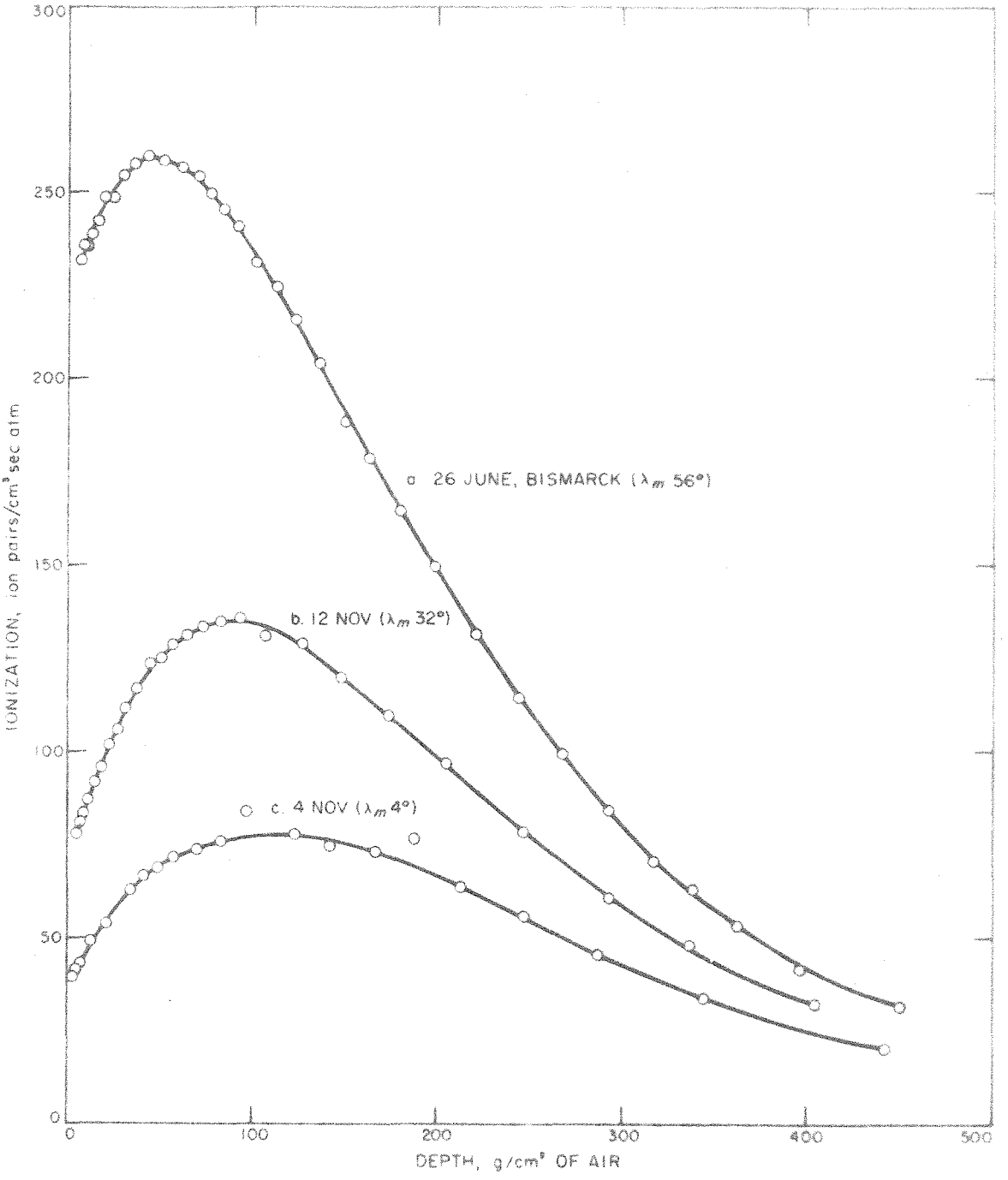

FIG. 3 TYPICAL IONIZATION vs DEPTH CURVES, SHOWING ORIGINAL DATA POINTS

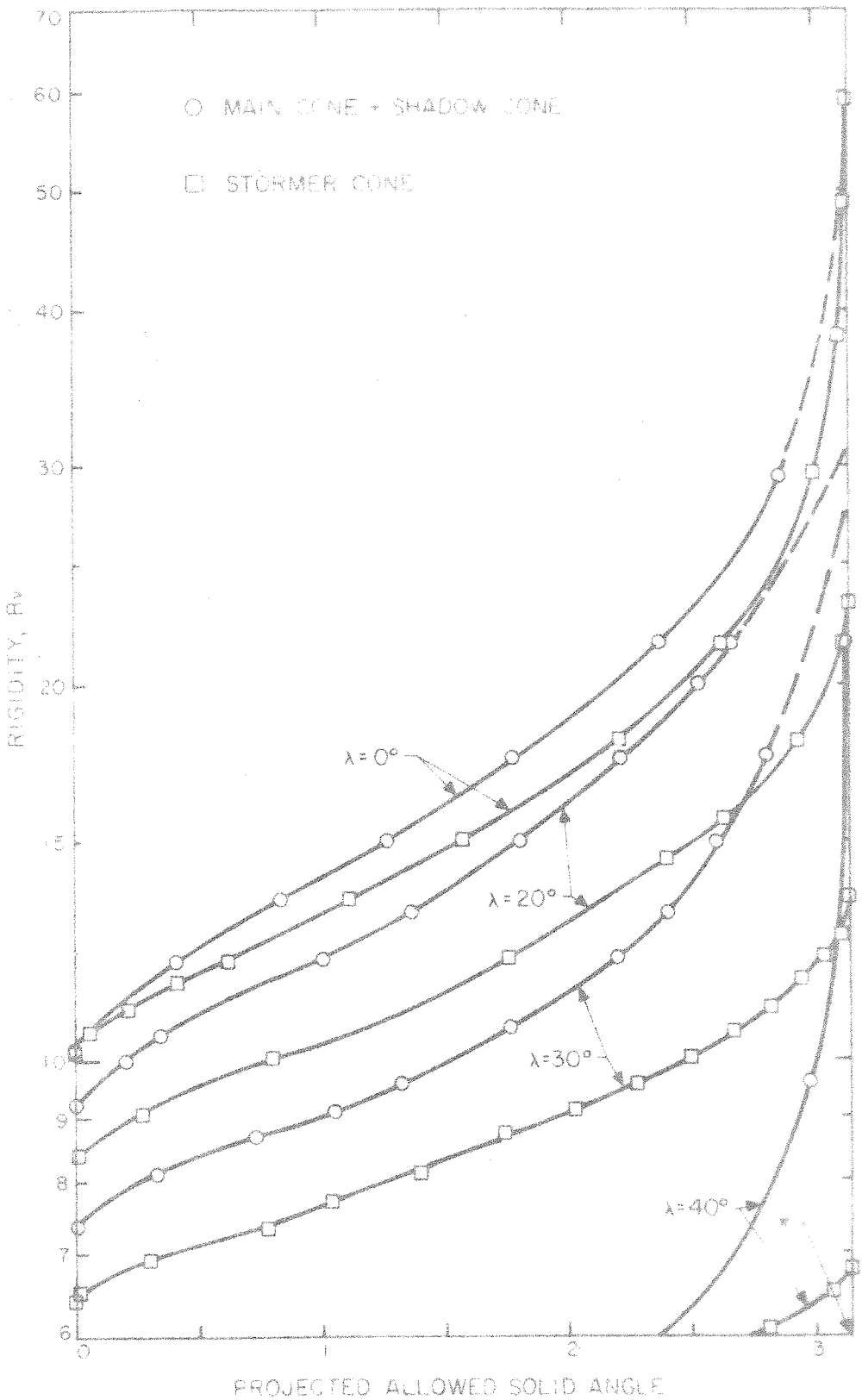

FIG 4 ALLOWED CONES vs RIGIDITY

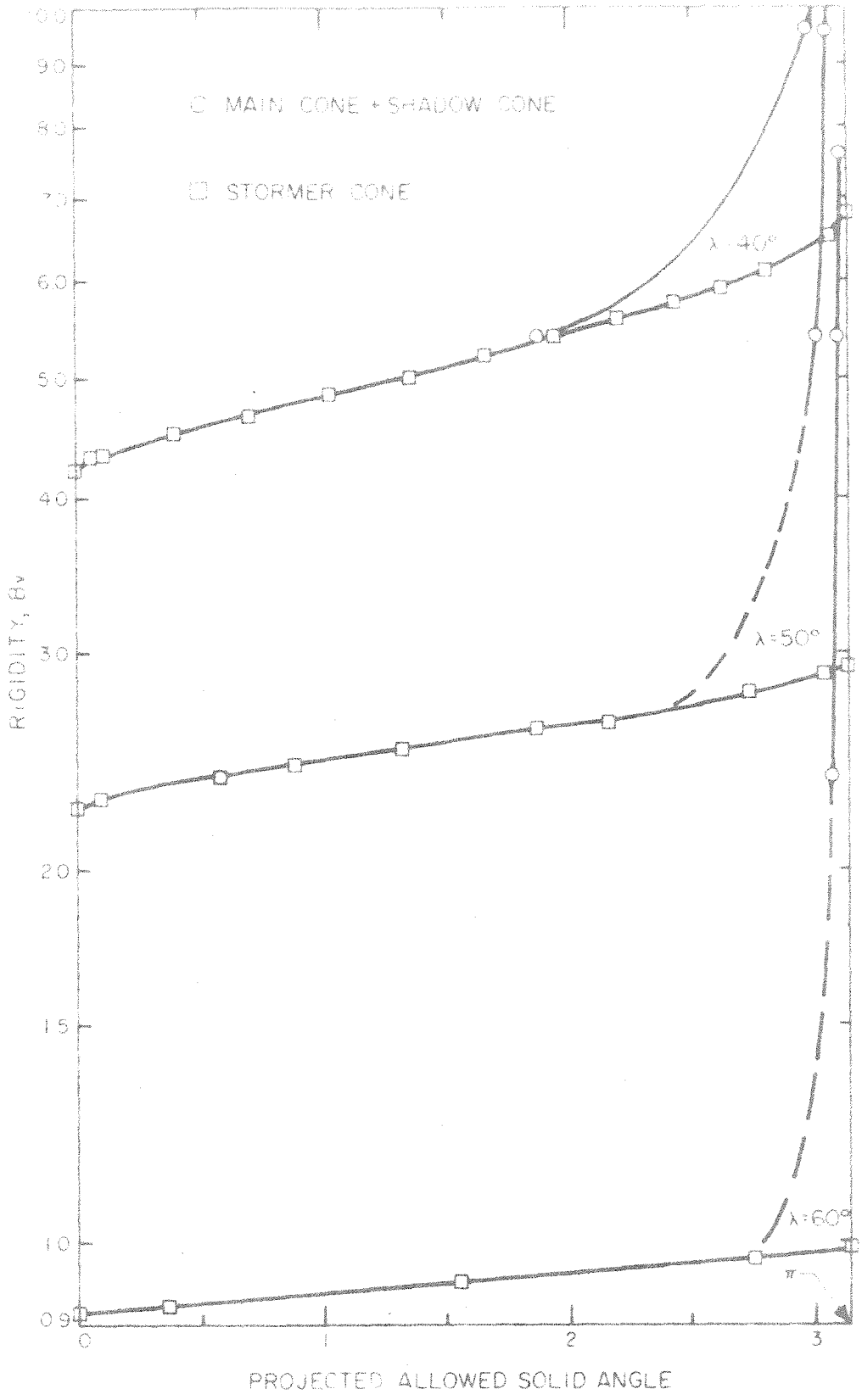

FIG 5 ALLOWED CONES vs RIGIDITY

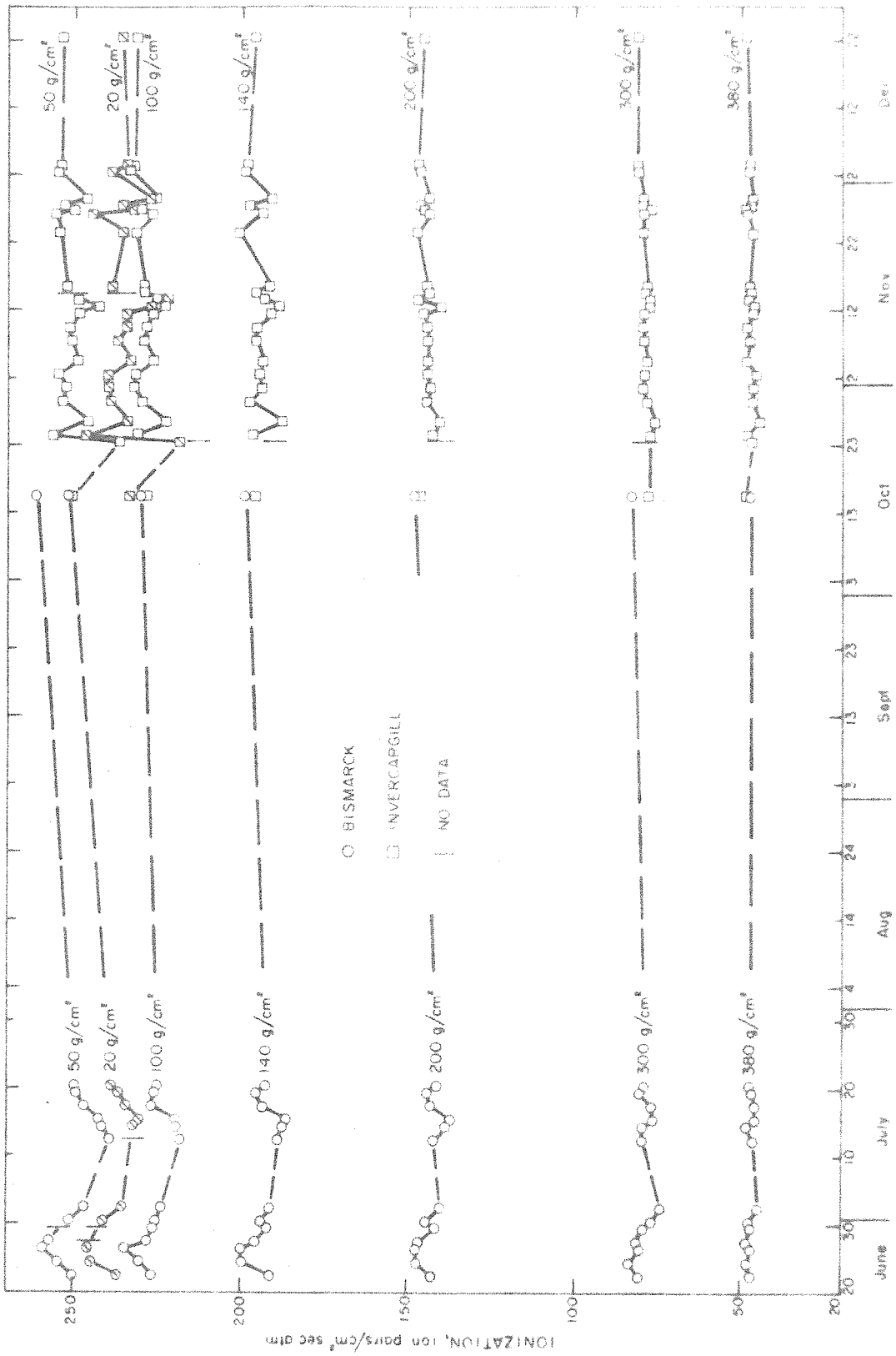

FIG 7 IONIZATION AT BASE STATIONS

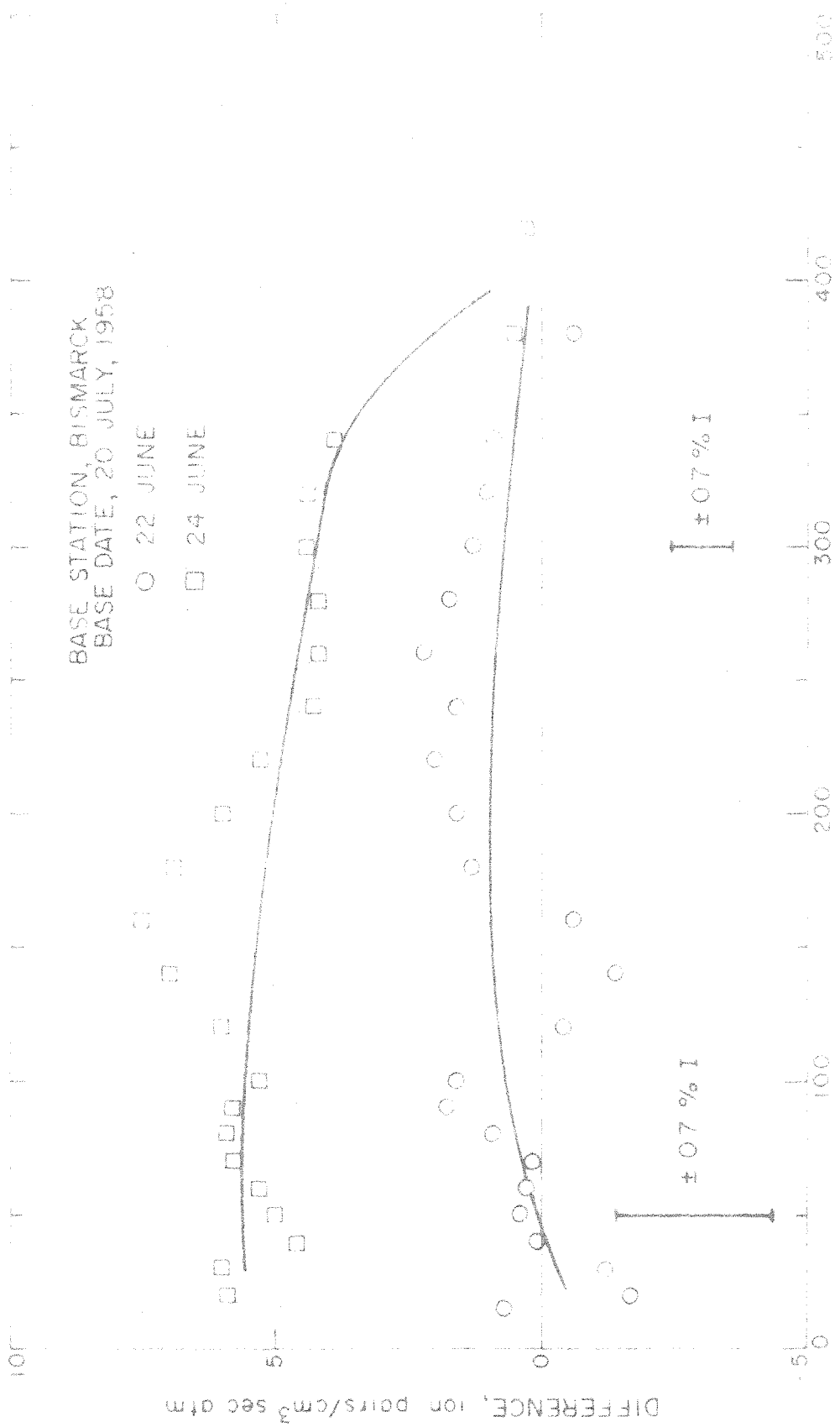

FIG 8a IONIZATION DIFFERENCE AT BISMARCK, DATE GIVEN MINUS BASE DATE

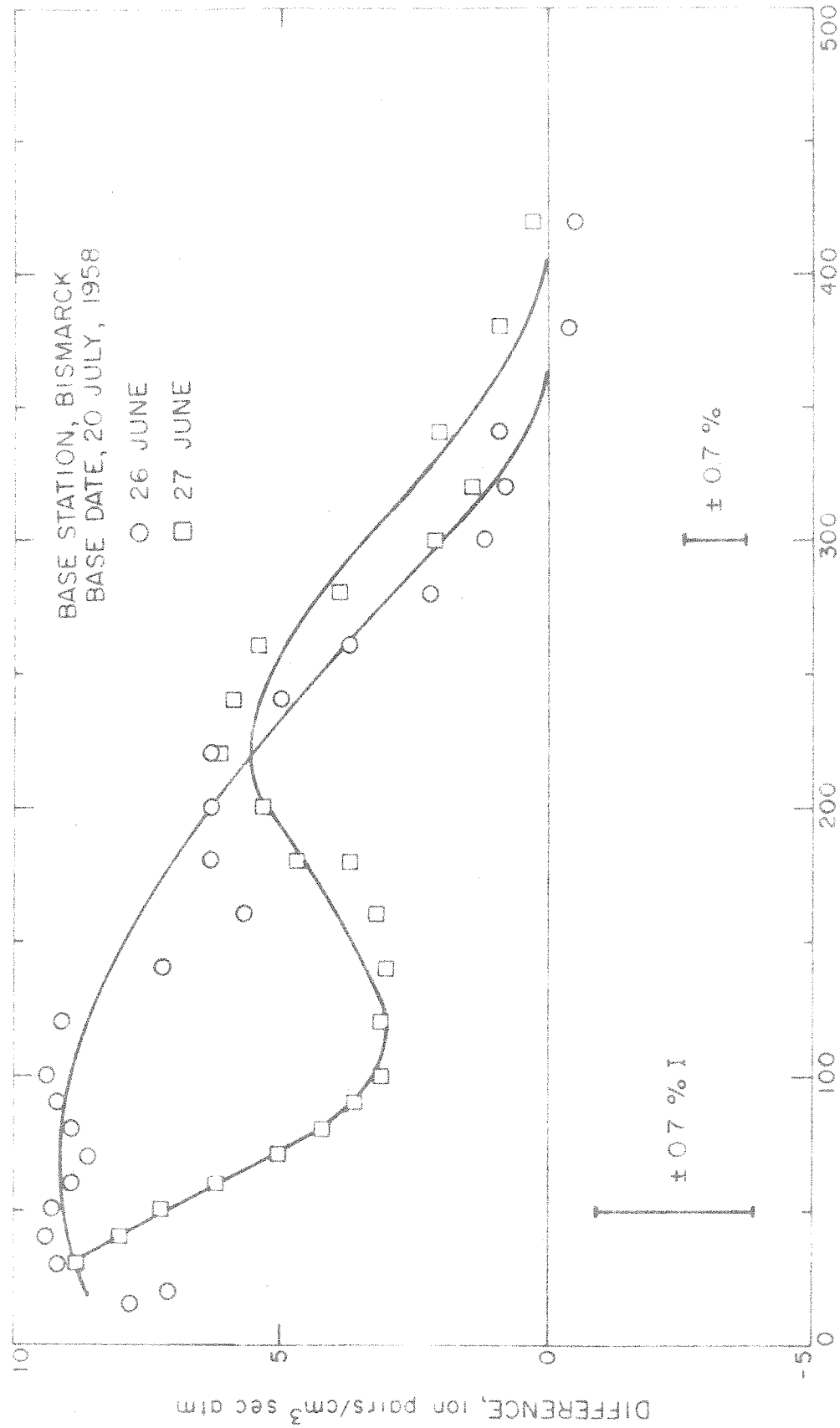

FIG 8b IONIZATION DIFFERENCE AT BISMARCK, DATE GIVEN MINUS BASE DATE

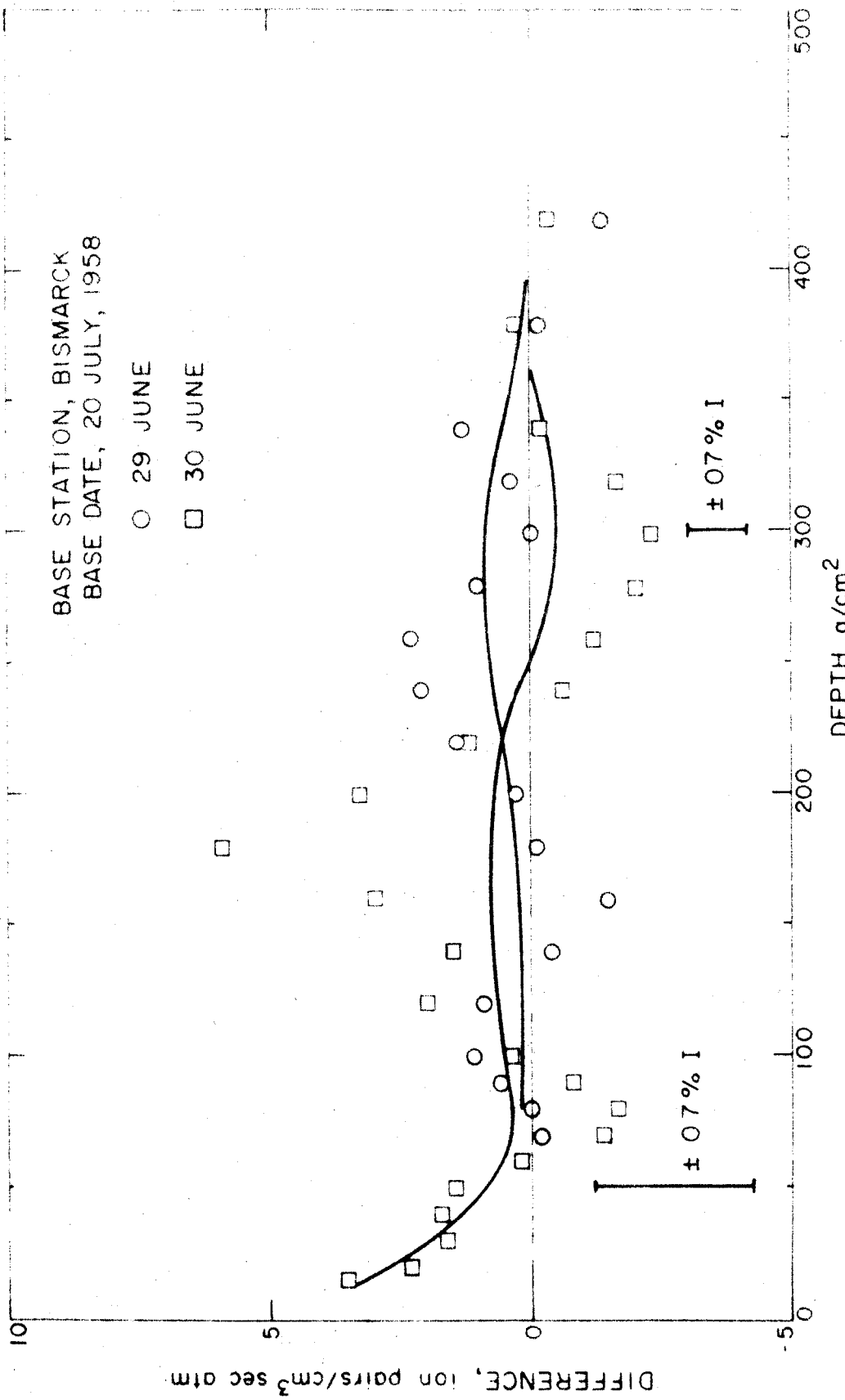

FIG 8c IONIZATION DIFFERENCE AT BISMARCK, DATE GIVEN MINUS BASE DATE

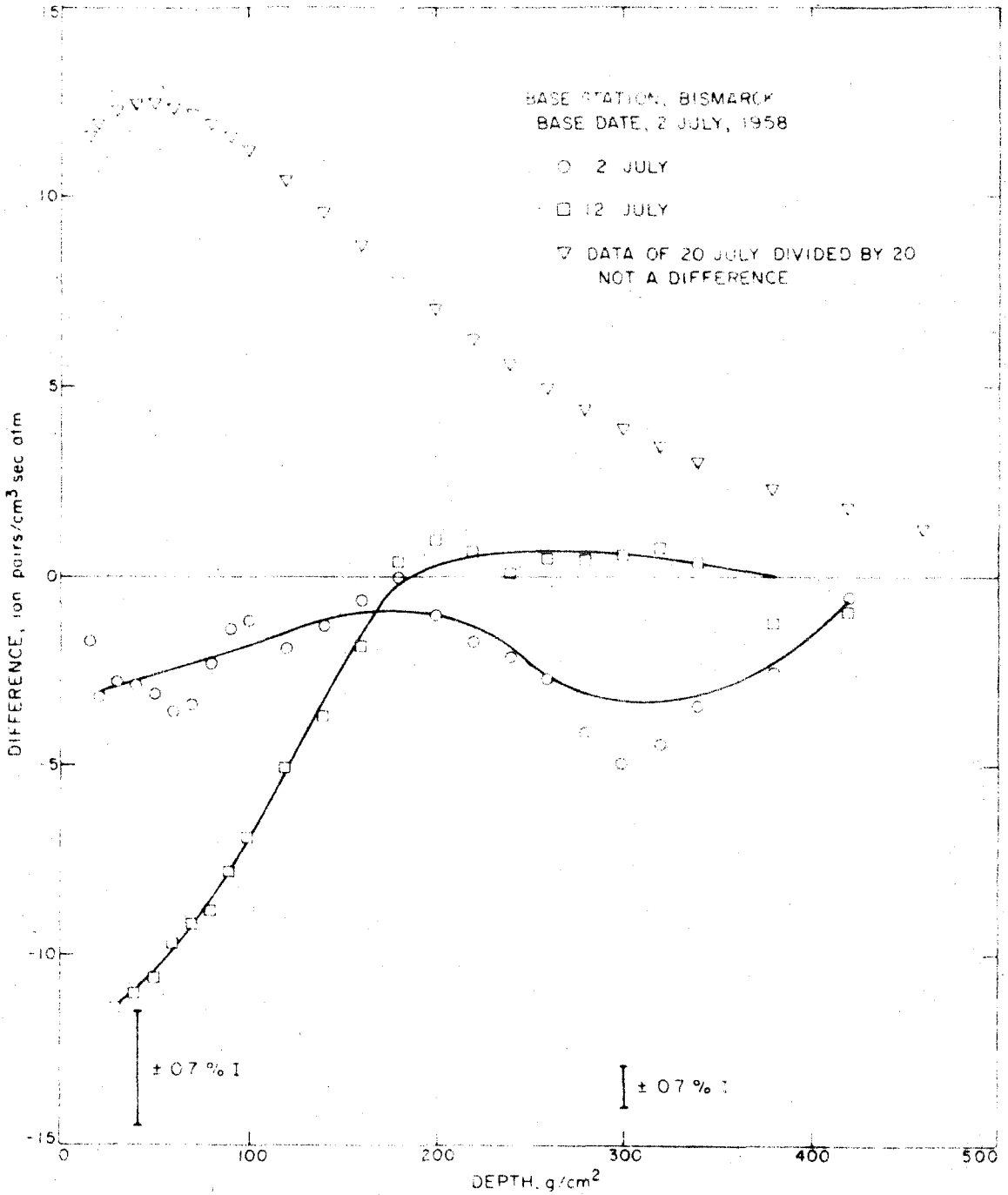

FIG 8d IONIZATION DIFFERENCE AT BISMARCK, DATE GIVEN MINUS BASE DATE

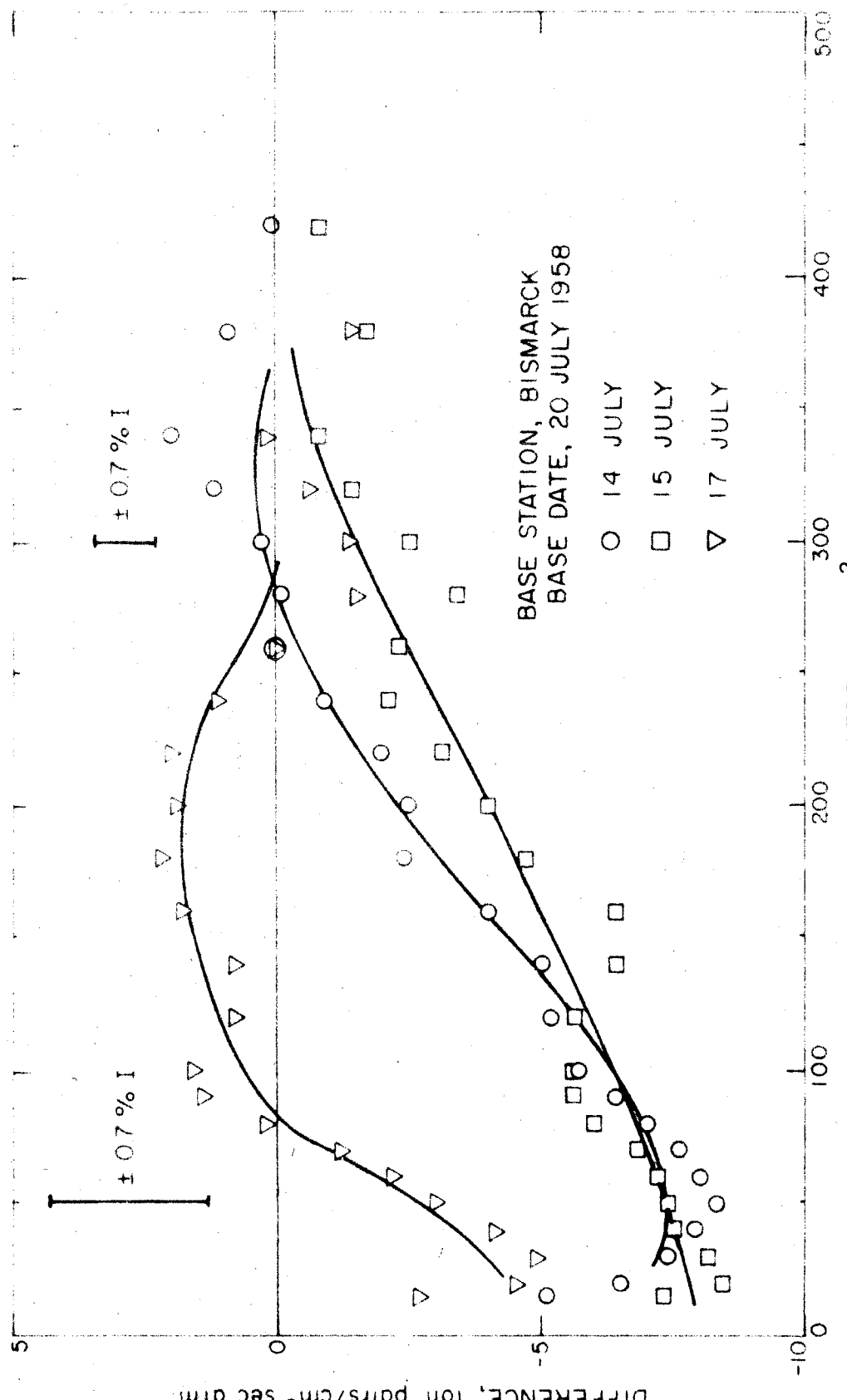

FIG 8e IONIZATION DIFFERENCE AT INVERCARGILL, DATE GIVEN MINUS BASE DATE

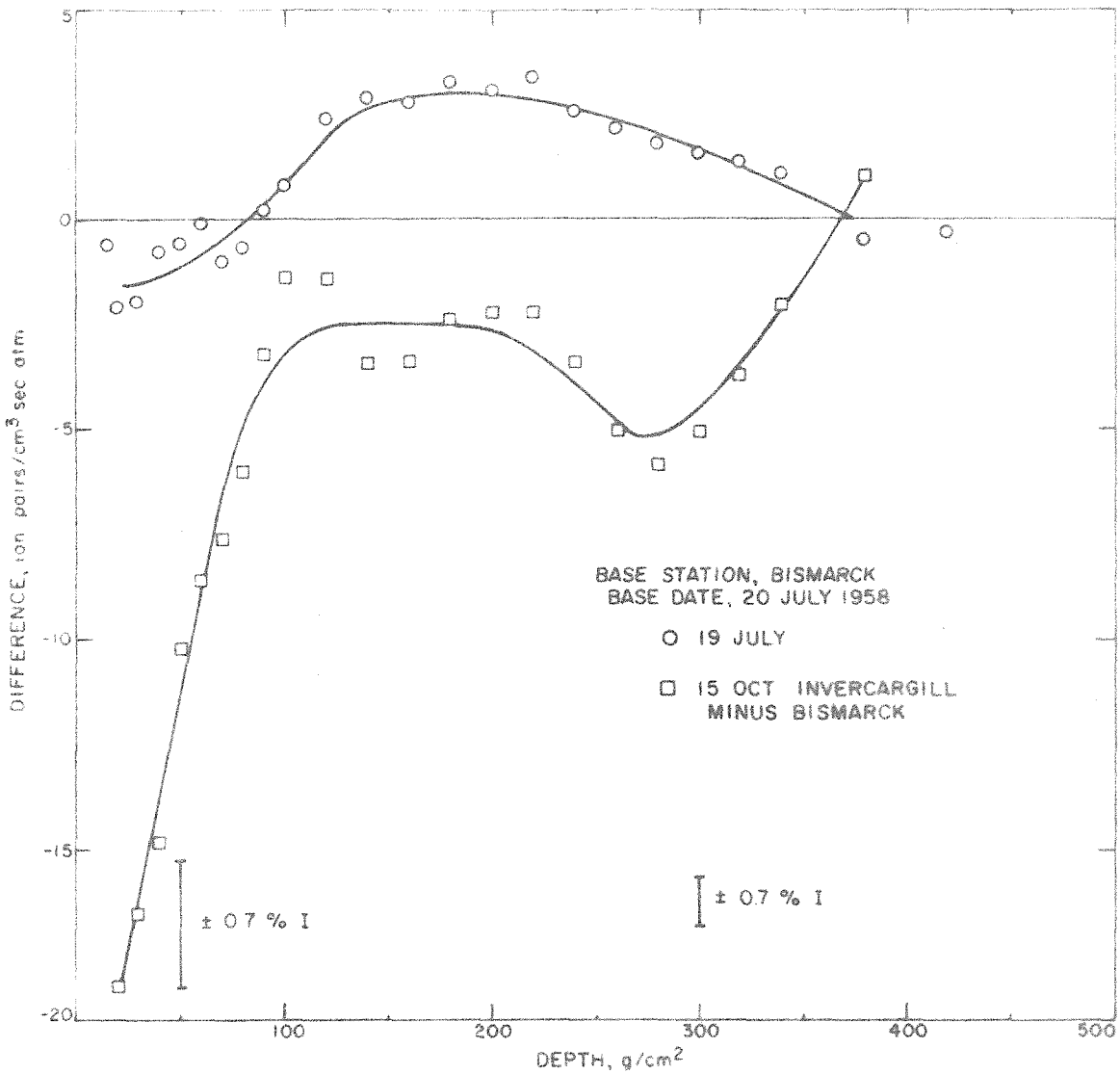

FIG 8f IONIZATION DIFFERENCE AT BISMARCK, DATE GIVEN MINUS BASE DATE

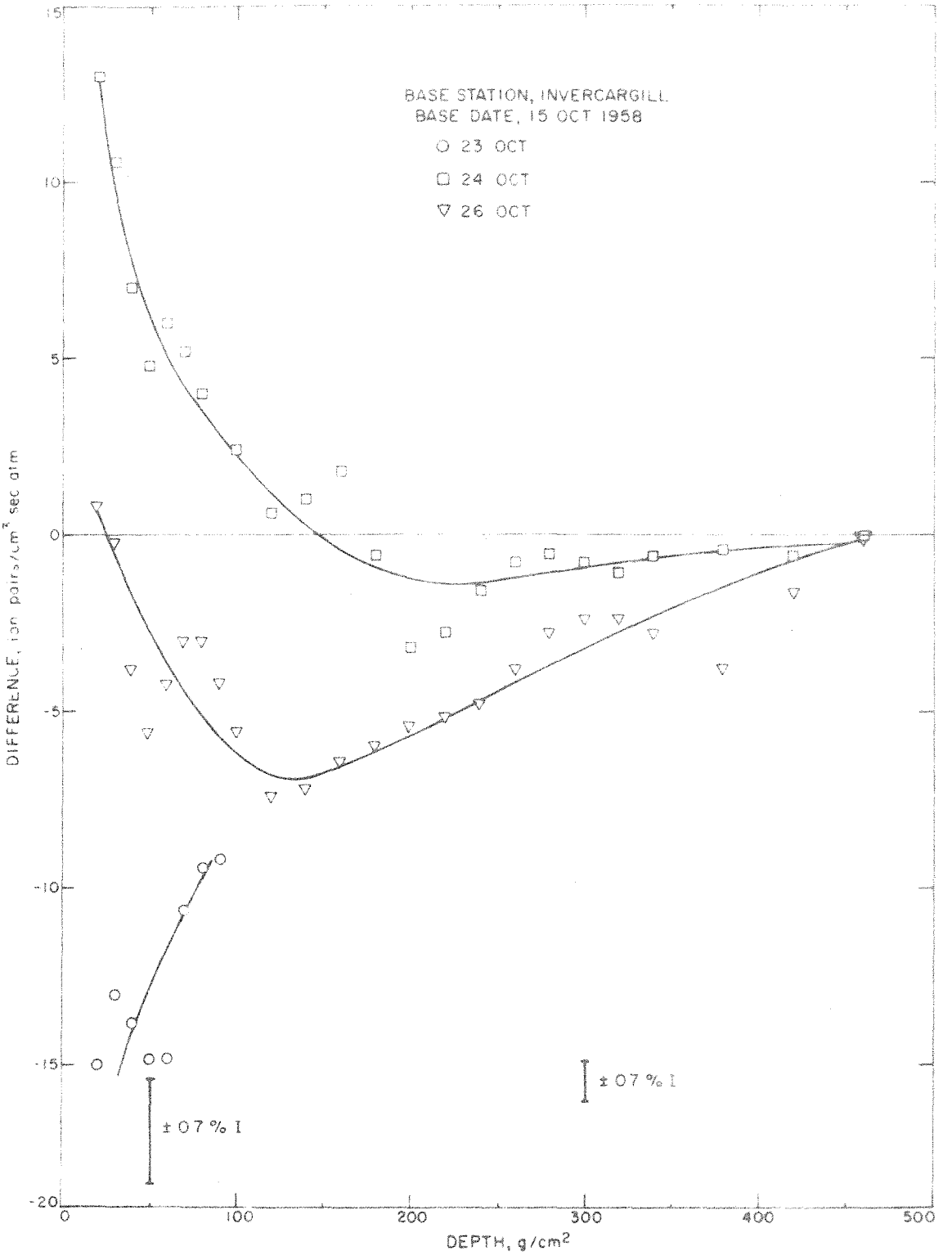

FIG 9a IONIZATION DIFFERENCE AT INVERCARGILL, DATE GIVEN MINUS BASE DATE

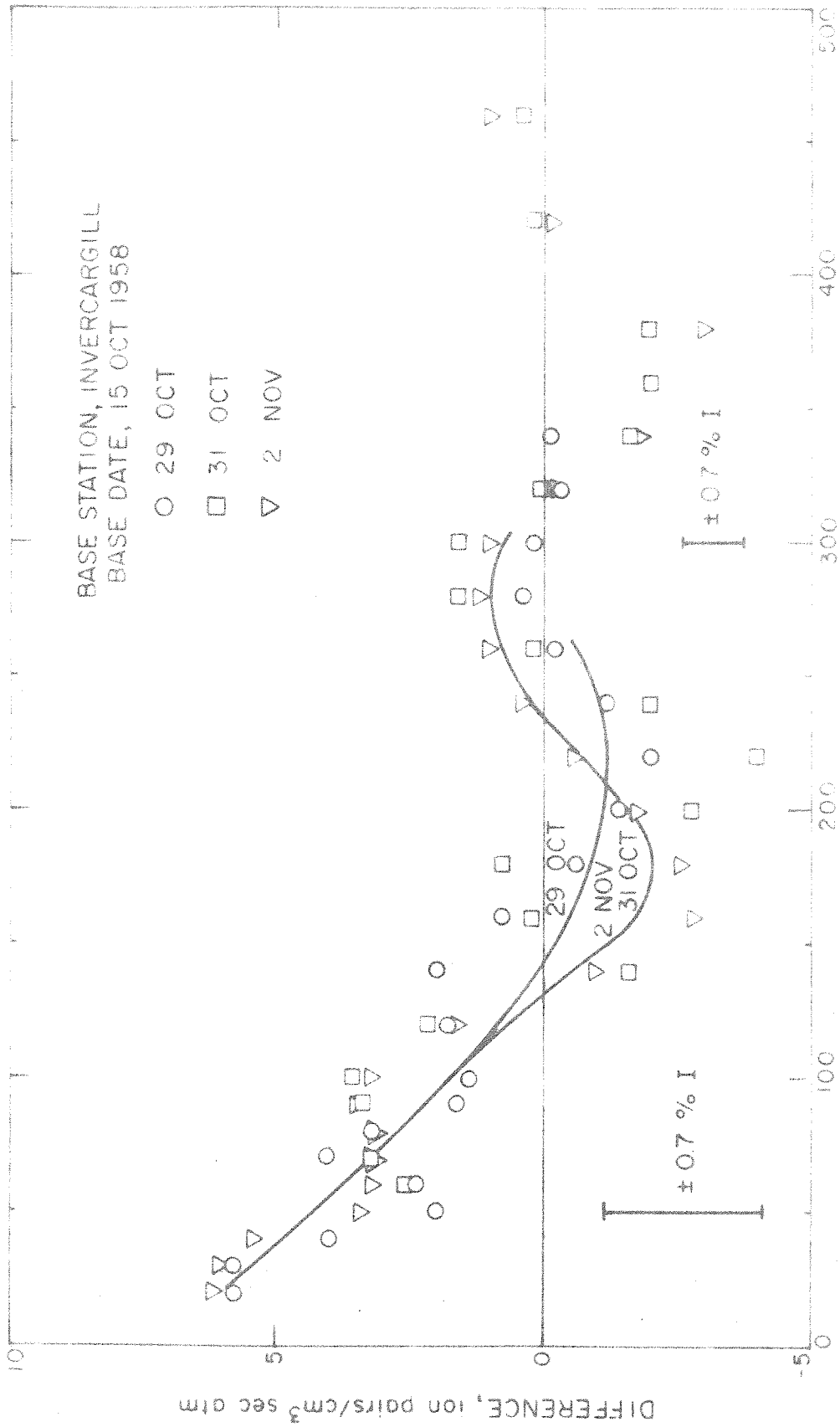

FIG 9b IONIZATION DIFFERENCE AT INVERCARGILL, DATE GIVEN MINUS BASE DATE

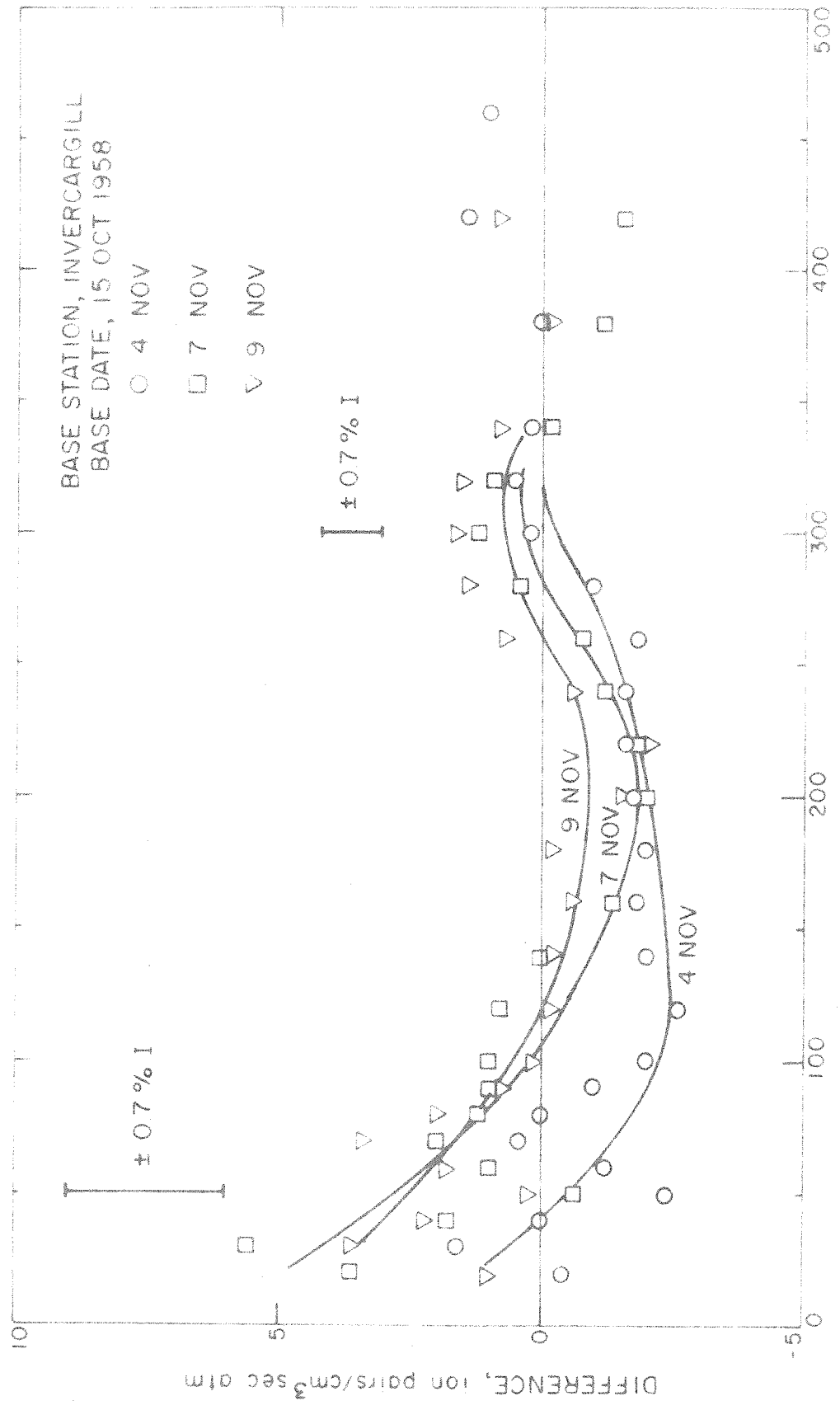

FIG 9c IONIZATION DIFFERENCE AT INVERCARGILL, DATE GIVEN MINUS BASE DATE

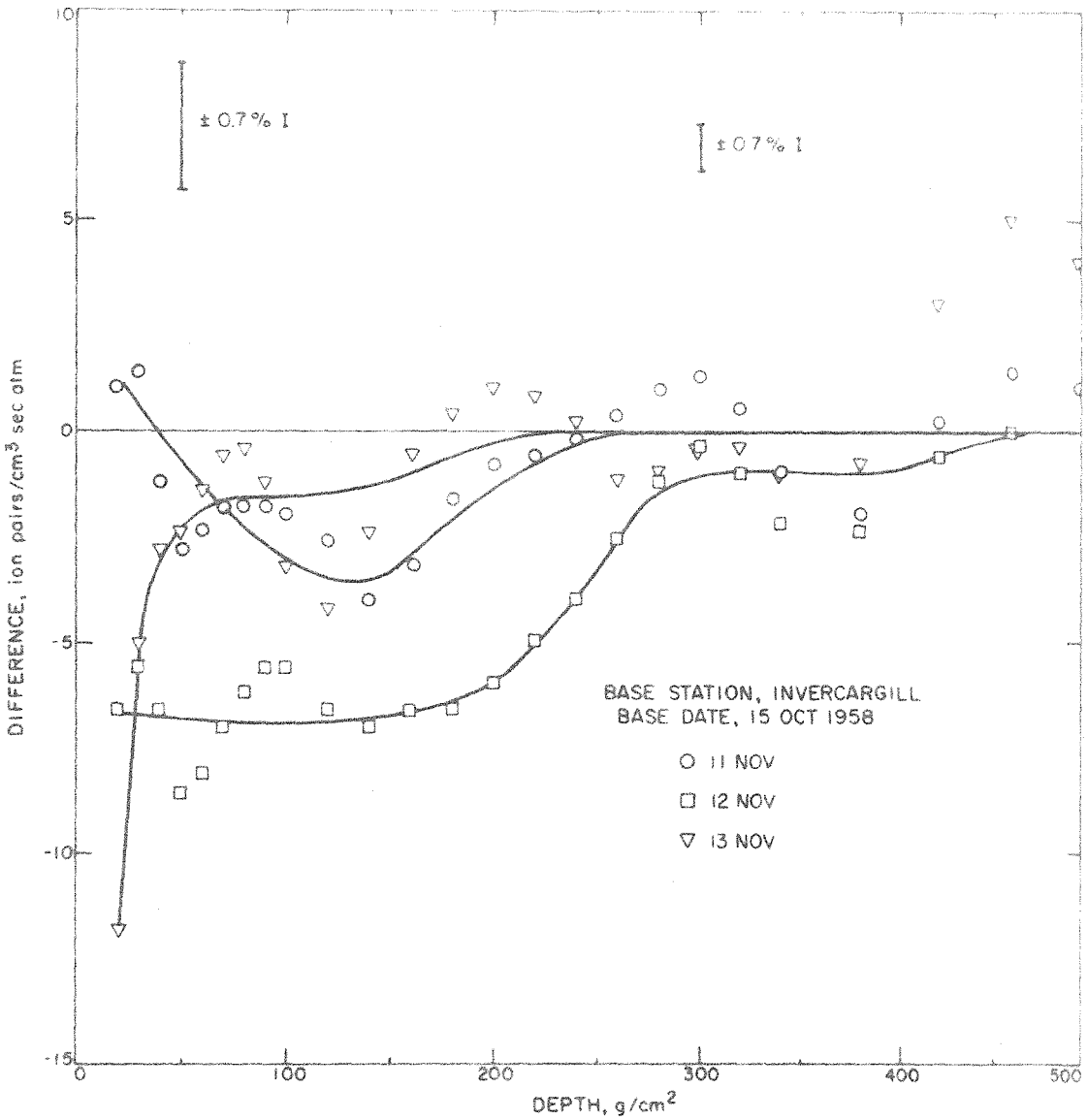

FIG 9d IONIZATION DIFFERENCE AT INVERCAGILL, DATE GIVEN MINUS BASE DATE

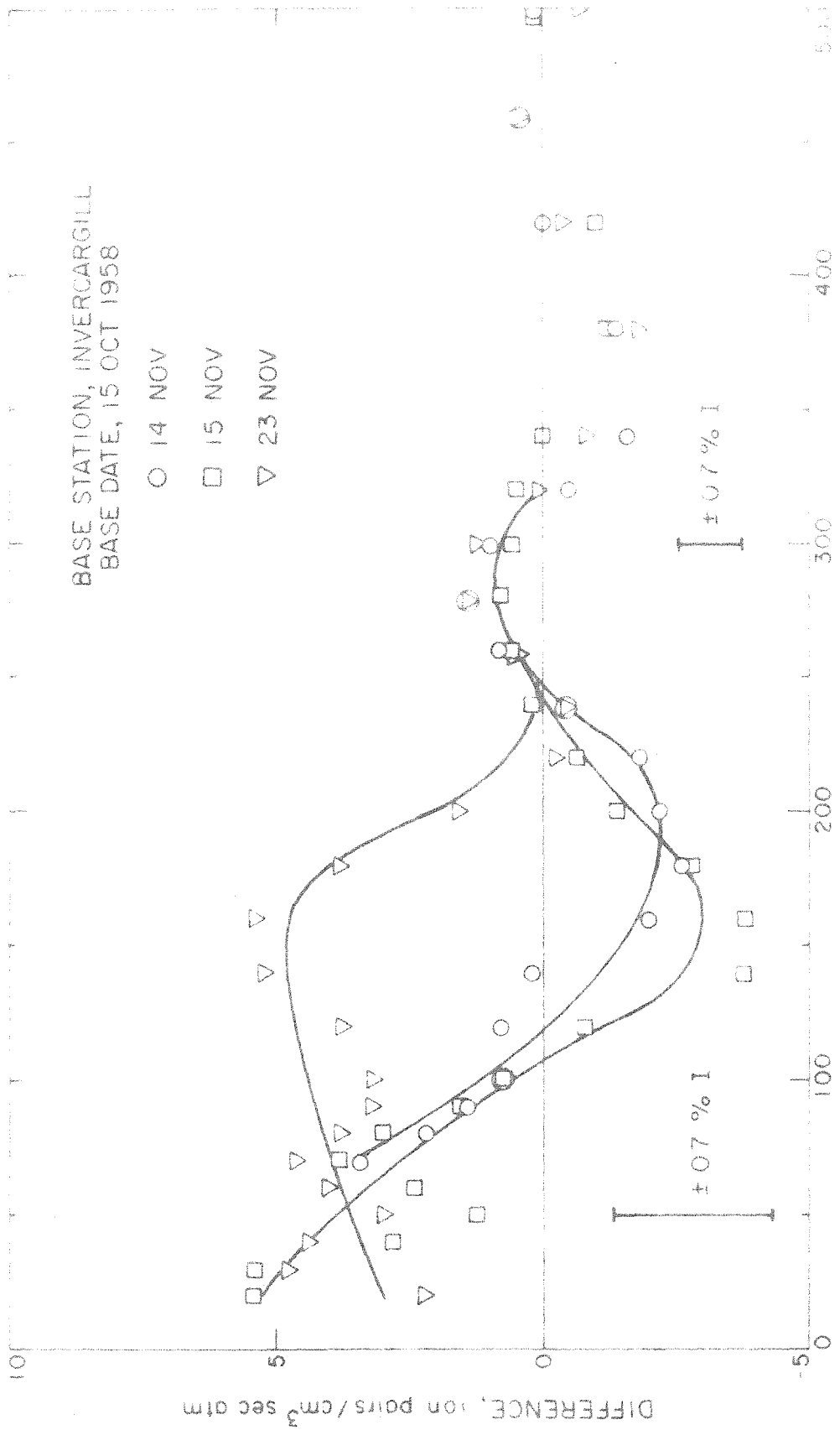

FIG 9e IONIZATION DIFFERENCE AT INVERCARGILL, DATE GIVEN MINUS BASE DATE

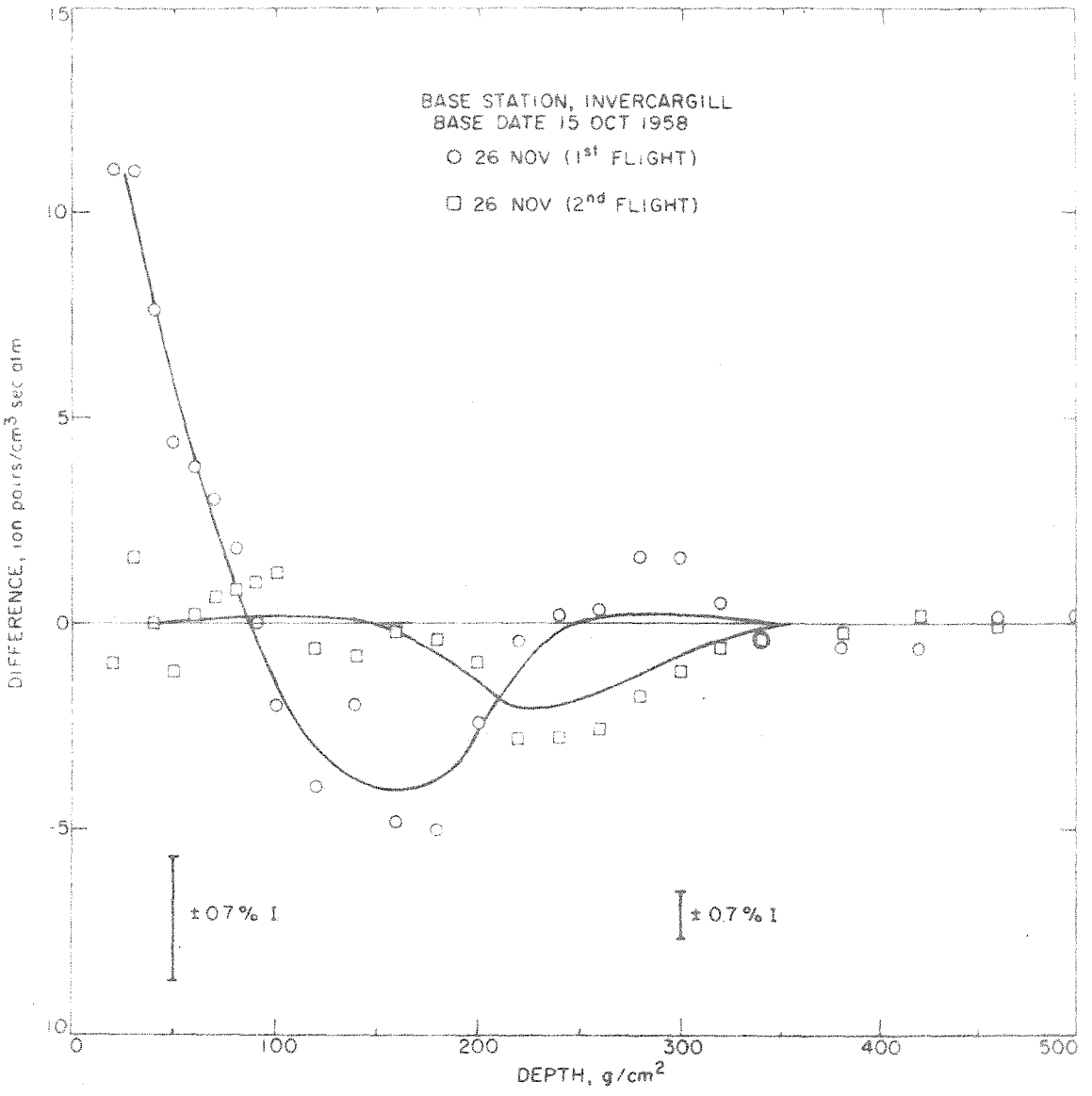

FIG 9f IONIZATION DIFFERENCE AT INVERCAGILL, DATE GIVEN MINUS BASE DATE

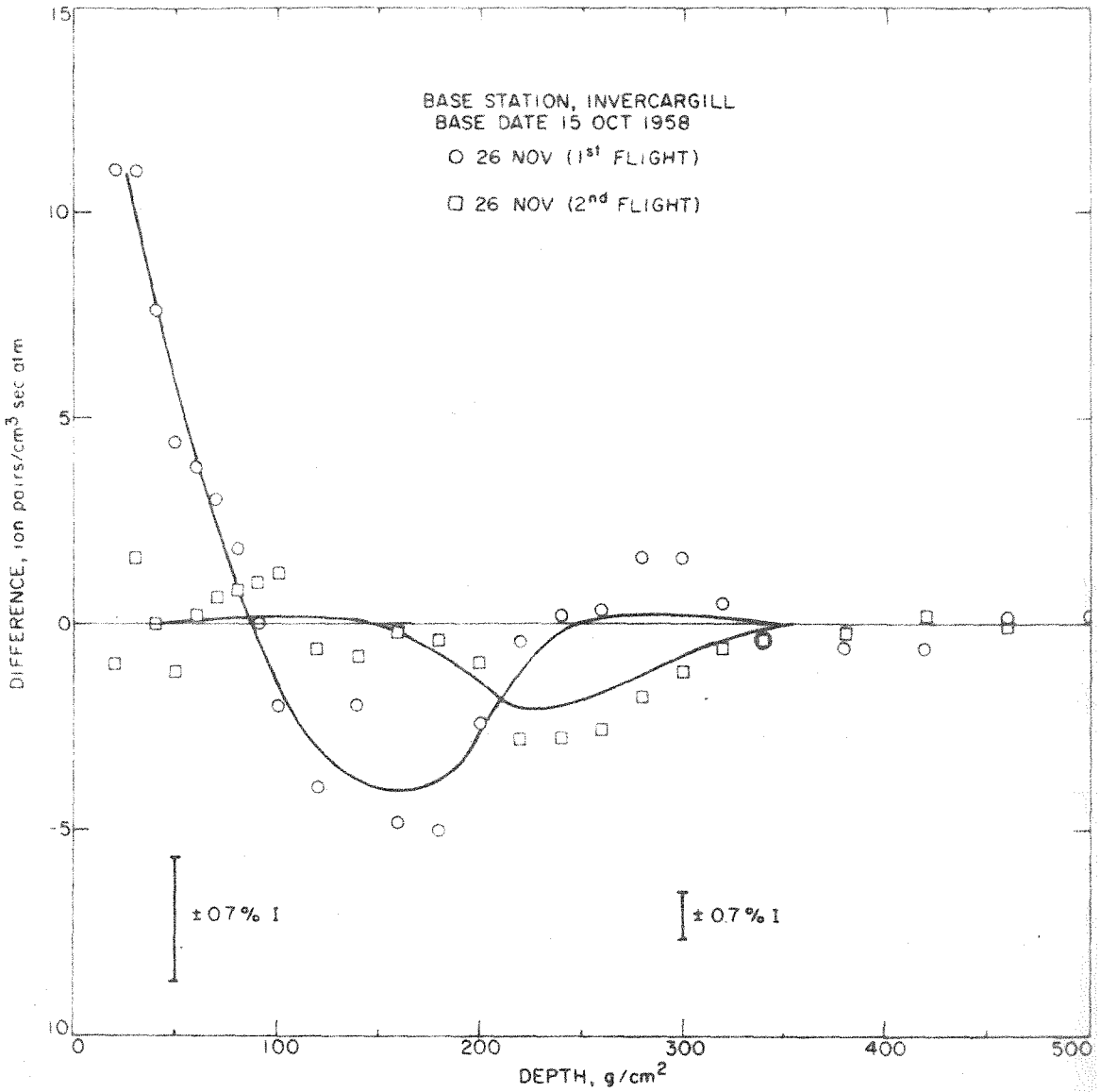

FIG 9f IONIZATION DIFFERENCE AT INVERCAGILL, DATE GIVEN MINUS BASE DATE

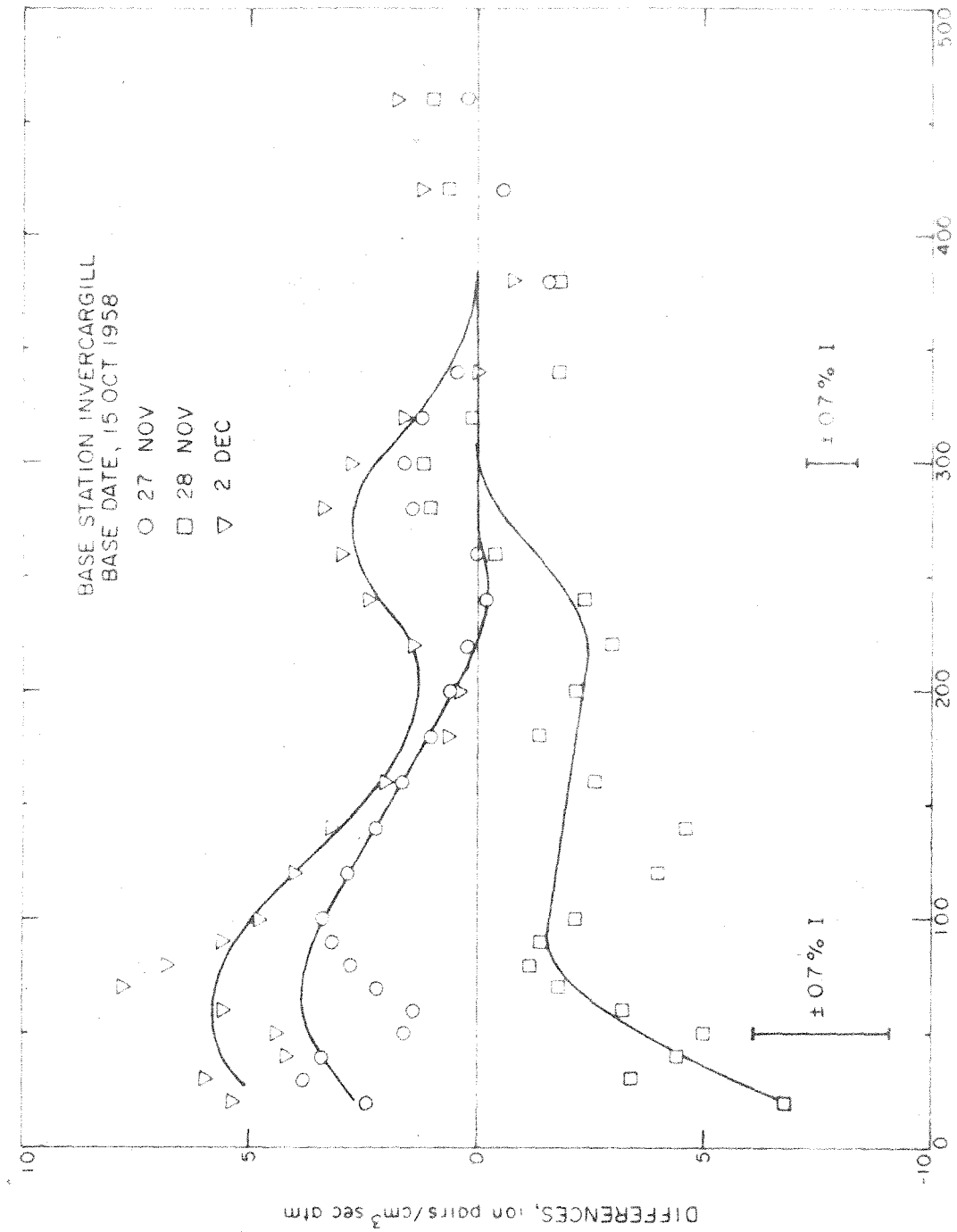

FIG 9g IONIZATION DIFFERENCE AT INVERCARGILL, DATE GIVEN MINUS BASE DATE

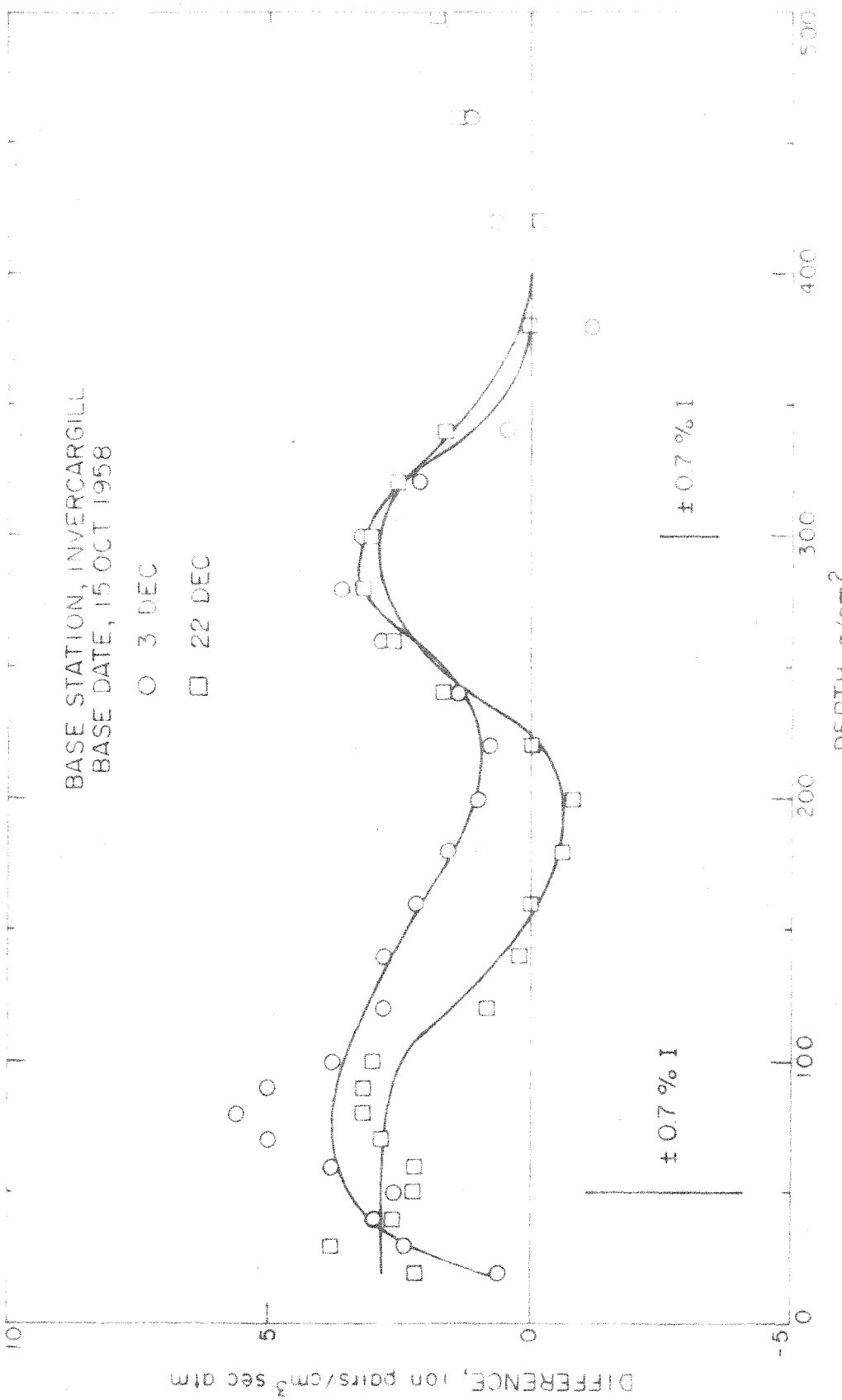

FIG 9h IONIZATION DIFFERENCE AT INVERCARGILL, DATE GIVEN MINUS BASE DATE

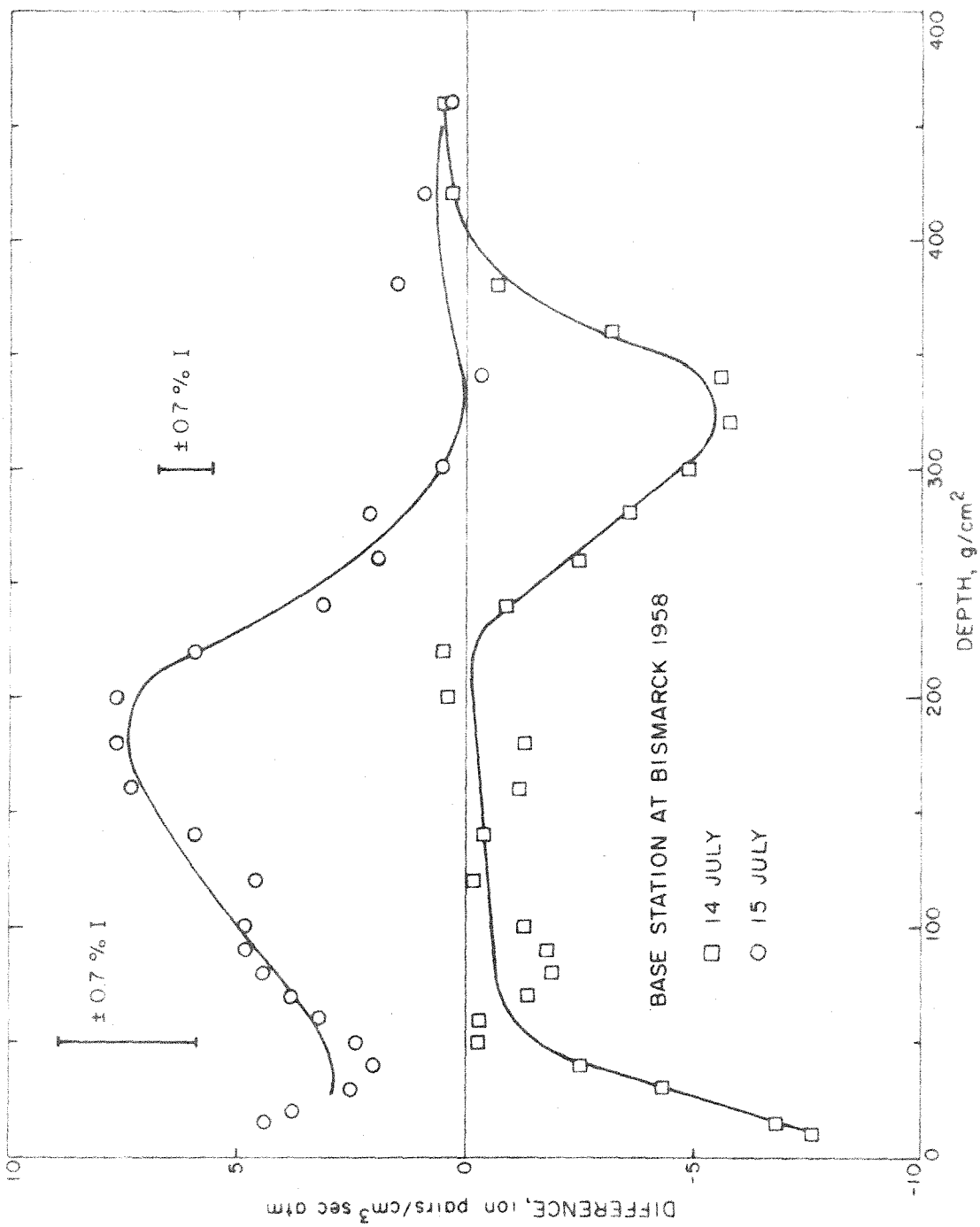

FIG 10a IONIZATION DIFFERENCE ROVING STATION MINUS BASE STATION AT SAME TIME

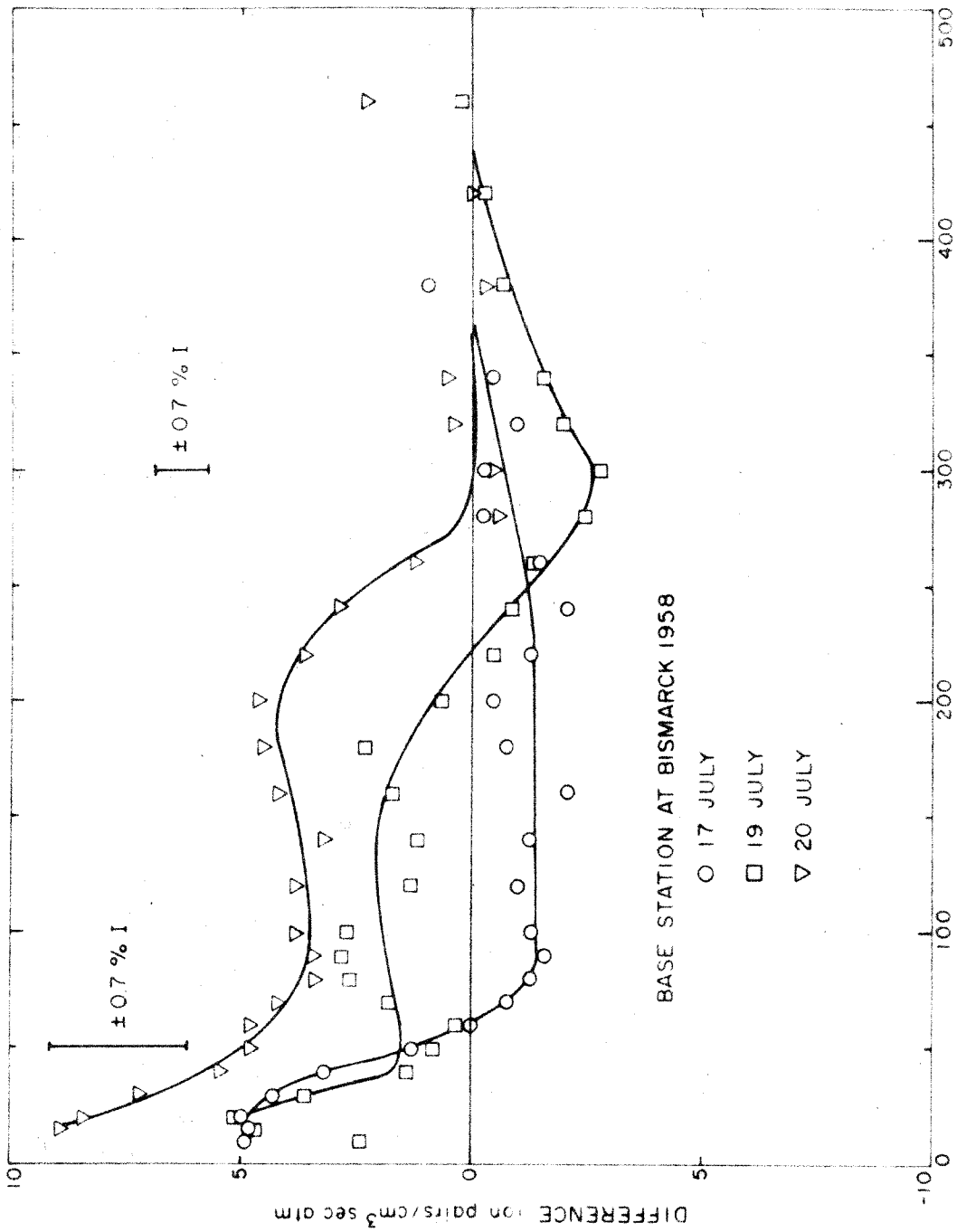

FIG 10a (cont) IONIZATION DIFFERENCES, ROVING STATION MINUS BASE STATION AT SAME TIME

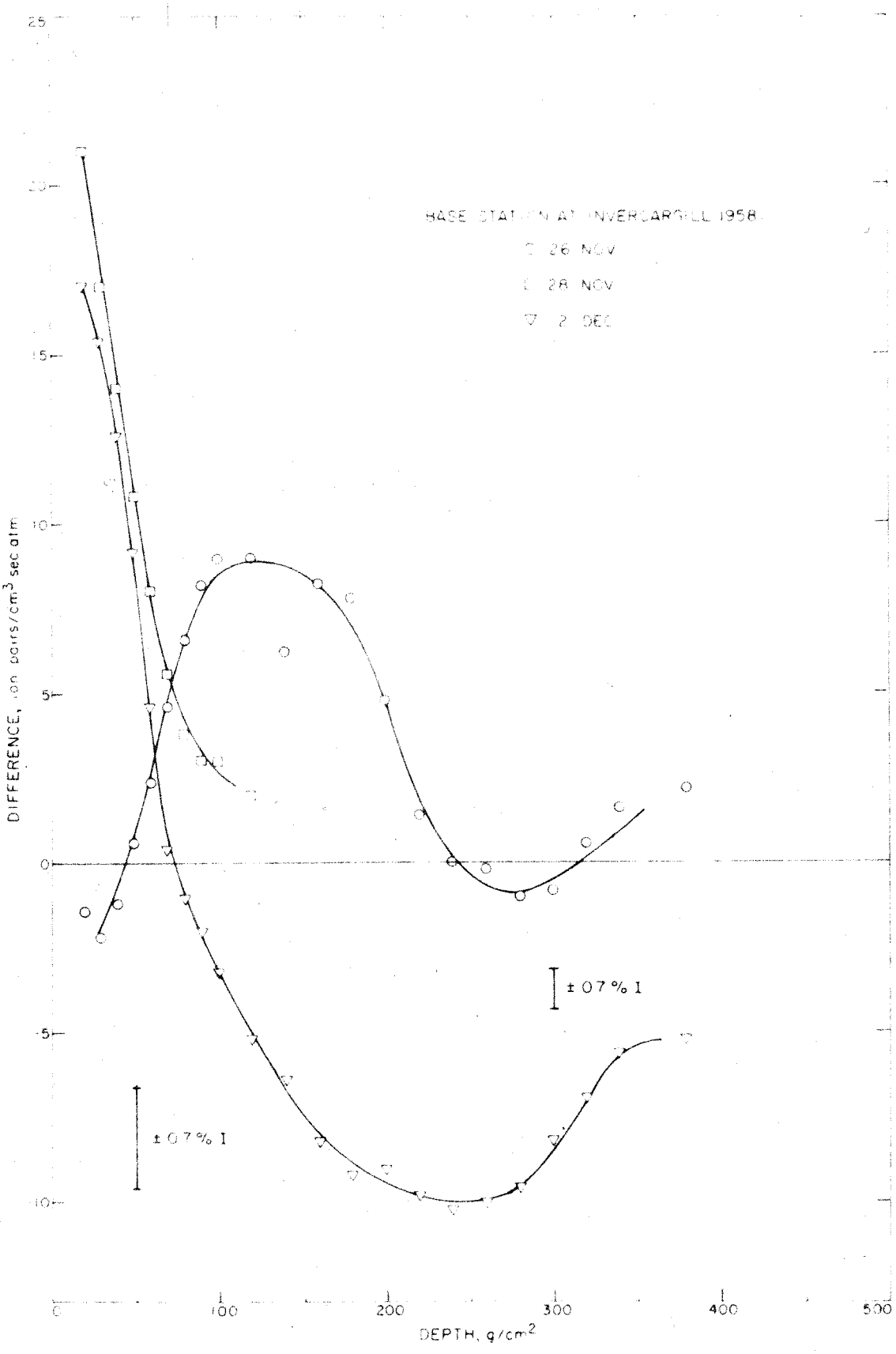

FIG 10b IONIZATION DIFFERENCE, ROVING STATION MINUS BASE STATION AT SAME TIME

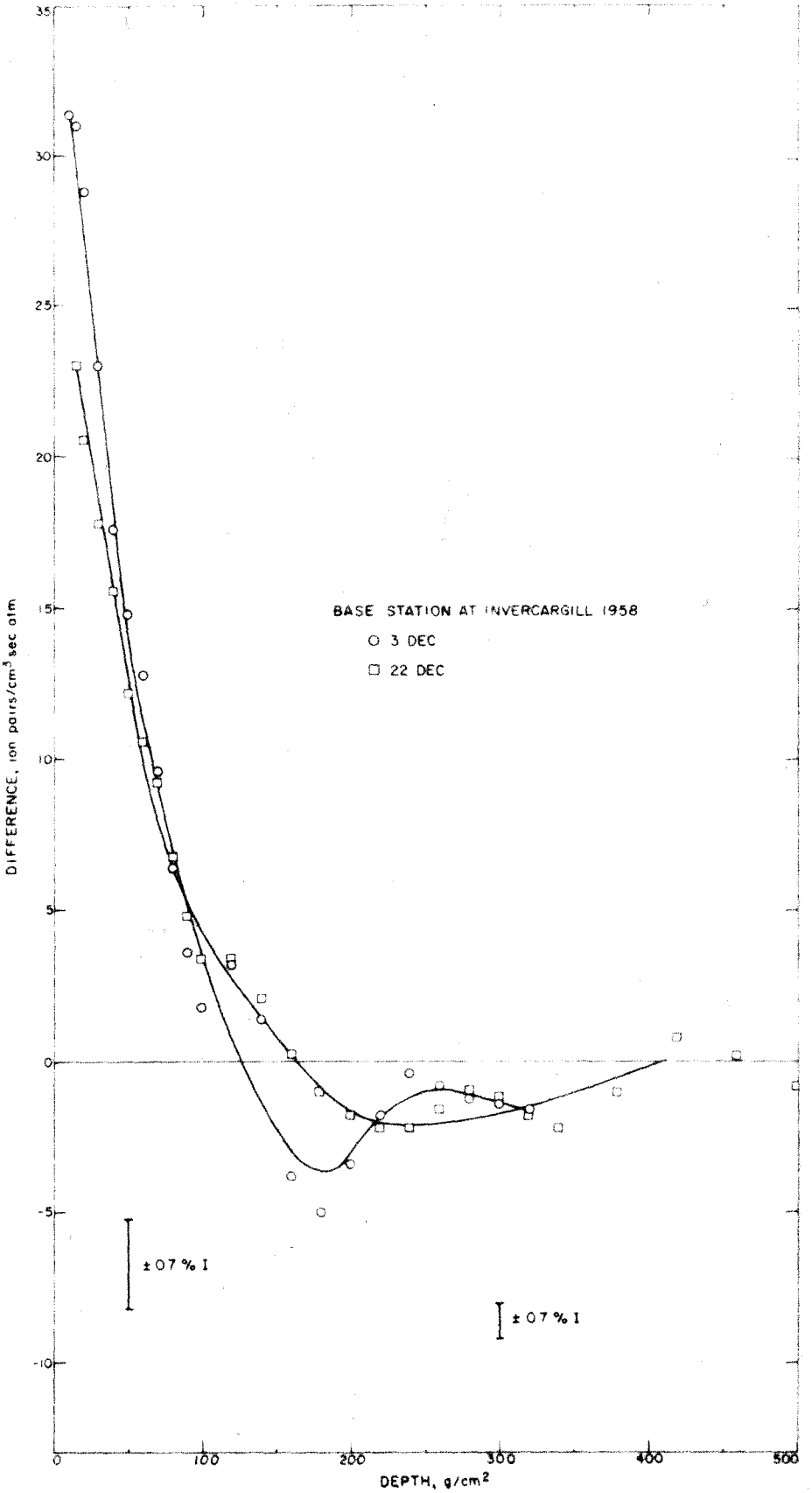

FIG 10b (cont) IONIZATION DIFFERENCE, ROVING STATION MINUS BASE STATION AT SAME TIME

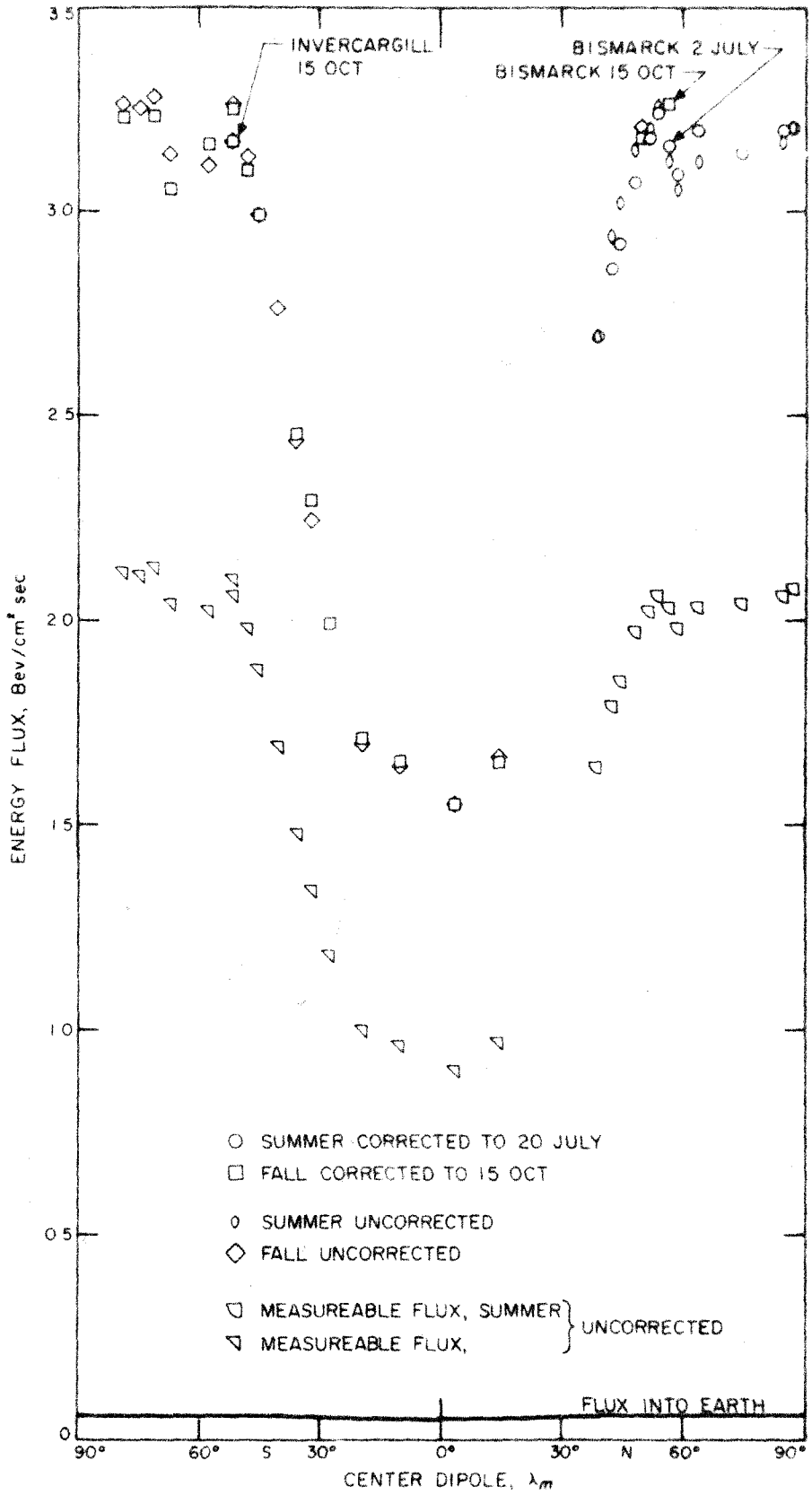

FIG 11a ENERGY FLUXES vs GEOMAGNETIC LATITUDE

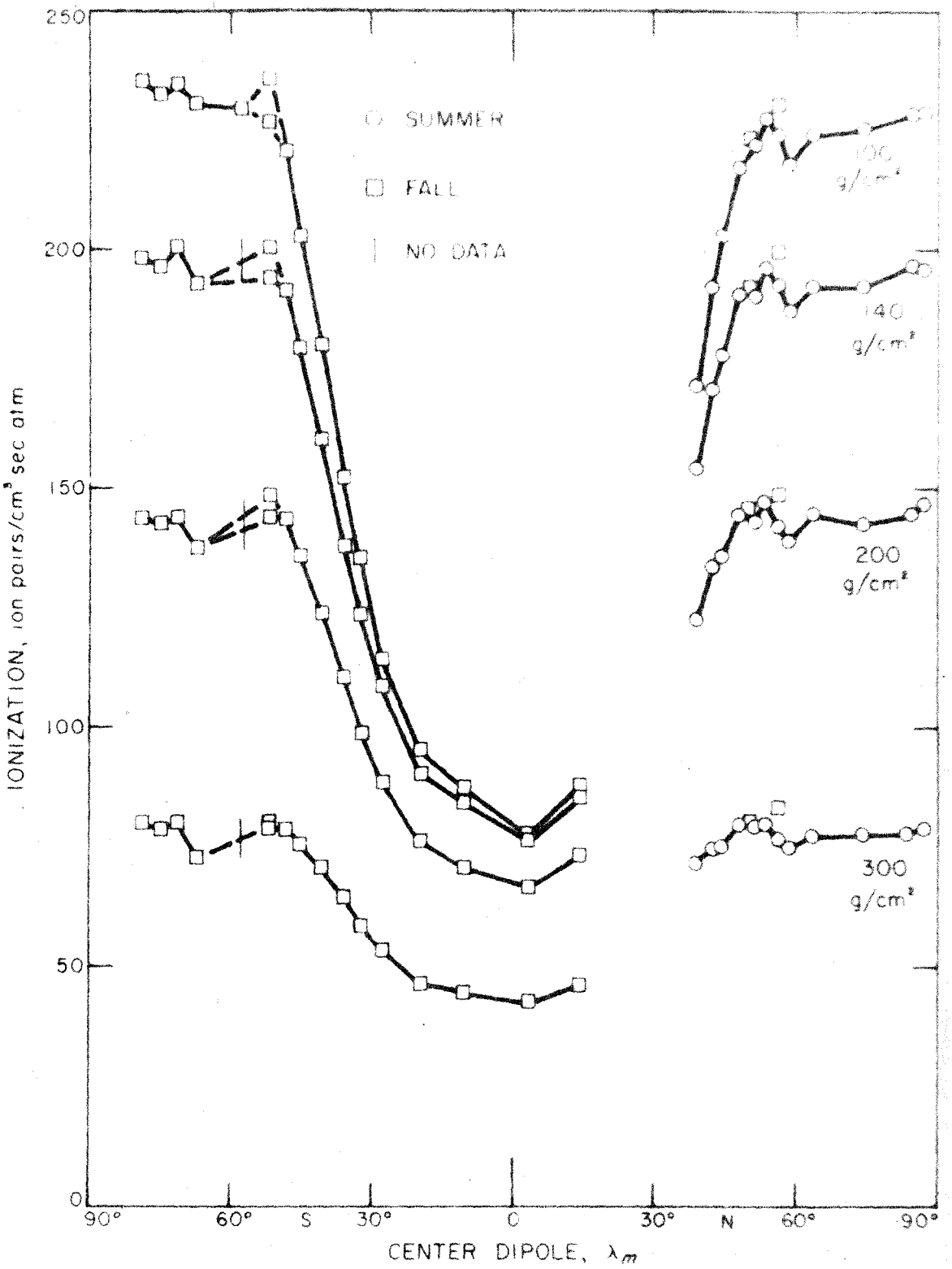

FIG. 11b OBSERVED IONIZATION vs
CENTER DIPOLE GEOMAGNETIC LATITUDE

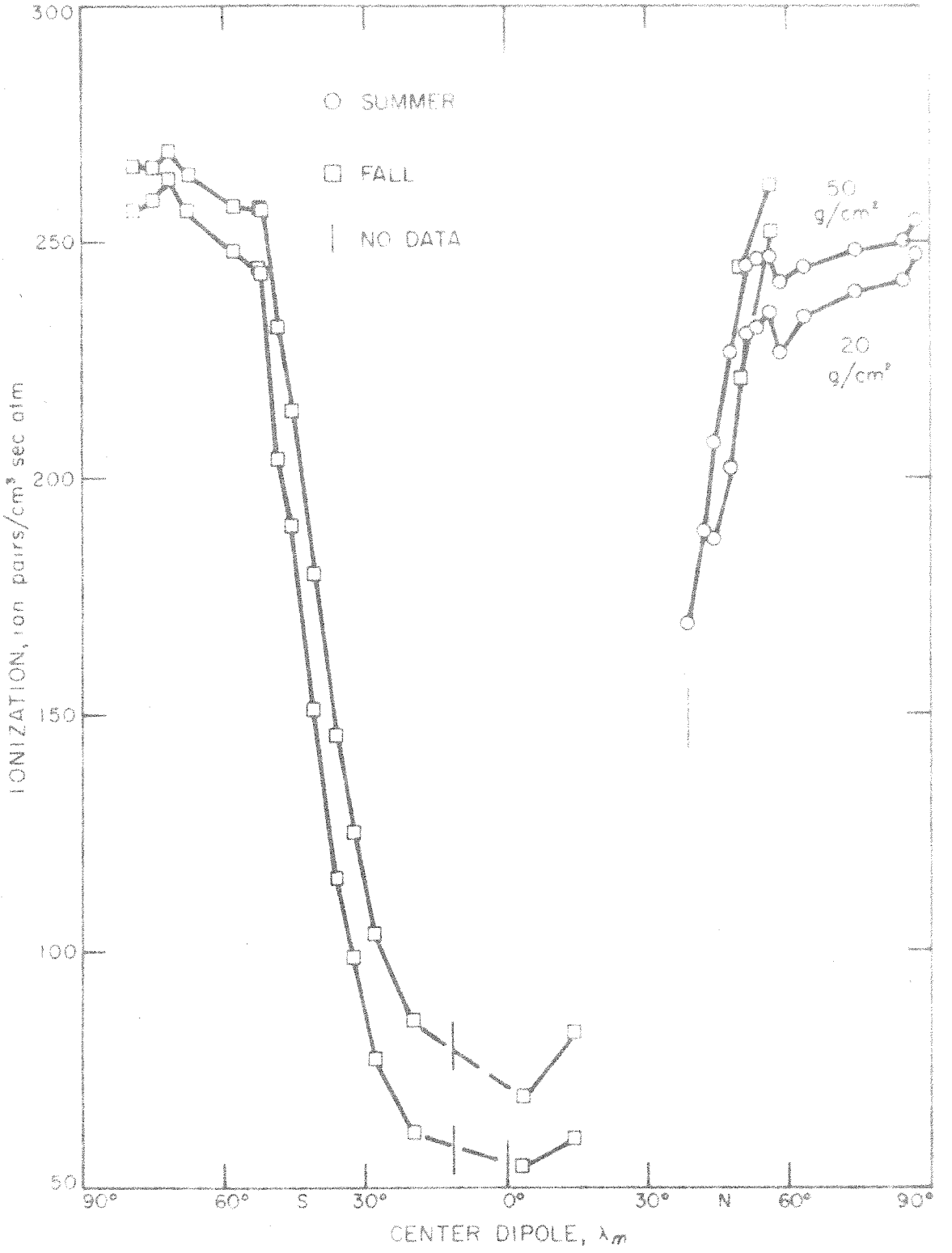

FIG. 11b (Cont'd) OBSERVED IONIZATION vs CENTER DIPOLE GEOMAGNETIC LATITUDE

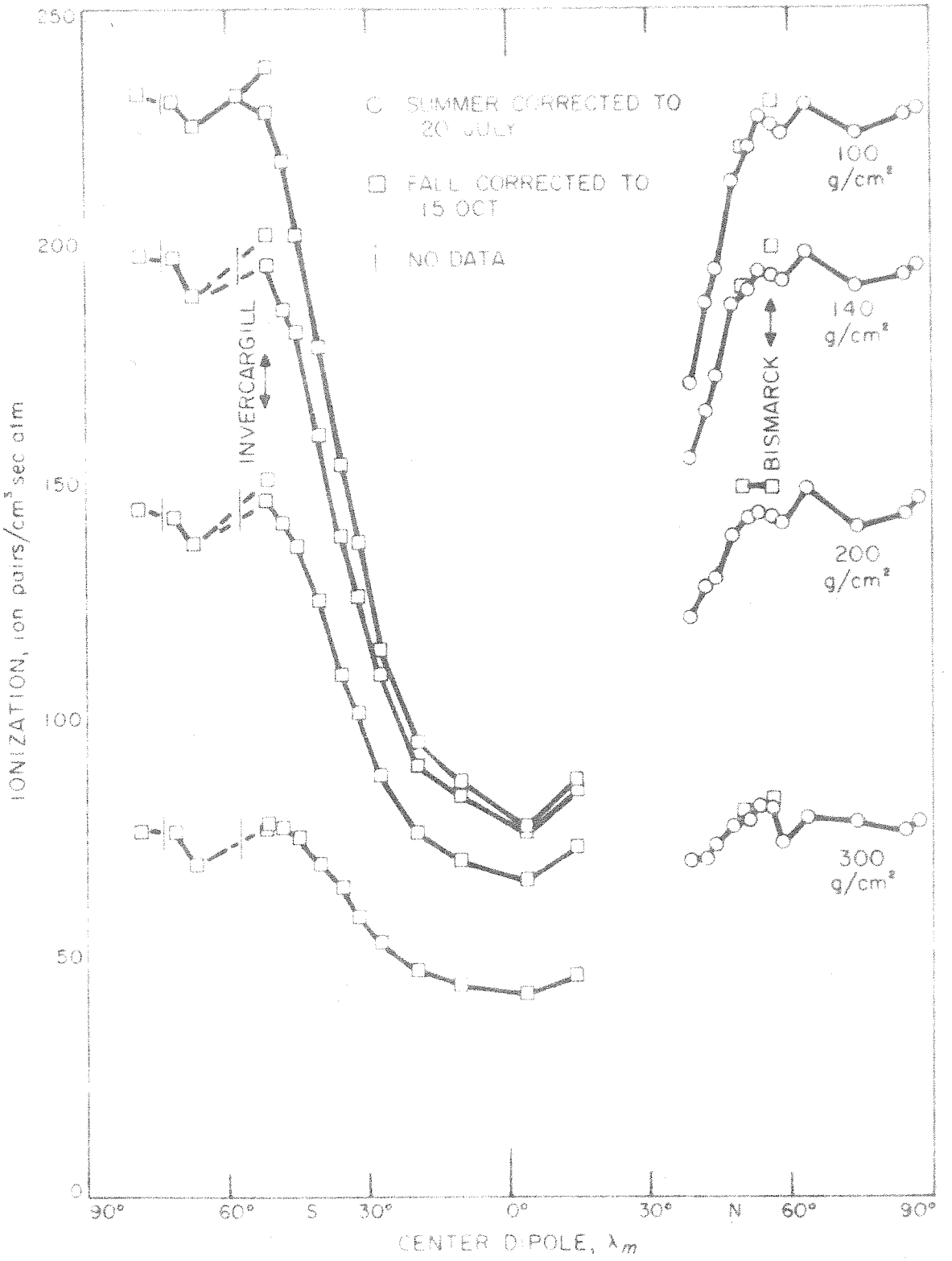

FIG. IIc CORRECTED IONIZATION vs CENTER DIPOLE GEOMAGNETIC LATITUDE

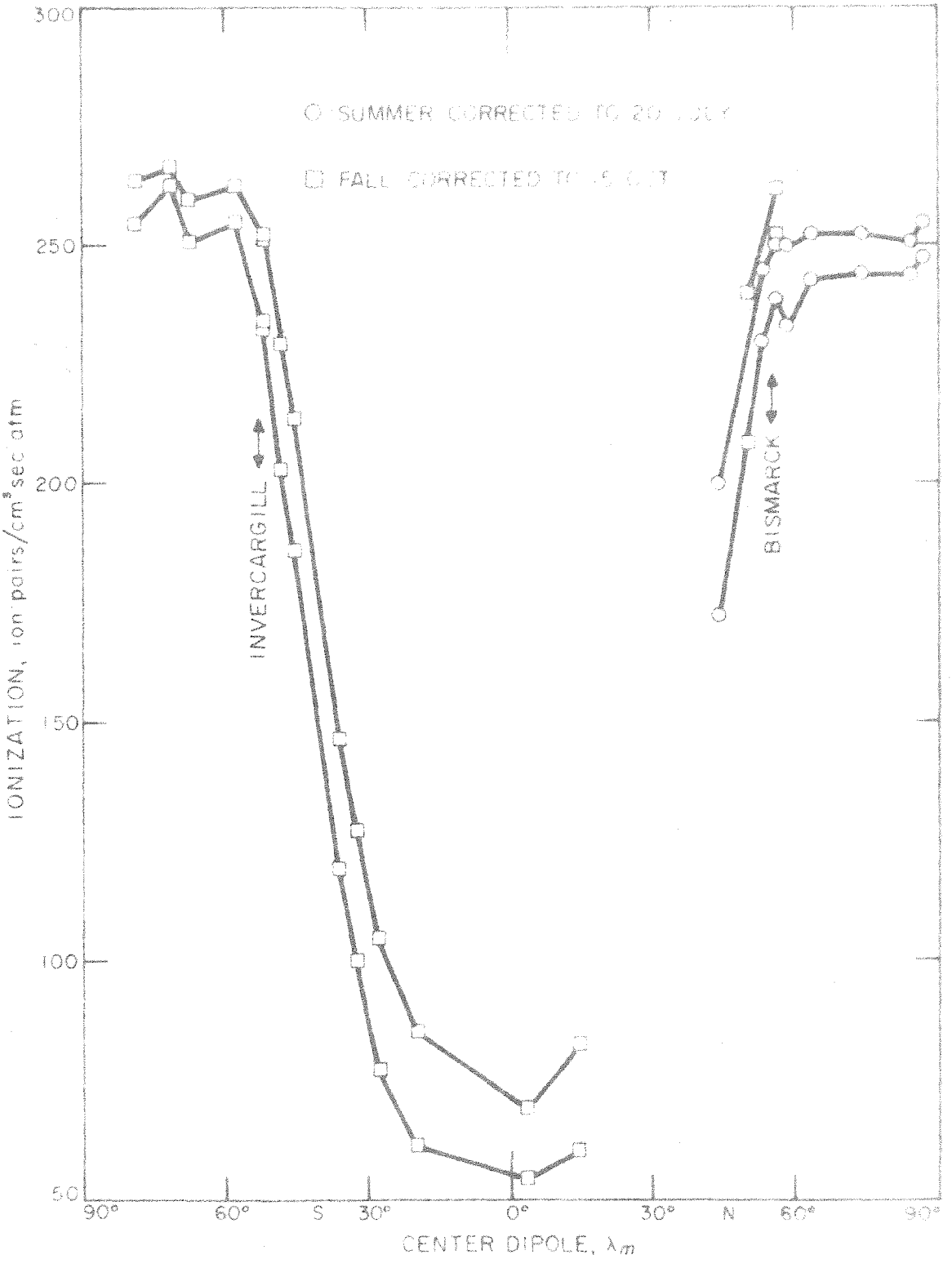

FIG. IIc (Cont'd) CORRECTED IONIZATION vs CENTER DIPOLE GEOMAGNETIC LATITUDE

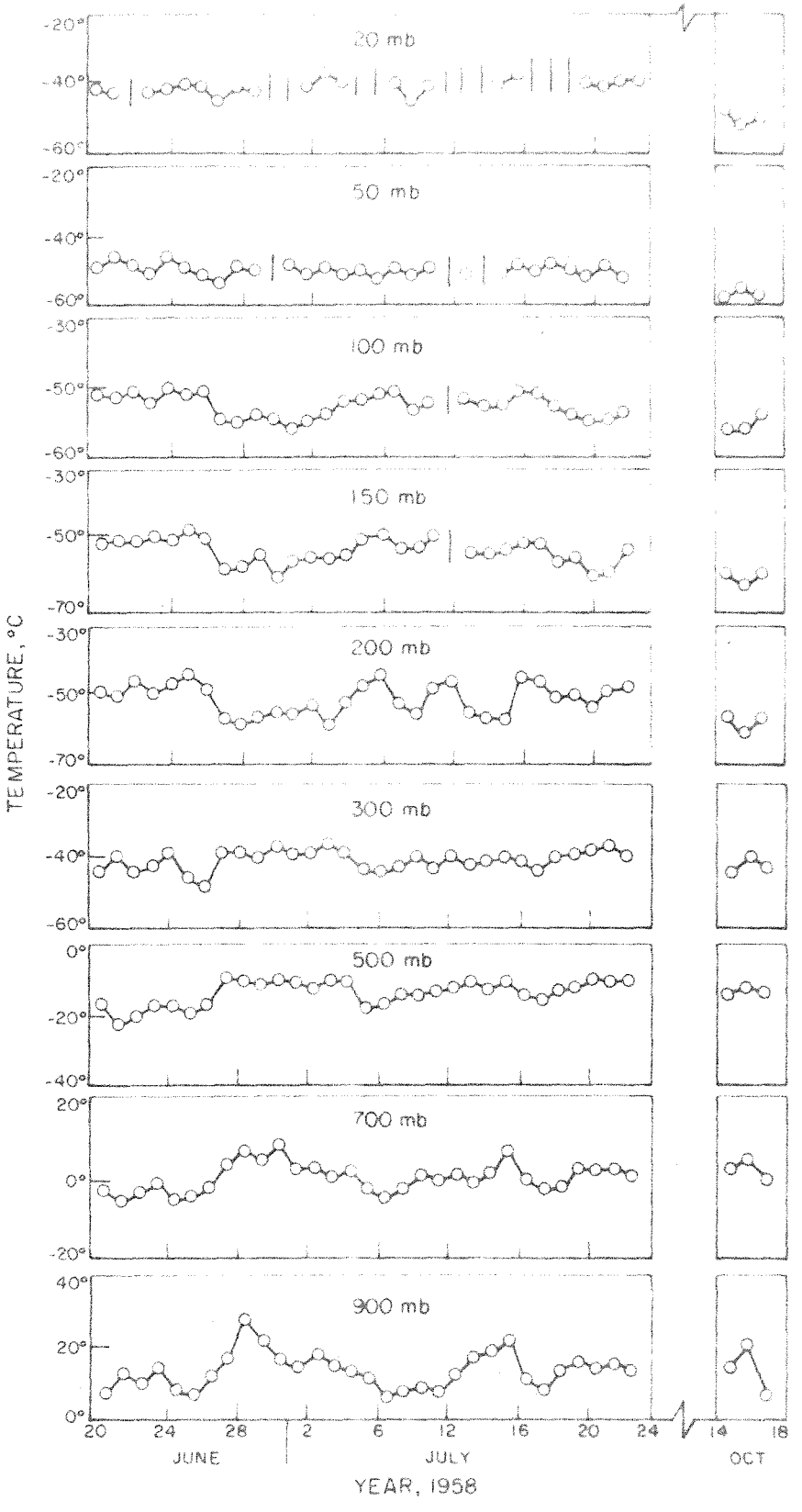

FIG. 12 TEMPERATURES AT CONSTANT PRESSURE AT BISMARCK, NO. DAKOTA FROM WBAN 33 CHARTS FOR 1200 GCT RELEASE

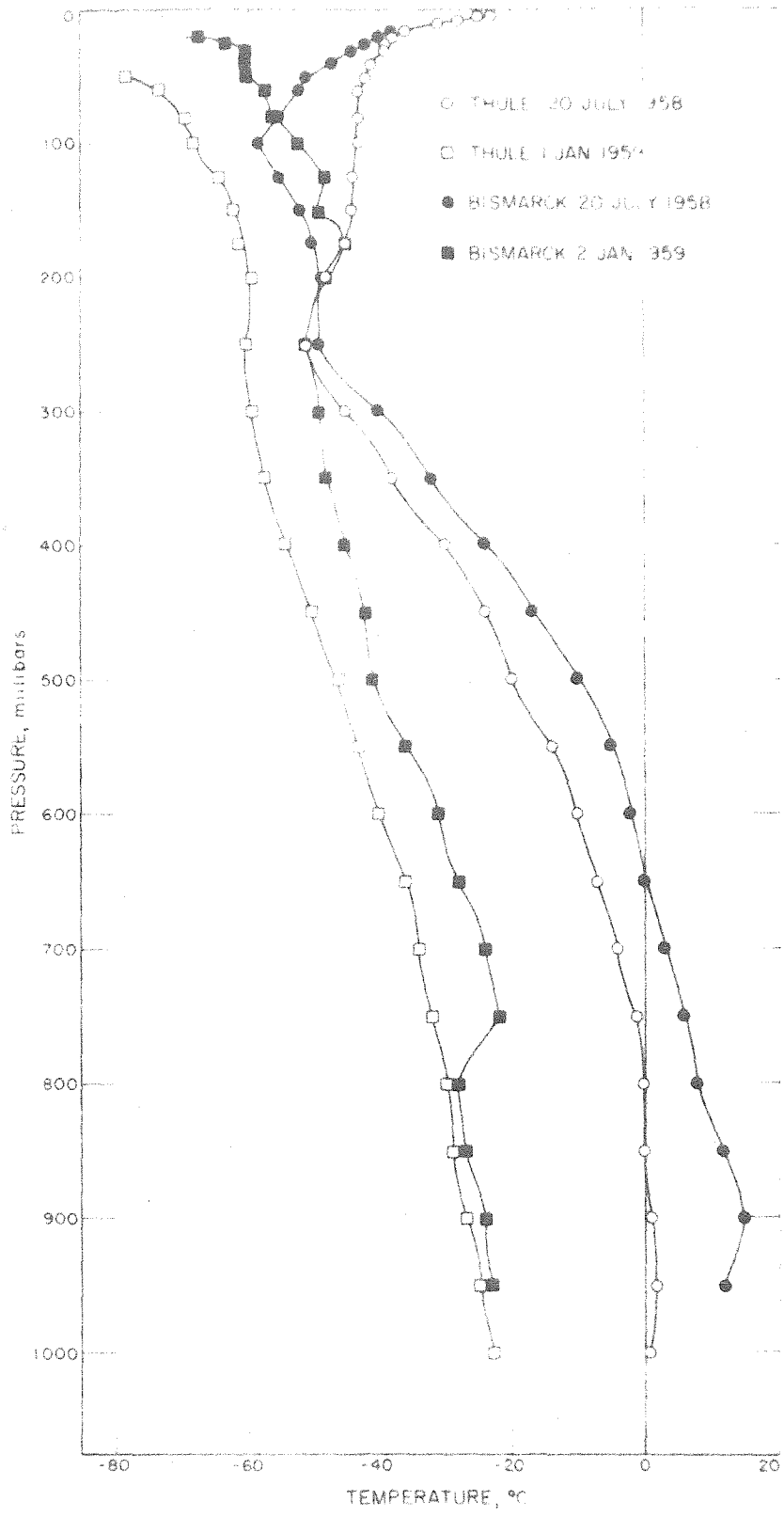

FIG 13 TEMPERATURE vs PRESSURE AT BISMARCK, NO. DAKOTA, AND THULE, GREENLAND, FROM 1200 GMT RELEASE

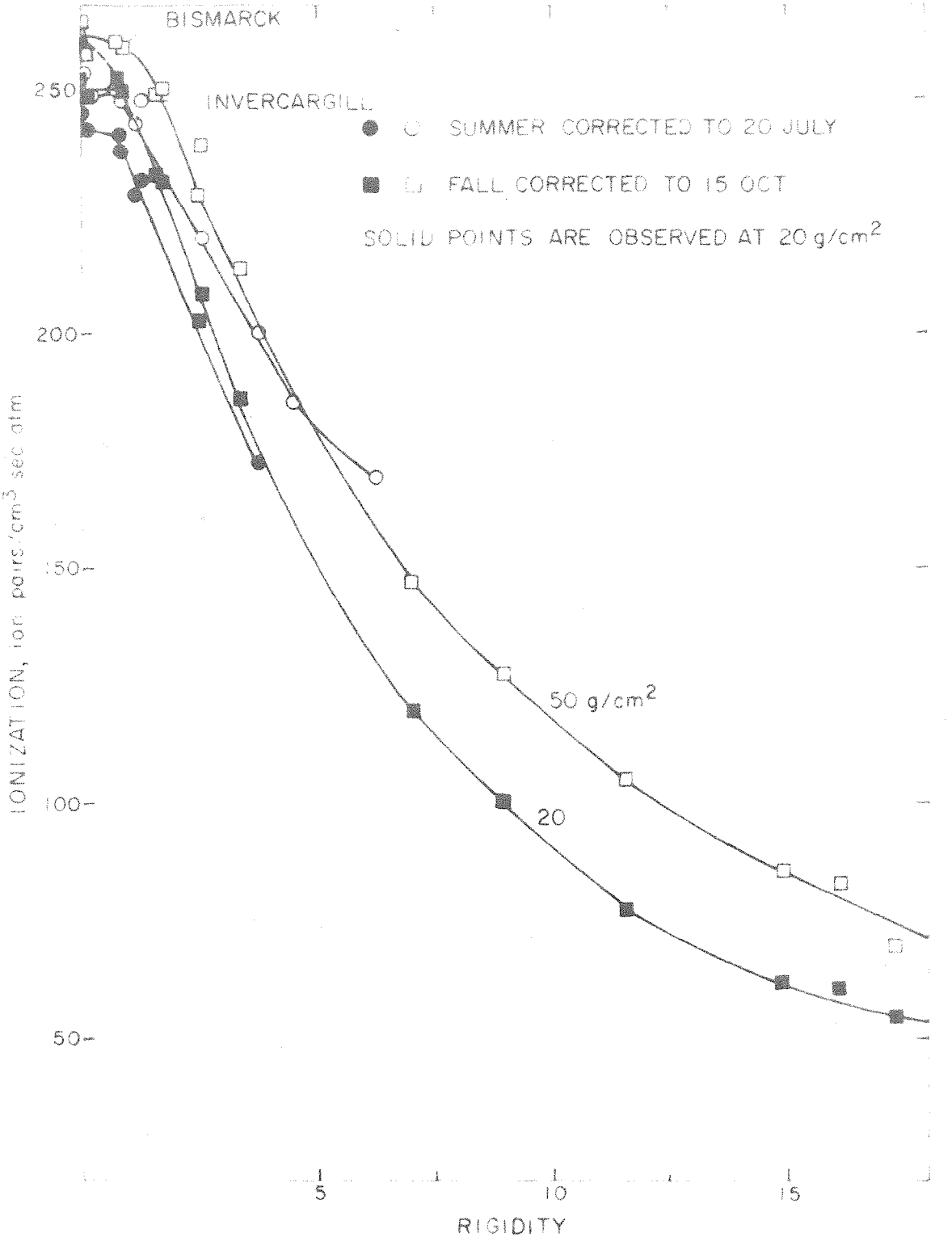

FIG 14a CORRECTED IONIZATION vs LOCAL FIELD CUTOFF

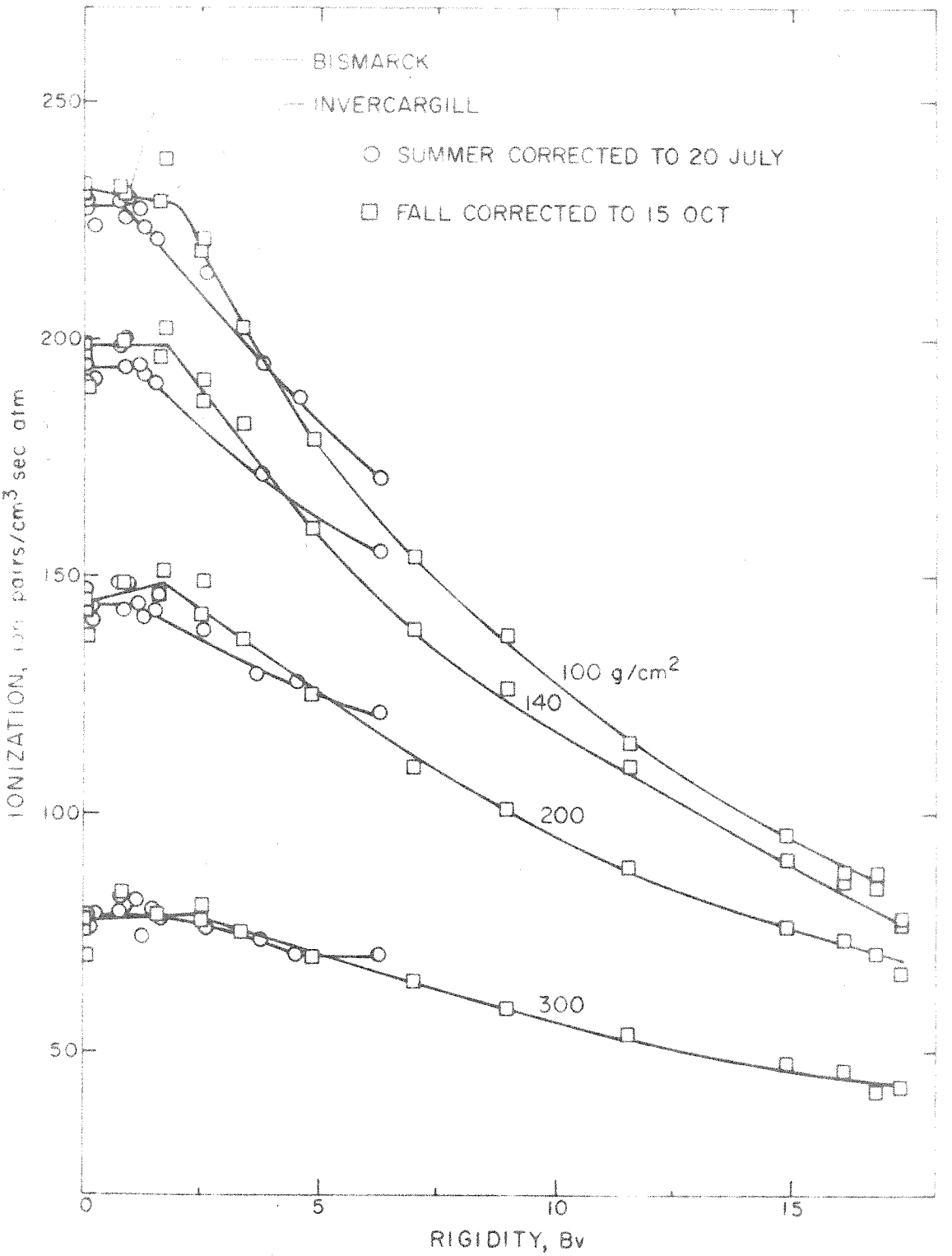

FIG 14b CORRECTED IONIZATION vs LOCAL FIELD CUTOFF

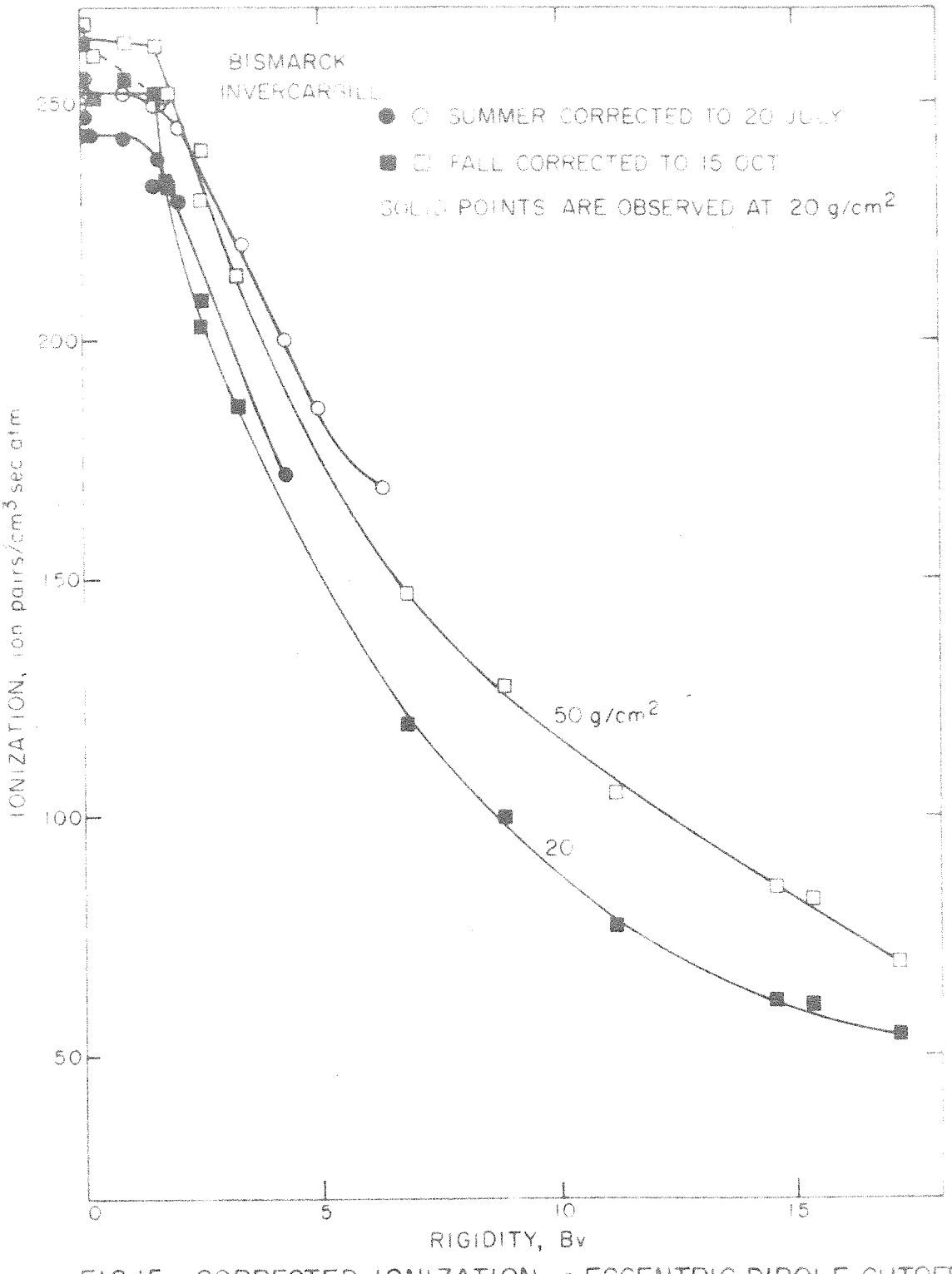

FIG 15a CORRECTED IONIZATION vs ECCENTRIC DIPOLE CUTOFF

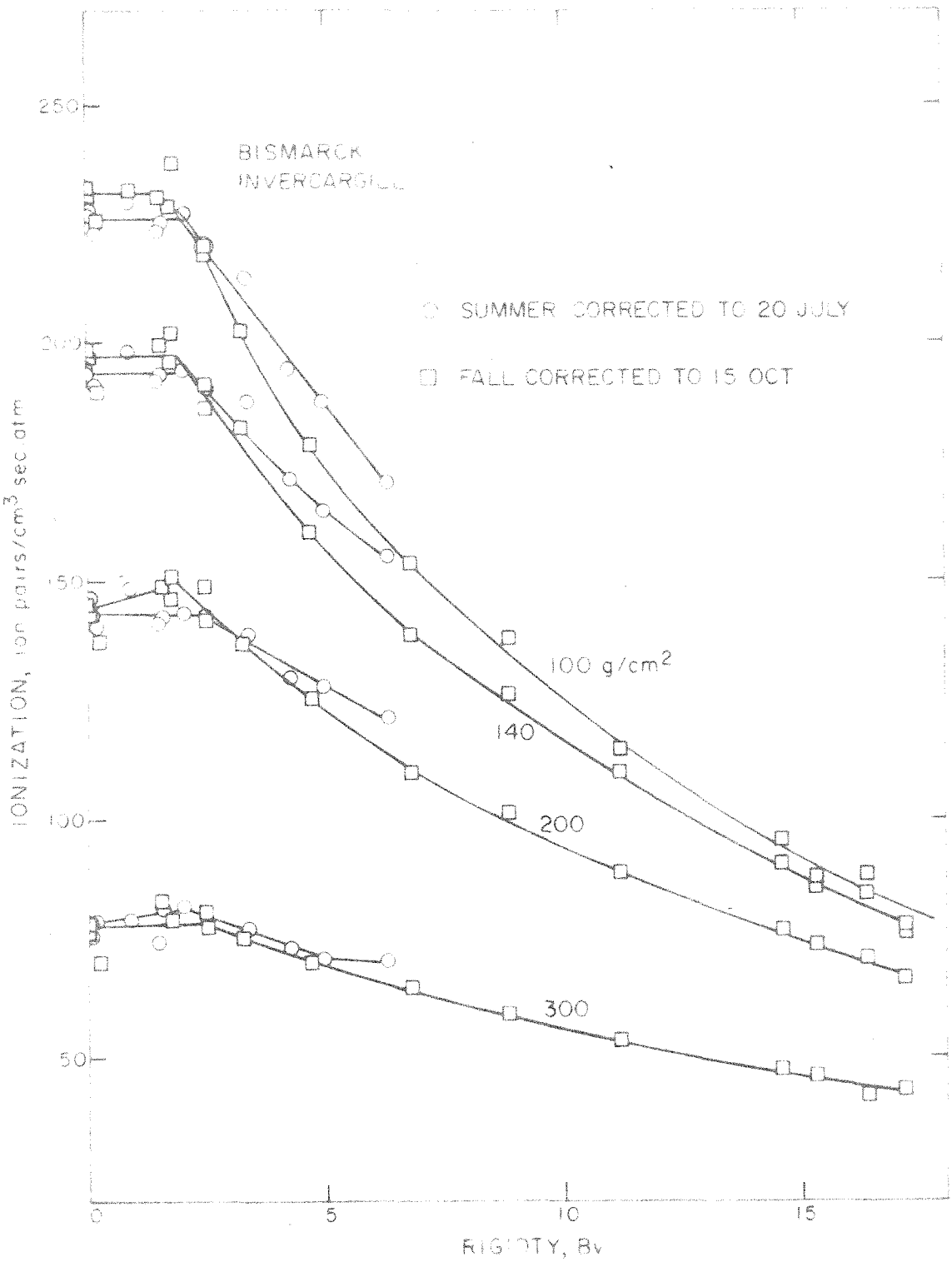

FIG 15b CORRECTED IONIZATION vs ECCENTRIC DIPOLE CUTOFF

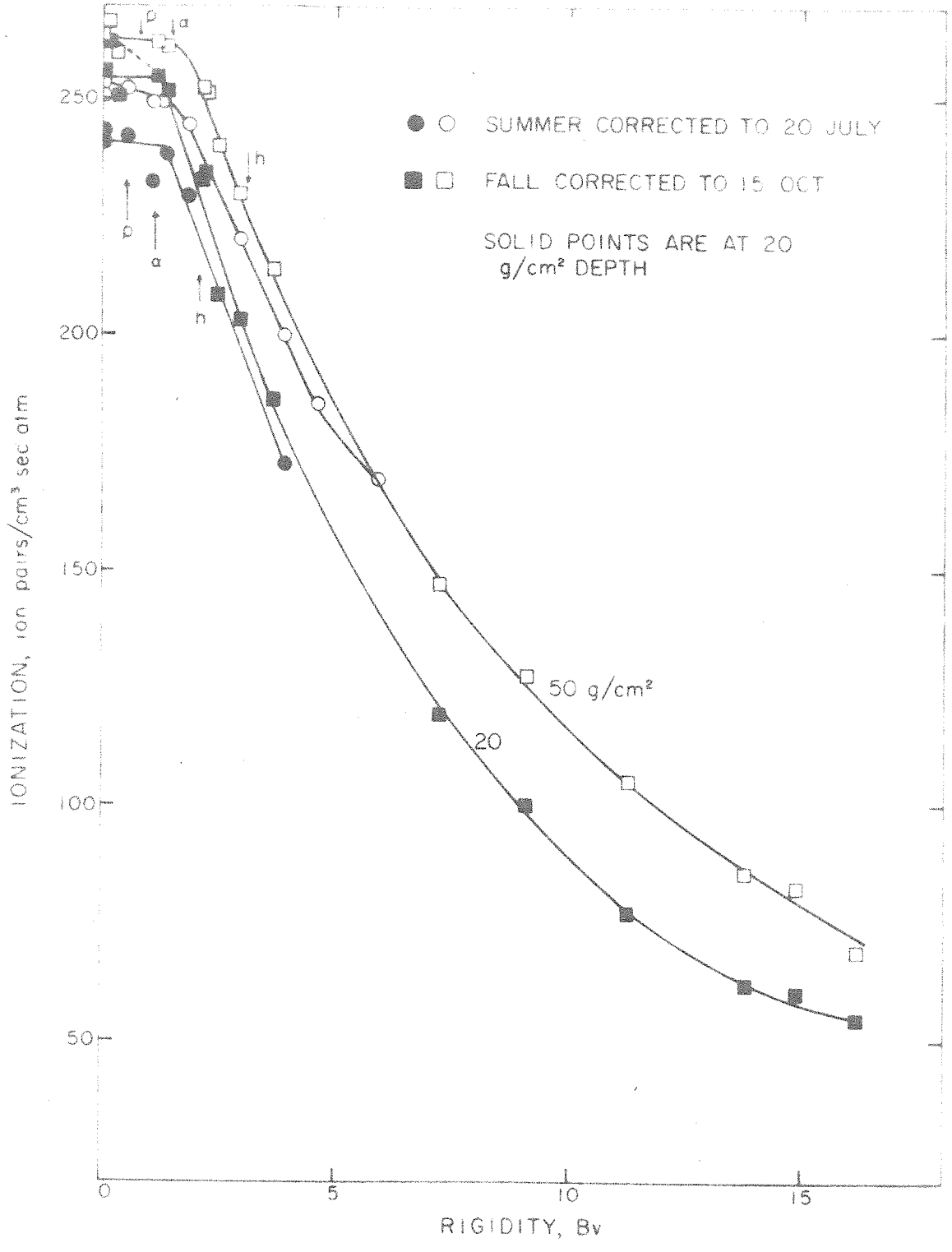

FIG. 16a CORRECTED IONIZATION vs CENTER DIPOLE R

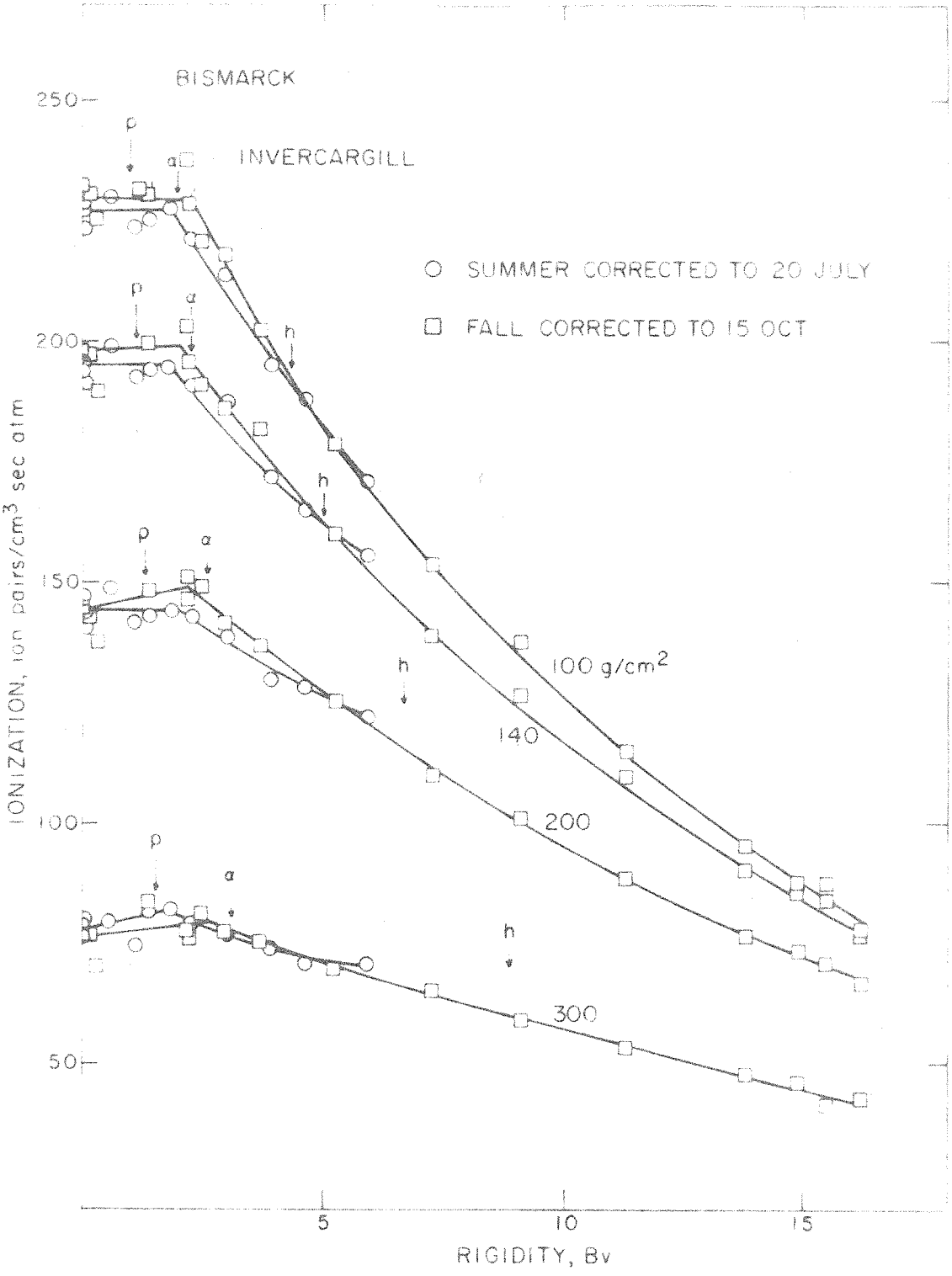

FIG 16b CORRECTED IONIZATION vs CENTER DIPOLE CUTOFF

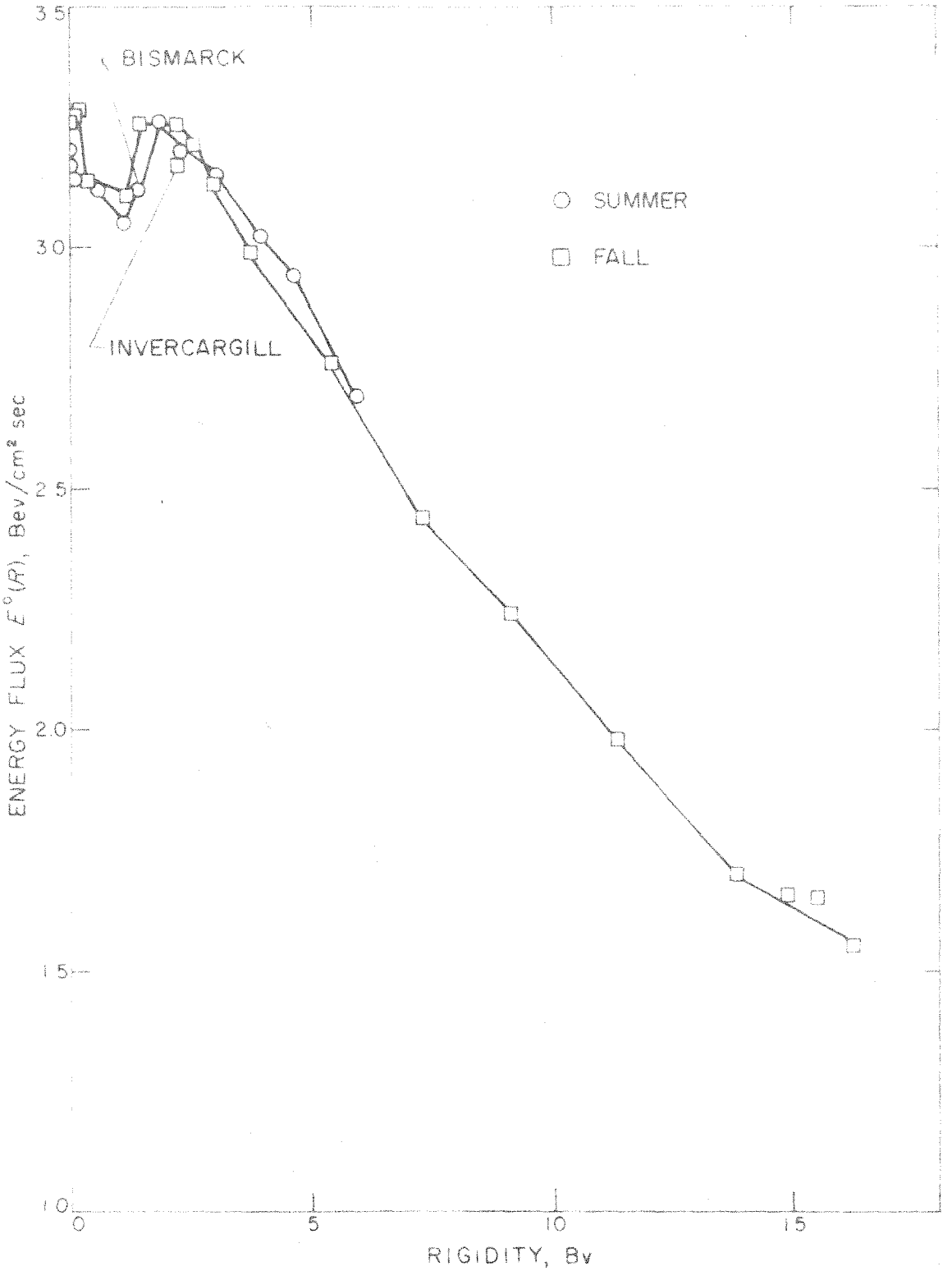

FIG 17 UNCORRECTED ENERGY FLUX vs CENTER DIPOLE R

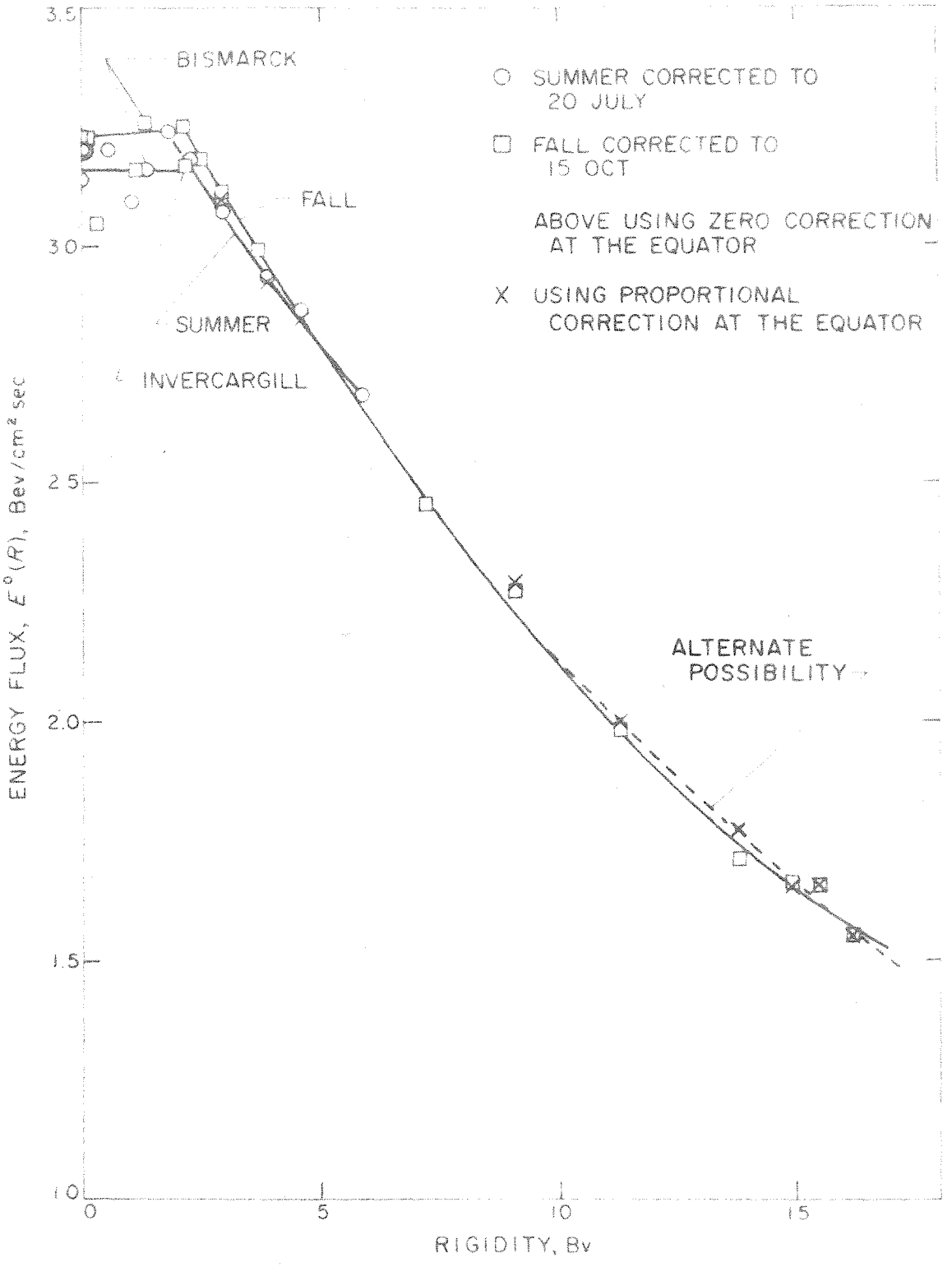

FIG. 18 CORRECTED ENERGY FLUX vs CENTER DIPOLE R

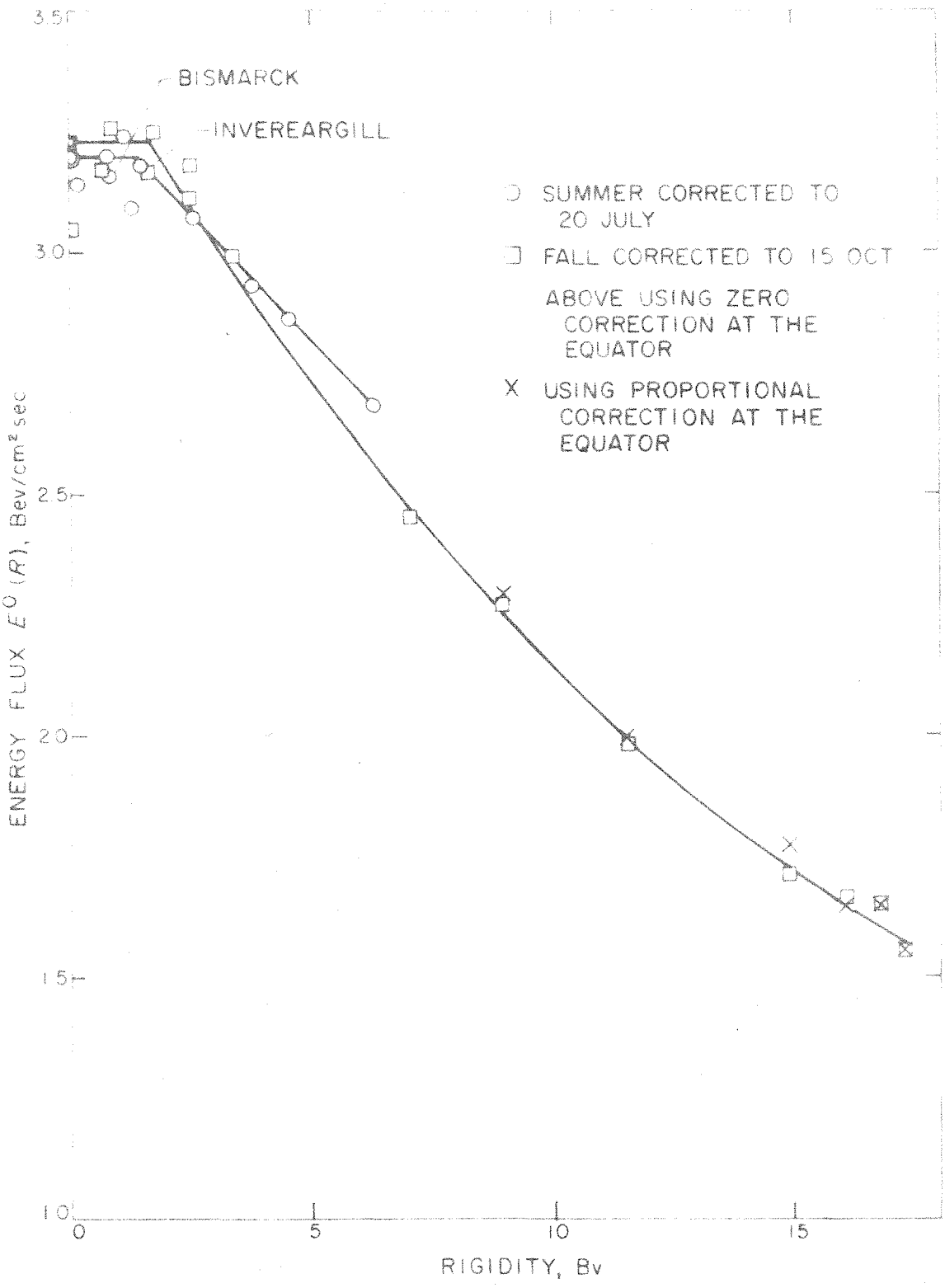

FIG. 19 CORRECTED ENERGY FLUX vs LOCAL FIELD R

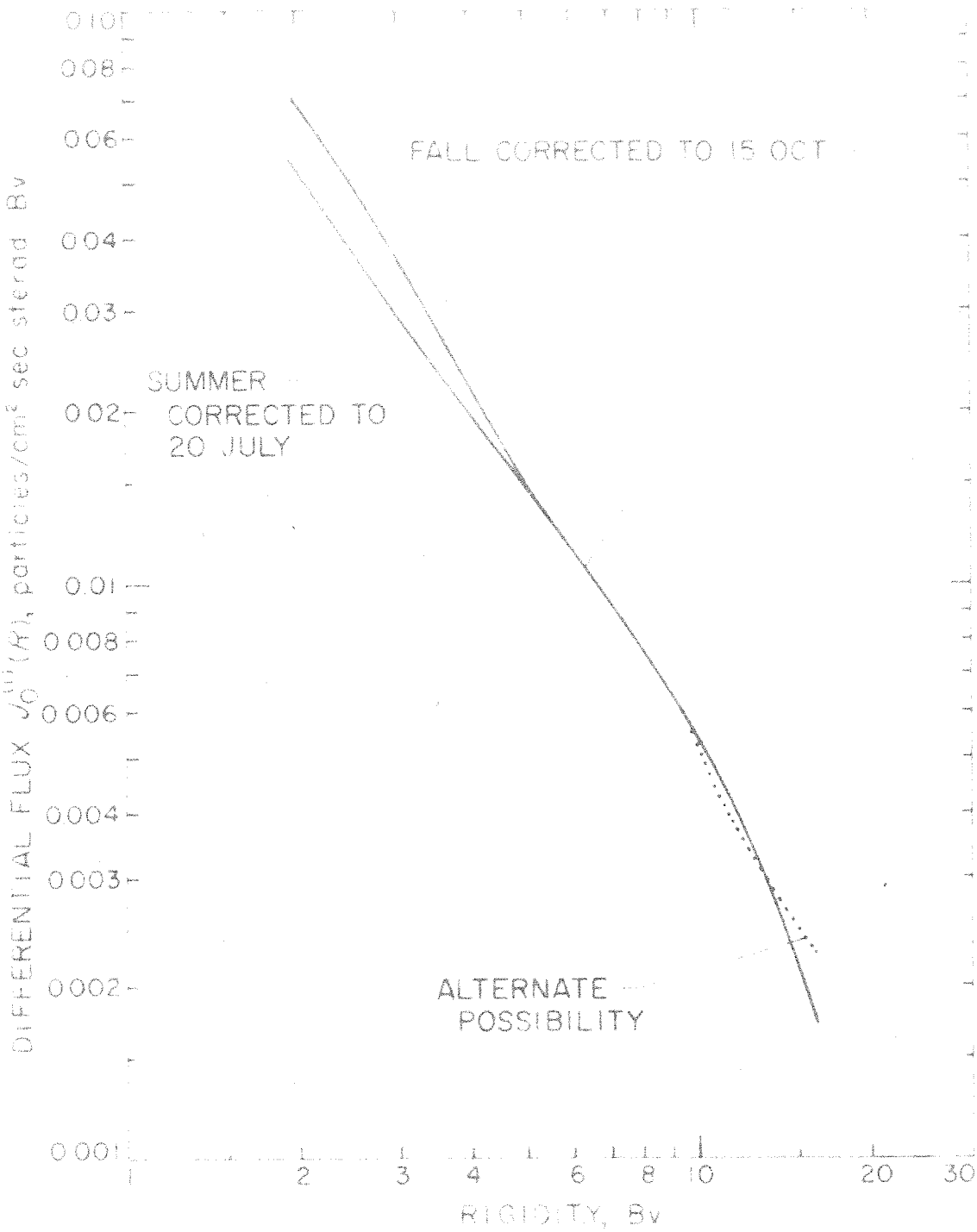

FIG 20 DIFFERENTIAL FLUX $J^{(1)}(R)$ vs RIGIDITY
CENTER DIPOLE R

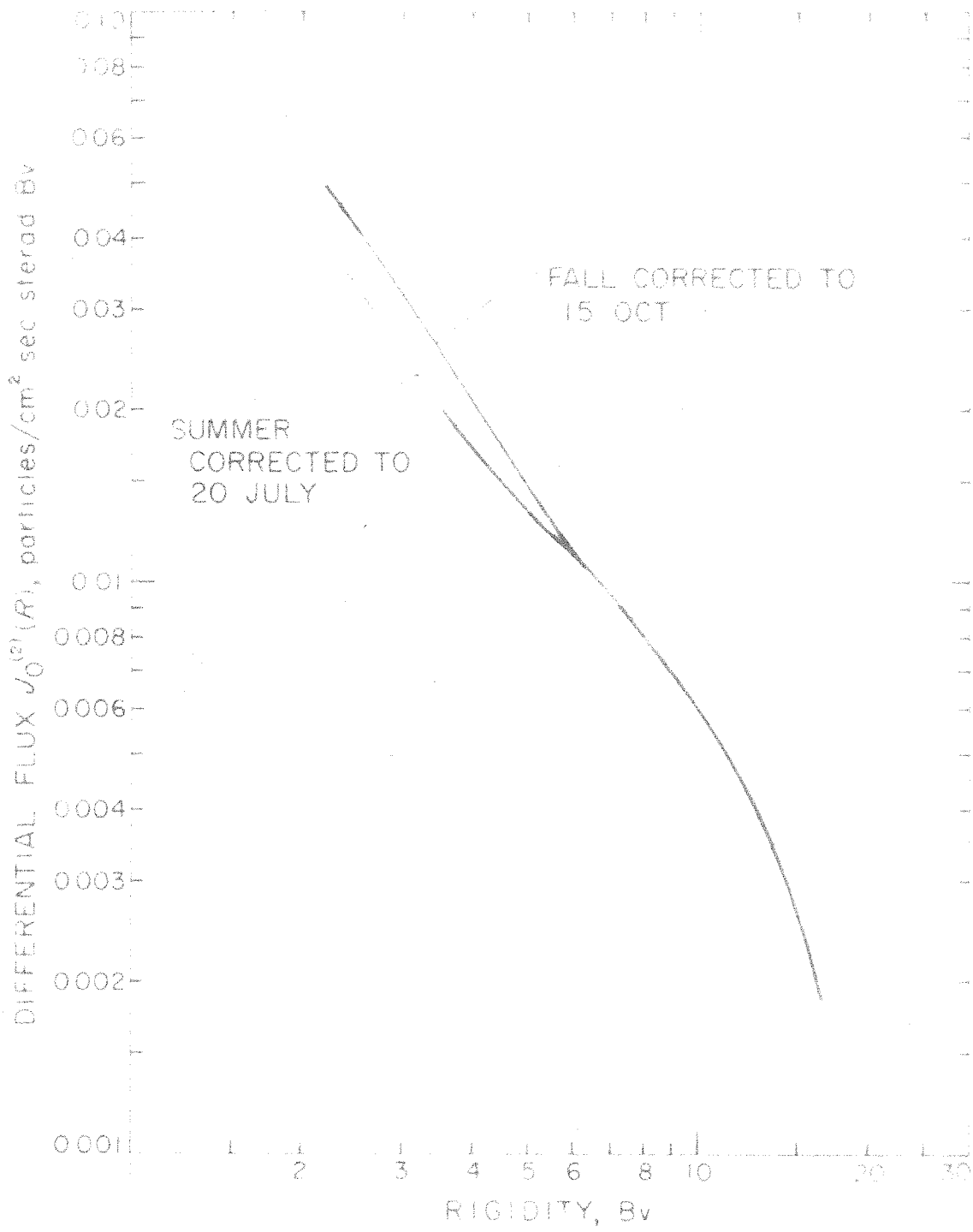

FIG. 21 DIFFERENTIAL FLUX $J_0^{(2)}(R)$ vs RIGIDITY, CENTER DIPOLE R

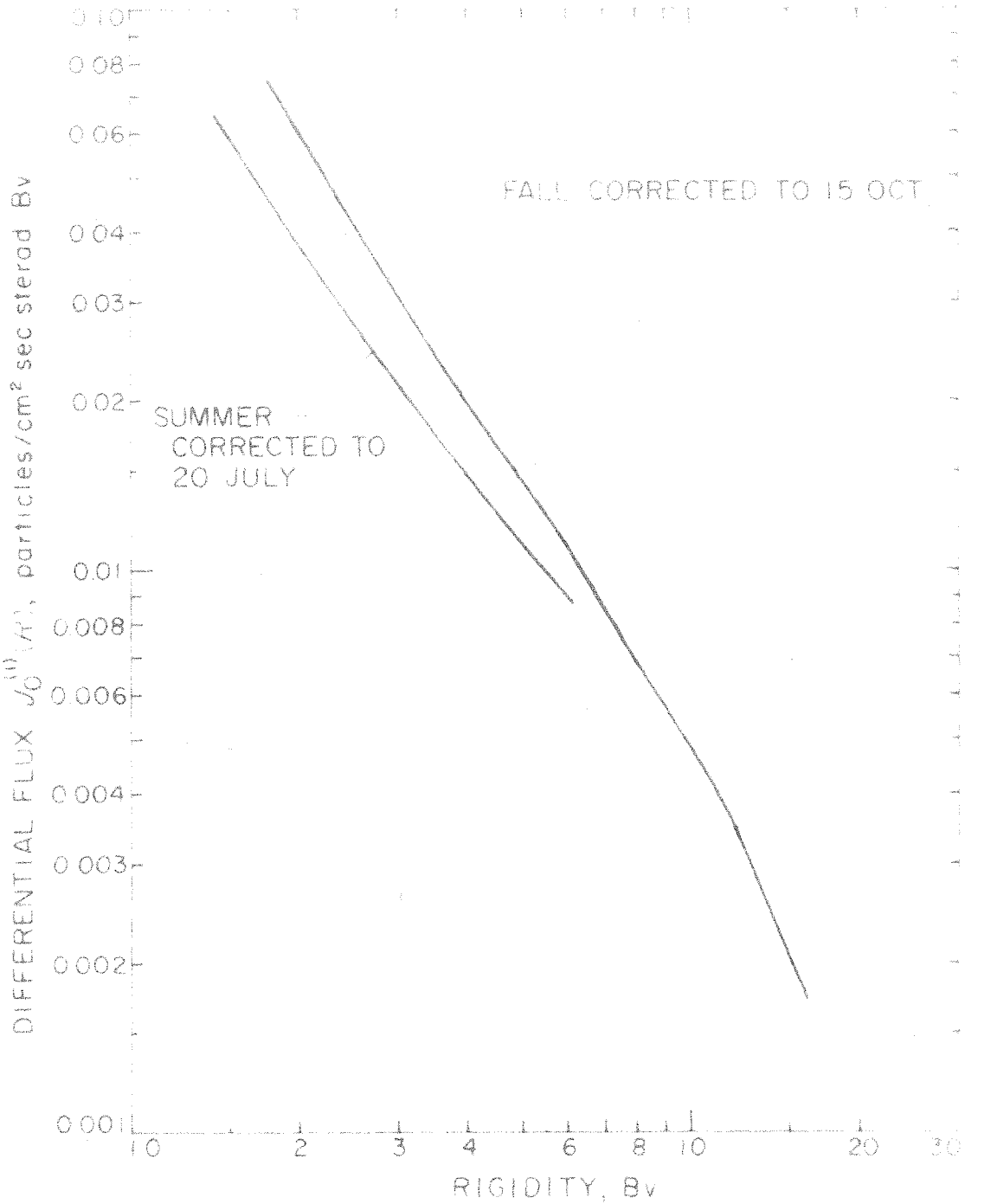

FIG. 22 DIFFERENTIAL FLUX $J_0^{(1)}(R)$ vs RIGIDITY, LOCAL FIELD DETERMINED R

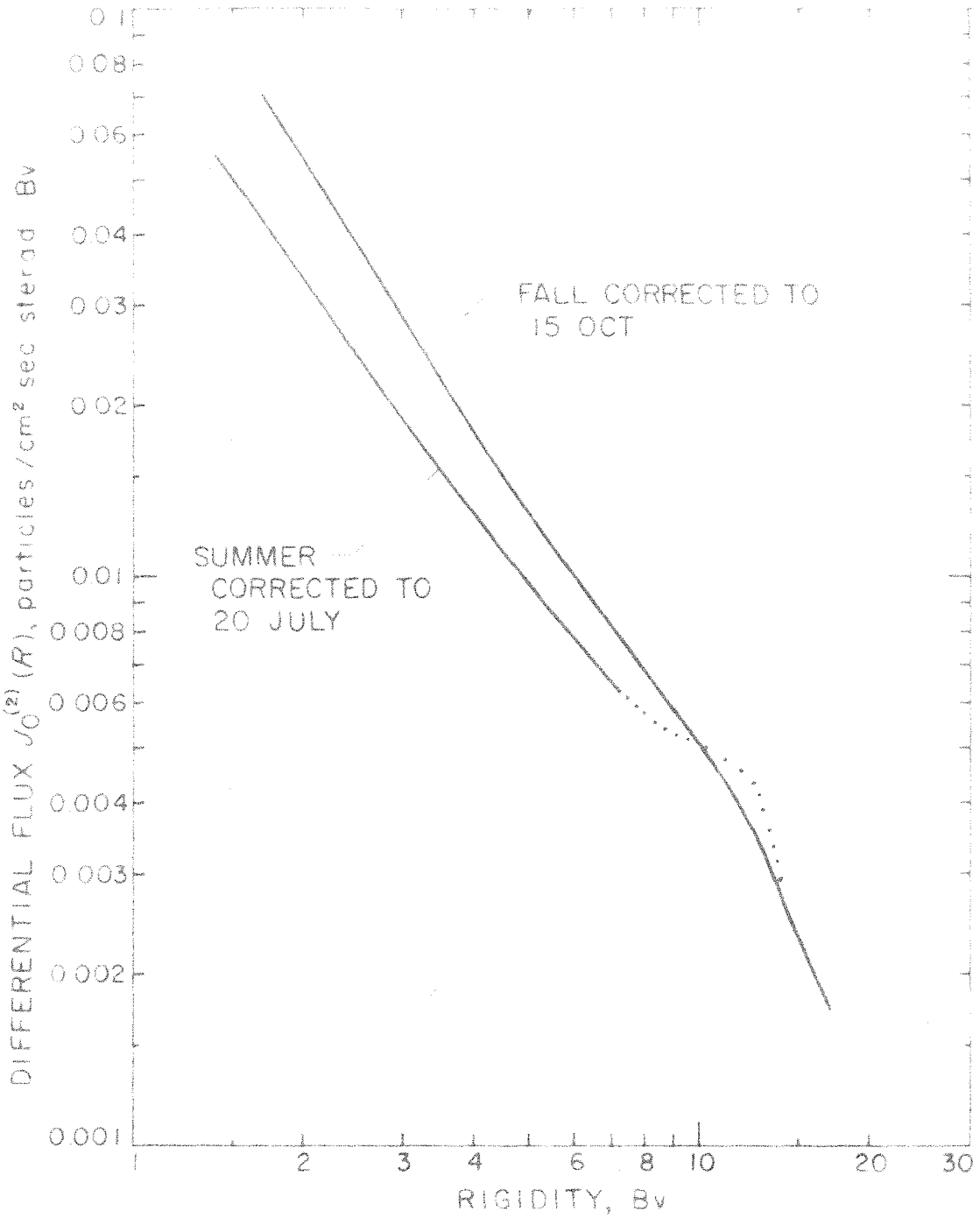

FIG 23 DIFFERENTIAL FLUX $J_0^{(2)}(R)$ vs RIGIDITY, LOCAL FIELD DETERMINED R

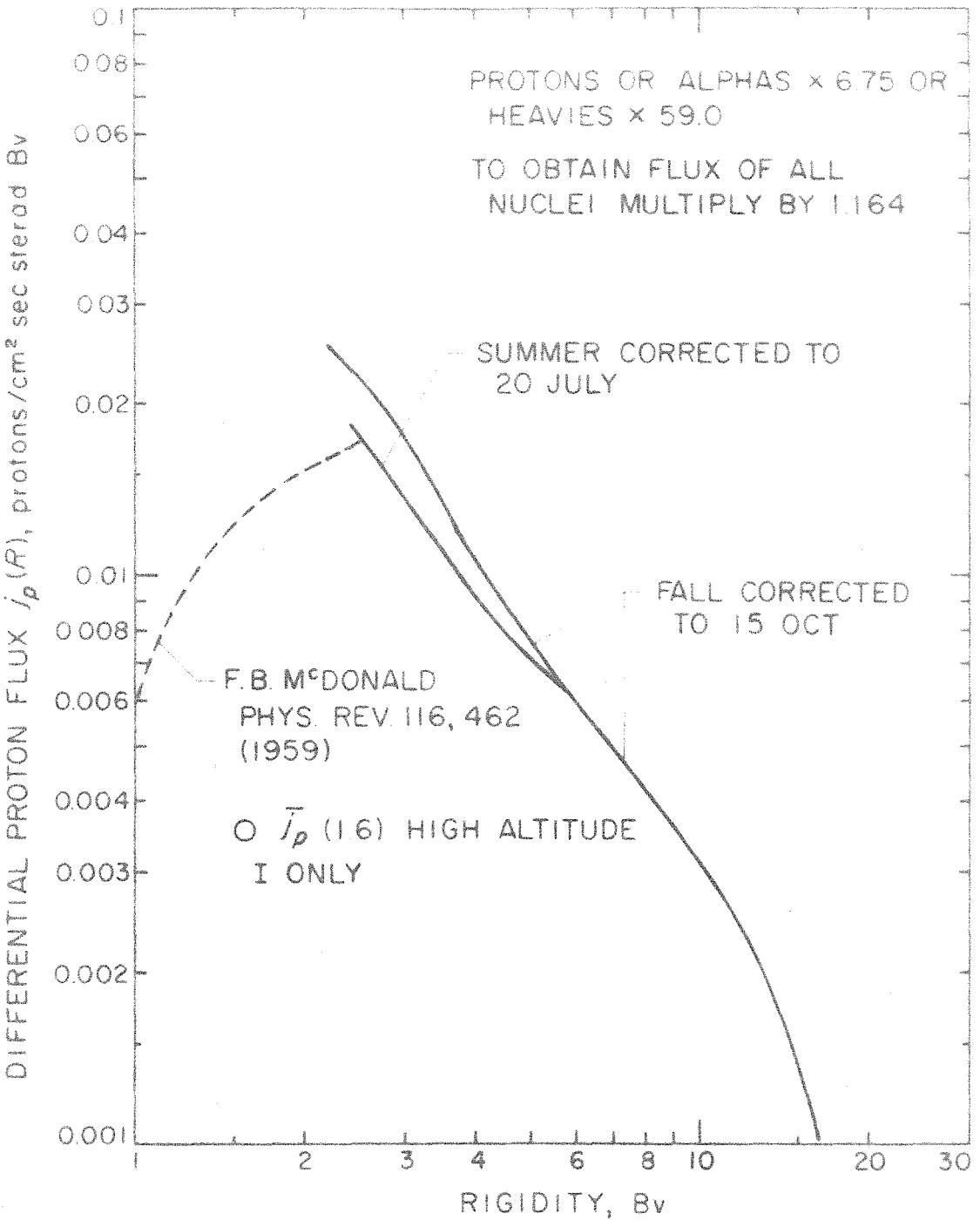

FIG. 24 DIFFERENTIAL RIGIDITY SPECTRUM OF PROTONS $j_p(R)$ vs RIGIDITY

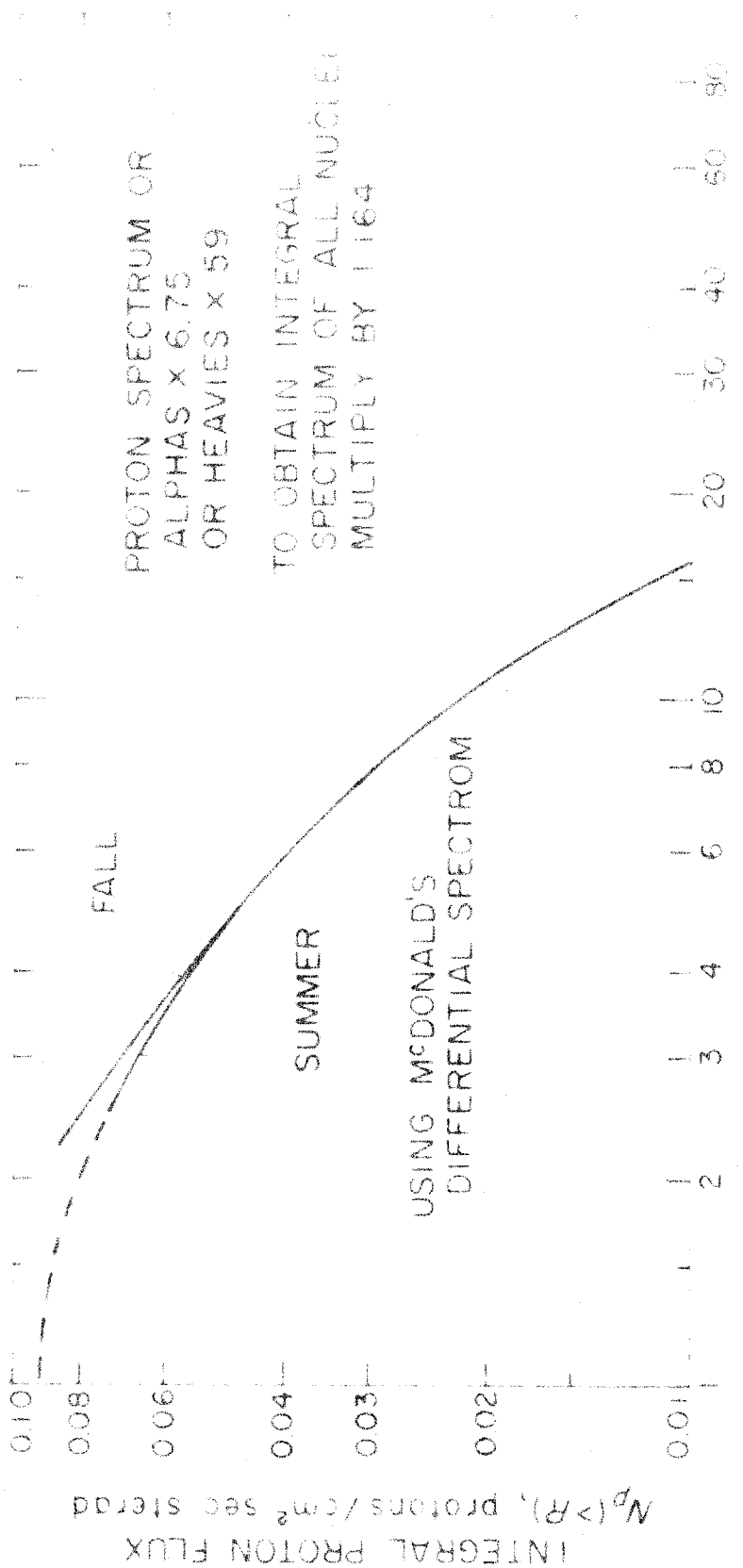

FIG. 25 INTEGRAL PROTON FLUX vs RIGIDITY

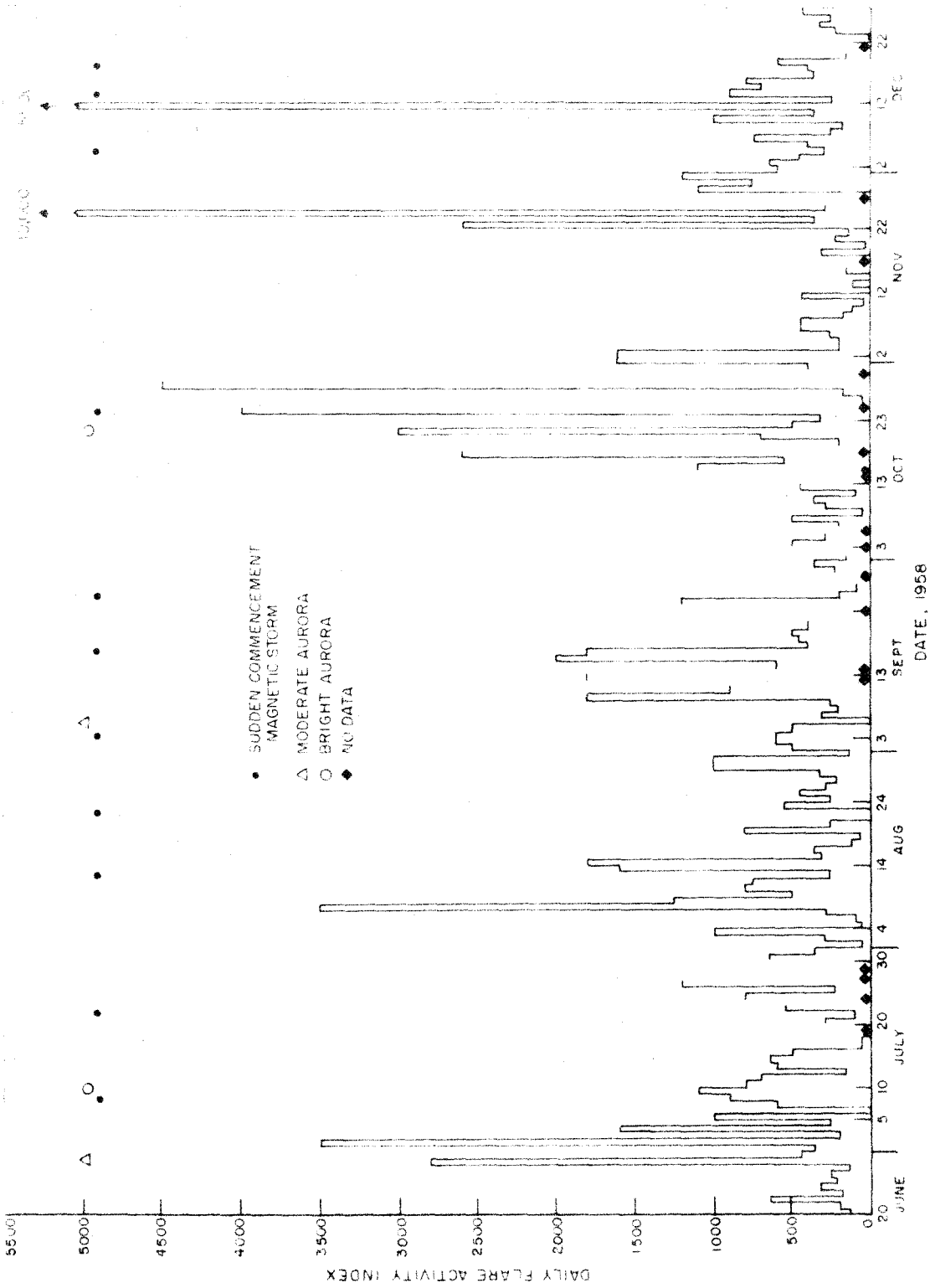

FIG 26 DAILY FLARE ACTIVITY INDEX vs TIME

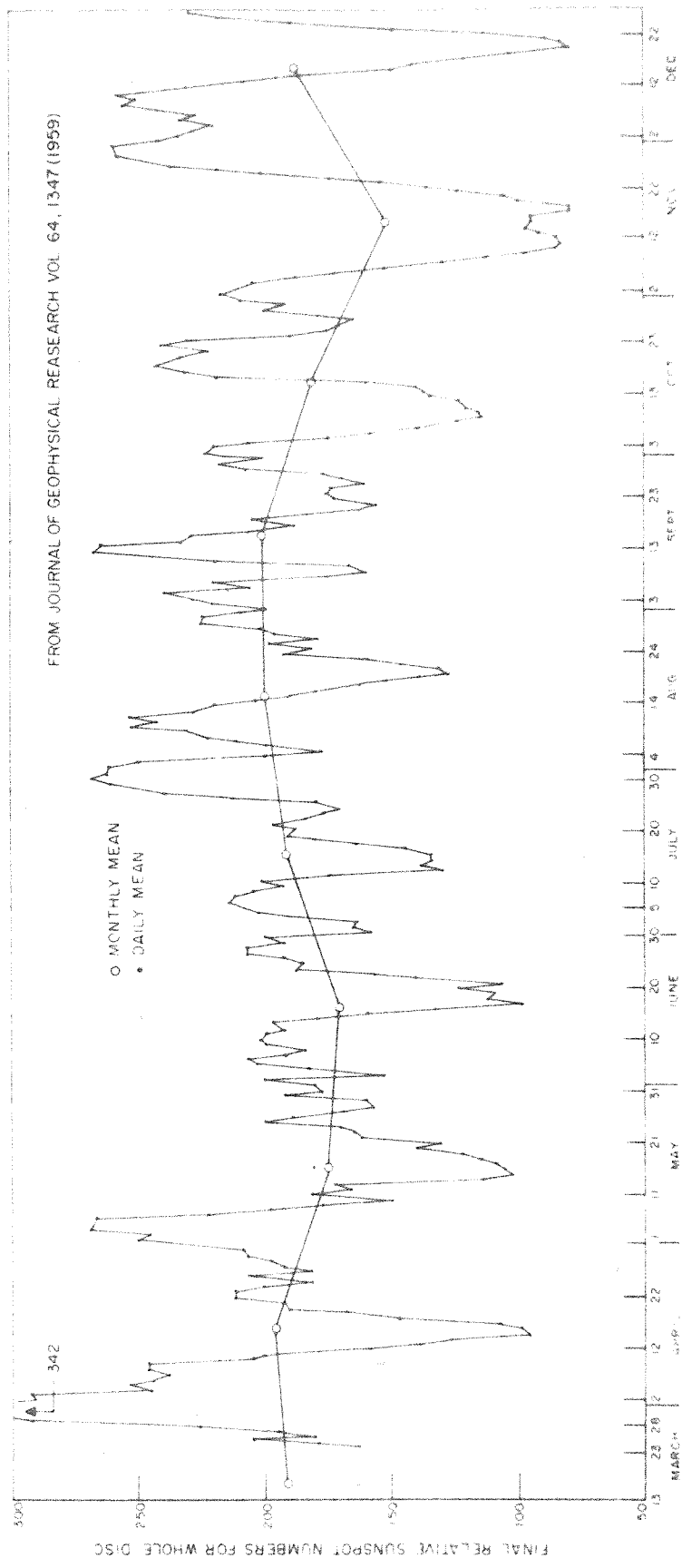

FIG 27 FINAL RELATIVE SUNSPOT NUMBERS

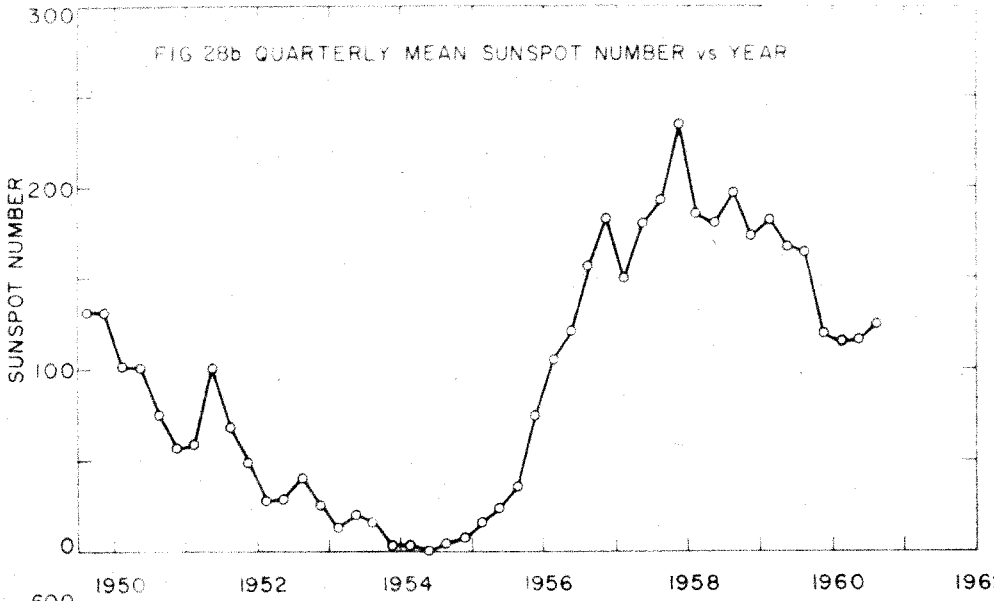
FIG 28b QUARTERLY MEAN SUNSPOT NUMBER vs YEAR
SUNSPOT NUMBER
300
200
100
0
1950
1952
1954
1956
1958
1960
1962

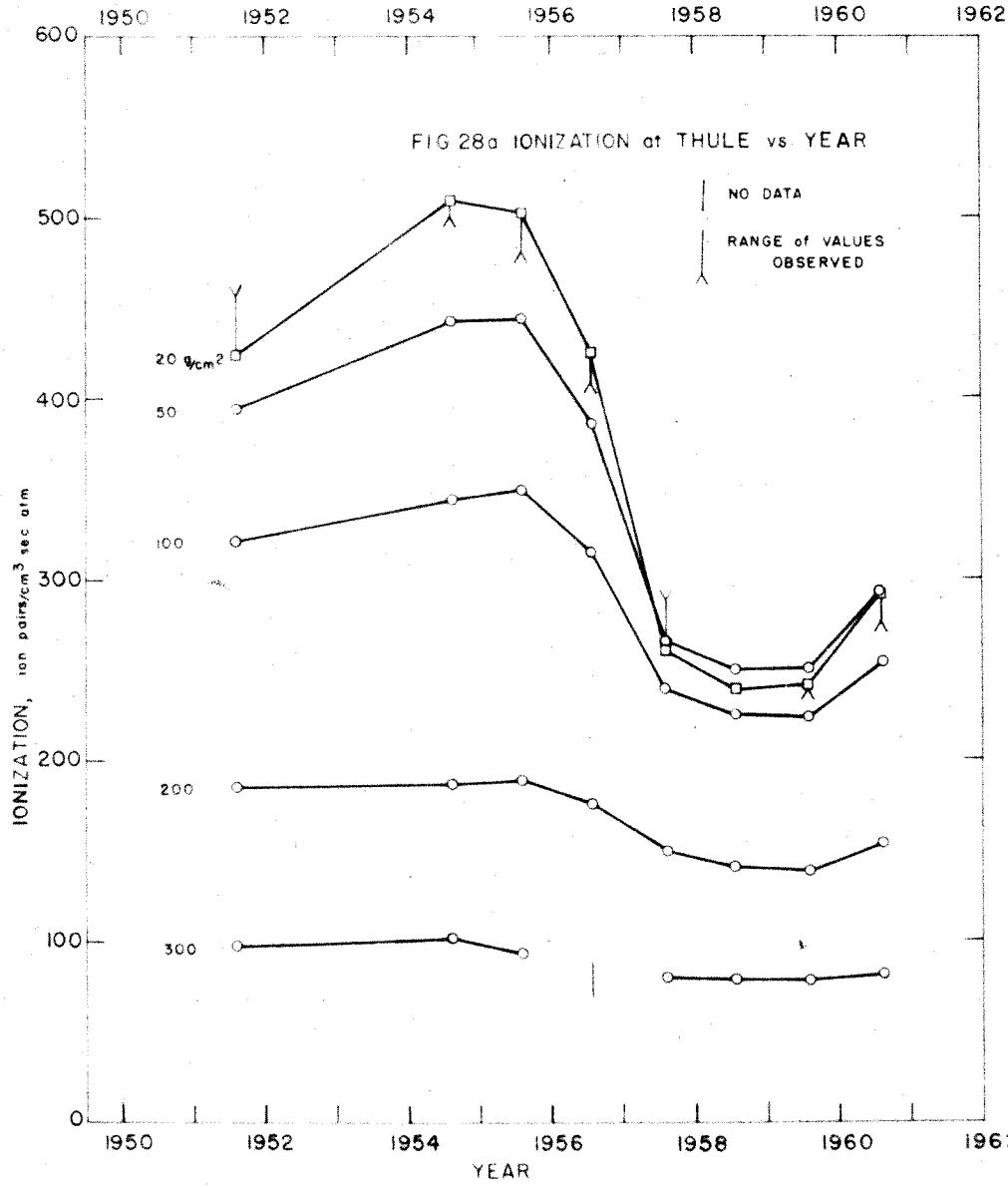
FIG 28a IONIZATION at THULE vs YEAR
NO DATA
RANGE of VALUES OBSERVED
20 g/cm²
50
100
200
300
IONIZATION, ion pairs/cm³ sec atm
600
500
400
300
200
100
0
1950
1952
1954
1956
1958
1960
1962
YEAR

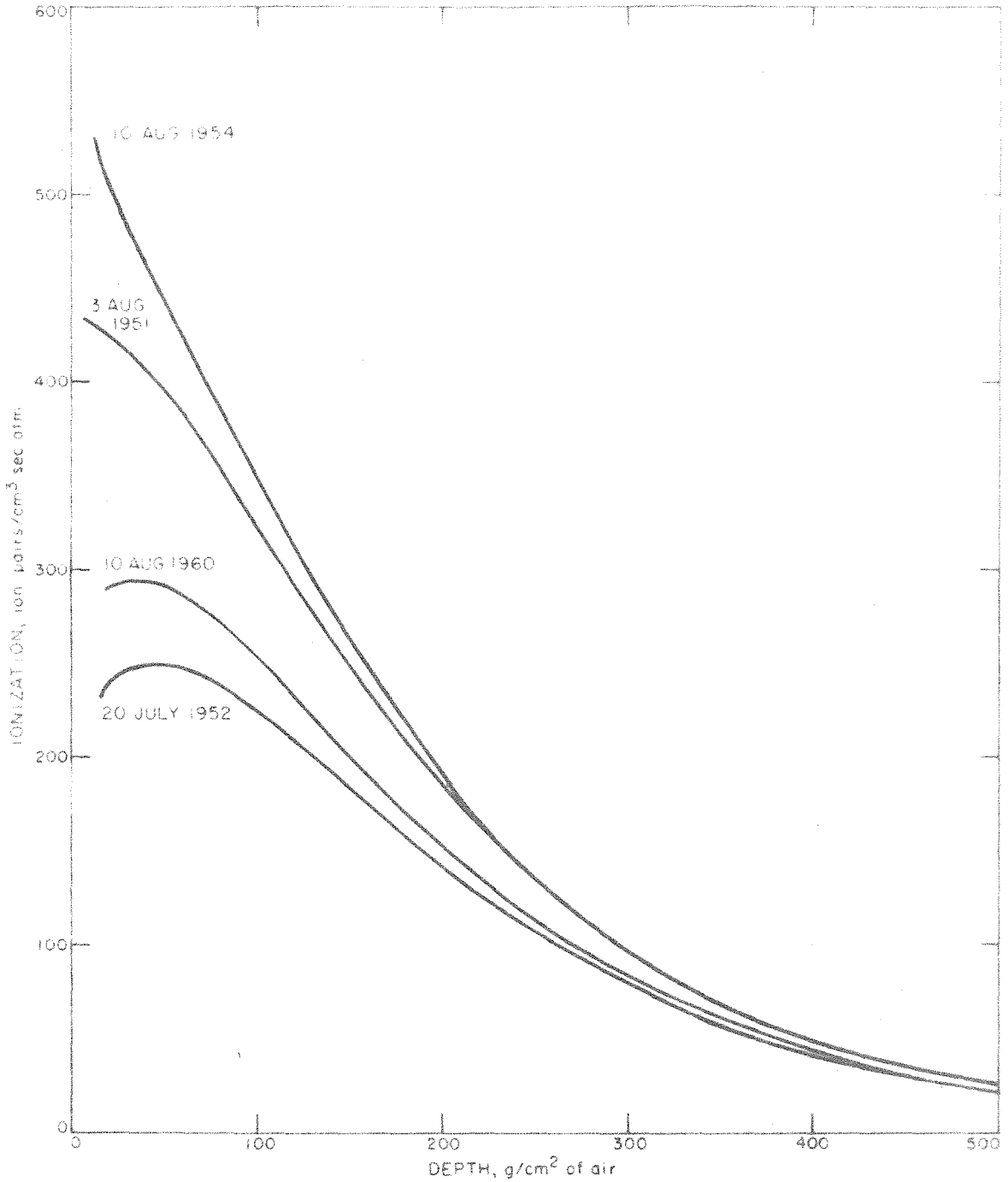

FIG 29 IONIZATION vs DEPTH IN THE ATMOSPHERE AT THULE, GREENLAND
$\lambda_m = 88°N$

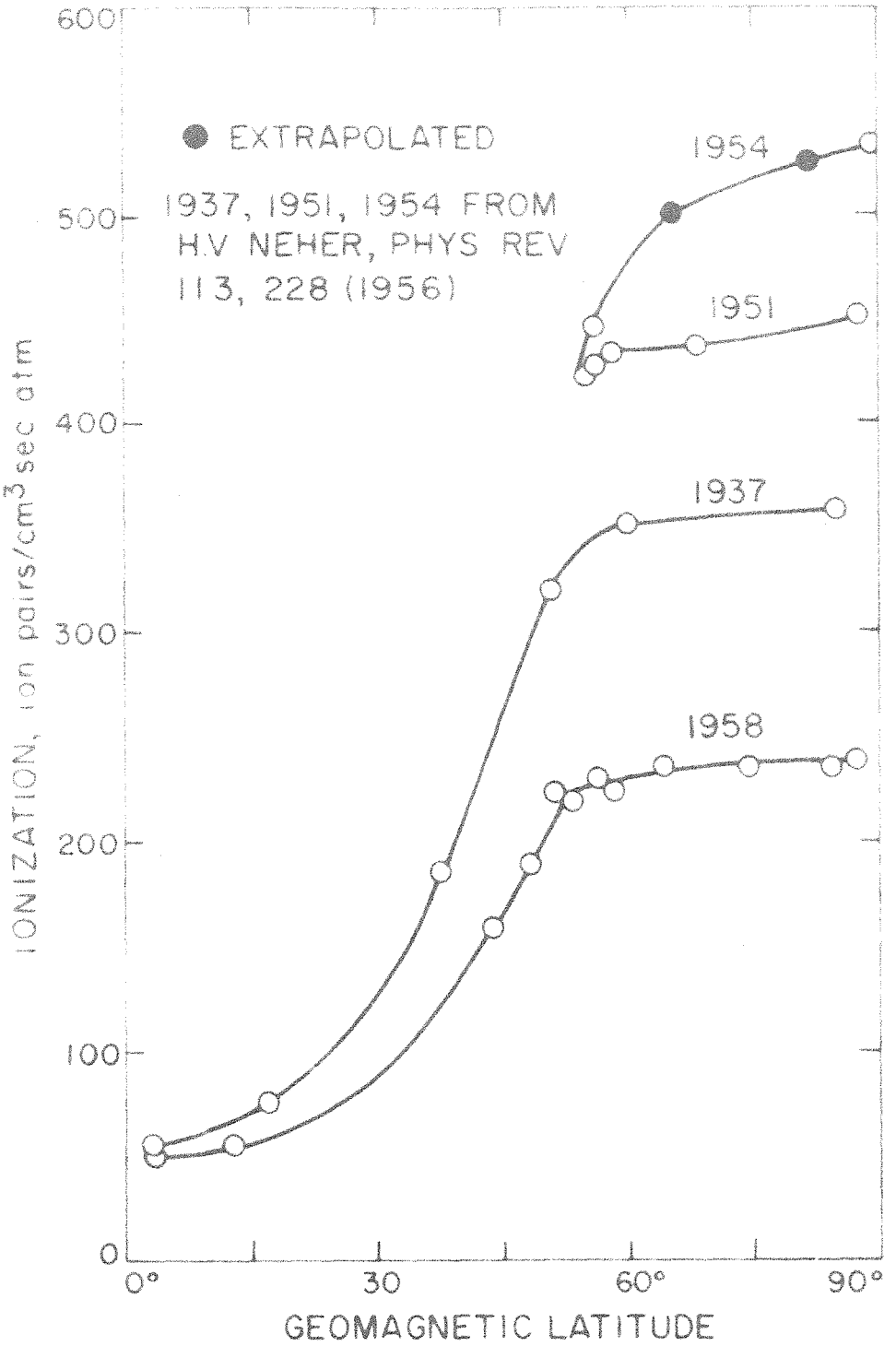

FIG 30 IONIZATION AT 15 g/cm^2 DEPTH vs LATITUDE

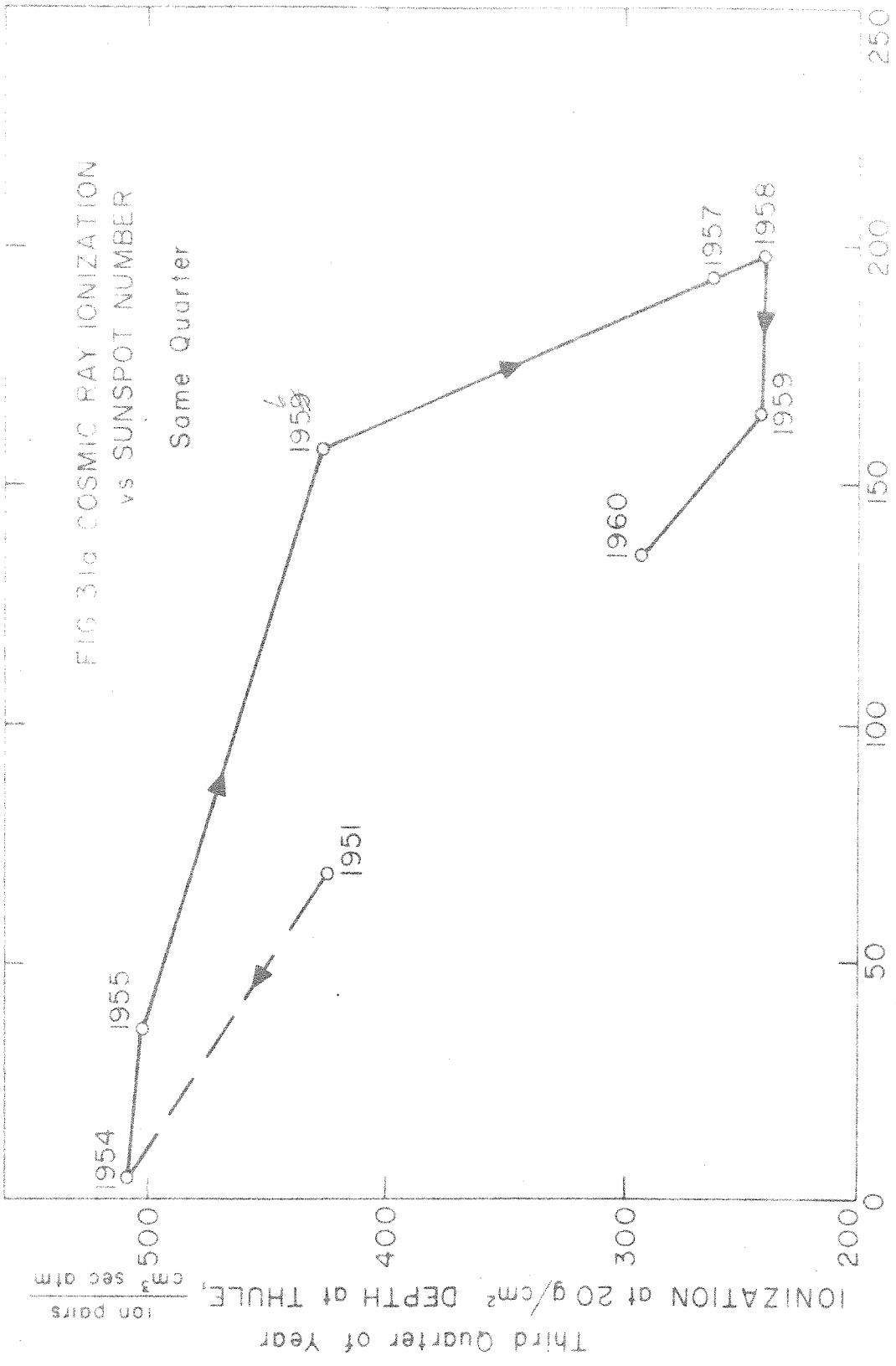
FIG 31a COSMIC RAY IONIZATION
vs SUNSPOT NUMBER
Same Quarter
IONIZATION at 20 g/cm² DEPTH at THULE, ion pairs / cm³ sec atm
Third Quarter of Year
QUARTERLY MEAN SUNSPOT NUMBER
3rd Quarter of Same Year
200
300
400
500
0
50
100
150
200
250
1954
1955
1951
1959
1957
1958
1959
1960

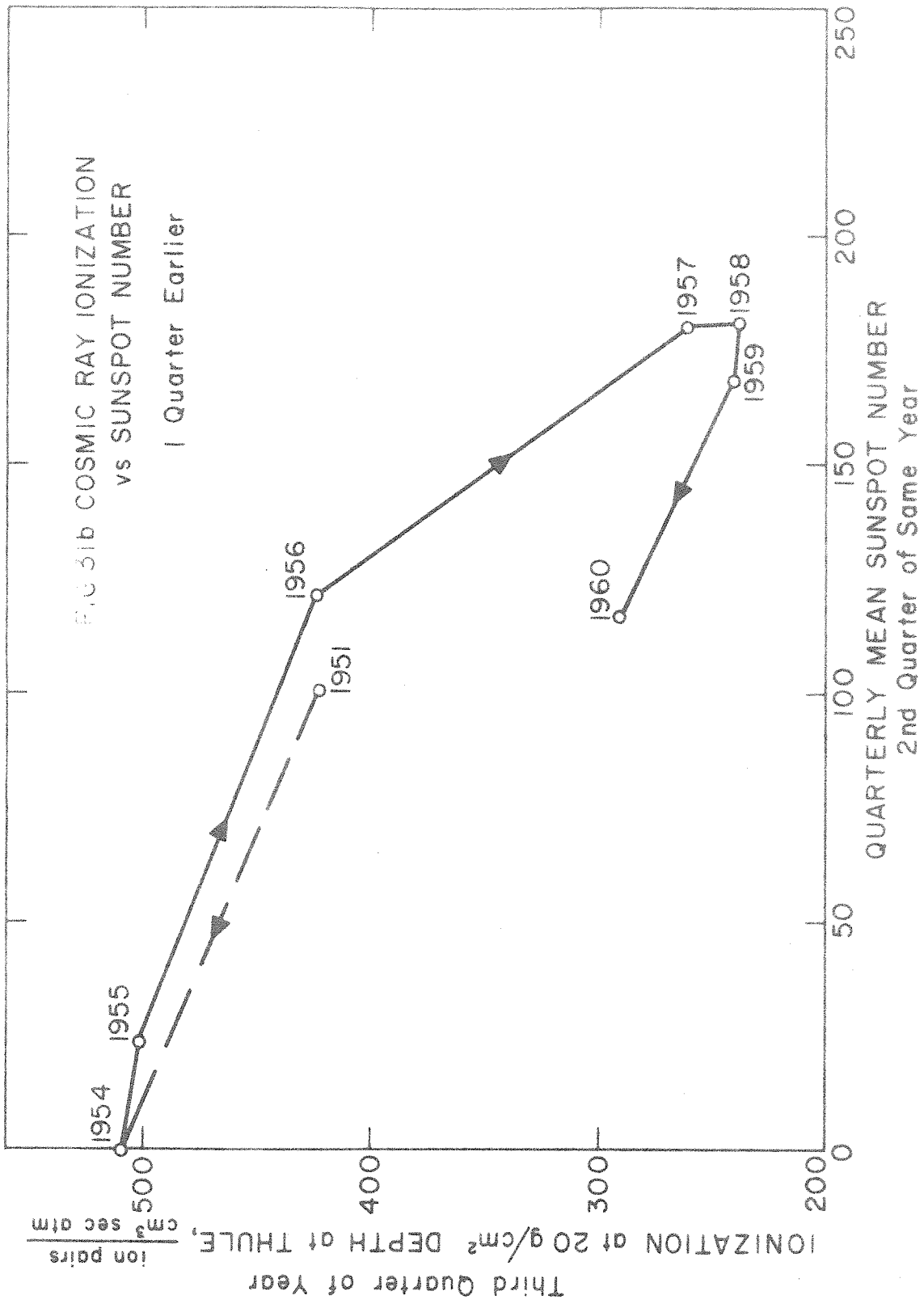
FIG 31b COSMIC RAY IONIZATION
vs SUNSPOT NUMBER
1 Quarter Earlier
1954
1955
1956
1951
1957
1958
1959
1960
200
300
400
500
0
50
100
150
200
250
QUARTERLY MEAN SUNSPOT NUMBER
2nd Quarter of Same Year
Third Quarter of Year
IONIZATION at 20 g/cm² DEPTH at THULE, ion pairs / cm³ sec atm

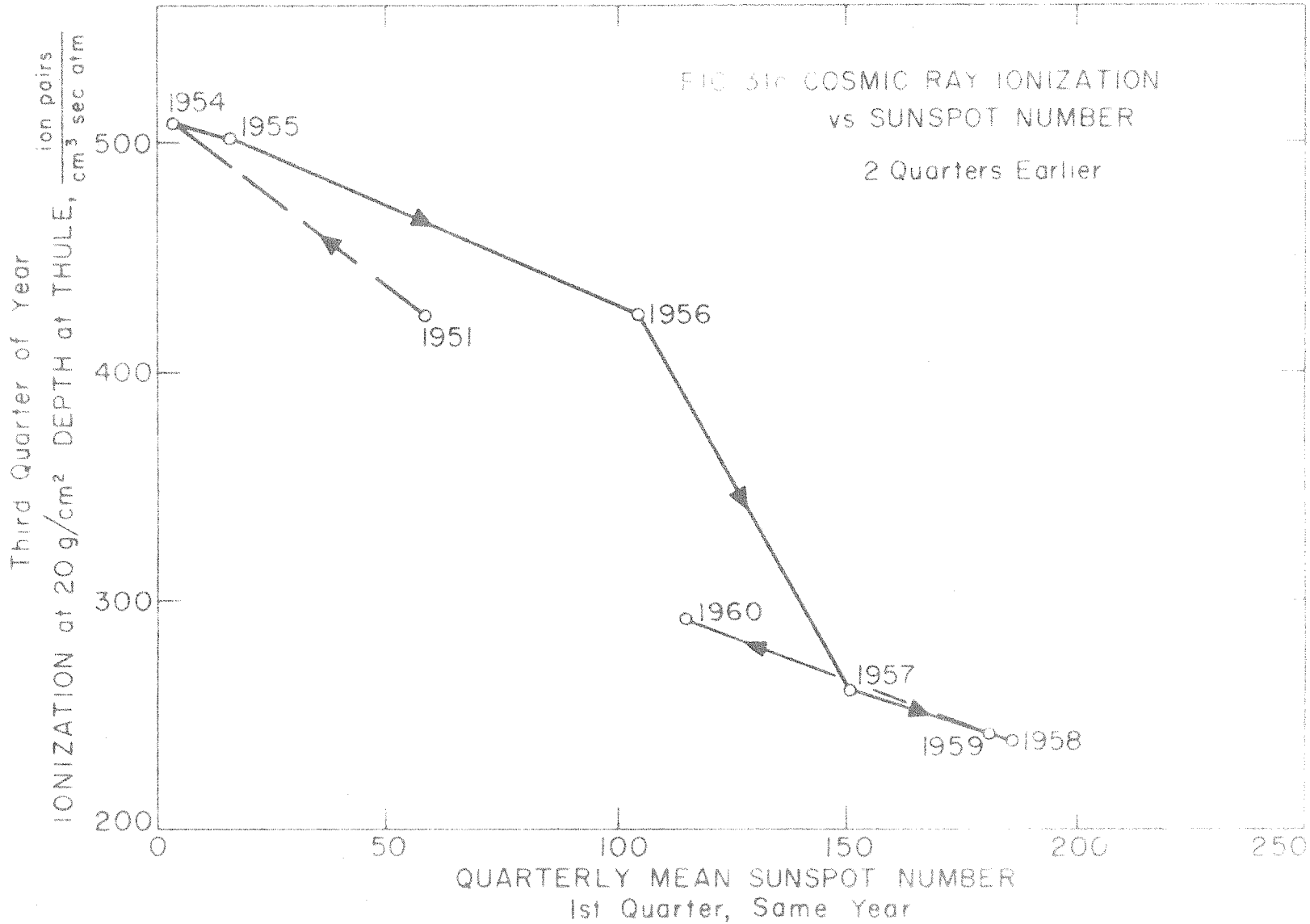
FIG. 51c COSMIC RAY IONIZATION
vs SUNSPOT NUMBER
2 Quarters Earlier
Third Quarter of Year
IONIZATION at 20 g/cm² DEPTH at THULE, ion pairs / cm³ sec atm
500
400
300
200
1954
1955
1956
1951
1960
1957
1959
1958
0
50
100
150
200
250
QUARTERLY MEAN SUNSPOT NUMBER
Ist Quarter, Same Year

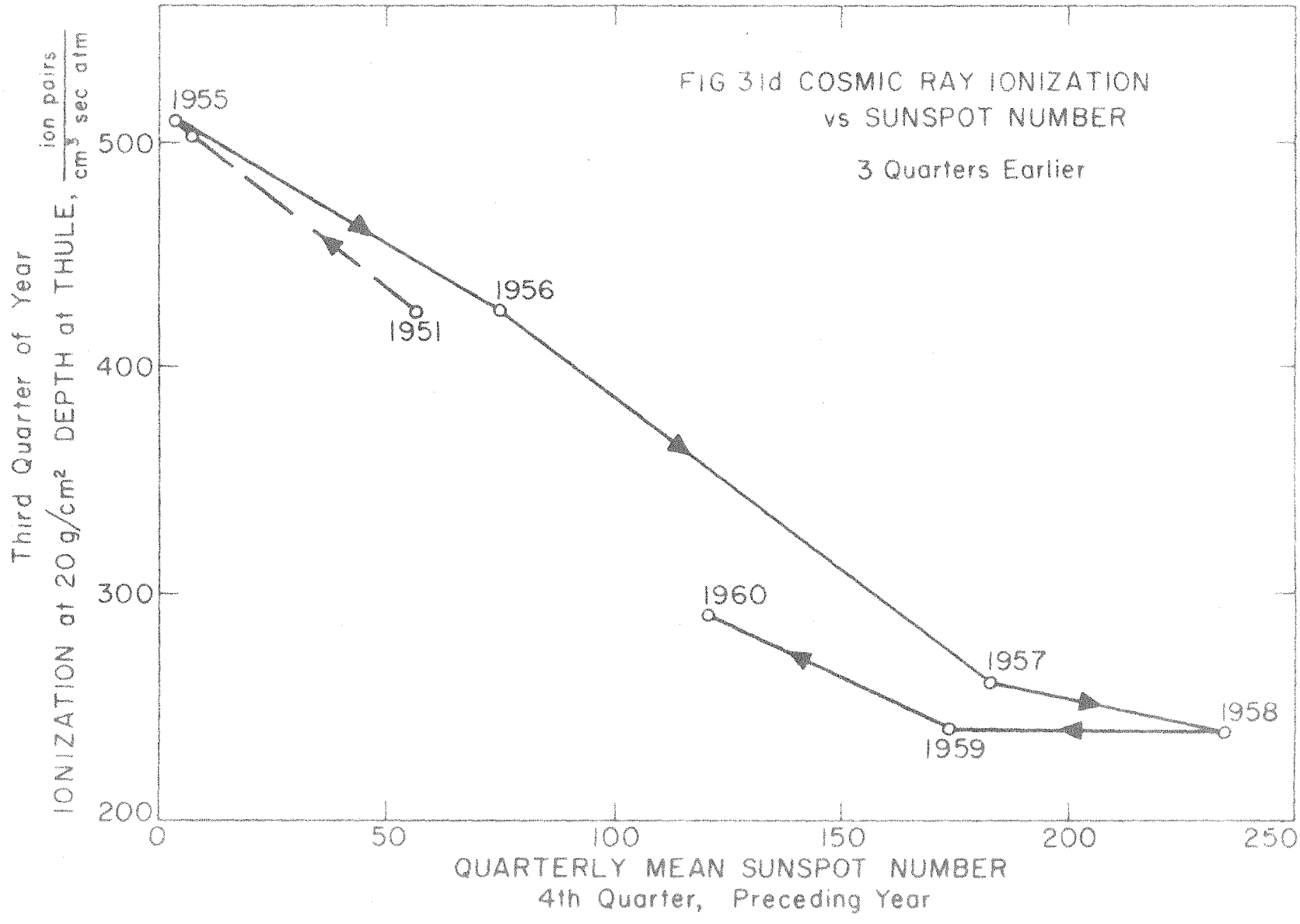
FIG 31d COSMIC RAY IONIZATION
vs SUNSPOT NUMBER
3 Quarters Earlier
Third Quarter of Year
IONIZATION at 20 g/cm² DEPTH at THULE, ion pairs / cm³ sec atm
500
400
300
200
0
50
100
150
200
250
QUARTERLY MEAN SUNSPOT NUMBER
4th Quarter, Preceding Year
1955
1956
1951
1960
1957
1958
1959

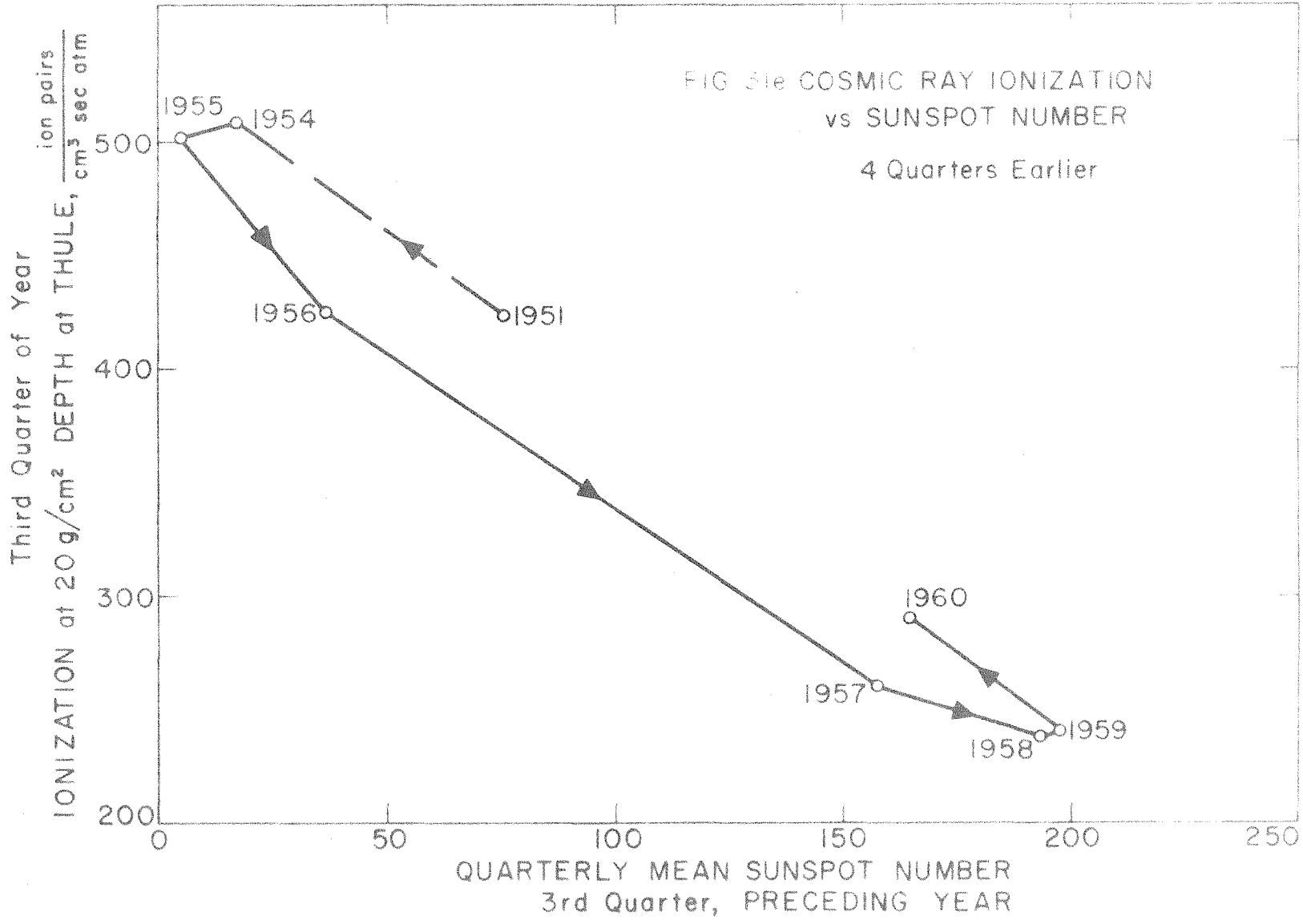
FIG 5le COSMIC RAY IONIZATION
vs SUNSPOT NUMBER
4 Quarters Earlier
Third Quarter of Year
IONIZATION at 20 g/cm² DEPTH at THULE, ion pairs / cm³ sec atm
500
400
300
200
0
50
100
150
200
250
1955
1954
1956
1951
1960
1957
1959
1958
QUARTERLY MEAN SUNSPOT NUMBER
3rd Quarter, PRECEDING YEAR

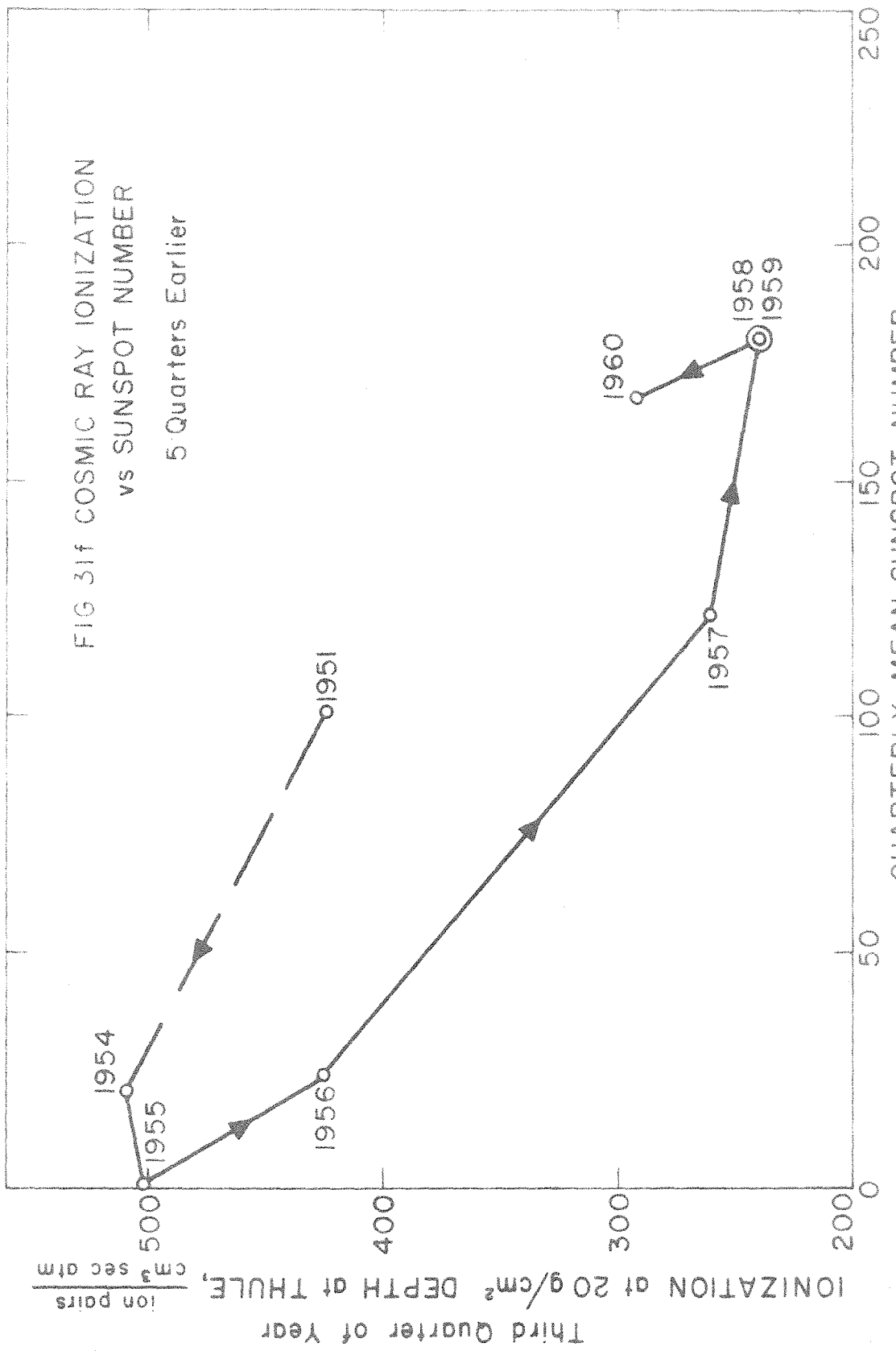
FIG 31f COSMIC RAY IONIZATION
vs SUNSPOT NUMBER
5 Quarters Earlier
Third Quarter of Year
IONIZATION at 20 g/cm² DEPTH at THULE, ion pairs / cm³ sec atm
500
400
300
200
0
50
100
150
200
250
QUARTERLY MEAN SUNSPOT NUMBER
2nd Quarter, Preceding Year
1954
1955
1956
1951
1957
1958
1959
1960

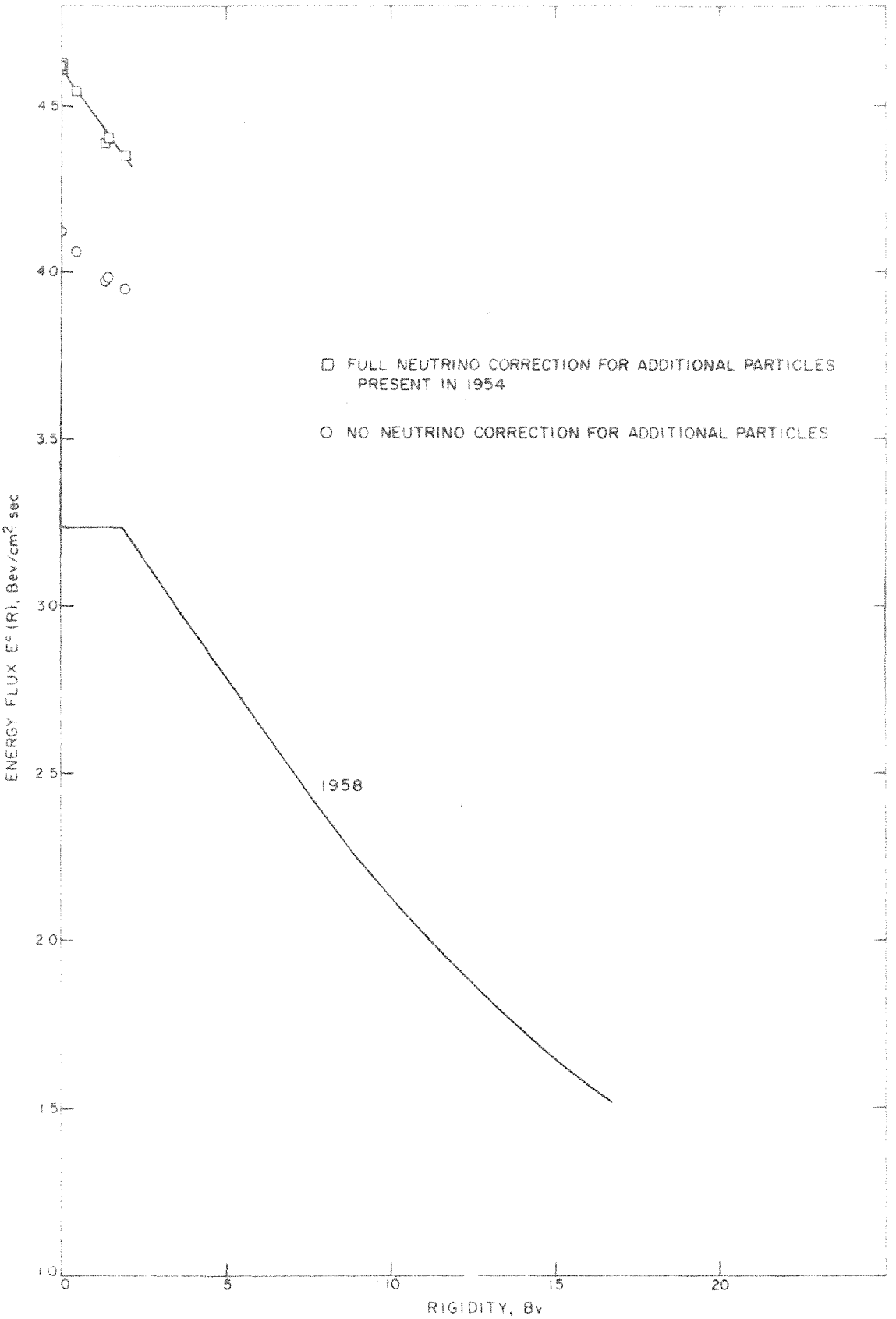

FIG 32 CORRECTED ENERGY FLUX vs CENTER DIPOLE CUTOFF

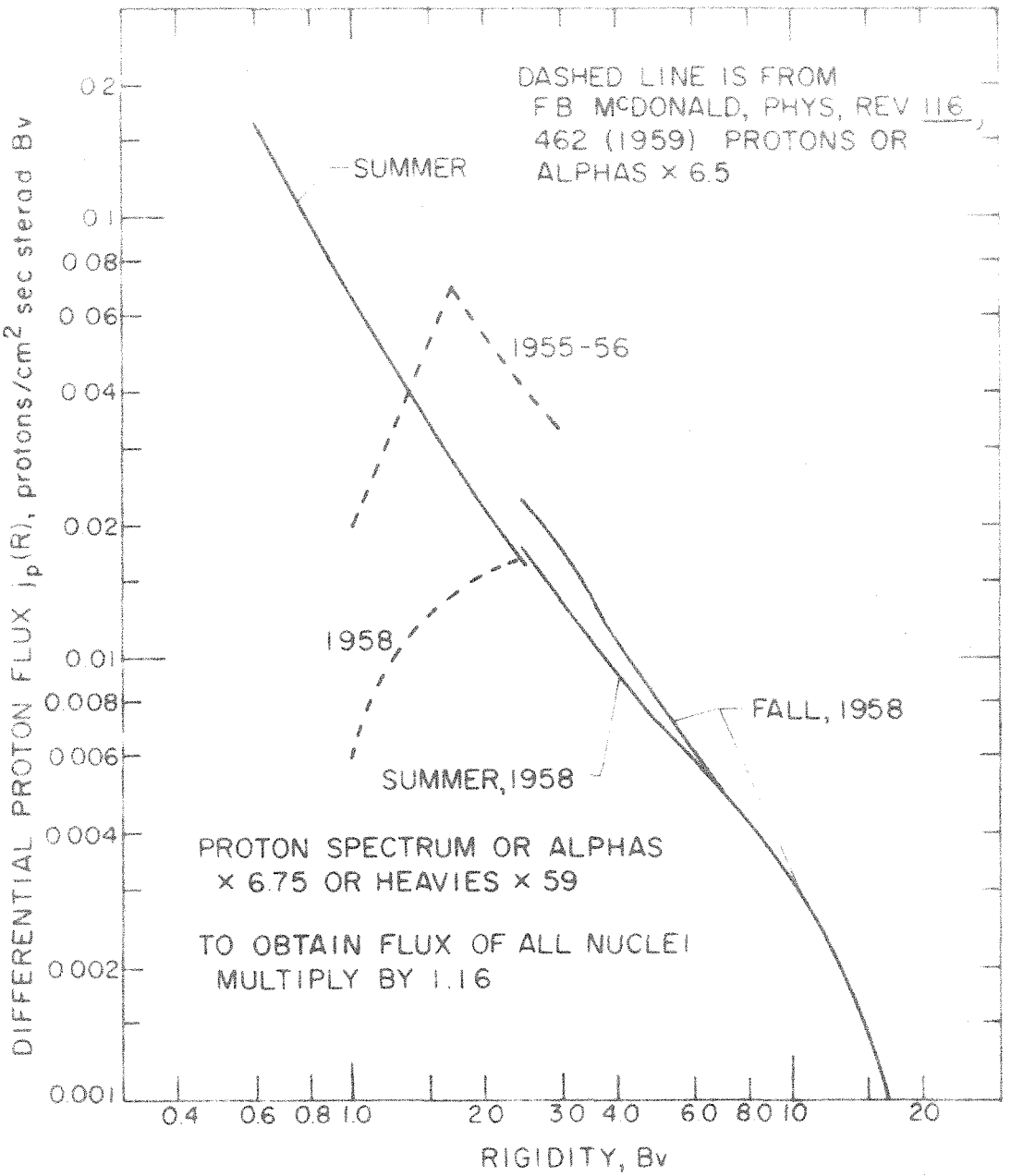

FIG 33 DIFFERENTIAL RIGIDITY SPECTRUM OF PROTONS

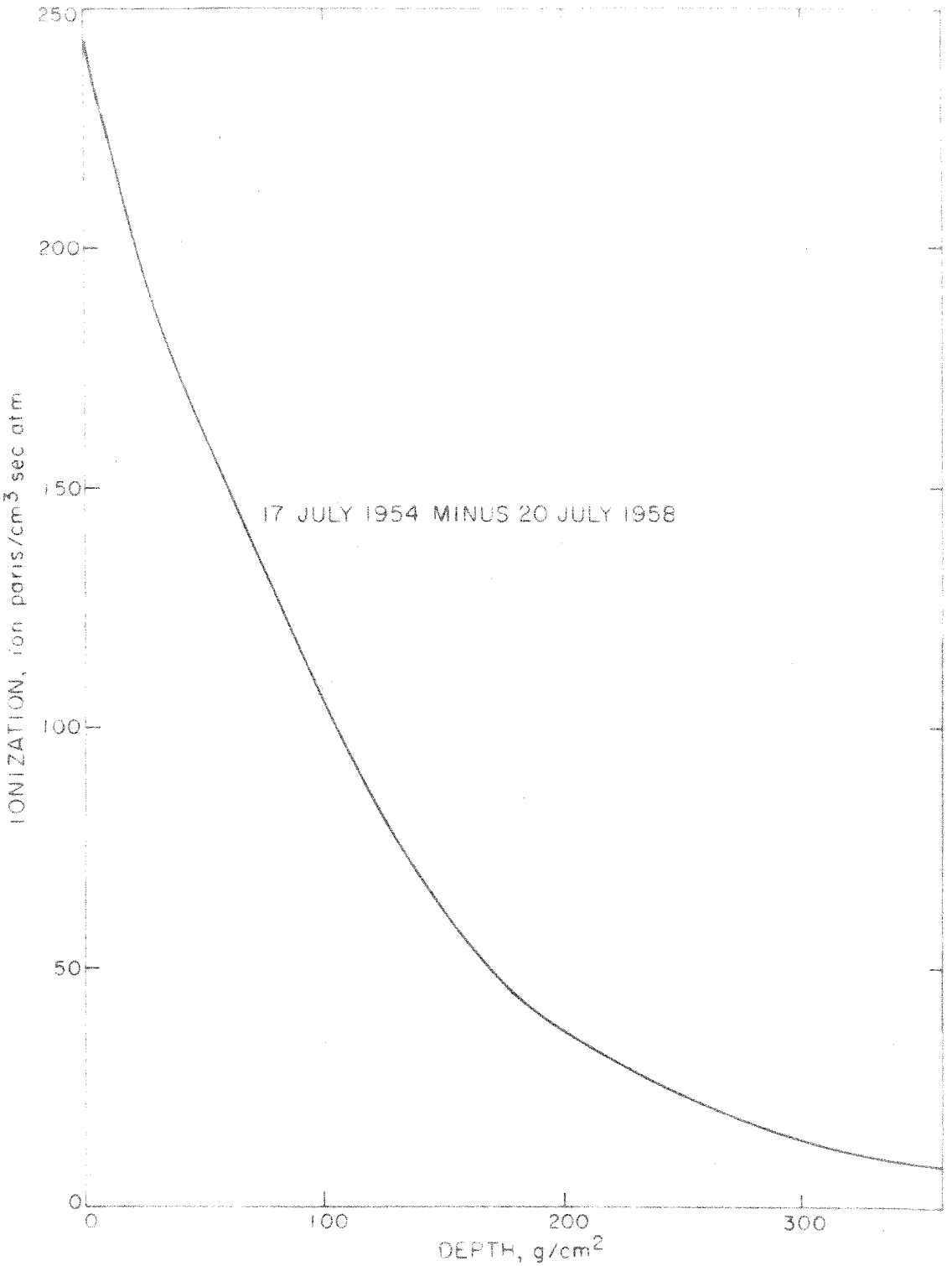

FIG 34 IONIZATION vs DEPTH, DIFFERENCE AT BISMARCK, 1954 MINUS 1958

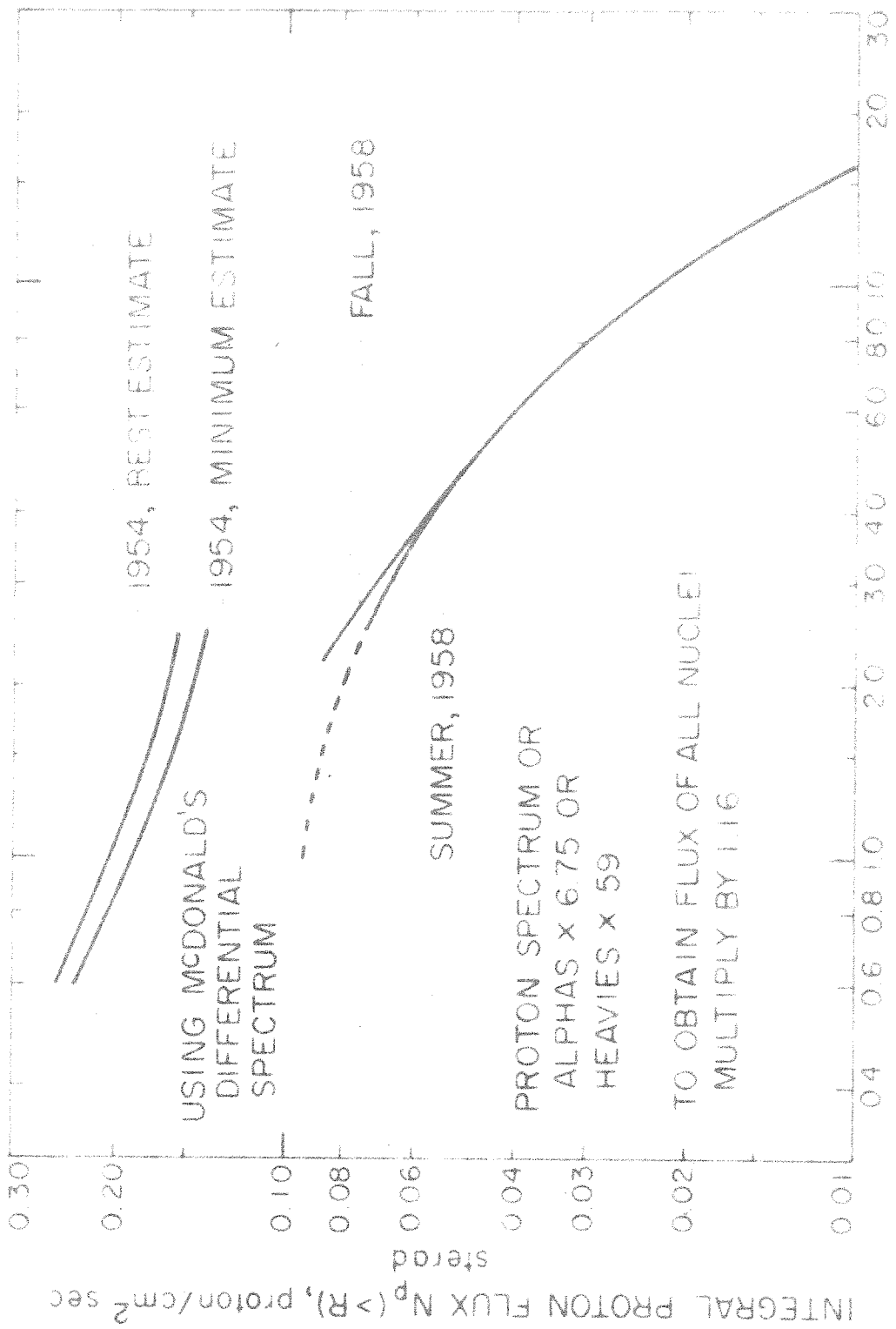

FIG 35 INTEGRAL PROTON FLUX VS RIGIDITY